DOTTORATO DI RICERCA IN

MECCANICA E SCIENZE AVANZATE DELL'INGEGNERIA

Ciclo 37

Settore Concorsuale: 09/C2 - FISICA TECNICA E INGEGNERIA NUCLEARE

Settore Scientifico Disciplinare: ING-IND/11 - FISICA TECNICA AMBIENTALE

NON-ITERATIVE NUMERICAL SIMULATION TECHNIQUES FOR NONLINEAR STRING VIBRATION IN MUSICAL ACOUSTICS

Presentata da: Riccardo Russo

Coordinatore Dottorato	**Supervisore**
Lorenzo Donati	Michele Ducceschi
	Co-supervisore
	Cesare Biserni

Esame finale anno 2025

Abstract

Physics-based sound synthesis of musical instruments has seen growing interest in recent years, as it allows for reproducing realistic and natural sounds while offering great flexibility and minimal storage requirements. This research falls within the scope of the NEMUS project, which is dedicated to the digital reproduction of the sound of ancient stringed instruments using physical modelling techniques. Specifically, this work focuses on the numerical simulation of nonlinear string vibration. Nonlinearities are a critical factor in accurately replicating the sound of real-world instruments. Much of the recent literature has employed energy-based methods to ensure algorithmic stability when nonlinear behaviour is present, often resulting in fully implicit schemes requiring iterative root-finding methods. While effective, these schemes are computationally expensive and introduce additional complexities.

Recent developments in numerical analysis have, in some cases, enabled real-time simulation of strongly nonlinear systems using non-iterative algorithms. However, several challenges remain unresolved. This thesis aims to advance the use of finite-difference time-domain and modal methods to address nonlinearities in string vibration, which capture salient perceptual features. The emphasis is on the efficiency of the algorithms, while also developing a framework for the sound synthesis of nonlinear strings.

The work begins with a comprehensive review of string models and simulation techniques, covering both historical and modern approaches. Linear models are then used as a starting point, allowing for the introduction of impedance-type boundary conditions. The research then investigates typical nonlinear effects in string vibration, such as geometric nonlinearities, collisions, and friction, using newly developed non-iterative approaches, including quadratisation-based methods for conservative forces. These techniques significantly reduce computation times, making real-time simulation feasible for most systems. However, the quality of the simulations is still highly dependent on tailored discretisation choices. The thesis concludes with two case studies that apply these methods to physical models of musical instruments.

Acknowledgements

This thesis is the product of three years of research, coinciding with the start of the NEMUS project and the formation of the musical acoustics research group at the University of Bologna. It has been an intense journey; much has changed since the beginning, and along the way, I have had the chance to meet many people who have sustained me in various ways, for which I am deeply grateful.

First, I would like to thank my supervisor, Michele Ducceschi, for his invaluable help and support. My work under his guidance began during my Master's thesis when he was in Edinburgh, and to him, I owe much of what I know: not just about physical modelling and numerical schemes but about research itself. Needless to say, this thesis would not have seen the light without him. In the first year of my PhD, I was the only NEMUS student, and everything had to be built from scratch. While providing excellent supervision, Michele also had to take on the challenge of navigating the administrative bureaucracy of the University of Bologna, new to both of us, in order to assemble the team.

I am extremely grateful to Stefan Bilbao, who effectively acted as a co-supervisor, even though this role had not been formalised. During my time at the University of Edinburgh, he dedicated significant time and great effort to my supervision, regularly checking in on my progress and offering indispensable advice. He has been a great source of inspiration, and I have learned an incredible amount from him: much of this work would not have been possible without his guidance.

Furthermore, I would like to sincerely thank Stefania Serafin, coordinator of the Sound and Music Computing Master's programme at Aalborg University Copenhagen. She introduced me to physical modelling sound synthesis, and it was thanks to her that I found the inspiration to pursue a PhD.

Many thanks to all my colleagues from NEMUS: Sebastian Duran, Craig Webb, Henna Tahvanainen and Matthew Hamilton, for the fruitful work done together and for the scientific meetings at La Frasca; a special mention to Craig for proof-reading this thesis. I am also grateful to my current and former colleagues from the acoustics group: Giulia Fratoni, Gioia Fusaro, Domenico De Salvio, Vincenzo Pettoni Possenti and Matteo Cingolani, especially

for making me feel welcome when I had just started and knew no one in the department; thanks also to Virginia Tardini and Alessia Nora.

I would also like to thank the people from the Acoustics and Audio Group at the University of Edinburgh (in addition to Stefan): Alistair Carlson, Thomas McKenzie, Tom Mudd, Alec Wright and Mike Newton, for warmly welcoming me into their research group; it has been an amazing six months. I am also grateful to Romain Michon, Tanguy Risset, Pierre Cochard and Yann Orlarey from the Emeraude team at INSA Lyon for making my visit an exciting week.

I am particularly thankful to the reviewers of my thesis: Vincent Debut and Maarten Van Walstijn, for the valuable comments and constructive critiques, which have significantly improved the value of this work. Furthermore, thanks to Maarten and Vasileios Chatziioannou for the fruitful scientific discussions.

Thanks to Stefania for being an incredibly supportive partner and especially for keeping me sane during the write-up period. Finally, I am infinitely grateful to my parents: Maria Luisa and Paolo, for allowing me to make mistakes while always encouraging and sustaining me in every decision that ultimately led me to this point. This work is dedicated to you.

Table of contents

List of figures

List of tables

Acronyms

1-D 1-dimensional. 2–4, 6–9, 11, 32

3-D 3-dimensional. 8

BVP boundary value problem. 33

CAD computer-aided design. 7

CFL Courant-Fredrichs-Lewy. 70, 106

DoF degree(s) of freedom. 29–31

DWG digital waveguide(s). 4, 5, 7, 9–11, 15

FD finite-difference. 49, 51–53, 56, 63, 69, 73, 165, 166

FDTD finite-difference time-domain. 4–7, 10–13, 15, 16, 49, 74, 167

FE forward euler. 61, 134

FEM finite element method. 7, 10, 12, 13

FTM functional transformation method. 7, 10

GE geometrically exact. 8–12, 16, 17, 104, 166, 168

IEQ invariant energy quadratisation. 16, 22, 82, 86, 92, 104, 109

IVP initial value problem. 20, 22, 61

KC Kirchhoff-Carrier. 8–10, 16, 17, 166

LTE local truncation error. 56, 57, 59, 70, 71

MI Morse-Ingard. 9, 11, 12, 17, 86

ODE ordinary differential equation. 5–7, 10, 17, 19, 20, 23, 29, 31, 36, 42, 44, 61, 129, 133, 165

OF oversampling factor. xvii, 97, 106, 116, 134, 141, 145

PDE partial differential equation. 2, 3, 6, 7, 19, 31, 41, 49, 83

PHS port-Hamiltonian systems. 10, 16, 25, 131, 138, 140

SAV scalar auxiliary variable. 16, 22, 79, 82, 86, 90, 92, 99, 103–105, 109, 118, 119, 147, 166–168

SHO simple harmonic oscillator. 23, 32, 35, 36, 45, 53, 57, 71, 79, 80, 97, 107, 129, 131

Chapter 1

Introduction

This work fits into the context of the NEMUS project[1], which is dedicated to the digital reproduction of the sound of ancient stringed instruments. In particular, the major focus of this thesis is the string, the basic sound production mechanism, or resonator, of these instruments. Stringed instruments play a major role in music production in virtually every culture and have been built for thousands of years. Therefore, countless types are available: a comprehensive summary can be found in [94, 40, 50]. They are traditionally classified into three main categories based on the primary method used to excite the string [173]: bowed instruments, such as violins and cellos; plucked instruments, like the guitar and harpsichord; and hammered instruments, including the piano.

Given the ubiquity of the string in music, it is unsurprising that, with the development of sound synthesis in the mid-20th century, great effort was directed toward artificially reproducing its sound. Particularly with the advent of digital sound synthesis, a great variety of techniques were developed, which can be grouped into four categories [191]: abstract synthesis, including FM and Karplus-Strong [124]; recording-based synthesis, such as sampling and wavetable; spectral synthesis and physical modelling. Further details on these approaches can be found in [171]. While sampling methods are undoubtedly the most widespread nowadays, physical modelling has seen growing interest in recent years [25]. The latter refers to a group of techniques that rely on the digital simulation of physical systems: the core concept involves describing a specific musical instrument with a mathematical model, resulting in a set of equations. Subsequently, suitable numerical algorithms are employed to solve the models in real-time and produce sound. The appeal of these methods lies in the extreme flexibility provided: the mathematical models describing the instruments depend on a set of parameters linked to, for instance, the instrument's geometry and materials. This allows direct and (often) real-time control over the sound characteristics, something not available

---

[1] https://site.unibo.it/nemus-numerical-sound-restoration/en

in recording-based synthesis. Moreover, the absence of recorded material implies that no large storage capacities are needed. The downside of physical modelling is the significant computational power required for the simulations, which can sometimes hinder real-time processing. This challenge becomes particularly pronounced when dealing with mathematical models that exhibit nonlinear behaviour, which is necessary for accurate reproductions of real-world instruments' sound. In NEMUS, where the focus is on faithful reproductions of musical instruments, nonlinear systems play a major role, and state-of-the-art numerical methods are required to simulate these models efficiently.

The work presented in this thesis is concerned with the numerical simulation of nonlinear string models, whose vibration captures salient perceptual features. Particular attention is paid to the efficiency of the algorithms, aligning with recent advances in numerical analysis that, in some cases, have enabled real-time simulation of strongly nonlinear systems. Newly developed numerical methods are adapted here to address nonlinearities of different kinds, and various case studies are presented.

The rest of this introductory chapter overviews the most relevant string mathematical models and the numerical techniques employed to simulate them. It begins by introducing linear models and the most common simulation techniques. Subsequently, nonlinear effects are described, and a thorough list of significant simulation works is provided. This examination covers historical and contemporary approaches, illustrating the evolution of string simulation techniques and their applications in musical acoustics. Finally, the objectives and structure of the thesis are outlined.

1.1   Linear string

Early scientific investigations on the vibration of strings can be traced back to Pythagoras, who first related the length of a string to the pitch of the emitted sound. He also examined the sound produced by strings of different lengths under tension, discovering that pleasing results were obtained when the relative lengths were in integer ratios. Several centuries later, Galileo formulated the relation between the number of vibrations per unit time (frequency) to the pitch [Chapter 1][173]. The first mathematical model of string vibration had to wait until the mid-XVIII century, when D'Alembert, building on Taylor's work [99, Chapter 2], formulated the hyperbolic 1-D wave equation [133], representing the first ever example of a partial differential equation (PDE) [222]. The wave equation remains important to this day, beyond its historical relevance, as it serves as a crude model for string vibration and air motion inside an enclosed tube. Moreover, it possesses a closed-form solution in the form

of D'Alembert's travelling waves, and it may be solved exactly via numerical methods [24, Chapter 6].

The wave equation alone is of little utility in musical acoustics, as it omits physical aspects which lead to important perceptual features. In particular, stiffness is responsible for the inharmonicity of the partials in the emitted sound, which is perceived as a widening of the octaves [61], and helps mitigate the beating effect when multiple notes are played simultaneously [101]. Assorted mathematical models for stiff strings are available in the literature, relying on different levels of approximation. From a physical standpoint, a stiff string is a beam under tension in the longitudinal direction; thus, the governing equations are typically derived from beam theories. The most accurate models of beams available are based on geometric arguments [19, 119] and offer a complete 3D description of the motion. In musical acoustics applications, approximate theories are sufficient, typically obtained by treating the effects along the cross-section globally [Chapter 3][104]. This is also called thin beam approximation and is considered valid for wavelengths greater than the beam thickness [169]. Four different beam theories were developed under this hypothesis: Timoshenko, shear, Rayleigh and Euler-Bernoulli [109].

The Timoshenko model is the most complete of the four, describing both transverse and shear waves, and it comes in the form of two coupled PDEs, which can be combined into one single fourth-order equation. The other three models can be derived from this one by introducing various simplifications. Different tests were conducted to validate the model [62, 169, 197], and they reported agreement with experimental results, indicating the validity of the Timoshenko model as a reference. On the other hand, the Euler-Bernoulli model is the simplest of the four and, for this reason, has seen the most applications in musical acoustics. It typically appears in the form of a stiffness term incorporated into the 1-D wave equation, a model referred to as "Euler-Bernoulli stiff string". This beam model suffers from unphysical behaviour of the phase and group velocities, which are unbounded at high frequencies [104, Chapter 3], an issue the Timoshenko model solves. The shear model is derived from Timoshenko by neglecting rotary inertia, an approximation that holds for musical strings, which are always fixed at both ends. This simplification retains the asymptotic limits for phase and group velocities while making the model less complex than the original. The Rayleigh model extends the Euler-Bernoulli theory by including an extra term describing rotatory inertia. The last two models have had limited application in musical acoustics. A broad review of these four beam theories, with a particular focus on musical acoustics applications, can be found in [71]. It is reported that the Euler-Bernoulli model exhibits little deviations from Timoshenko in the audible frequency spectrum, thus justifying the popularity of the Euler-Bernoulli stiff string in musical applications.

For realistic string simulations, loss cannot be neglected. In fact, the 1-D wave equation is perfectly energy conserving, so a damping mechanism must be included. The crudest model involves adding an extra term dependent on the string velocity, as per [24, Chapter 6]. This is referred to as "frequency-independent" damping term in the literature because it leads to constant attenuation times across the entire frequency spectrum. This is not realistic behaviour, as real strings exhibit complex decay profiles. As a first approximation, loss increases with frequency. The earliest time-domain model capturing this effect, proposed by Ruiz [179], relied on a third-order time derivative. However, Bensa later demonstrated that this model is ill-posed and introduced a well-posed alternative incorporating a mixed space-time derivative [18]. Experimental studies to measure the decay profiles of real strings were conducted by Cuesta and Valette [60, 206]. In these pioneering works, the authors develop a theory explaining their results by considering three damping mechanisms: air viscosity, viscoelasticity and thermoelasticity. The loss characteristics provided here link the decay times to the frequency and can be easily included in models expressed in the frequency domain. In [67], Desvages develops a time domain expression of the Cuesta and Valette model.

1.1.1   Simulation techniques

Early studies on the numerical simulation of string vibration in the context of sound synthesis were conducted in the late 1960s by Ruiz and Hiller [179, 111, 112], who employed finite-difference time-domain (FDTD) methods for numerically solving the 1-D wave equation. A few years later, Bacon and Bowsher [10] expanded the model by including excitation with a hammer and a frequency-independent damping term. Boutillon used a similar technique [35] to test an improved piano hammer model.

In later years, the use of FDTD methods faced a setback due to the introduction, in the 1980s, of digital waveguide(s) (DWG) by Julius O. Smith III at CCRMA, Stanford University [193]. This method was initially developed as a generalisation of the non-physical Karplus-Strong synthesis technique [124], and, in its simplest form, it discretises D'Alembert's travelling-wave solution through a pair of delay lines, requiring only bit-shifting operations to update the state of the system [195]. Exploiting such unprecedented efficiency, DWG served as the major building block of early synthesis techniques, allowing for real-time simulation of strings, tubes and percussive instruments [194]. The extreme success of this technique led to a patent filed by Smith and Yamaha, which formed the basis for the VL1 synthesizer. Within this framework, the simulation of inharmonicity due to stiffness was achieved through lumped all-pass filters [86]. Similarly, frequency-dependent damping effects were reproduced with lumped filters placed at the end of the delay lines [18]. The Acoustics group at the

Helsinki University of Technology made extensive use of DWG in the early 2000s, targeting instruments such as the harpsichord [221] and the guitar [131]. A thorough collection of works employing this technique is found in [220].

When applied to more complex systems, DWG methods have faced certain challenges, such as modelling highly inharmonic systems such as bars [17]. Additionally, D'Alembert's solution applicability diminishes when distributed nonlinearities are included into the model, and closed-form solutions are generally unavailable for most physical systems, including systems of interest for this work.

The interest in FDTD methods rose again in the 1990s, mainly thanks to improvements in the computational capabilities of computer processors. This technique has a long history, tracing back to the pioneering work by Courant, Friedrichs and Lewy [138] (see [201] for further historical details), and the literature on the topic is vast [170, 137, 198]. The principle is relatively straightforward: it involves discretising the spatial domain with a finite grid, on which the numerical solution is defined, and then approximating the partial derivatives in space through suitable discrete finite difference operators. Doing this results in a system of coupled ordinary differential equations (ODEs), which can be integrated in time through time-stepping methods. In spite of a conceptually simple approach, many complications arise in musical acoustics. In turn, the designer often faces the challenge of balancing stability, accuracy, and efficiency. Additionally, for realistic sound synthesis, one needs to resolve a wideband frequency spectrum, and the local discretisation process introduces a fair amount of numerical dispersion, especially toward high frequencies.

FDTD methods were systematically introduced in acoustics by Chaigne and associates at ENSTA [47–49]. Their work on the piano was extended by Bensa et al. [18, 17] and by Giordano through the addition of a soundboard model [102]. In the last years, the body of work on this topic has been rapidly growing: since the textbook by Bilbao [24], FDTD has become one of the standards techniques for physical modelling sound synthesis in the academic environment (the industry has only recently begun to approach it timidly) and several methods were explored [44]. The five years-long NESS project[2] represented a flourishing laboratory for state-of-the-art research on the topic [25]. In her dissertation [67], Desvages presents a two-polarisation vibration model of an Euler-Bernoulli stiff string. Extensive work was conducted by Willemsen at the ME Lab, Aalborg University Copenhagen, with a focus on real-time simulation [223]. There were also attempts to formalize a higher-level framework for approaching this technique in the FAUST programming language [182, 199]. Most of the listed works focus on the Euler-Bernoulli stiff string model, which is

---

[2]http://www.ness.music.ed.ac.uk/

prominent in acoustics. Timoshenko beam vibration was simulated with FDTD methods mostly outside the musical acoustics field, with some examples being: [72, 183, 132, 123].

In parallel with Chaigne and the ENSTA team, IRCAM-based researchers laid the foundations of modal synthesis [2, 1, 151, 87]. This method exploits the Fourier representation of signals, which describes the system's solution as a superposition of an orthogonal set of eigenfunctions, or "modes". In the modal synthesis strategy, the first step is to solve the eigenvalue problem associated with the space variable to compute the mode shapes and the related eigenvalues, the latter corresponding to the square of the system's eigenfrequencies. The model PDEs are then discretised in space by performing a projection onto the set of modes, yielding a system of ODEs. This is then integrated in time with suitable time-stepping methods, not dissimilar to those employed in a finite difference setting. This synthesis technique presents several advantages. For linear models, the system of ODEs that is obtained from modal decomposition corresponds to a bank of damped, uncoupled oscillators. Aside from being extremely cheap to simulate, this may be integrated through an exact time-stepping method [24, Chapter 3], presenting an advantage over locally defined discretisation strategies, which suffer from numerical dispersion. Additionally, applying refined frequency-dependent loss profiles, such as those by Cuesta and Valette [206], is direct in the modal domain. The main drawback of modal synthesis lies in the computation of the eigenfunctions, which for most systems is not straightforward: these are highly dependent on the boundary conditions, and analytical solutions exist only in particular cases [148]. This makes dealing with coupled systems particularly difficult; specifically, the implementation of modular physical models such as those seen in [27] is not simple.

The modal expansions of the 1-D wave equation and the Euler-Bernoulli bar in musical settings are detailed in [24, Chapter 6, 7] and [67]. A frequency domain simulation of the linear string is utilised in [144] for simulating a Portuguese guitar, while [145] includes inharmonicity into the model. For general modal synthesis frameworks, see [37, 209, 232]. Chabassier and Imperiale present the frequency domain representation of the Timoshenko beam in: [45]. Outside the musical acoustics field, the main application of the modal description of vibrating objects is in mechanical engineering. Assorted works on systems of coupled beams are presented in [139, 65, 217, 114].

Applications are also found in industry: for instance, MODO BASS by IK Multimedia[3] uses modal methods to simulate bass string vibrations, while Modus[4] from Physical Audio is a synthesizer that employs modal strings and plates with nonlinear interconnections.

---

[3]https://www.ikmultimedia.com/products/modobass2
[4]https://physicalaudio.co.uk/products/modus/

A variation of this technique is the functional transformation method (FTM), developed by Rabenstein and Trautmann [205]. Here, the modal expansion is performed through the Laplace Transform to obtain point-to-point transfer functions.

The finite element method (FEM) [108, Chapters 5,6] sits somehow in between FDTD and modal methods. It is commonly used in mechanical engineering because it easily handles problems with complex geometries. Similarly to the previously described approaches (except DWG), the goal is to discretise the spatial domain, to turn the model's PDEs into a system of ODEs in time, that can be integrated with time-stepping methods. Instead of using a grid, the solution is approximated here by a set of basis functions with compact support (elements), typically polynomials in the 1-D case. The system is discretised through a projection onto this basis functions, similar to what happens in the modal expansion. Unlike in modal analysis, where basis functions are defined over the entire domain, FEM basis functions are defined onto a subset of the domain, making the projection local.

This technique presents the same issues affecting FDTD methods: namely, efficiency, stability and numerical dispersion. Yet, the possibility of choosing arbitrary shape functions allows for simpler treatment of irregular shapes compared to FDTD methods. The downside is that the mathematical procedure for discretisation is particularly involved. Thus, the process is often run automatically by software, leading to a loss of control over the algorithm's efficiency. Consequently, FEM simulations typically focus on determining the modal frequencies and shapes of the instrument rather than on sound synthesis. This is especially true for simple problems such as the linear string, which can be easily discretised with FDTD methods without losing control over efficiency. For this reason, FEM simulations of linear strings are quite rare in the literature, with some exceptions: [11, 196, 66], the latter including time-domain simulation. Lately, FEM analysis has been used together with modal synthesis to automatically determine modal parameters of computer-aided design (CAD) models. Some examples include: [149, 37].

1.2   Nonlinear string

As the amplitude of vibration of a string increases, nonlinear effects become more significant, resulting in perceptually salient phenomena such as tension modulation [88], phantom partials [58, 12] and whirling [122, 156, 178]. Tension modulation causes a downward pitch glide due to increased tension from large amplitude motion, an effect not replicable by linear systems where modes have fixed frequencies. Phantom partials are overtones appearing at inharmonic frequencies, generated by the coupling between transverse and longitudinal motion. Whirling is a three-dimensional effect resulting from the instability of nonlinear

string motion, giving rise to beating sounds. Nonlinearities describing these effects emerge as a consequence of large strains and are thus geometric, meaning that the nonlinear behaviour of the string material is not considered here.

First studies on the problem of nonlinear string vibration were conducted by Kirchhoff [127]. Later, Carrier [41] extended Kirchhoff's work by formalising an equation of undamped motion commonly referred to as the Kirchhoff-Carrier (KC) string [24, Chapter 8]. This model considers a single transverse polarisation and negligible longitudinal motion, meaning that tension is assumed constant along the string length. The equation resembles the 1-D wave equation, with the difference being an additional term where the tension depends on the squared string slope, average over its length. Thus, the primary nonlinear phenomenon reproduced by this model is tension modulation, giving rise to pitch glide. A more subtle effect introduced is a mild spectral enrichment, deriving from the mode coupling provided by the nonlinear term, particularly in the case of finite impedance boundaries. Further details can be found in [136].

Thanks to its simplicity, the KC equation has been widely used for analysing nonlinear phenomena, particularly in the case of forced vibration. Notable examples include the works by Oplinger [155], Miles [150], and Johnson [122]. Dickey proposed techniques for finding analytical solutions [69, 70], while Murthy and Ramakrishna [153] extended the study to double polarization, analysing non-planar motion and providing an analytical explanation for the whirling behaviour observed in experiments. Anand [4] later included viscous damping into the model. Investigations in a musical acoustics context include the works by Gough [103] and Legge [136].

The studies above do not include stiffness effects. Woinowsky-Krieger [226] was the first to extend the KC nonlinearity to the case of an Euler-Bernoulli bar, a model that continues to be used in recent years [106, 55]. See [24, Chapter 8] for a musical case including loss. Outside the musical acoustics area, extensive work on a Timoshenko-Kirchhoff beam was conducted by Arosio [7, 8].

In the late 1960s, Narasimha [154], Anand [5] and Morse [152, Chapter 14] independently developed a derivation of the KC equation starting from an exact 3-dimensional (3-D) model of string vibration, taking into account longitudinal motion. As a matter of fact, the KC equation is obtained by neglecting the coupling between longitudinal and transverse motion. Although this assumption is generally incorrect due to the inevitable energy transfer between these motions [174], it can be disregarded in certain cases for simulation purposes [12].

The exact 3-D model of string vibration is commonly referred to as geometrically exact (GE) [46] or Euler-Lagrange [156] in the literature and can be related to the geometrically exact theory of beams [19, 119]. It describes the motion of a perfectly flexible string,

including longitudinal motion and two polarisations for the transverse motion, thereby accounting for variations in tension along the string length. In many practical cases, the double transverse polarisation is restricted to planar vibration [24, Chapter 8], removing the whirling effects altogether. The longitudinal modes contribute significantly to the string sound [13]. Moreover, the motion coupling creates vibration modes at frequencies that are not merely multiples of the fundamental, as in the KC case: these depend on the sum and difference of the longitudinal and transverse base frequencies [58, 12], resulting in the so-called phantom partials appearing at inharmonic intervals. It should be noted that a recent study [172] identified production of phantom partials in the structural components of the piano. However, the relative contributions of harmonic distortion introduced by the string and the structure have yet to be compared. The GE string model was the subject of many works, such as [156, 178]. Kurmyshev [129] and Leamy [134] extended the study to include material nonlinearities. A classic mathematical derivation can be found in the book by Morse and Ingard [152, Chapter 14]. As in the KC case, adding stiffness to the model is quite direct, as shown in [78] for the Euler-Bernoulli and in [43] for the Timoshenko models.

Approximated forms of the GE string are commonly derived through a Taylor expansion of the nonlinear potential, thus simplifying the model. The standard form by Morse and Ingard [152, Chapter 14] truncates the Taylor series to the fourth order. In [13, 14], Bank employed third-order approximations while truncating at the second-order decouples the motion, resulting in the 1-D wave equation for both longitudinal and transverse motions. The first two approximations exhibit an unphysical issue: the associated Hamiltonian is not positive definite and therefore unbounded [23]. Anand's form [5] is correct up to the third order. It is derived from the fourth-order approximation by truncating an additional term; however, it ensures energy conservation. Detailed justification for this approach is provided in [23], [24, Chapter 8]. Note that Chabassier [42, 46] points out that this latter form does not fulfil the hypothesis of weak degeneracy, as per [200], and is therefore theoretically unstable. However, no instability has been observed in empirical studies, and numerous works are based on this model, as discussed later in this chapter. The approximated forms of the GE string will be referred to here using the generic term Morse-Ingard (MI) strings, while the third order approximation as per Anand will be called simply "Anand's" model.

1.2.1   Numerical simulations

Kirchhoff-Carrier

Unlike in the linear case, analytic solutions are unavailable for nonlinear string models. Therefore, methods that rely on the discretization of solutions, such as DWG, cannot generally

be extended to handle nonlinearities accurately, the only exception being the pitch-glide effect. Between the 1990s and the 2000s, extensive research focused on simulating tension modulation using DWG. In [162], Pierce and Van Duyne employed a delay line terminated by a double nonlinear spring. Researchers from the Helsinki University of Technology explored both lumped [208, 203, 89, 88] and distributed [159, 160] structures of all-pass filters. Additionally, they developed a technique [88] to replicate the spectral enrichment effect caused by finite impedance boundaries terminations in the KC string model, although this approach is considered unphysical [160].

One of the earliest numerical simulations of the KC string was conducted by Gough [103], though the specific numerical technique employed was not detailed. Pakarinen [160] developed a FDTD-based solver to compare with DWG. However, since stability was not his primary focus, the detailed algorithm is explicit and thus highly unstable. Bilbao [31],[24, Chapter 8] systematically explored FDTD methods, placing significant importance on stability. In fact, classic frequency-based techniques, such as Von Neumann analysis [198], do not apply to nonlinear problems; instead, different methods can be used, which typically rely on the conservation of a numerical quantity with the dimension of energy. These are usually commonly called "the energy method" [170, 107]. Recent works include GPU-based simulations to achieve efficient computation [29]. More recently, a version of the KC string terminating in an energy-storing boundary condition was proposed, solved using an efficient, newly developed numerical method [82].

Though feasible, modal methods face certain limitations when treating nonlinear problems, and alternative techniques, such as Nonlinear Normal Modes [126], come into play. In fact, the standard procedure in this case is to project the nonlinear equations onto the eigenfunctions of the corresponding linear problem [83]. This way, the resulting ODEs system is usually densely coupled, and efficiency is thus greatly impaired. Nevertheless, due to the spatial invariance of its nonlinearity, the KC string model is well-suited for modal simulations, as showed by Bilbao [22], [24, Chapter 8]. Researchers from NOVA University in Lisbon have extensively employed this modal formulation, for instance, in the context of guitar modelling [64]. In recent years, the same authors carried out substantial research on modal systems, comprising KC strings, using the Udwadia-Kalaba formulation [6, 63, 121, 92]. The FTM has also been employed: [204].

FEM simulations of the KC string are relatively rare due to the simplicity of the nonlinear term. Chabassier and Joly [46] described a method for discretising generic nonlinear Hamiltonian systems of wave equations that applies to the GE and its approximations. Recently, Roze et al. presented a model in port-Hamiltonian form [177]. Further information on port-Hamiltonian systems (PHS) can be found in [84, 210].

Other techniques have been employed: researchers from IRCAM-Sorbonne have made significant investigations using Volterra series [116, 176, 175]; so-called energy estimation methods have also been developed [9], and recent trends include the use of neural networks [185].

Morse-Ingard

Taylor approximations of the GE string have found extensive applications in sound synthesis due to their simplicity and lower computational cost compared to the full model. Bank conducted significant research on this topic, focusing on piano simulation [12]. To enhance computational efficiency, he often considered the coupling from transverse to longitudinal motion only, ignoring the reverse. In this approach, the transverse motion is represented by a linear stiff string, while the longitudinal motion is in the form of a 1-D wave equation with a nonlinear forcing term deriving from the transverse waves. The paper [13] proposes two algorithms: one models transverse vibration with DWG, and longitudinal vibration with FDTD methods. The second one, more efficient, reproduces both directions of motion and phantom partials using three DWG in parallel. In [14], a full FDTD integrator for the third-order MI string is introduced, featuring bi-directional coupling and hammer excitation. However, stability concerns due to the high wave speed of the longitudinal motion lead to a very high sampling rate, making real-time computation impractical. To address this issue, the longitudinal vibration is modelled as a bank of uncoupled modes excited by transverse motion. The work presented in [15] is based on Anand's form: the transverse and longitudinal vibration are simulated with modal synthesis, neglecting bi-directional coupling. The same technique is employed in [16] for developing a real-time piano synthesizer.

Extensive investigation on FDTD methods for MI strings was conducted by Bilbao, focusing particularly on the stability of the numerical schemes through discrete energy conservation. In [23], he introduces interleaved algorithms tailored to different approximation levels of the MI string in a state-space (transmission line) form. The textbook [24, Chapter 8] presents various schemes for Anand's model, each with distinct properties. Notably, a solution to the issue of high longitudinal motion wave speed, previously identified by Bank, is here introduced, employing separate grids for the longitudinal and transverse waves and interpolation to couple them.

The latter model has served as the basis for many recent studies. For instance, it is used in [79] by Ducceschi et al., incorporating a shear correction for stiffness, in the context of collision simulations. In [75], it is applied to simulate a prepared piano, while [135] proposes a GPU acceleration, although it does not appear to achieve significant performance improvements.

A solver based on FEM is proposed by Chabassier in [46], where a comparison is conducted between the results obtained with the GE and Anand's models.

Geometrically exact

The most comprehensive body of work on the GE string in the context of musical acoustics is attributed to Chabassier [42], who systematically studied it for piano simulation, modelling a full system including the hammer, the string, the soundboard and sound radiation. The string employed by Chabassier includes a GE nonlinear potential, with a stiffness term as per Timoshenko and double vibration polarisation. Damping is modelled using the frequency-dependent formulation from [18], with coefficients obtained through fitting measurements [43]. The equations are discretised in space with FEM. In [46], a new class of pseudo-energy-conserving time-stepping schemes is developed, applicable to a category of problems termed "nonlinear Hamiltonian systems of wave equations," which includes the GE and MI string models. The time integrators are fully implicit and solved using Newton's method. Given the complexity, the focus is not on efficient computation; thus, to address the issue of different wave speeds for longitudinal and transverse motion, the former is modelled with a parametrized theta-scheme, allowing for relaxing the stability condition by making the linear part implicit as well. More recently, Marazzato et al. proposed an explicit solver for a FEM-discretised GE model [143].

Extensive work on this topic has been conducted by Bilbao and Ducceschi, with a focus on efficient computation. In [73], the system is integrated in time with a recently developed, linearly implicit, energy-conserving time-stepping method. In [78], the GE string in single polarization is discretised by making use of FDTD methods for the transverse part and modal methods for the longitudinal part. This is to avoid sampling rate issues due to the different wave speeds. In [26], both motion directions are discretised with FDTD methods, and time integration is performed with a state-of-the-art, explicit numerical scheme, achieving real-time computation. The same model is combined with nonlinear hammer excitation in [77]. However, despite the computational efficiency achieved by these new numerical solvers, some issues remain, as will be discussed later.

1.3 Other nonlinearities

The nonlinear effects discussed thus far are intrinsic to the models and influence the string vibration in isolation. However, additional nonlinearities arise in musical acoustics due to the interaction between the string and other components. Notably, collision and friction forces play significant roles.

1.3.1   Collisions

Collision modelling is a significant area within mechanics, with numerical simulations applied across various disciplines [228]. In musical acoustics, collisions are vital in sound production of many instruments. In stringed instruments, examples include hammer strikes in pianos [35, 48, 49, 34, 14, 15, 43] and clavichords [202]; interactions between strings and fingers [68]; string-fretboard contacts [33, 90, 91, 117, 118]; string-slide contacts [20]; string-string contacts [158]; and string-bridge contacts in Indian instruments [207, 213, 36, 142, 211, 190, 219].

Some of the earliest studies in musical acoustics are attributed to Raman in the 1920s, who investigated hammer excitation [167] and the collision of strings against obstacles, a problem particularly relevant to Indian string instruments [166]. Other notable historical works include studies by Barghava [21] and Ghosh [100] on piano hammers, as well as research by Amerio [3] and Burridge [39] on string collisions against rigid obstacles.

The main challenge in collision modelling is detecting interactions between objects based on their geometry and calculating the resulting forces. Objects can be modelled as lumped, such as piano hammers, or as fully distributed in space, such as the string-fretboard interaction. Two primary mathematical models are generally employed. The first describes rigid contacts and has been widely used to describe string collisions with obstacles using various techniques; examples are: [39, 168, 128, 125, 219, 190, 117, 63, 121]. The second model, known as the penalty method, allows for interpenetration between objects [34]. This approach involves a one-sided power law [113] and is modelled through a suitable potential function [161], based on Hertz's contact formulation [110], which can be extended to include collision-induced losses [115].

The penalty method has recently become increasingly popular in sound synthesis, with different numerical simulation techniques being employed. Researchers have concentrated on creating stable time-stepping schemes, frequently using energy-based approaches. Important contributors in this area include van Walstijn, Chatziioannou, and Bilbao. Notable studies have used FDTD methods [52, 32, 53, 34, 33, 79, 54, 51], modal methods [211–213], and FEM [43, 42]. While these works primarily used fully implicit discretization, recent trends have shifted towards linearly implicit or fully explicit methods [74, 75, 27, 81, 77, 175, 214–216], aiming to improve computational efficiency, making real-time applications more feasible.

1.3.2   Friction: the bow

Friction in stringed instruments is predominantly associated with the bowing mechanism, a central topic in musical acoustics for decades. Initial insights into bowed string motion were made by Helmholtz in the 19th century [218], who observed the "stick-slip" phenomenon first identified by Duhamel [Chapter 10][94], a behaviour now known as Helmholtz motion. This motion occurs when the string alternately sticks to the bow (sticking phase) and then slips across it (slipping phase) once per period, producing musically pleasing tones. In the early 20th century, Raman developed a mathematical theory for bow-string dynamics, where the friction force at a single contact point depends on the relative velocity between the bow and the string [165]. Schelleng later expanded on Raman's work, developing "Schelleng diagrams," which depict regions in the bow force-bow position plane where musical tones are produced [184]. Similarly, Guettler's diagrams consider bow acceleration instead of bow position [105].

It is common to consider point-wise excitation [81], though finite-width effects can influence the string torsional motion [164]. The force is typically described by a characteristic friction curve (a dimensionless quantity) as a function of the relative velocity between the string and the bow. The simplest model is Coulomb dry friction, whose force magnitude is independent of relative velocity. A more sophisticated model was developed by Smith and Woodhouse through experimental studies of a mass on a rosin-coated conveyor belt [192]. Here, the friction force decreases with increasing relative velocity until it reaches a steady value. This is sometimes called the "classical" friction curve [98], as it has been referenced in earlier works by Friedlander [97], McIntyre and Woodhouse [146], and others. Galluzzo proposed a modified version of Smith and Woodhouse's characteristic friction curve, known as the "reconstructed" friction curve, based on measurements of the force drop at the bridge during the slip phase [98]. These friction characteristics often exhibit a discontinuity at zero velocity, posing challenges during simulation. To address this, Bilbao has proposed a family of smoother "soft" friction characteristics [24, Chapter 4], designed not on physical principles but solely for simulation convenience.

The friction characteristic model effectively replicates various bowing phenomena, such as Helmholtz motion, raucous motion, multi-stick-slip motion, and anomalous low-frequency waves [67]. However, experimental studies have demonstrated that the mechanical properties of rosin vary with temperature [192]. To account for this, Woodhouse proposed a friction curve that includes thermal exchanges, which allows the capture of the hysteretic behaviour observed experimentally [227]. Despite these improvements, there are still some discrepancies when this curve is compared to actual measurements [98]. Another class of models has been developed to address the hysteretic nature of friction curves, incorporating

the bristle-string interaction effects. These include the Dahl model, the LuGre model, and an elasto-plastic model [85]. For a thorough review, see[186].

Early real-time simulations of the bowed string used DWG [194]. Later, Serafin implemented an elasto-plastic model [187], and more recent applications include a finite-width bow with hair dynamics and thermal friction [141]. Time-domain methods were also employed in the early studies [147, 163]. Recently, Desvages [68, 67] utilized FDTD methods to simulate a model incorporating two vibration polarizations, Smith and Woodhouse's "classical" friction curve, and the interaction of the player's finger within an energy-consistent framework. However, this simulation did not achieve real-time performance. The first real-time FDTD implementations of the bowed string, based on fully-implicit schemes, were developed by Willemsen [224, 225, 223], whose research included the integration of elasto-plastic friction models.

1.4 Thesis motivation & objectives

As previously mentioned, traditional frequency-domain techniques cannot be used to ensure stability when nonlinear terms are involved, and much of the recent literature relies upon energy methods to this end. These methods often result in fully implicit schemes, which require solving nonlinear algebraic equations at every time step. Iterative solvers, such as Newton's method, are typically employed for this purpose. However, several issues arise, especially in real-time simulations: the iterative process is computationally intensive and inherently serial, often requiring multiple iterations per time step; the number of iterations depends on system parameters, necessitating an arbitrary cap to control computational load [51], and the existence and uniqueness of the numerical solution are not always guaranteed [95].

Recent advancements in numerical analysis have enabled the simulation of certain nonlinear systems using linearly implicit or explicit schemes. Linearly implicit schemes are formulated as linear systems that must be solved at each time step, while explicit schemes avoid linear systems solving completely and can be integrated through a recursion relation.

In a recent study, Marazzato et al. [143] introduced an explicit Hamiltonian integrator that preserves numerical energy exactly for polynomial potentials. For general nonlinear potentials, quadrature methods are used instead of exact integration, leading to an approximate conservation of pseudo-energy. Furthermore, when the energy of the model system is non-negative, conditions for numerical stability do not immediately follow.

When the nonlinear potential energy is bounded from below, it can always be expressed as the square of a function. Building on this concept, three methods were recently proposed

based on energy quadratisation. The first, proposed by Lopes, Hélie and Falaize [140], within the context of PHSs is obtained when one of the state variables is substituted by a quadratised one in the expression for the energy. Thus, the number of variables to be solved for remains unchanged. Though compact, this form does not apply to non-invertible potentials, and multivariate potentials are also not easily treated in this framework. In spite of this, the technique has been successfully applied to audio circuit modelling [93] and the KC string [175]. Two other frameworks have been developed in the context of gradient flows for diffusive systems. The invariant energy quadratisation (IEQ) method [229, 230, 233] performs a quadratisation that results in one added state variable compared to the original system. While this extra state variable must be solved for, the framework can handle non-invertible potentials and straightforwardly address multivariate cases. Finally, the scalar auxiliary variable (SAV) method was introduced [188], where the nonlinear energy is treated as one single scalar rather than a distributed potential density. This approach allows for fully explicit solvers when specific matrix structures [189] are exploited [26, 77, 28]. The IEQ method has been applied to collisions problems, both lumped and distributed [74, 75, 27, 81, 215], as well as to the GE string model [73, 78]. Similarly, SAV has been used in the context of collisions [77, 214, 216, 30], and geometric nonlinarities [26, 77].

In the case of non-conservative forces, such as friction and damping, there is no nonlinear potential to quadratise, rendering the previously discussed methods inapplicable. However, a different approach was recently introduced within the context of virtual-analogue models [80, 76], allowing for a linearly-implicit solving procedure for systems including nonlinear forces depending on the first derivative of the state variable.

Despite the advancements introduced by these new approaches, several critical issues remain unsolved. Both IEQ and SAV have exhibited unphysical behaviour in certain context, notably in collision modelling [74]. While a solution was proposed within this area [216] after the beginning of this research, a comprehensive investigation of the performance of these methods in nonlinear string modelling is still lacking. Furthermore, the stability properties of the non-iterative method designed to address non-conservative forces have not been fully explored or understood [76]. The primary objective of this thesis is to advance the use of FDTD and modal methods to effectively address nonlinearities in string vibration. The newly developed techniques will be tested with a focus on utilizing the structured update matrices they produce to develop highly efficient algorithms. Furthermore, contrary to classic numerical integrators, quadratisation-based methods provide a versatile discretization approach, allowing the same numerical procedure to be applied across different nonlinear systems. Therefore, part of this work is dedicated to developing a general framework for nonlinear sound synthesis. Additional emphasis will be placed upon incorporating refined,

finite-impedance boundary conditions into the string models to simulate the interaction between the string and other components of the instrument, such as the bridge.

As previously mentioned, the energy method has become a standard in physical modelling over the past few decades. Ensuring numerical stability a priori is especially crucial for real-time models, as it guarantees that the virtual instrument will not "blow up" during operation. Moreover, monitoring numerical energy can serve as an effective debugging tool to detect sources of error. However, in the case of nonlinear systems, stability is insufficient to guarantee that the solution will converge to the exact one: convergence is the property guaranteeing that, as the sample rate increases, the numerical solution approaches the exact analytical one. In linear systems, stability and convergence of the numerical scheme are linked through the Lax-Richtmyer theorem [198, Chapter 10]. However, this does not hold for nonlinear systems, meaning a stable scheme may still produce incorrect results. Therefore, this study will particularly focus on testing the convergence of these numerical algorithms.

1.5   Thesis outline

This work is organised into eight chapters. The main research contributions are presented in Chapters 4, 5, 6, 7, and are summarised in the conclusions. A companion GitHub repository with code and audiovisual examples is available online[5].

Chapter 2 introduces linear equations, starting with a discussion on generic ODEs and the concept of potential quadratisation. It then presents the linear oscillator equations, followed by coupled mass-spring systems. The discussion extends to the distributed case, covering the ideal string and incorporating bending stiffness, loss, and forcing. The modal expansion is then developed for both string models, including a lumped finite-impedance boundary. Finally, a model of a stiff string with a spatially distributed boundary is presented.

Chapter 3 describes numerical techniques, starting with time-domain methods applied to the linear oscillator and introducing the concepts of accuracy, consistency, and convergence. Next, the finite difference method for spatial discretisation is presented and applied to both ideal and stiff strings. Finally, finite difference schemes for both models are introduced, and the numerical eigenfrequencies and eigenvectors for the stiff string with a spatially distributed boundary, as presented in Chapter 2, are derived.

Chapter 4 discusses geometric nonlinearities. It begins with the lumped case study of the Duffing oscillator and then extends to the GE string. From this, MI string models are derived, concluding with the KC string model, which is also presented in the modal domain and with double vibration polarisation. Quadratised numerical methods are introduced here in the case

---

[5]https://github.com/Rickr922/phdThesis-companion

of lumped and spatially distributed systems. These are then applied to systems of interest, with illustrative results. Additionally, a technique for limiting an unphysical behaviour of these quadratised methods, based on a physical constraint, is introduced.

Chapter 5 address collision problems. The mass-barrier collision is first examined, and various quadratisation-based methods are compared. The constraint technique introduced in Chapter 4 is adapted for collision scenarios. Subsequently, lumped and distributed collisions in strings are explored, focusing on finger/hammer-string and string-fretboard/frets interactions, which are solved using quadratised numerical methods. Additionally, the constraint technique is extended to handle distributed collisions.

Chapter 6 examines nonlinear friction induced by a bow. It begins with a case study of a bowed mass-spring system, introducing a numerical method that enables solving non-conservative nonlinear problems without iterative techniques. The discussion then extends to the ideal string. For both lumped and distributed cases, comparisons are made between traditional iterative methods and the newly introduced approach.

Chapter 7 illustrates the application of the models presented in previous chapters to the physical modelling of musical instruments. This chapter corresponds to two papers presented at the International Conference on Digital Audio Effects (DAFx): [30] and [181]. Finally, Chapter 8 concludes the dissertation.

Chapter 2

Linear vibration

The physical models presented in this work are formulated using (systems of) differential equations, which describe the relationships between one or more unknown functions and their derivatives, defined over specific space-time regions with given boundary conditions. Specifically, ordinary differential equations (ODEs) involve functions of a single variable, and since this work is centred on vibrations, they are assumed to be dependent on time. Partial differential equations (PDEs) involve functions of multiple independent variables: here, they describe systems distributed in space and their evolution over time. This chapter first introduces generic ODEs and the concept of potential energy quadratisation: a fundamental aspect of so-called quadratised methods. The discussion then narrows to linear models, which are valid for small-amplitude vibrations. It begins by describing lumped systems and ODEs, including single oscillators and systems of coupled oscillators. These systems serve as fundamental building blocks in musical acoustics. In fact, distributed oscillating systems can be approximated as coupled or uncoupled oscillators after spatial discretization, an essential concept in modal methods. Following the discussion on lumped systems, the chapter continues to distributed systems, introducing linear string models. Part of the content is based on the textbooks by Bilbao [24] and Meirovitch [148].

2.1   Time-dependent ODEs

Consider a function $u(t) : \mathbb{R}_0^+ \to \mathbb{R}$, representing the displacement of a lumped object of mass m at time t. Here u is assumed to be sufficiently smooth, meaning it is differentiable multiple times, with all derivatives being well-defined and bounded over the positive time axis $t \in \mathbb{R}_0^+$. Furthermore, the mass m is treated as constant throughout this text. The object

is subject to a force given by:

$$F = -\frac{\mathrm{d}V}{\mathrm{d}u},$$

(2.1)

where $V = V(u) : \mathbb{R} \to \mathbb{R}_0^+$ is a generic, differentiable potential function, assumed to be non-negative, a natural choice in most musical acoustic applications. This may be further generalised by considering the potential to be bounded from below; however, non-negativity will be adopted here for simplicity. According to Newton's second law, the equation of motion can be expressed as:

$$m\frac{\mathrm{d}^2 u}{\mathrm{d}t^2} = -\frac{\mathrm{d}V}{\mathrm{d}u}.$$

(2.2)

This equation is an example of an autonomous ODE, meaning there is no explicit dependence on the independent variable t. Thus, the equation is time-invariant. To solve this problem means finding a function u that satisfies the differential equation. Because this is a second order ODE in time, a unique solution can only be found by specifying two initial conditions: the initial displacement and velocity. This forms an initial value problem (IVP):

$$u(0) = u_0, \qquad \left.\frac{\mathrm{d}u}{\mathrm{d}t}\right|_0 = v_0.$$

(2.3)

Note that, to ensure the uniqueness of the solution, the ODE must satisfy appropriate Lipschitz continuity conditions, which are assumed to hold here (see [137, Chapter 5] for more information). Before proceeding, it is helpful to list some useful derivative identities that will be employed throughout this text:

$$\frac{\mathrm{d}u}{\mathrm{d}t}\frac{\mathrm{d}^2 u}{\mathrm{d}t^2} = \frac{\mathrm{d}}{\mathrm{d}t}\left(\frac{1}{2}\left(\frac{\mathrm{d}u}{\mathrm{d}t}\right)^2\right),$$

(2.4a)

$$\frac{\mathrm{d}u}{\mathrm{d}t}u = \frac{\mathrm{d}}{\mathrm{d}t}\left(\frac{1}{2}u^2\right),$$

(2.4b)

$$\frac{\mathrm{d}u}{\mathrm{d}t}u^3 = \frac{\mathrm{d}}{\mathrm{d}t}\left(\frac{1}{4}u^4\right).$$

(2.4c)

2.1.1 Energy analysis

As anticipated, this text will heavily rely on energy arguments to verify the stability of physical systems. To illustrate this approach, it is beneficial to demonstrate the process referred to here as energy analysis. The procedure begins by multiplying the equation of motion (2.2) by the velocity $\frac{\mathrm{d}u}{\mathrm{d}t}$, obtaining:

$$m\frac{\mathrm{d}u}{\mathrm{d}t}\frac{\mathrm{d}^2 u}{\mathrm{d}t^2} + \frac{\mathrm{d}u}{\mathrm{d}t}\frac{\mathrm{d}V}{\mathrm{d}u} = 0.$$

(2.5)

Applying the identity (2.4a) to the left-hand side and using the chain rule $\frac{dV}{dt} = \frac{dV}{du}\frac{du}{dt}$ on the right-hand yields:

$$\frac{d}{dt}\left(\frac{m}{2}\left(\frac{du}{dt}\right)^2 + V\right) = 0. \tag{2.6}$$

The expression within the derivative represents the system energy or Hamiltonian and can be interpreted as a sum of kinetic and potential energies:

$$H = \frac{m}{2}\left(\frac{du}{dt}\right)^2 + V. \tag{2.7}$$

An equation of the type (2.6) is called here energy balance because it describes the variation of the system energy over time. In this case, the energy is conserved, and the value is determined by the initial conditions:

$$H_0 = \frac{mv_0^2}{2} + V, \qquad H(t) = H_0 \; \forall \; t. \tag{2.8}$$

Energy conservation is a fundamental principle in physics, and it must be verified for any system of equations describing physical systems. A system in which energy is conserved is referred to as conservative. If a loss mechanism is included, energy should decrease over time, and in this case, the system is described as dissipative. Throughout this text, both conservative and dissipative systems will be collectively referred to as passive systems, meaning that no spontaneous energy production takes place in the system.

Energy conservation alone is not sufficient to ensure the stability of the system at hand. In fact, the non-negativity of the energy is crucial, as it leads to the boundedness of the solutions. The kinetic energy is inherently positive, and the potential was assumed to be non-negative. Then the following inequalities hold:

$$0 \leq \frac{m}{2}\left(\frac{du}{dt}\right)^2 \leq H_0, \qquad 0 \leq V \leq H_0. \tag{2.9}$$

Examining the kinetic term, one has:

$$\frac{m}{2}\left(\frac{du}{dt}\right)^2 \leq H_0 \qquad \Rightarrow \qquad \left|\frac{du}{dt}\right| \leq \sqrt{\frac{2H_0}{m}} \; \forall \; t, \tag{2.10}$$

which shows that the velocity is always bounded in terms of the initial energy. If V is radially unbounded, meaning $V \to +\infty$ iif $|u| \to +\infty$, a bound on $|u|$ may be derived as well, and the system is said to be stable, meaning that the solution will not experience infinite growth.

2.1.2   Potential energy quadratisation

If the potential V is non-negative, an auxiliary variable may be defined [28] as:

$$\psi \triangleq \sqrt{2V}, \tag{2.11}$$

and the equation of motion (2.2) becomes:

$$m\frac{\mathrm{d}^2 u}{\mathrm{d}t^2} = -\psi\frac{\mathrm{d}\psi}{\mathrm{d}u}. \tag{2.12}$$

Furthermore, applying the chain rule yields:

$$\frac{\mathrm{d}\psi}{\mathrm{d}t} = \frac{\mathrm{d}\psi}{\mathrm{d}u}\frac{\mathrm{d}u}{\mathrm{d}t}. \tag{2.13}$$

Then, one may define:

$$g \triangleq \frac{\mathrm{d}\psi}{\mathrm{d}u} = \frac{1}{\sqrt{2V}}\frac{\mathrm{d}V}{\mathrm{d}u}, \tag{2.14}$$

and equation (2.2) can be re-written as a system of two equations as:

$$m\frac{\mathrm{d}^2 u}{\mathrm{d}t^2} = -\psi g; \qquad \frac{\mathrm{d}\psi}{\mathrm{d}t} = g\frac{\mathrm{d}u}{\mathrm{d}t}. \tag{2.15}$$

Formulating an IVP now requires an additional initial condition for the auxiliary variable, $\psi(0) \triangleq \psi_0$. The concept of potential quadratisation is fundamental to the IEQ and SAV methods. Indeed, if g is known at any time instant, equations (2.15) are linear in u and ψ, regardless of the form of g. As will be shown later, this system can be efficiently integrated using numerical methods.

2.1.3   Potential splitting

In many cases in musical acoustics, the expression for the potential energy can be written in the form of a quadratic potential plus a nonlinear contribution:

$$V(u) = \frac{Ku^2}{2} + \phi(u), \tag{2.16}$$

with $K \in \mathbb{R}^+$ and $\phi(u) \geq 0$. One can then quadratise only the nonlinear part by defining:

$$\psi \triangleq \sqrt{2\phi}, \tag{2.17}$$
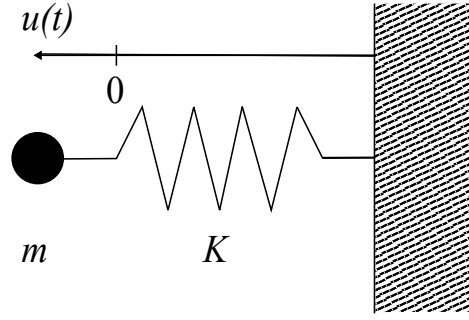
Fig. 2.1 Mass–spring system, with a mass m and a spring of stiffness K. The displacement $u(t)$ is measured about an equilibrium distance (marked as 0).

which is well-defined thanks to the non-negativity of ϕ. This results in the system of equations:

$$m\frac{\mathrm{d}^2 u}{\mathrm{d}t^2} = -Ku - \psi g, \qquad \frac{\mathrm{d}\psi}{\mathrm{d}t} = g\frac{\mathrm{d}u}{\mathrm{d}t}, \qquad g = \frac{1}{\sqrt{2\phi}}\frac{\mathrm{d}\phi}{\mathrm{d}u}. \tag{2.18}$$

As will be shown subsequently, this approach allows the linear and nonlinear parts to be treated with different numerical methods, thereby offering greater flexibility in numerical method design. In this chapter and the following one, the nonlinear part is assumed to be zero, as the focus is on linear systems.

2.2 Simple harmonic oscillator

Equation (2.18), in absence of the nonlinear potential g, is found in many physical systems; one example is the mass-spring system is illustrated in Figure 2.1. Here, $u(t)$ represents the displacement of the mass m from the equilibrium point in m, and K is the spring's constant, measured in N/m. Dividing the equation by the mass m (assumed constant) yields a general model for undamped harmonic motion:

$$\frac{\mathrm{d}^2 u}{\mathrm{d}t^2} = -\omega_0^2\, u. \tag{2.19}$$

This is an equation of a simple harmonic oscillator (SHO). Here, ω_0 is the natural frequency, or angular frequency of the oscillator in radians per second, related to the frequency f_0 in Hertz by $\omega_0 = 2\pi f_0$. It is well known that this particular ODE admits an analytic solution in various forms. When initial conditions u_0 and v_0 are specified, all yield the same result. The analytic solution, denoted here with $\bar{u}$, can be expressed as:

$$\bar{u}(t) = A\cos(\omega_0\, t) + B\sin(\omega_0\, t), \qquad A_0 = u_0, \qquad B_0 = \frac{v_0}{\omega_0}. \tag{2.20}$$

Alternatively, a phase-shifted form is:

$$\bar{u}(t) = C_0 \cos(\omega_0\, t + \theta_0), \qquad C_0 = \sqrt{A_0 + B_0}, \qquad \mathrm{V}_0 = \tan^{-1}\left(-\frac{B_0}{A_0}\right). \qquad (2.21)$$

Another useful expression for the solution is in complex form:

$$\bar{u}(t) = \hat{u}_+ e^{j\omega_0 t} + \hat{u}_- e^{-j\omega_0 t}, \qquad (2.22)$$

with $\hat{u}_+, \hat{u}_- \in \mathbb{C}$. Then, following Euler's formula:

$$\begin{aligned}
\bar{u}(t) &= \hat{u}_+[\cos(\omega_0 t) + j\sin(\omega_0 t)] + \hat{u}_-[\cos(\omega_0 t) - j\sin(\omega_0 t)] \\
&= (\hat{u}_+ + \hat{u}_-)\cos(\omega_0 t) + j(\hat{u}_+ - \hat{u}_-)\sin(\omega_0 t).
\end{aligned} \qquad (2.23)$$

By remembering the initial conditions $u(0) = u_0$ and $v_0 = \frac{\mathrm{d}u(0)}{\mathrm{d}t}$ and inserting them into (2.22) one gets:

$$u_0 = \hat{u}_+ + \hat{u}_-, \qquad v_0 = -j\omega_0\hat{u}_+ + j\omega_0\hat{u}_-. \qquad (2.24)$$

Thus, the constants $\hat{u}_+$ and $\hat{u}_-$ are complex conjugates. Substituting these expressions into equation (2.23) yields (2.20).

The energy analysis is again conducted by multiplying equation (2.19) by the velocity $\frac{\mathrm{d}u}{\mathrm{d}t}$. Then, by means of the identities (2.4) one gets:

$$\frac{\mathrm{d}}{\mathrm{d}t}\left(\frac{1}{2}\left(\frac{\mathrm{d}u}{\mathrm{d}t}\right)^2 + \frac{\omega_0^2 u^2}{2}\right) = 0 \qquad (2.25)$$

The expression within the parentheses does not yet have the dimension of energy. To get the total energy of the system, multiply by the mass m, obtaining:

$$\frac{\mathrm{d}}{\mathrm{d}t}H = 0, \qquad H = \frac{m}{2}\left(\frac{\mathrm{d}u}{\mathrm{d}t}\right)^2 + \frac{Ku^2}{2}. \qquad (2.26)$$

Note that this step ensures the correct dimensionality of energy but is unnecessary for stability analysis, as the mass is a positive constant. The balance (2.26) leads to energy conservation. The system's velocity is bounded by the kinetic energy, following (2.10). Additionally, a bound on the solution size derives from the quadratic form of the potential:

$$|u(t)| \leq \sqrt{\frac{2H_0}{K}} \; \forall\, t. \qquad (2.27)$$

2.2.1 First-order form

It is useful to express the oscillator in first-order form. To this end, a change of variables is necessary. For oscillators with constant mass and stiffness, the generalised coordinates q and p take the form:

$$q \triangleq \omega_0 \, u, \qquad p \triangleq \frac{\mathrm{d}u}{\mathrm{d}t}. \tag{2.28}$$

Here, p represents the momentum normalised by mass, with the dimensions of velocity. Now, one may substitute the expressions for p and q into the quantity between parenthesis in (2.25), obtaining:

$$H(q, p) = \frac{p^2}{2} + \frac{q^2}{2}, \tag{2.29}$$

which, as (2.25), has the dimension of energy divided by mass. Equation (2.19) becomes:

$$\frac{\mathrm{d}\mathbf{x}}{\mathrm{d}t} = \mathbf{J}\nabla_{\mathbf{x}}H. \tag{2.30}$$

The system state $\mathbf{x}$ and the matrix $\mathbf{J}$ are expressed as:

$$\mathbf{x} = \begin{bmatrix} q \\ p \end{bmatrix}, \qquad \mathbf{J} = \begin{bmatrix} 0 & \omega_0 \\ -\omega_0 & 0 \end{bmatrix}, \tag{2.31}$$

and the gradient with respect to the state has the form $\nabla_{\mathbf{x}} = \begin{bmatrix} \partial_q \\ \partial_p \end{bmatrix}$. Thus:

$$\nabla_{\mathbf{x}}H = \mathbf{x}. \tag{2.32}$$

Note that, when defining the gradient, the notation for partial derivatives used throughout the text was introduced: the n-th order partial derivative with respect to the variable α is here denoted as ∂_α^n.

An energy balance can be obtained by left-multiplying (2.30) by $\nabla_{\mathbf{x}}H$. Since $\mathbf{J}$ is skew-symmetric, and owing to the chain rule $\frac{\mathrm{d}}{\mathrm{d}t}H = (\nabla_{\mathbf{x}}H)^{\mathsf{T}}\frac{\mathrm{d}\mathbf{x}}{\mathrm{d}t}$, one obtains again a conservative balance:

$$\frac{\mathrm{d}}{\mathrm{d}t}H = 0. \tag{2.33}$$

The particular choice of variables allows the matrix $\mathbf{J}$ to be written in skew-symmetric form, which is a typical structure of port-Hamiltonian systems (PHSs) [210, 84]. Equations (2.19) and (2.30) are entirely equivalent in the continuous domain.

2.2.2 Loss

Real physical systems are never perfectly conservative, and different damping mechanisms come into play. A common form is viscous damping, where the force is proportional to the system's velocity. This model is typically used to describe frictional forces such as air resistance. It can be introduced into the oscillator's equation (2.19) as follows:

$$\frac{\mathrm{d}^2 u}{\mathrm{d}t^2} = -\omega_0^2 u - 2\sigma_0 \frac{\mathrm{d}u}{\mathrm{d}t}. \tag{2.34}$$

Here, $\sigma_0 \geq 0$ is a constant measured in s^{-1}, known as the damping coefficient of the system, regulating the decay time. Solutions to this equation can be found using an ansatz, or a test solution of the form: $u = \hat{u}e^{st}$, with $\hat{u}, s \in \mathbb{C}$. Substituting this into (2.34) yields

$$(s^2 + 2\sigma_0 s + \omega_0^2)\hat{u} = 0, \tag{2.35}$$

implying the characteristic equation:

$$s^2 + 2\sigma_0 s + \omega_0^2 = 0. \tag{2.36}$$

Solving for s, the roots are found to be:

$$s_\pm = -\sigma_0 \pm \sqrt{\sigma_0^2 - \omega_0^2}. \tag{2.37}$$

The nature of the roots $s_\pm$ determines the oscillator's behaviour: If damping is small ($\sigma_0 < \omega_0$), the system is underdamped. In this case, the roots are complex:

$$s_\pm = -\sigma_0 \pm j\sqrt{\omega_0^2 - \sigma_0^2}, \tag{2.38}$$

and the general solution (2.22) may be written as:

$$\bar{u}(t) = \hat{u}_+ e^{s_+ t} + \hat{u}_- e^{s_- t} = e^{-\sigma_0 t}\left(\hat{u}_+ e^{j\sqrt{\omega_0^2 - \sigma_0^2}t} + \hat{u}_- e^{-j\sqrt{\omega_0^2 - \sigma_0^2}t} \right). \tag{2.39}$$

By defining the damped natural frequency $\omega_d \triangleq \sqrt{\omega_0^2 - \sigma_0^2}$, the solution becomes:

$$\bar{u}(t) = e^{-\sigma_0 t}\left(\hat{u}_+ e^{j\omega_d t} + \hat{u}_- e^{-j\omega_d t} \right). \tag{2.40}$$

This form is similar to the undamped form (2.22), with notable differences: the solution is now modulated by an exponential decay factor $e^{-\sigma_0 t}$ and oscillates at a frequency ω_d which

is lower than the natural frequency ω_0. When the initial conditions are substituted, following a procedure similar to that seen for the undamped case, the solution takes the real form:

$$\bar{u}(t) = e^{-\sigma_0 t}\left(u_0\cos(\omega_d t) + \frac{v_0 + \sigma_0 u_0}{\omega_d}\sin(\omega_d t)\right),\qquad(2.41)$$

which generalises (2.21) to the damped case.

When $\sigma_0 \geq \omega_0$, the roots become real numbers. The system is critically damped when $\sigma_0 = \omega_0$, and overdamped when $\sigma_0 > \omega_0$. In both cases, the roots remain negative, and the solution is strictly decaying, preventing any oscillatory motion; therefore, these scenarios are not considered within the scope of this work.

Because damping is an important perceptual feature in acoustics, it is crucial to set the decay times of physical models accurately. To this end, it is useful to relate the constant σ_0 to a more practical quantity, such as the decay time T_{60}, which is defined as the time taken by the oscillator to reduce its amplitude of vibration by 60 dB. Using the definition of dB, one has:

$$20\log e^{2\sigma_0 T_{60}} = 60.\qquad(2.42)$$

Then, changing the logarithm base: $20\ln e^{2\sigma_0 T_{60}} = 60\ln 10$, yielding:

$$T_{60} = \frac{3\ln 10}{\sigma_0}.\qquad(2.43)$$

The energy analysis for system (2.34) is a straightforward extension of the procedure seen for system (2.19). By multiplying both sides of the equation by $m\frac{\mathrm{d}u}{\mathrm{d}t}$, one has:

$$\frac{\mathrm{d}}{\mathrm{d}t}H = -2m\sigma_0\left(\frac{\mathrm{d}u}{\mathrm{d}t}\right)^2 \triangleq -Q(t) \leq 0.\qquad(2.44)$$

Here, $Q \geq 0$ is the power dissipated by the oscillator, and H has the same form of the energy (2.26). Thus, the energy is a positive definite and monotonically decreasing function of time, and the system is now dissipative. Because the energy is still positive definite, the solution remains bounded.

2.2.3 Forcing component

A thorough analysis of the behaviour of a forced oscillator is outside the scope of this text (more information on this topic can be found in [148, Chapters 3,4]). Nevertheless, it is useful to introduce the notation relative to a forcing component. A source term may be

included as

$$\frac{\mathrm{d}^2 u}{\mathrm{d}t^2} = -\omega_0^2 u - 2\sigma_0 \frac{\mathrm{d}u}{\mathrm{d}t} + \frac{1}{m} F, \tag{2.45}$$

where $F = F(t)$ is a time-dependent external forcing function. Energy analysis leads to the following balance

$$\frac{\mathrm{d}}{\mathrm{d}t} H = -Q(t) + P(t), \tag{2.46}$$

where $P(t) = \frac{\mathrm{d}u}{\mathrm{d}t} F$ is the injected power, and H is as per (2.26).

2.2.4 Preamble 1: Vector inner products

Before moving on, it is useful to introduce the vector notation employed in this text. Given two real vectors $\mathbf{u}$, $\mathbf{v}$, the inner product and norm are written as:

$$\langle \mathbf{u}, \mathbf{v} \rangle \triangleq \mathbf{u}^\mathsf{T} \mathbf{v}, \qquad \|\mathbf{u}\| = \sqrt{\langle \mathbf{u}, \mathbf{u} \rangle}. \tag{2.47}$$

The norm is positive by definition, and the usual properties of symmetry and linearity hold for the inner product [130, Chapter 5]. The Cauchy-Schwartz and Triangle inequalities read:

$$|\langle \mathbf{u}, \mathbf{v} \rangle| \leq \|\mathbf{u}\| \|\mathbf{v}\| \tag{2.48a}$$

$$\|\mathbf{u} + \mathbf{v}\| \leq \|\mathbf{u}\| + \|\mathbf{v}\|. \tag{2.48b}$$

Now, consider a symmetric, positive definite matrix $\mathbf{A}$. One has:

$$\langle \mathbf{u}, \mathbf{A}\mathbf{u} \rangle \geq 0, \tag{2.49}$$

and, given the properties of the transposition operator:

$$\langle \mathbf{u}, \mathbf{A}\mathbf{v} \rangle = \mathbf{u}^\mathsf{T} \mathbf{A} \mathbf{v} = (\mathbf{A}\mathbf{u})^\mathsf{T} \mathbf{v} = \mathbf{v}^\mathsf{T} \mathbf{A} \mathbf{u} = (\mathbf{A}\mathbf{v})^\mathsf{T} \mathbf{u}. \tag{2.50}$$

Furthermore, the norm of $\mathbf{u}$ can be bounded in terms of the smallest and largest eigenvalues of $\mathbf{A}$:

$$0 \leq \min(\mathrm{eig}(\mathbf{A})) \|\mathbf{u}\| \leq \mathbf{u}^\mathsf{T} \mathbf{A} \mathbf{u} \leq \max(\mathrm{eig}(\mathbf{A})) \|\mathbf{u}\|, \tag{2.51}$$

where $\mathrm{eig}(\mathbf{A})$ indicates the set of eigenvalues (or spectrum) of $\mathbf{A}$.

2.2.5   Multiple degrees of freedom

So far, only single-degree of freedom (DoF) systems were considered. A multi-DoF system has multiple natural frequencies, known as natural modes of vibration: the number of these modes equals the system's DoF. The extension to multiple DoF is achieved through ODEs coupled together: a system of N coupled oscillators may be written as:

$$\mathbf{M}\frac{\mathrm{d}^2\mathbf{u}}{\mathrm{d}t^2} = -\mathbf{K}\mathbf{u}. \tag{2.52}$$

Here, $\mathbf{u} = [u_1, u_2 \ldots, u_N]$ is a vector containing the displacements of the individual masses, $\mathbf{M}$ is a diagonal, positive definite matrix called the mass matrix, storing the individual oscillators masses, and $\mathbf{K}$ is a positive definite square matrix referred to as the stiffness matrix.

System (2.52) may be diagonalised by formulating a generalised eigenvalue problem as:

$$\mathbf{K}\mathbf{U} = \mathbf{M}\mathbf{U}\mathbf{S}^2, \tag{2.53}$$

where $\mathbf{U}$ is a matrix whose columns are composed of the eigenvectors and $\mathbf{S}$ is a diagonal matrix with the square roots of the eigenvalues. Under oscillating conditions, the entries of $\mathbf{S}$ are purely imaginary, so $\mathbf{S} = j\mathbf{\Omega}$, where $\mathbf{\Omega}$ is a diagonal matrix containing the real eigenvalues:

$$\mathbf{\Omega} = \begin{bmatrix} \omega_1 & & \\ & \ddots & \\ & & \omega_N \end{bmatrix}. \tag{2.54}$$

When $\mathbf{M}^{-1}\mathbf{K}$ is symmetric, the spectral theorem [130, Chapter 8] ensures the existence of a basis of eigenvectors in $\mathbb{R}^N$, with N associated real and distinct eigenvalues. Therefore, $\mathbf{U}$ is orthogonal and contains the mode shapes, while $\mathbf{\Omega}$ stores the correspondent real eigenfrequencies, one for each eigenvector. Otherwise, the eigenvectors may not be linearly independent, and $\mathbf{U}$ could be rank-deficient. In this case, some eigenvalues are repeated, i.e., ω_i has an algebraic multiplicity greater than one for some i. Considering again the eigenvalue problem (2.53), and assuming $\mathbf{M}^{-1}\mathbf{K}$ to be symmetric, one may left-multiply by $\mathbf{M}^{-1}$ and right-multiply by $\mathbf{U}^{-1}$, obtaining the eigendecomposition:

$$\mathbf{M}^{-1}\mathbf{K} = -\mathbf{U}\mathbf{\Omega}^2\mathbf{U}^{-1}. \tag{2.55}$$

Defining $\mathbf{w} \triangleq \mathbf{U}^{-1}\mathbf{u}$, yields:

$$\frac{\mathrm{d}^2\mathbf{w}}{\mathrm{d}t^2} = -\mathbf{\Omega}^2\mathbf{w}. \tag{2.56}$$

Since $\mathbf{\Omega}$ is a diagonal matrix, this system is completely decoupled. Each line represents the equation of a harmonic oscillator for the modal coordinate w_i with resonant frequency ω_i. The original coordinates $\mathbf{u}$ are retrieved with the projection $\mathbf{u} = \mathbf{U}\mathbf{w}$.

An energy analysis for system (2.52) is obtained by taking an inner product with $\frac{d\mathbf{u}}{dt}$:

$$\left\langle \frac{d\mathbf{u}}{dt}, \mathbf{M}\frac{d^2\mathbf{u}}{dt^2} \right\rangle = -\left\langle \frac{d\mathbf{u}}{dt}, \mathbf{K}\mathbf{u} \right\rangle. \tag{2.57}$$

The derivative identities (2.4) still hold in the vector case; thus, the energy balance becomes:

$$\frac{d}{dt}H = 0, \qquad H = \frac{1}{2}\left\langle \frac{d\mathbf{u}}{dt}, \mathbf{M}\frac{d\mathbf{u}}{dt} \right\rangle + \frac{1}{2}\left\langle \mathbf{u}, \mathbf{K}\mathbf{u} \right\rangle, \tag{2.58}$$

leading to energy conservation. Additionally, the energy is non-negative if both $\mathbf{M}$ and $\mathbf{K}$ are symmetric and positive definite, given the property (2.49), and the following bounds can be derived:

$$\left\langle \frac{d\mathbf{u}}{dt}, \mathbf{M}\frac{d\mathbf{u}}{dt} \right\rangle \le \sqrt{\frac{2H_0}{\min(\text{eig}(\mathbf{M}))}}, \quad \left\langle \mathbf{u}, \mathbf{K}\mathbf{u} \right\rangle \le \sqrt{\frac{2H_0}{\min(\text{eig}(\mathbf{K}))}}, \tag{2.59}$$

where H_0 is the initial energy. Hence, proving that the mass and stiffness matrices are symmetric and positive definite is sufficient to ensure the stability of a generic system of the form (2.52).

2.2.6 Loss and Forcing

Viscous loss and a forcing term can be easily included into system (2.52) as follows:

$$\mathbf{M}\frac{d^2\mathbf{u}}{dt^2} = -\mathbf{K}\mathbf{u} - \mathbf{C}\frac{d\mathbf{u}}{dt} + \mathbf{f}. \tag{2.60}$$

Here, $\mathbf{f} = [F_1, \ldots, F_N]^\intercal$ is a time-dependent vector containing the source terms for each oscillator while $\mathbf{C}$ is a positive definite damping matrix yet to be defined. Equation (2.60) represents the extension of system (2.45) to multiple DoF. The energy analysis is run analogously by taking an inner product with $\frac{d\mathbf{u}}{dt}$:

$$\frac{d}{dt}H = -Q(t) + P(t), \qquad Q(t) = \left\langle \frac{d\mathbf{u}}{dt}, \mathbf{C}\frac{d\mathbf{u}}{dt} \right\rangle, \qquad P(t) = \left\langle \frac{d\mathbf{u}}{dt}, \mathbf{f} \right\rangle, \tag{2.61}$$

where H has the form (2.58). A passive energy balance is obtained when $P(t) = 0$.
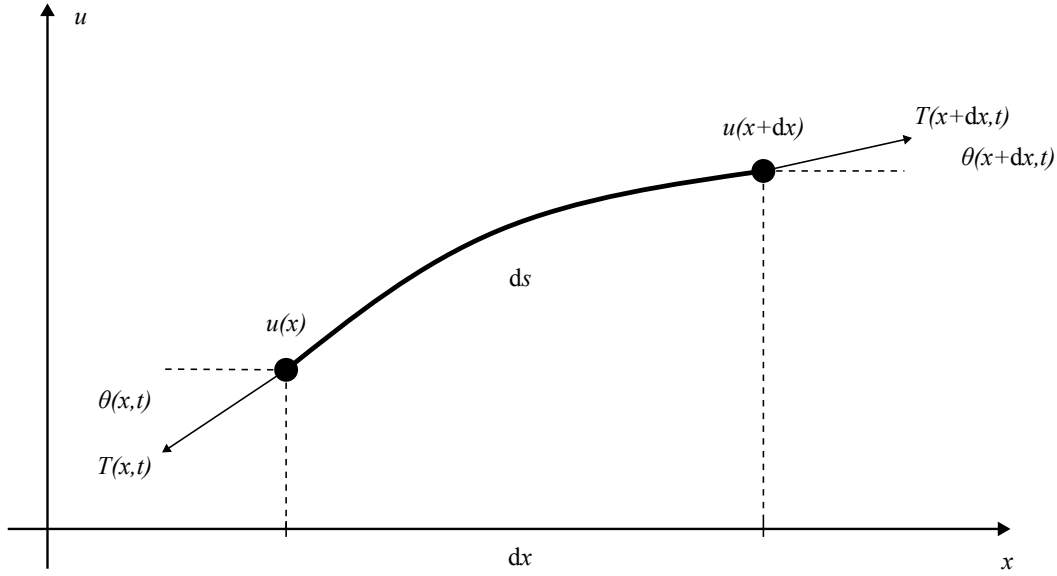
Fig. 2.2 An infinitesimal section of the ideal string.

If proportional damping [148, Chapter 7] is assumed, the damping matrix is expressed in the form:

$$\mathbf{C} = \sigma_0 \mathbf{M} + \sigma_1 \mathbf{K}. \tag{2.62}$$

Here, σ_0 is a non-negative constant damping coefficient, as in the single-DoF case, and σ_1 is another non-negative constant regulating a frequency-dependent damping value. Under this assumption, system (2.60) can be fully diagonalized, as in the unforced, undamped case.

2.3 The 1-D wave equation

The framework detailed above treated discrete systems, or lumped systems, which are governed by ODEs. If the system has a spatial dimension, it must be treated as distributed. The displacement is given as a function of space, and the system is governed by time-dependent PDEs. Because the focus is on strings, only one spatial dimension will be considered in this text. The displacement of a distributed object is represented by a function $u(x,t) : \mathcal{D} \times \mathbb{R}_0^+ \to \mathbb{R}$, where x is defined over a simply connected domain $\mathcal{D} \subseteq \mathbb{R}$; as before, u is assumed to be sufficiently smooth.

Consider an ideal string, i.e., the string is lossless and has no stiffness. A string segment $\mathrm{d}s$ is represented in Figure 2.2. The string lies on the x axis and is subject to a tension $T_0(x,t)$. The vertical displacement is denoted by $u(x,t)$. θ is the deflection angle, and the mass of the segment is given by the volume density ρ (measured in Kg/m^3) multiplied by the

volume of the string element, $\mathrm{d}m = \mathrm{d}s\rho A$, where A is the cross-sectional area of the string (in m^2), assumed constant. For small displacements, the deflection angle is minimal. With this assumption, and by considering the tension to be uniform over the spatial domain, one may arrive at the equation of motion:

$$\rho A \partial_t^2 u = T_0 \partial_x^2 u. \tag{2.63}$$

The complete derivation is outside the scope of this work; further details can be found in [94, Chapter 2]. Equation (2.63) represents the ideal string equation. When divided by a constant with the dimension of mass, it is usually called 1-D wave equation or simply the wave equation. In this context, it will be referred to as the wave equation also in the form (2.63).

As the SHO, the 1-D wave equation (2.63) is a second-order differential equation in time and requires two initial conditions. Usually, these are the values of the state u and the velocity $\partial_t u$ at $t = 0$, and one may define

$$u_0(x) \triangleq u(x, 0), \qquad v_0(x) \triangleq \partial_t u\Big|_{t=0}. \tag{2.64}$$

Since the system is distributed in space, the initial conditions now depend on x.

2.3.1 Preamble 2: spatial inner product and integral relations

Before proceeding, it is useful to introduce the mathematical notation employed in this text for continuous spatial inner products. Consider two functions $a(x, t)$, $b(x, t)$, defined over a domain $\mathcal{D} \subseteq \mathbb{R}$, with endpoints d_- and d_+. Then, the L^2 inner product and related norm are defined as [130, Chapter 5]:

$$\langle a, b \rangle_{\mathcal{D}} \triangleq \int_{\mathcal{D}} ab \, \mathrm{d}x, \qquad \|a\|_{\mathcal{D}} \triangleq \sqrt{\langle a, a \rangle_{\mathcal{D}}} \tag{2.65}$$

Note that, because a and b depend on time, $\langle a, b \rangle$ is a function of time: $\langle a, b \rangle (t)$. The usual properties of symmetry and linearity hold, and the norm is positive definite.

The Cauchy-Schwartz and triangle inequalities read, respectively:

$$|\langle a, b \rangle_{\mathcal{D}}| \leq \|a\|_{\mathcal{D}} \|b\|_{\mathcal{D}} \tag{2.66a}$$

$$\|a + b\|_{\mathcal{D}} \leq \|a\|_{\mathcal{D}} + \|b\|_{\mathcal{D}}. \tag{2.66b}$$

For another another generic function $c(x, t) : \mathcal{D} \times \mathbb{R}_0^+ \to \mathbb{R}$, it holds that:

$$\langle a, bc \rangle_{\mathcal{D}} = \langle ab, c \rangle_{\mathcal{D}}.$$ (2.67)

It is worth explicitly writing the integration by parts rule, which will be extensively employed in this text:

$$\langle a, \partial_x b \rangle_{\mathcal{D}} = \int_{\mathcal{D}} a(\partial_x b)\, \mathrm{d}x = -\int_{\mathcal{D}} (\partial_x a) b\, \mathrm{d}x + ab\Big|_{d_-}^{d_+} = -\langle \partial_x a, b \rangle_{\mathcal{D}} + ab\Big|_{d_-}^{d_+}.$$ (2.68)

This rule can be extended to second derivatives by applying the formula twice:

$$\left\langle a, \partial_x^2 b \right\rangle_{\mathcal{D}} = \left\langle \partial_x^2 a, b \right\rangle_{\mathcal{D}} + (\partial_x a) b\Big|_{d_-}^{d_+} - a(\partial_x b)\Big|_{d_-}^{d_+}.$$ (2.69)

If the endpoints of the domain are not time-dependent, Leibniz's rule holds:

$$\frac{\mathrm{d}}{\mathrm{d}t} \int_{\mathcal{D}} a\, \mathrm{d}x = \int_{\mathcal{D}} \partial_t a\, \mathrm{d}x.$$ (2.70)

Since the integral is over space, what remains after integration has no spatial dependence; therefore, the partial derivative becomes a total derivative outside the integral. For an inner product, this results in:

$$\frac{\mathrm{d}}{\mathrm{d}t} \langle a, b \rangle = \langle \partial_t a, b \rangle + \langle a, \partial_t b \rangle.$$ (2.71)

For two vectors of functions $\mathbf{a} = [a_1, a_2, \ldots, a_N]^\mathsf{T}$ and $\mathbf{b} = [b_1, b_2, \ldots, b_N]^\mathsf{T}$, the inner product becomes:

$$\langle \mathbf{a}, \mathbf{b} \rangle_{\mathcal{D}} = \int_{\mathcal{D}} \mathbf{a}^\mathsf{T} \mathbf{b}\, dx.$$ (2.72)

2.3.2   Energy analysis and boundary conditions

Since the string has a finite length, it is necessary to specify boundary conditions: this process is known as defining a boundary value problem (BVP). Boundary conditions can be derived using energy arguments. Consider a string of length L. Thus, two boundary points are introduced at $x = 0$ and $x = L$. The energy analysis, similar to the lumped case, is obtained by taking the inner product of the equation of motion (2.63) with the velocity:

$$\rho A \left\langle \partial_t u, \partial_t^2 u \right\rangle_{\mathcal{D}} = T_0 \left\langle \partial_t u, \partial_x^2 u \right\rangle_{\mathcal{D}},$$ (2.73)

where $\mathcal{D} = [0, L]$, and the limits of integration are 0 and L. Employing integration by parts (2.68) yields:

$$\rho A \left\langle \partial_t u, \partial_t^2 u \right\rangle_{\mathcal{D}} + T_0 \left\langle \partial_t \partial_x u, \partial_x u \right\rangle_{\mathcal{D}} = T_0 (\partial_x u \partial_t u) \Big|_{x=0}^{x=L}. \tag{2.74}$$

Using the relation (2.71), the inner product at the left-hand side can be written as:

$$\left\langle \partial_t u, \partial_t^2 u \right\rangle_{\mathcal{D}} = - \left\langle \partial_t^2 u, \partial_t u \right\rangle_{\mathcal{D}} + \frac{\mathrm{d}}{\mathrm{d}t} \left\langle \partial_t u, \partial_t u \right\rangle_{\mathcal{D}}. \tag{2.75}$$

Due to the symmetry of the inner product, this simplifies to:

$$\left\langle \partial_t u, \partial_t^2 u \right\rangle_{\mathcal{D}} = \frac{1}{2} \frac{\mathrm{d}}{\mathrm{d}t} \left\langle \partial_t u, \partial_t u \right\rangle_{\mathcal{D}} \tag{2.76}$$

The same relations hold for the right-hand side, and equation (2.74) can be written as:

$$\frac{\mathrm{d}}{\mathrm{d}t} H = T_0 (\partial_x u \partial_t u) \Big|_{x=0}^{x=L}, \tag{2.77}$$

where the energy H takes the form:

$$H = \frac{\rho A}{2} \| \partial_t u \|_{\mathcal{D}}^2 + \frac{T_0}{2} \| \partial_x u \|_{\mathcal{D}}^2. \tag{2.78}$$

Equation (2.77) represents the energy balance for the wave equation (2.63), which depends on the boundary conditions. Specifically, it is expressed as the product of force ($T_0 \partial_x u$) and velocity ($\partial_t u$) at the boundary points. There are two primary approaches to ensure energy conservation. The first involves setting the displacement or velocity to zero as:

$$u(0, t) = 0, \ u(L, t) = 0 \qquad \forall t \geq 0. \tag{2.79}$$

This is known as a fixed or Dirichlet-type condition. The second approach corresponds to imposing a vanishing force at the boundary:

$$\partial_x u \Big|_{x=0} = 0, \ \partial_x u \Big|_{x=L} = 0 \qquad \forall t \geq 0. \tag{2.80}$$

This is referred to as a free (free of load) or Neumann-type condition and corresponds to a string free to move in the transverse direction. Neumann boundaries are typically of little interest in the context of strings since they are usually attached to a bridge or soundboard. However, this form becomes useful when dealing with finite impedance boundaries, as will be discussed later. Note that mixed boundaries are also possible. Under fixed or free

boundary conditions, the balance (2.77) is passive. Additionally, the positivity of the energy ensures that the solution remains bounded, analogously to the behaviour observed in the simple harmonic oscillator (SHO). Thus:

$$\|\partial_t u\|_{\mathcal{D}} \leq \sqrt{\frac{2H_0}{\rho A}}, \qquad \|\partial_x u\|_{\mathcal{D}} \leq \sqrt{\frac{2H_0}{T_0}}, \tag{2.81}$$

where the initial energy is given by the initial conditions (2.64):

$$H_0 = \frac{\rho A}{2}\|v_0\|_{\mathcal{D}}^2 + \frac{T_0}{2}\|\partial_x u_0\|_{\mathcal{D}}^2. \tag{2.82}$$

Under fixed boundary conditions, bounds on u, rather than its derivatives, may be obtained [24, Chapter 6]. Note that the subscript of the inner product will be dropped henceforth if the domain is finite, assuming the integration is performed over the domain $\mathcal{D} = [0, L]$ unless otherwise specified.

2.3.3   Modal expansion

Consider again equation (2.63), defined over a length L, with both ends fixed as in (2.79). A modal description is obtained when the motion is synchronous. In this case, the string presents a displacement pattern, or profile, with a fixed shape, which changes only in amplitude over time. Then, the solution is said to be separable and can be written as:

$$u(x, t) = \chi(x)w(t), \tag{2.83}$$

where χ represents the string profile as a function of space only, and w is the time-dependent amplitude. Inserting into equation (2.63) gives:

$$\rho A \chi \frac{\mathrm{d}^2 w}{\mathrm{d}t^2} = T_0 \frac{\mathrm{d}^2 \chi}{\mathrm{d}x^2} w \quad \Rightarrow \quad \frac{\mathrm{d}^2 w}{\mathrm{d}t^2}\frac{1}{w} = c^2 \frac{\mathrm{d}^2 \chi}{\mathrm{d}x^2}\frac{1}{\chi}, \qquad c \triangleq \sqrt{\frac{T_0}{\rho A}}, \tag{2.84}$$

where c is the wave speed. Since the left-hand side depends only on time and the right-hand side depends only on space, the solution is indeed separable, and it can be written:

$$\frac{\mathrm{d}^2 w}{\mathrm{d}t^2}\frac{1}{w} = c^2 \frac{\mathrm{d}^2 \chi}{\mathrm{d}x^2}\frac{1}{\chi} \triangleq \lambda, \tag{2.85}$$

where $\lambda \in \mathbb{R}$, because all the constants are real. This leads to two separate ODEs:

$$\frac{\mathrm{d}^2 w}{\mathrm{d}t^2} - \lambda w = 0, \tag{2.86a}$$

$$\frac{\mathrm{d}^2 \chi}{\mathrm{d}x^2} - \frac{\lambda}{c^2} \chi = 0. \tag{2.86b}$$

Consider the equation (2.86a) first. The characteristic polynomial and its solutions are:

$$s^2 - \lambda = 0 \qquad \Rightarrow \qquad s_\pm = \pm\sqrt{\lambda}. \tag{2.87}$$

If λ is positive the solution diverges, which is incompatible with string oscillations; thus, it must be either zero or negative. Now, one may introduce the notation: $\lambda = -\omega^2$, with $\omega \geq 0$. The roots then become $s_\pm = \pm\sqrt{-\omega^2} = \pm j\omega$, and the solution to the ODE is:

$$w(t) = \hat{w}_+ e^{j\omega t} + \hat{w}_- e^{-j\omega t}, \tag{2.88}$$

which corresponds to the solution of a SHO. Thus, the temporal solution is harmonic, with a frequency ω.

The value (or values) of the frequency ω and the nature of the displacement configuration $\chi(x)$ can be determined by examining the spatial equation (2.86b), which constitutes a differential eigenvalue problem. First, rewrite the ODE and the boundary conditions:

$$\frac{\mathrm{d}^2 \chi}{\mathrm{d}x^2} + \beta^2 \chi = 0, \qquad \chi(0) = \chi(L) = 0, \tag{2.89}$$

where it was defined $\beta^2 \triangleq \omega^2/c^2$. This is another harmonic equation, and the solution may be written in the form:

$$\chi(x) = A\sin(\beta x) + B\cos(\beta x), \tag{2.90}$$

where A and B are real-valued constants to be determined. Since at the left boundary $\chi(0) = 0$ then it must be that $B = 0$, and:

$$\chi(x) = A\sin(\beta x). \tag{2.91}$$

On the other hand, at the right boundary, one has $\chi(L) = 0$, thus:

$$A\sin(\beta L) = 0. \tag{2.92}$$

This is the characteristic equation of the differential eigenvalue problem. It is a transcendental equation, leading to an infinite number of nontrivial solutions, or wavenumbers:

$$\beta_m = \frac{m\pi}{L}. \tag{2.93}$$

Note that the trivial solution $\beta = 0$, which corresponds to the zero-frequency case $\omega = 0$, must be excluded. In fact, to satisfy the boundary conditions, one would obtain $\chi(x) = 0\ \forall x$, preventing any oscillatory motion. Thus, $m \in \mathbb{N}$.

Inserting equation (2.93) into (2.91) gives an infinite set of eigenfunctions:

$$\chi_m(x) = A_m \sin\left(\frac{m\pi x}{L}\right), \tag{2.94}$$

usually referred to as mode shapes or eigenmodes of the system, where A_m are constant amplitudes. Each mode shape is associated with a temporal solution $w_m(t)$, called also modal coordinate, oscillating at a frequency ω_m, which depends on the wavenumber β_m:

$$\omega_m = \beta_m = \frac{m\pi c}{L}. \tag{2.95}$$

These are the system's eigenfrequencies. Each eigenfrequency-mode shape couple is a mode of vibration of the system. The general solution $u(x,t)$ can now be written as a linear combination of the individual solutions:

$$u(x,t) = \sum_{m=1}^{\infty} \chi_m(x)w_m(t). \tag{2.96}$$

For practical applications, the modes are usually limited to a finite number M. Thus, the solution (2.96) can be written in vector form:

$$u(x,t) = \boldsymbol{\chi}^{\mathsf{T}}(x)\mathbf{w}(t), \tag{2.97}$$

where $\boldsymbol{\chi}$ is a vector of eigenfunctions, and $\mathbf{w}$ contains the modal coordinates. Both have length M.

Modal projection

Consider a solution of the type (2.97) and substitute it into the wave equation (2.63):

$$\rho A \boldsymbol{\chi}^{\mathsf{T}} \frac{\mathrm{d}^2 \mathbf{w}}{\mathrm{d}t^2} = T_0 \frac{\mathrm{d}^2 \boldsymbol{\chi}^{\mathsf{T}}}{\mathrm{d}x^2}\mathbf{w}. \tag{2.98}$$
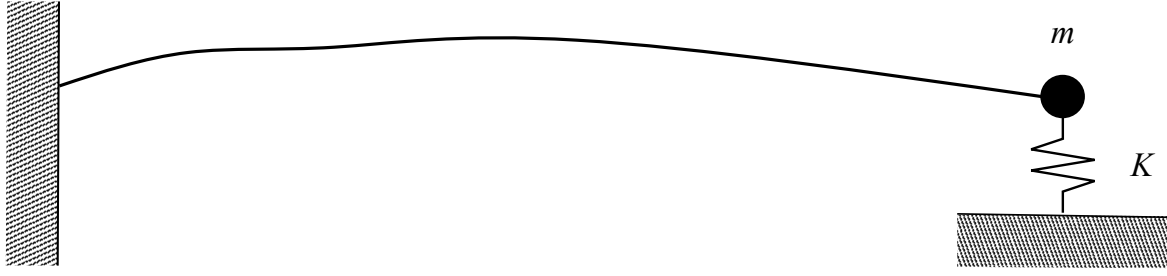
Fig. 2.3 Ideal string connected to a lumped mass-spring system at one boundary.

Next, left-multiply by another vector $\boldsymbol{\chi}$ and integrate over the string length. This corresponds to taking an inner product in L^2:

$$\rho A \int_0^L \boldsymbol{\chi}\boldsymbol{\chi}^{\mathsf{T}}\mathrm{d}x \frac{\mathrm{d}^2\mathbf{w}}{\mathrm{d}t^2} = T_0 \int_0^L \boldsymbol{\chi}\frac{\mathrm{d}^2\boldsymbol{\chi}^{\mathsf{T}}}{\mathrm{d}x^2}\mathrm{d}x\,\mathbf{w}, \tag{2.99}$$

where the integration sign applies individually to each element of the matrices resulting from the outer products. Through integration by parts on the right-hand side and dividing through by ρA, one gets:

$$\langle \boldsymbol{\chi}, \boldsymbol{\chi}^{\mathsf{T}} \rangle \frac{\mathrm{d}^2\mathbf{w}}{\mathrm{d}t^2} = -c^2 \left\langle \frac{\mathrm{d}\boldsymbol{\chi}}{\mathrm{d}x}, \frac{\mathrm{d}\boldsymbol{\chi}^{\mathsf{T}}}{\mathrm{d}x} \right\rangle \mathbf{w} + c^2\boldsymbol{\chi}\frac{\mathrm{d}\boldsymbol{\chi}^{\mathsf{T}}}{\mathrm{d}x}\Big|_0^L. \tag{2.100}$$

The boundary term vanishes due to Dirichlet boundaries. The modes can be proved to be orthogonal; furthermore, by choosing $A_m = A \triangleq \sqrt{2/L}$, the modes become orthonormal and are called normal modes. Then, equation (2.100) may be written as:

$$\frac{\mathrm{d}^2\mathbf{w}}{\mathrm{d}t^2} = -\boldsymbol{\Omega}^2\mathbf{w}, \qquad \boldsymbol{\Omega} = \begin{bmatrix} \omega_1 & & \\ & \ddots & \\ & & \omega_M \end{bmatrix}, \tag{2.101}$$

where ω_m are the eigenfrequencies (2.95), and equation (2.101) is now equivalent to the system of decoupled oscillators (2.56). This method is known as modal projection and is the procedure for expressing a system in modal form when the mode shapes and eigenfrequencies are known.

2.3.4   Lumped mass at the boundary

Dirichlet and Neumann conditions serve as useful idealizations for the boundaries. However, more realistic conditions should also be considered. For instance, consider a fixed-free string, where the right boundary is attached to a mass-spring system, modelling a bridge. This

scenario is depicted in Figure 2.3. The equation governing the mass-spring system is:

$$m\frac{\mathrm{d}^2 U}{\mathrm{d}t^2} = -KU + F, \tag{2.102}$$

where $F = F(t)$ is the force exerted by the string onto the mass, and one may set the contact condition $U(t) = u(L, t)$ $\forall t$ since the mass is attached to the string's end. The force is determined from the energy balance expression (2.77):

$$F(t) = -T_0 \partial_x u\Big|_{x=L}, \tag{2.103}$$

where the negative sign indicates that the force is exerted by the string onto the mass.

To derive an energy balance, first multiply equation (2.102) by the velocity $\frac{\mathrm{d}U}{\mathrm{d}t}$. Using the usual derivative identities, the definition (2.103) and noting that $U(t) = u(L, t)$ yields:

$$\frac{\mathrm{d}}{\mathrm{d}t} \underbrace{\left(\frac{m}{2} \left(\frac{\mathrm{d}U}{\mathrm{d}t} \right)^2 + \frac{KU^2}{2} \right)}_{H_m} = F\frac{\mathrm{d}U}{\mathrm{d}t} = -T_0 (\partial_x u \partial_x u)\Big|_{x=L}. \tag{2.104}$$

Next, consider equation (2.77): the term corresponding to the left boundary vanishes due to the Dirichlet condition. Substituting equation (2.104) into the left-hand side yields:

$$\frac{\mathrm{d}}{\mathrm{d}t} H = -\frac{\mathrm{d}}{\mathrm{d}t} H_m, \tag{2.105}$$

where H is as per equation (2.78). This indicates that the system is conservative. Such a boundary condition has a nonzero, finite impedance, unlike the fixed condition (infinite impedance) or the free condition (zero impedance).

Consider now an eigenvalue problem of the form (2.89), with the boundary condition at the right-end specified by (2.103). Since the left end remains fixed, the modes continue to be described by (2.91). At the right end, one has $\chi(L) = A\sin(\beta L)$. Thus, one may consider the contact condition in separable form $U(t) = \chi(L)w(t)$, substituting it into the boundary equation (2.102) and into the force expression (2.103). The time-dependent part simplifies, yielding:

$$(-m\omega^2 + K)\sin(\frac{\omega L}{c}) = -T_0 \frac{\omega}{c} \cos(\frac{\omega L}{c}). \tag{2.106}$$

This is the system's characteristic equation, which may be solved for ω numerically to determine the system eigenfrequencies. There are three significant cases to consider: when $m, K \to \infty$, the left-hand side dominates, resulting in eigenfrequencies characteristic of a fixed-fixed string; when $m, K \to 0$, the right-hand side dominates, yielding eigenfrequencies
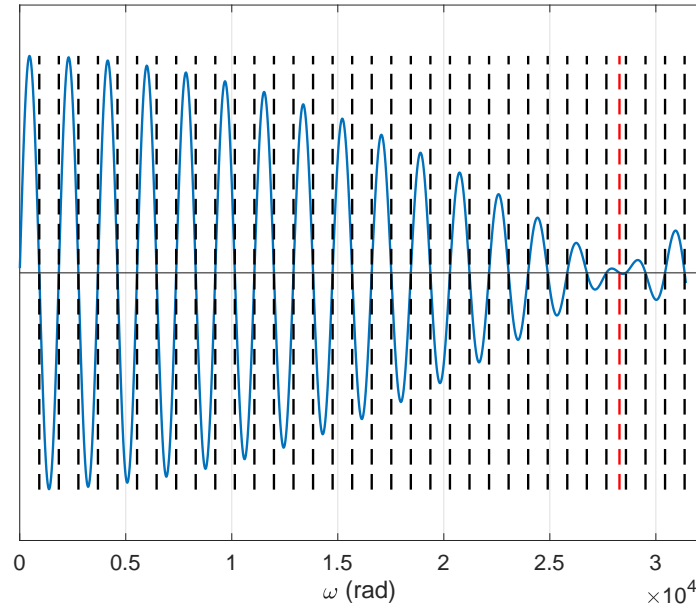
Fig. 2.4 Graphical solution of the transcendental equation for an ideal string attached to a mass-spring system. The characteristic equation is shown in blue, with intersections on the horizontal axis (solid line) representing the eigenfrequencies, highlighted by dashed lines. The red dashed line corresponds to the oscillator's natural frequency, and the black lines mark the frequencies of a fixed-fixed string. The string physical values are: $\rho = 5535$ Kg/m^3; $L = 0.69$ m; $A = 6.5 \times 10^{-7}$ m^2; $T_0 = 147.7$ N. The mass-spring values are: $m = 0.01$ Kg; $K = 8 \times 10^6$ N/m.

characteristic of a fixed-free string; and when $m, K > 0$, the system exhibits an additional degree of freedom, leading to eigenfrequencies characteristic of a fixed-fixed string plus one supplementary modal frequency corresponding to the natural frequency of the oscillator. The latter situation is depicted in Figure 2.4.

2.4   Stiff string

The ideal string is assumed to be perfectly flexible, which is a simplistic approximation. Various models account for finite thickness, as reviewed in Chapter 1. Here, a stiffness term following the Euler-Bernoulli model will be considered, as it has been found sufficient for musical acoustics applications [71]. A stiffness term may be added to equation (2.63) as:

$$\rho A \partial_t^2 u = T_0 \partial_x^2 u - E I_0 \partial_x^4 u, \qquad (2.107)$$

where E is Young's modulus for the string's material in Pa, and $I_0 = \frac{\pi r^4}{4}$ is the moment of inertia, with r being the string's radius in m. This equation remains a second-order PDE in time and can be complemented with initial conditions similar to those detailed for the wave equation.

2.4.1 Energy analysis and boundary conditions

Consider the string to be defined over the domain $\mathcal{D} = [0, L]$. The energy analysis of equation (2.107) is again performed by taking an inner product with the velocity:

$$\rho A \left\langle \partial_t u, \partial_t^2 u \right\rangle = T_0 \left\langle \partial_t u, \partial_x^2 u \right\rangle - E I_0 \left\langle \partial_t u, \partial_x^4 u \right\rangle. \tag{2.108}$$

By applying integration by parts (twice on the rightmost term), the following balance equation is obtained:

$$\frac{\mathrm{d}}{\mathrm{d}t} H = T_0 (\partial_x u \partial_t u) \Big|_{x=0}^{x=L} - E I_0 \left(\partial_t u \partial_x^3 u - \partial_x \partial_t u \partial_x^2 u \right) \Big|_{x=0}^{x=L}, \tag{2.109}$$

where the energy H takes the form:

$$H = \frac{\rho A}{2} \|\partial_t u\|^2 + \frac{T_0}{2} \|\partial_x u\|^2 + \frac{E I_0}{2} \|\partial_x^2 u\|^2. \tag{2.110}$$

In addition to the velocity and slope, the curvature of the stiff string is also bounded in terms of the string's initial energy:

$$\left\| \partial_x^2 u \right\| \le \sqrt{\frac{2 H_0}{E I_0}}. \tag{2.111}$$

Thus, the solution remains bounded.

The boundary term vanishes under the following conditions, valid $\forall t$:

$$u(0,t) = 0, \quad \partial_x u \Big|_{x=0}, \quad u(L,t) = 0, \quad \partial_x u \Big|_{x=L} = 0 \qquad \text{clamped}, \tag{2.112a}$$

$$u(0,t) = 0, \quad \partial_x^2 u \Big|_{x=0}, \quad u(L,t) = 0, \quad \partial_x^2 u \Big|_{x=L} = 0 \qquad \text{simply supported}, \tag{2.112b}$$

$$\left.\begin{array}{l} \partial_x^2 u \Big|_{x=0} = 0, \quad -T_0 \partial_x u \Big|_{x=0} + E I_0 \partial_x^3 u \Big|_{x=0} = 0 \\ \partial_x^2 u \Big|_{x=L} = 0, \quad -T_0 \partial_x u \Big|_{x=L} + E I_0 \partial_x^3 u \Big|_{x=L} = 0 \end{array}\right\} \qquad \text{free}. \tag{2.112c}$$

In the clamped conditions, both the position and the slope are set to zero. Imposing $\partial_x^2 u = 0$ indicates that the bending moment is null, meaning that simply supported conditions correspond to fixed ends that are free to rotate; these are also known as pivoting conditions. The second term in the free conditions has two components: one is the familiar string force

at the boundary, and the other corresponds to the shearing force of the beam, which opposes bending. Since this shearing force is zero, the end is free to vibrate. Clamped conditions are not commonly used, as strings are typically assumed to be simply supported. Free conditions have limited applications in musical acoustics, but they become useful when addressing more complex boundaries. Mixed boundary conditions can also be employed.

2.4.2 Modal expansion

Consider a stiff string of length L, simply supported at both ends. As for the ideal string, a modal description is obtained when the stiff string executes synchronous motion. First, insert a separable solution of the form (2.83), resulting in:

$$\rho A \chi \frac{\mathrm{d}^2 w}{\mathrm{d}t^2} = T_0 \frac{\mathrm{d}^2 \chi}{\mathrm{d}x^2} w - EI_0 \frac{\mathrm{d}^4 \chi}{\mathrm{d}x^4} w \quad \Rightarrow \quad \frac{\mathrm{d}^2 w}{\mathrm{d}t^2} \frac{1}{w} = c^2 \frac{\mathrm{d}^2 \chi}{\mathrm{d}x^2} \frac{1}{\chi} - \kappa^2 \frac{\mathrm{d}^4 \chi}{\mathrm{d}x^4} \frac{1}{\chi} \triangleq \lambda, \quad (2.113)$$

where it was defined:

$$\kappa \triangleq \sqrt{\frac{EI_0}{\rho A}}. \tag{2.114}$$

As before, this results in two separate ODEs. One is second-order in time, leading to the same conclusions as for the ideal string, with w having the form (2.88). Now, consider the fourth-order, homogenous ODE:

$$-\kappa^2 \frac{\mathrm{d}^4 \chi}{\mathrm{d}x^4} + c^2 \frac{\mathrm{d}^2 \chi}{\mathrm{d}x^2} + \omega^2 \chi = 0. \tag{2.115}$$

Assuming a solution $\chi(x) = e^{j\beta x}$, with $\beta \in \mathbb{C}$, the characteristic polynomial and related roots are obtained:

$$\omega^2 - c^2 \beta^2 - \kappa^2 \beta^4 = 0 \quad \Rightarrow \quad \beta = \pm \sqrt{\frac{-c^2 \pm \sqrt{c^4 + 4\omega^2 \kappa^2}}{2\kappa^2}}. \tag{2.116}$$

Thus, there are four distinct solutions for β, two real and two purely imaginary: $\beta = \pm\beta_1, \pm j\beta_2$, with:

$$\beta_1 \triangleq \sqrt{\frac{\sqrt{c^4 + 4\omega^2 \kappa^2} - c^2}{2\kappa^2}}, \qquad \beta_2 \triangleq \sqrt{\frac{\sqrt{c^4 + 4\omega^2 \kappa^2} + c^2}{2\kappa^2}}. \tag{2.117}$$

Therefore, the general solution to the ODE may be written in the form:

$$\chi(x) = \hat{\chi}_1 e^{j\beta_1 x} + \hat{\chi}_2 e^{-j\beta_1 x} + \hat{\chi}_3 e^{\beta_2 x} + \hat{\chi}_4 e^{-\beta_2 x}, \qquad \hat{\chi}_{1,2,3,4} \in \mathbb{C}, \tag{2.118}$$

or

$$\chi(x) = A \sin(\beta_1 x) + B \cos(\beta_1 x) + C \sinh(\beta_2 x) + D \cosh(\beta_2 x). \qquad (2.119)$$

Considering simply supported boundaries, one has:

$$\chi(0) = B + D = \partial_x^2 \chi \big|_0 = -B + D = 0 \quad \Rightarrow \quad B = D = 0. \qquad (2.120)$$

At the right boundary:

$$\chi(L) = A \sin(\beta L) + C \sinh(\beta L) = \partial_x^2 \chi \big|_L = \beta^2(-A \sin(\beta L) + C \sinh(\beta L)) = 0, \quad (2.121)$$

leading to the conclusion that $C = 0$. Thus, the characteristic equation is analogous to that of the ideal string: $A \sin(\beta L) = 0$, and $\beta_m = m\pi/L$, with $n \in \mathbb{N}$. The mode shapes are then:

$$\chi_m = A_m \sin(\beta_m x), \qquad (2.122)$$

and, as for the ideal string, it may be normalized by setting $A_m = A = \sqrt{2/L}$. The eigenfrequencies can be found by considering $\beta_1 = \beta_m$, and solving for ω:

$$\omega_m = \sqrt{c^2 \beta_m^2 + \kappa^2 \beta_m^4}. \qquad (2.123)$$

Note that the natural frequencies are no longer equally spaced, leading to a phenomenon known as inharmonicity. A thorough study on the parameter adjustments required to tune stiff strings is found in [67]. A modal projection may be now performed, analogously to the case of the ideal string, leading to a system of uncoupled oscillators of the form (2.101), where the eigenfrequencies now take the form (2.123). The pinned-pinned stiff string is the only combination that admits a closed form for the eigenfrequencies.

2.4.3   Lumped mass at the boundary

The study of a stiff string with a finite-impedance boundary is similar to that of the ideal string. Consider simply supported boundary conditions at the left end and a connection to a mass-spring system at the right end. The right boundary is defined as:

$$\partial_x^2 u \big|_{x=L} = 0, \quad -T_0 \partial_x u \big|_{x=L} + EI_0 \partial_x^3 u \big|_{x=L} = m \frac{\mathrm{d}^2 U}{\mathrm{d}t^2} + KU, \qquad (2.124)$$

with the further constraint that $u(L, t) = U(t)$. Note that, with respect to the ideal string case, there is now a condition on the bending moment, which is zero because the string end is free to bend. Additionally, the force at the boundary now includes the shearing force term.

An energy analysis can be conducted similarly to the ideal string case, leading to energy conservation.

A modal analysis is performed by inserting a separable solution. The resulting ODE in time is the same as in the pinned-pinned case, leading to a harmonic solution. Regarding the spatial part, a differential eigenvalue problem of the form (2.119) results, which must be solved using the current boundary conditions and the contact condition. This process is more involved than in the ideal string case, but through some algebra, the constants B, C, and D may be retrieved in terms of A, leading to modes of the form:

$$\chi(x) = A \left[\sin(\beta_2 x) + \frac{\beta_2^2 \sin(\beta_2 L)}{\beta_1^2 \sinh(\beta_1 L)} \sinh(\beta_1 x) \right], \tag{2.125}$$

with A begin a normalisation factor yet to be specified, and β_1, β_2 are as per (2.117). The characteristic equation becomes:

$$-T_0 \frac{d\chi}{dx}\bigg|_L + EI_0 \frac{d^3\chi}{dx^3}\bigg|_L + (\omega^2 - K)\chi(L) = 0, \tag{2.126}$$

which is a transcendental equation that can be solved for ω to retrieve the system's eigen-frequencies ω_m. A modal projection is performed by inserting a solution of the type $u(x) = \boldsymbol{\chi}(x)^\mathsf{T}\mathbf{w}(t)$ and taking an inner product with another mode set $\boldsymbol{\chi}$ onto the string length. After integration by parts, the resulting expression is:

$$\rho A \left\langle \boldsymbol{\chi}, \boldsymbol{\chi}^\mathsf{T} \right\rangle \frac{d^2\mathbf{w}}{dt^2} = \boldsymbol{\chi}(L)\mathbf{B}^\mathsf{T}\mathbf{w} - T_0 \left\langle \frac{d\boldsymbol{\chi}}{dx}, \frac{d\boldsymbol{\chi}^\mathsf{T}}{dx} \right\rangle \mathbf{w} - EI_0 \left\langle \frac{d^2\boldsymbol{\chi}}{dx^2}, \frac{d^2\boldsymbol{\chi}^\mathsf{T}}{dx^2} \right\rangle \mathbf{w}, \tag{2.127}$$

with:

$$\mathbf{B} \triangleq T_0 \frac{d\boldsymbol{\chi}}{dx}\bigg|_L - EI_0 \frac{d^3\boldsymbol{\chi}}{dx^3}\bigg|_L. \tag{2.128}$$

By considering the boundary conditions (2.124) and the contact condition, the system can be finally represented as a bank of oscillators:

$$\mathbf{M}\frac{d^2\mathbf{w}}{dt^2} = \mathbf{K}\mathbf{w}, \tag{2.129}$$

with

$$\mathbf{M} = \rho A \left[\left\langle \boldsymbol{\chi}, \boldsymbol{\chi}^\mathsf{T} \right\rangle + m\boldsymbol{\chi}(L)(\boldsymbol{\chi}(L))^\mathsf{T} \right], \tag{2.130a}$$

$$\mathbf{K} = T_0 \left\langle \frac{d\boldsymbol{\chi}}{dx}, \frac{d\boldsymbol{\chi}^\mathsf{T}}{dx} \right\rangle + EI_0 \left\langle \frac{d^2\boldsymbol{\chi}}{dx^3}, \frac{d^3\boldsymbol{\chi}^\mathsf{T}}{dx^2} \right\rangle + K\boldsymbol{\chi}(L)(\boldsymbol{\chi}(L))^\mathsf{T}. \tag{2.130b}$$

Note that the mass and stiffness matrices are diagonal and positive definite, and the oscillators are uncoupled. Consequently, one can write $\mathbf{M}^{-1}\mathbf{K} = \Omega^2$, where Ω is a diagonal matrix whose elements are the frequencies given in (2.126). Furthermore, the eigenmodes are orthogonal; the normalisation constants $\mathbf{A} = [A_0, A_1, ..., A_M]^\intercal$ can be determined so that either the mass matrix or the stiffness matrix is normalized to the identity matrix.

2.4.4 Viscous loss

A model for viscous loss can be incorporated into the stiff string equation similarly to the SHO, by adding a term proportional to the string's velocity, scaled by a constant σ_0, which can be related to the T_{60} as seen above. However, this would result in constant, frequency-independent damping, which does not reflect realistic string behaviour; in fact, real strings have complex decay profiles, as mentioned in Chapter 1. As seen in [67], implementing refined frequency-dependent damping in the time domain, such as the Valette and Cuesta model, is challenging. A simpler approach, easier to implement, is presented in [18], and reads:

$$\rho A \partial_t^2 u = T_0^2 \partial_x^2 u - E I_0 \partial_x^2 u - 2\rho A \left(\sigma_0 - \sigma_1 \partial_x^2 \right) \partial_t u, \qquad (2.131)$$

Here, σ_0 is the usual non-negative constant that controls a uniform decay rate across all frequencies, while σ_1 is another non-negative constant that introduces frequency-dependent characteristics to the loss. For practical implementation details, see [24, Chapter 7].

Consider a string of the type (2.131) defined over the domain $\mathcal{D} = [0, L]$. The energy balance is obtained the usual way, by taking an inner product with the velocity. Through integration by parts, one gets the balance:

$$\frac{\mathrm{d}}{\mathrm{d}t} H = B(t) - Q(t), \qquad (2.132)$$

where the energy H is as per (2.110), the boundary term has the form:

$$B(t) \triangleq \left[T_0 \partial_x u \partial_t u - E I_0 \left(\partial_t u \partial_x^3 u - \partial_x \partial_t u \partial_x^2 u \right) - 2\sigma_1 \rho A \partial_t u \partial_t \partial_x u \right] \Big|_{x=0}^{x=L}, \qquad (2.133)$$

and the dissipated power now reads:

$$Q(t) = 2\sigma_0 \rho A \|\partial_t u\|^2 + 2\sigma_1 \rho A \|\partial_t \partial_x u\|^2. \qquad (2.134)$$

The boundary term B vanishes for clamped and simply supported boundary conditions, while free boundary conditions must be modified to ensure energy conservation. It is important to note that the lumped mass boundary condition discussed earlier is not valid

when $\sigma_1 \neq 0$. However, frequency-dependent damping may be included directly in modal form, as mentioned in the next paragraph.

2.4.5 Forcing and modal expansion

A forcing term may be added to equation (2.131) as:

$$\rho A \partial_t^2 u = \mathcal{L} u + \mathcal{F}_{\text{e}}(x,t), \quad \mathcal{L} = T_0 \partial_x^2 - EI_0 \partial_x^2 - 2\rho A \left(\sigma_0 - \sigma_1 \partial_x^2 \right) \partial_t, \tag{2.135}$$

where $\mathcal{L}$ is a linear operator and the external source term $\mathcal{F}_{\text{e}}$ is typically separable in x and t. Point-wise forcing is quite common in musical acoustics, which may be modelled with a Dirac delta centred on the input point x_i as $\mathcal{F}_{\text{e}}(x,t) = \delta(x - x_i)F(t)$. The string is considered to be simply supported at both ends. An energy analysis yields the balance:

$$\frac{\mathrm{d}}{\mathrm{d}t} H = -Q(t) + P(t), \qquad P(t) = \partial_t u \Big|_{x=x_i} F(t), \tag{2.136}$$

where H and Q have the expressions (2.110) and (2.134), respectively. With simply supported boundaries, a modal expansion may be performed, using the normalised mode shapes (2.122), resulting in:

$$\frac{\mathrm{d}^2 \mathbf{w}}{\mathrm{d}t^2} = -\boldsymbol{\Omega}^2 \mathbf{w} - \mathbf{C} \frac{\mathrm{d}\mathbf{w}}{\mathrm{d}t} + \boldsymbol{\chi}(x_i) \frac{F}{\rho A}. \tag{2.137}$$

Here, $\boldsymbol{\Omega}^2$ is a diagonal matrix containing the eigenfrequencies (2.123), and $\mathbf{C}$ is the diagonal damping matrix, where the diagonal elements are given by:

$$C_{m,m} = 2\sigma_0 + 2(m\pi/L))^2 \sigma_1 \tag{2.138}$$

However, there is now no restriction on assigning a unique damping coefficient to each mode by employing a generalized loss matrix $\mathbf{C}$. This lets each vibration mode have its own T_{60}, allowing for the direct introduction of more complex frequency-dependent damping profiles, such as that described by Valette and Cuesta [206].

2.4.6 Distributed bridge at the boundary

The lumped bridge presented earlier in this chapter is a simplified approximation; a more accurate model would account for spatial distribution. A distributed bridge can be described by an Euler-Bernoulli bar, modelled as a stiff string without the tension term. The governing

equations can then be formulated similarly to those proposed in [157]:

$$\rho_s A_s \partial_t^2 u_s = T_s \partial_x^2 u_s - E_s I_s \partial_x^4 u_s, \tag{2.139a}$$

$$\rho_p A_p \partial_t^2 u_p = -E_p I_p \partial_z^4 u_p + \delta(z - z_s) F(t). \tag{2.139b}$$

Here, subscripts s, p refer to the string and the bridge, respectively. $u_s = u_s(x, t)$ represents the transverse displacement of the string of length L_s, while $u_p = u_p(z, t)$ denotes the displacement of the beam of length L_p, defined over the domain $z \in [0, L_p]$. The term F represents the force exerted by the string onto the bridge, directed point-wise at location z_s. The string is considered simply supported at the left end, while the right end determines the force exerted by the string, analogously to the case of the lumped mass at the boundary:

$$F(t) = -T_s \partial_x u_s \Big|_{x=L_s} + E_s I_s \partial_x^3 u_s \Big|_{x=L_s}, \qquad \partial_x^2 u_s \Big|_{x=L_s} = 0. \tag{2.140}$$

The bar is simply supported at both ends:

$$\partial_z^2 u_p \Big|_{z=0} = u_p(0, t) = \partial_z^2 u_p \Big|_{z=L_p} = u_p(L_p, t) = 0. \tag{2.141}$$

A rigid contact is assumed between the string and the bridge, leading to the condition:

$$\int_0^{L_p} \delta(z - z_s) u_p(z, t) \, \mathrm{d}z = u_p(z_s, t) = u_s(L_s, t). \tag{2.142}$$

An energy balance is obtained by taking an inner product of equation (2.139a) with $\partial_t u_s$ and (2.139b) with $\partial_t u_p$. By integrating by parts and considering the boundary and contact conditions, the following is derived:

$$\frac{\mathrm{d}}{\mathrm{d}t} H_p = \frac{\mathrm{d}}{\mathrm{d}t} u_p(z_s, t) F = \frac{\mathrm{d}}{\mathrm{d}t} u_s(L_s, t) F = -\frac{\mathrm{d}}{\mathrm{d}t} H_s, \quad \Rightarrow \quad \frac{\mathrm{d}}{\mathrm{d}t}(H_p + H_s) = 0, \tag{2.143}$$

with:

$$H_p = \frac{\rho_p A_p}{2} \|\partial_t u_p\|^2 + \frac{E_p I_p}{2} \|\partial_z^2 u_p\|^2, \tag{2.144a}$$

$$H_s = \frac{\rho_s A_s}{2} \|\partial_t u_s\|^2 + \frac{T_s}{2} \|\partial_x u_s\|^2 + \frac{E_s I_s}{2} \|\partial_x^2 u_s\|^2. \tag{2.144b}$$

The balance (2.143) is conservative, and the energy expressions (2.144) are non-negative, indicating that the continuous system is stable. Unlike in the lumped case, an analytic form of the modes is not readily available. Thus, the eigenvalue problem will be solved numerically in Chapter 3.

Chapter 3

Numerical discretisation techniques and applications to linear systems

The PDEs encountered in musical acoustics typically do not have analytic solutions, requiring the use of numerical methods. This chapter introduces the notation and principles of the finite-difference (FD) method and illustrates its usage in the context of linear systems. Following the approach of the previous chapter, the FD method is first applied in the time domain, followed by spatial discretization, which introduces finite-difference time-domain (FDTD) methods. Part of the content in this chapter is based on textbooks by Bilbao [24] and LeVeque [137].

3.1 Time difference operators

In time-stepping methods, time is discretised with a time step k (in seconds), yielding a sample rate $f_s = 1/k$. The sample rate is typically predetermined in audio applications and remains constant through the simulation. Common sample rates are are 44.1, 48 and 96 kHz. The continuous function $u(t)$ is approximated at time step $t = nk$ by the time series u^n, where $n \in \mathbb{N}$ is the time index. The most basic operators in discrete time are identity and shift, defined as:

$$1u^n = u^n, \qquad e_{t+}u^n = u^{n+1}, \qquad e_{t-}u^n = u^{n-1}. \tag{3.1}$$

From these, time difference operators, also known as FD operators in time, can be defined as:

$$\delta_{t+} \triangleq \frac{e_{t+} - 1}{k} \approx \frac{\mathrm{d}}{\mathrm{d}t}, \qquad \delta_{t-} \triangleq \frac{1 - e_{t-}}{k} \approx \frac{\mathrm{d}}{\mathrm{d}t}, \qquad \delta_{t\cdot} \triangleq \frac{e_{t+} - e_{t-}}{2k} \approx \frac{\mathrm{d}}{\mathrm{d}t}. \tag{3.2}$$
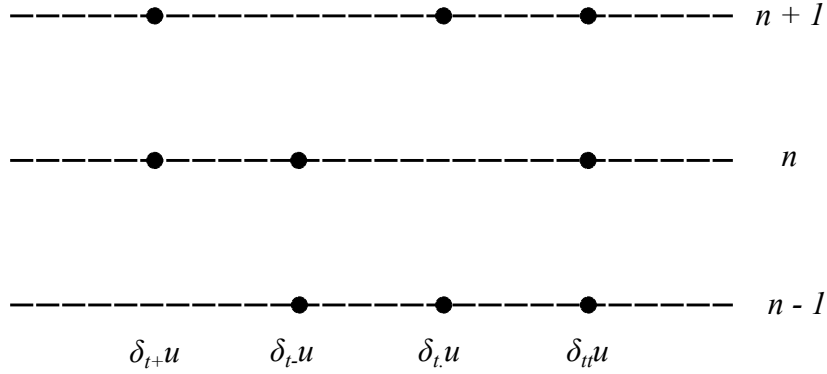
Fig. 3.1 Illustration of stencils for various time difference operators approximating the first and second time derivatives.

These represent the forward, backwards, and centred difference operators, respectively, and approximate the first derivative operator. When applied to a time series, they provide different finite approximations of the difference quotient:

$$\delta_{t+}u^n = \frac{(u^{n+1} - u^n)}{k}, \qquad \delta_{t-}u^n = \frac{(u^n - u^{n-1})}{k}, \qquad \delta_{t\cdot}u^n = \frac{(u^{n+1} - u^{n-1})}{2k}. \quad (3.3)$$

Additionally, averaging operators can be defined to approximate the identity operator:

$$\mu_{t+} = \frac{e_{t+} + 1}{2} \approx 1, \quad \mu_{t-} = \frac{1 + e_{t-}}{2} \approx 1, \quad \mu_{t\cdot} = \frac{e_{t+} + e_{t-}}{2} \approx 1. \quad (3.4)$$

These are particularly useful in constructing stable schemes. The operators above are the foundational building blocks for time-stepping algorithms and can be combined in various ways. One significant combination provides an approximation of the second-order derivative:

$$\delta_{tt} \triangleq \delta_{t+}\delta_{t-} = \frac{e_{t+} + 2 - e_{t-}}{k^2} \approx \frac{\mathrm{d}^2}{\mathrm{d}t^2}, \quad (3.5)$$

where the constant "2" is intended as twice the identity operator. Since higher-order time derivatives will not be encountered in this text, higher-order difference operators are not discussed. The temporal width, or stencil, of an operator is defined as the number of distinct time steps required for its approximation. Thus, δ_{t+}, δ_{t-}, μ_{t+} and μ_{t-} have a stencil of width 1, while $\delta_{t\cdot}$ and δ_{tt} have a stencil width of 2. A graphical representation of the stencil widths for the difference operators is shown in Figure 3.1. Various identities exist between the

operators; useful ones include:

$$\mu_{t\cdot} = 1 + \frac{k^2}{2}\delta_{tt}, \tag{3.6a}$$

$$\delta_{t\cdot} = \delta_{t+}\mu_{t-} = \delta_{t-}\mu_{t+} = \frac{1}{2}(\delta_{t+} + \delta_{t-}), \tag{3.6b}$$

$$\delta_{tt} = \frac{1}{k}(\delta_{t+} - \delta_{t-}) = \frac{2}{k}(\delta_{t\cdot} - \delta_{t-}), \tag{3.6c}$$

$$1 = \mu_{t\pm} \mp \frac{k\delta_{t\pm}}{2}, \tag{3.6d}$$

$$e_{t\pm} = \mu_{t\pm} \pm \frac{k\delta_{t\pm}}{2} = 1 \pm k\delta_{t\pm}, \tag{3.6e}$$

$$\mu_{t\cdot} = k\delta_{t\cdot} + e_{t-}. \tag{3.6f}$$

Discrete versions of the continuous relations (2.4a) and (2.4b) can be derived, along with other identities:

$$(\delta_{t\cdot}u^n)\delta_{tt}u^n = \delta_{t+}\left(\frac{1}{2}(\delta_{t-}u^n)^2\right), \tag{3.7a}$$

$$(\delta_{t\cdot}u^n)u^n = \delta_{t+}\left(\frac{1}{2}u^n e_{t-}e^n\right), \tag{3.7b}$$

$$(\delta_{t+}u^n)\mu_{t+}u^n = \delta_{t+}\left(\frac{1}{2}(u^n)^2\right), \tag{3.7c}$$

$$(\mu_{t\cdot}u^n)u^n = \mu_{t+}(u^n e_{t-}u^n), \tag{3.7d}$$

$$(\mu_{t\cdot}u^n)(\delta_{t\cdot}u^n) = \delta_{t\cdot}\left(\frac{1}{2}(u^n)^2\right), \tag{3.7e}$$

$$u^n e_{t-}u^n = (\mu_{t-}u^n)^2 - \frac{(k\delta_{t-}u^n)^2}{4}, \tag{3.7f}$$

while a discrete version of the relation (2.4c) is not immediately derived. All the equivalences above can be proved through simple algebraic operations.

3.2   Accuracy: truncation error

It was mentioned that FD operators approximate derivative operators; however, the accuracy of these approximations has not yet been discussed. A common method for analyzing this accuracy involves using Taylor series, which requires assuming that the continuous function $u(t)$ is sufficiently smooth. Under this assumption, the function values can be expanded
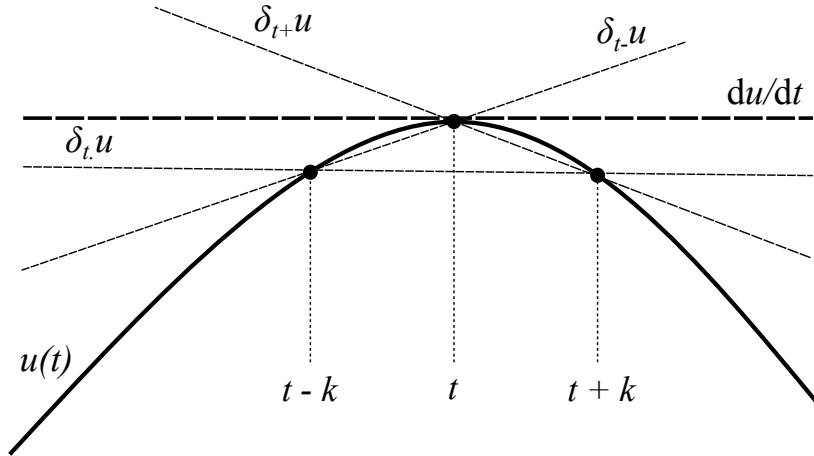
Fig. 3.2 Graphical representation of the backward, forward and centred time difference operators, interpreted as the secant lines between two points of the continuous function $u(t)$.

around a point $\bar{t}$:

$$u(\bar{t} \pm k) = u(\bar{t}) \pm k \frac{\mathrm{d}u(\bar{t})}{\mathrm{d}t} + \frac{k^2}{2} \frac{\mathrm{d}^2 u(\bar{t})}{\mathrm{d}t^2} \pm \frac{k^3}{6} \frac{\mathrm{d}^3 u(\bar{t})}{\mathrm{d}t^3} + \mathcal{O}(k^4), \qquad (3.8)$$

where $\mathcal{O}(k^p)$ indicates that the error term is on the order of k^p. Applying the backward and forward difference operators to the continuous function $u(\bar{t})$ gives:

$$\delta_\pm u(\bar{t}) = \pm \frac{(u(\bar{t} \pm k) - u(\bar{t}))}{k} = \frac{\mathrm{d}u(\bar{t})}{\mathrm{d}t} \pm \frac{k}{2} \frac{\mathrm{d}^2 u(\bar{t})}{\mathrm{d}t^2} + \frac{k^2}{6} \frac{\mathrm{d}^3 u(\bar{t})}{\mathrm{d}t^3} + \mathcal{O}(k^3). \qquad (3.9)$$

Because $\bar{t}$ is a fixed point, the derivatives are constants, making k the only variable parameter. For sufficiently small k, the second term $\pm \frac{k}{2} \frac{\mathrm{d}^2 u(\bar{t})}{\mathrm{d}t^2}$ dominates over the following ones. Thus, the backward and forward difference operators approximate the first derivative with an error that behaves as k multiplied by a constant and are defined as first-order accurate. This error is known as the truncation error of the FD operators.

A similar procedure may be applied to the centred operator, yielding:

$$\delta_{t\cdot} u(\bar{t}) = \frac{(u(\bar{t} + k) - u(\bar{t} - k))}{2k} = \frac{\mathrm{d}u(\bar{t})}{\mathrm{d}t} + \frac{k^2}{6} \frac{\mathrm{d}^3 u(\bar{t})}{\mathrm{d}t^3} + \mathcal{O}(k^4). \qquad (3.10)$$

This indicates that the error behaves as k^2, making the centred operator second-order accurate. Similarly, the backward and forward mean operators can be shown to be first-order accurate, while the centred mean operator is second-order accurate. Figure 3.2 provides a graphical representation of the behaviour of these difference operators when applied to a continuous function. The accuracy order of the second difference operator can be explicitly expressed
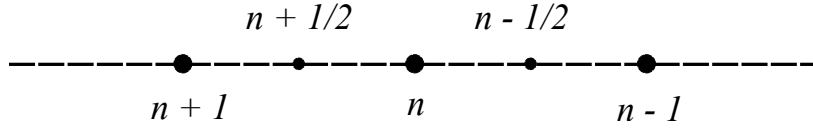
Fig. 3.3 Illustration of a staggered time grid.

as:

$$\delta_{tt} = \frac{\mathrm{d}2}{\mathrm{d}t^2} + \mathcal{O}(k^2). \tag{3.11}$$

Higher-accuracy operators can be constructed, typically by using a larger stencil; however, they tend to yield unstable simulations. Furthermore, initialization concerns arise, particularly when the stencil order exceeds the order of the problem (i.e., the highest derivative order in continuous time).

Sometimes, time series defined at interleaved or staggered time instants are employed [23]. Given a continuous function $\psi(t)$, this may be approximated at time step $t = (n - 1/2)k$ by the series $\psi^{n-1/2}$, on the grid depicted in Figure 3.3. The same formal definitions of the difference operators apply to series defined on staggered time grids, for example: $\delta_{t+}\psi^{n-1/2} = (\psi^{n+1/2} - \psi^{n-1/2})/k$. The advantage of this approach is that one-step operators applied to staggered series become centred. For instance, consider the Taylor expansion:

$$\psi(\bar{t} \pm k/2) = \psi(\bar{t}) \pm \frac{k}{2}\frac{\mathrm{d}\psi(\bar{t})}{\mathrm{d}t} + \frac{k^2}{4}\frac{\mathrm{d}^2\psi(\bar{t})}{\mathrm{d}t^2} \pm \frac{k^3}{12}\frac{\mathrm{d}^3\,\psi(\bar{t})}{\mathrm{d}t^3} + \mathcal{O}(k^4). \tag{3.12}$$

Then, applying the forward difference operator to $\psi(\bar{t})$ gives:

$$\delta_{t+}\psi(\bar{t} - k/2) = \frac{\psi(t + k/2) - \psi(t - k/2)}{k} = \frac{\mathrm{d}u(\bar{t})}{\mathrm{d}t} + \mathcal{O}(k^2), \tag{3.13}$$

making the forward operator applied to staggered series second-order accurate.

3.3   Harmonic motion in discrete time

Consider the SHO equation (2.19). The simplest FD scheme approximating the equation is obtained by considering the time series u^n approximating the solution $u(t)$, and then simply substituting the derivative with the second difference operator (3.5):

$$\delta_{tt}u^n = -\omega_0^2\,u^n. \tag{3.14}$$

Expanding the operator yields:

$$u^{n+1} = u^n(2 - \omega_0^2 \, k^2) - u^{n-1}, \tag{3.15}$$

This relation is called explicit because the unknown u^{n+1} is directly computed from the previous time series values, u^n and u^{n-1}. However, it is important to note that the validity of this scheme as an effective approximation for the continuous function $u(t)$ is not inherently guaranteed. Further analysis is required to establish this, which introduces the concepts of stability, consistency and convergence of the scheme.

3.3.1 Stability, consistency and convergence

Stability via energy analysis

As in the continuous case, the energy analysis is performed by multiplying equation (3.14) by a discrete velocity times mass $m\delta_{t.}u^n$. Through the identities (3.7a) and (3.7b) one gets:

$$m(\delta_{t.}u^n)(\delta_{tt}u^n) + K\,(\delta_{t.}u^n)u^n = 0 \qquad \rightarrow \qquad \delta_{t+}\mathfrak{h}^{n-1/2} = 0, \tag{3.16}$$

where it was defined
$$\mathfrak{h}^{n-1/2} \triangleq \frac{m(\delta_{t-}u^n)^2}{2} + \frac{K\,u^n\,e_{t-}u^n}{2}. \tag{3.17}$$

Equation (3.16) evidently resembles the continuous energy H in equation (2.26). Similarly, the multiplication by a constant with the dimensions of mass was performed solely to obtain the correct energy dimension and is unnecessary for the energy analysis itself. The quantity $\mathfrak{h}$ is often referred to in the literature as numerical, discrete or pseudo energy. Note that the energy series is defined on a staggered grid because the operators inside the expression are non-centred. The system conserves the discrete energy, leading to a discrete counterpart of the balance equation (2.26). Thus:

$$\mathfrak{h}^{n-1/2} = \mathfrak{h}^{1/2}, \tag{3.18}$$

where $\mathfrak{h}^{1/2}$ represents the initial numerical energy, set by the numerical initial conditions, which will be discussed later.

The conservation of this numerical energy is a necessary, but not sufficient, condition for ensuring the stability of the scheme. In fact, unlike expression (2.26), the discrete potential energy is not immediately positive definite. As in the continuous case, negative discrete energy may lead to unbounded solutions; therefore, it is necessary to establish a bound for
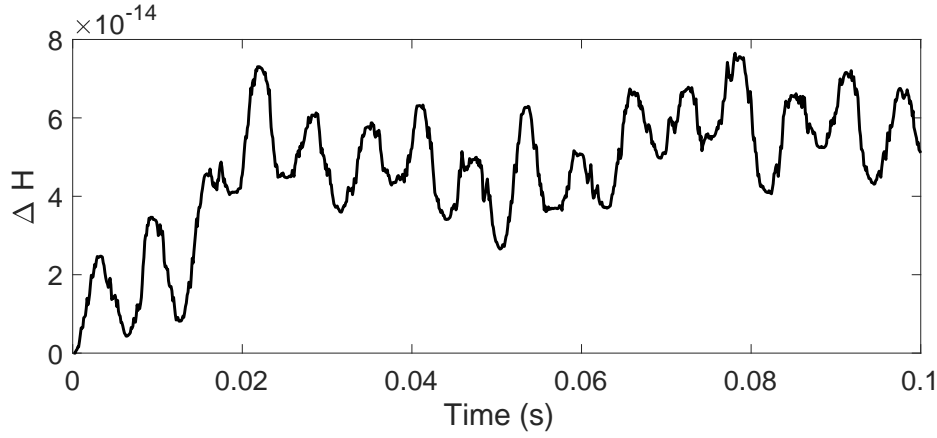
Fig. 3.4 Energy error ΔH for scheme (3.14). The oscillator has a natural frequency $\omega_0 = 500$ rad/s and it was initialised with $x_0 = v_0 = 1$.

the discrete potential. Using (3.7f) allows to write:

$$\mathfrak{h}^{n-1/2} = \frac{(\delta_{t-}u^n)^2}{2}\left(1 - \frac{\omega_0^2\, k^2}{4}\right) + \frac{\omega_0^2\,(\mu_{t-}u^n)^2}{2} \geq \frac{(\delta_{t-}u^n)^2}{2}\left(1 - \frac{\omega_0^2\, k^2}{4}\right). \tag{3.19}$$

Thus, energy positivity is ensured iif:

$$\left(1 - \frac{\omega_0^2\, k^2}{4}\right) > 0 \qquad \rightarrow \qquad k < \frac{2}{\omega_0}. \tag{3.20}$$

Equation (3.20) is called the stability condition of the finite difference scheme (3.14). If this is not satisfied, the solution will grow exponentially over time. On the other hand, when the stability condition is respected, one obtains bounds on the velocity and displacement in terms of the initial energy, analogous to those obtained in continuous time:

$$\left|\delta_{t-}u^n\right| \leq \sqrt{2\mathfrak{h}^{1/2}/m}, \quad \left|\mu_{t-}u^n\right| \leq \sqrt{2\mathfrak{h}^{1/2}/K}. \tag{3.21}$$

Figure 3.4 shows the energy error for scheme (3.14), defined as:

$$\Delta H \triangleq 1 - \mathfrak{h}^{n-1/2}/\mathfrak{h}^{1/2}. \tag{3.22}$$

Note that the discrete energy exhibits fluctuations on the order of 10^{-14}, which approaches the machine accuracy limit ϵ_m. According to the IEEE standard for double precision arithmetic, $\epsilon_m = 2^{-52} \approx 2.22 \times 10^{-16}$. Machine accuracy represents the smallest value $1 - \epsilon_m$ greater than 1 that a computer can represent. Several factors can contribute to discrepancies in

energy calculations that exceed the threshold of machine accuracy. In this chapter, only the truncation error of the finite difference operators was considered, without addressing round-off errors due to finite machine precision. In fact, while relation (3.21) holds under the assumption of infinite precision, finite precision introduces additional computation errors. These round-off errors affect not only energy calculations but also the numerical scheme itself, particularly in nonlinear systems. This can complicate performance evaluation for certain schemes.

Consistency: local truncation error

As previously mentioned, the FD operators approximate continuous derivatives. When these operators are applied to a discrete time series u^n, equation (3.14) is solved exactly. However, the time series only approximates the continuous solution. As one might expect, if the true solution, denoted here with $\bar{u}(t)$ to avoid confusion, is substituted into the scheme (3.14), the equation will not be solved exactly, resulting in a discrepancy. This discrepancy is called the local truncation error (LTE) and is denoted by τ^n:

$$\delta_{tt}\bar{u}(t_n) + \omega_0^2\,\bar{u}(t_n) = \tau^n, \quad t_n \triangleq nk. \tag{3.23}$$

By means of (3.11), one gets:

$$\left(\frac{\mathrm{d}^2\bar{u}(t_n)}{\mathrm{d}t^2} + \omega_0^2\,\bar{u}(t_n)\right) + \mathcal{O}(k^2) = \tau^n. \tag{3.24}$$

Since $\bar{u}(t)$ is the true solution, the term in parenthesis is solved exactly (and is equal to zero following (2.19)), leading to $\tau^n = \mathcal{O}(k^2)$. This indicates that the LTE decreases with the square of k. In other words, the time series u^n approaches the true solution with an accuracy of order k^2. Generally, if

$$\lim_{k \to 0} \tau^n = 0 \tag{3.25}$$

a scheme is said to be consistent, and the LTE can be used to assess the accuracy of the scheme. Specifically, if $\tau = \mathcal{O}(k^p)$ the scheme is said to be pth-order accurate.

This is valid only if the scheme is also stable and convergent. In fact, consistency alone does not guarantee that the numerical solution will converge to the true solution, as errors may accumulate and grow as the solution progresses through time steps.

Convergence: global error

The idea of convergence of the scheme is linked to the concept of global error. This is defined as:

$$E^n = \bar{u}(t_n) - u^n, \tag{3.26}$$

and is expected to reflect the trend of the LTE. In general, a scheme is convergent if

$$\lim_{k \to 0} E^n = 0. \tag{3.27}$$

Convergence is the property that ensures that, as the sampling step k is reduced to very small values, the time series will effectively approach the true solution. It is the most difficult property to prove mathematically for a finite difference scheme. For linear schemes, the Lax–Richtmyer theorem ensures that a stable and consistent scheme is also convergent [198, Chapter 1]. However, this does not apply to nonlinear schemes, where convergence must be independently demonstrated.

If an analytic solution is available, a common technique to verify convergence numerically is to compare the computed solution with the analytic solution at the same time instant for decreasing sampling steps, checking that the error decreases according to the expected power of k. If no analytic solution is available, other target solutions are employed, as will be discussed in the following chapters.

3.3.2 Frequency warping: an exact scheme

A significant issue introduced by scheme (3.14) is a frequency warping effect leading the oscillation frequency of the numerical solution to deviate from ω_0. Instead, it is given by [24, Chapter 3]:

$$\omega = \frac{1}{k} \cos^{-1} \left(1 - \frac{k^2 \omega_0^2}{2} \right). \tag{3.28}$$

Since $\omega > \omega_0$, the stability limit (3.20) becomes stricter than the Nyquist limit. This effect becomes more pronounced as ω_0 approaches the stability threshold.

Since the scheme is convergent, increasing the sampling rate could mitigate this effect, but this is not always feasible in audio applications. On the other hand, an exact, explicit, unconditionally stable integrator exists for the unforced, undamped SHO, in the form:

$$u^{n+1} - 2\cos(\omega_0 k)u^n + u^{n-1} = 0. \tag{3.29}$$
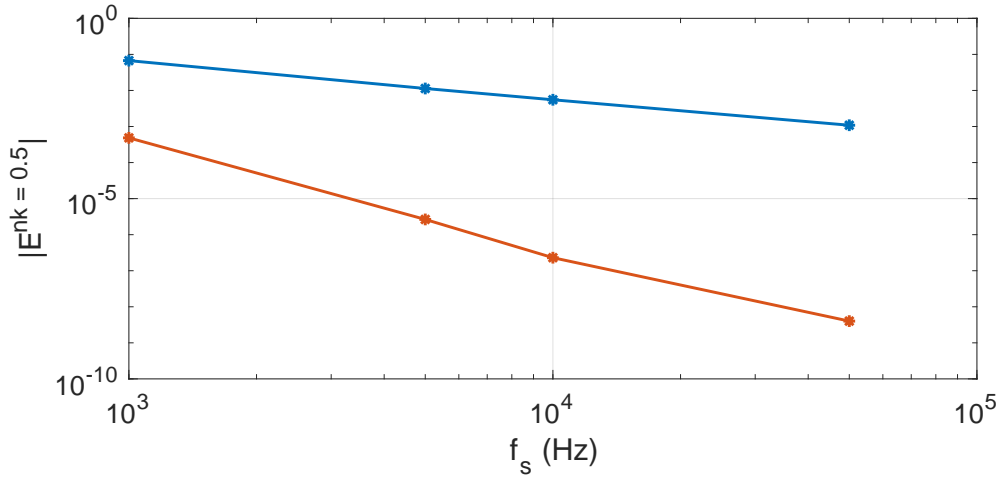
Fig. 3.5 Convergence rate analysis for scheme (3.14) initialised with condition (3.31) (blue) and (3.32) (orange). The log plot shows the global error, defined as in (3.26) and computed at time $nk = 0.5$ s, against the sampling rate. The slope of the blue line is 1: the error then decreases linearly with the time step k, suggesting that the scheme is first-order accurate with this initialization. In contrast, the orange line has a slope of 2: the error decreases quadratically with k, confirming that this initialization is second-order accurate.

A full proof is beyond the scope of this work; interested readers may refer to [56, 57] and [24, Chapter 3] for further details.

3.3.3 Initialisation

As its continuous counterpart, a numerical scheme must be provided with initial information. Schemes (3.14) and (3.29) are called two-step schemes because advancing in time requires knowledge of the state at both the current and previous time steps n and $n - 1$. Thus, given the initial position and velocity u_0 and v_0 one needs to retrieve information on u_0 and u_1. For the initial state, this is straightforward:

$$u^0 = u_0. \tag{3.30}$$

For the next state, one may be tempted to set:

$$\delta_{t+}u^0 = v_0 \qquad \rightarrow \qquad u^1 = u^0 + kv_0; \tag{3.31}$$

however, this approximation is only first-order accurate due to the use of a forward difference operator. The centred difference operator cannot be used here because it would require unavailable state information.

Consider now scheme (3.14) and the relation (3.6c): using the fact that $\delta_{tt} = -\omega_0$ from (3.14), one may write:

$$\delta_{t.}u^0 = v_0 \qquad \rightarrow \qquad u^1 = u^0 + kv_0 - \frac{k^2\omega_0^2}{2}u^0, \tag{3.32}$$

which provides a second-order accurate initialization. In general, it is good practice to adopt initial conditions with the same accuracy as the scheme. Figure 3.5 represents a convergence rate analysis of scheme (3.14) initialised with conditions (3.31) and (3.32).

When employing the exact scheme (3.29), an exact set of initial conditions may be specified [56, 216].

3.3.4 Loss

A discretisation for system (2.34) may be obtained as:

$$\delta_{tt}u^n = \omega_0^2 u^n - 2\sigma_0\delta_{t.}u^n. \tag{3.33}$$

The LTE is of order 2, making the scheme second-order accurate. An energy analysis can be performed by multiplying equation (3.33) by $m\delta_{t.}u^n$, leading, through the use of discrete derivative identities, to:

$$\delta_{t+}\mathfrak{h}^{n-1/2} = -2\sigma_0(\delta_{t.}u^n)^2 \leq 0. \tag{3.34}$$

This shows that the system is dissipative. The energy expression $\mathfrak{h}^{n-1/2}$ is defined as per (3.17), so the stability condition given by (3.20) still holds. Consequently, one can derive the following bound on the solution size:

$$|u^n| \leq \sqrt{\frac{2k^2\mathfrak{h}^{1/2}}{1 - \left(1 - \omega_0^2 k^2/2\right)^2}}. \tag{3.35}$$

Equation (3.33) exhibits the same frequency warping issues as in the undamped case. Additionally, it introduces a deviation in the decay time. An exact, unconditionally stable integrator also exists for the lossy case, given by [24, Chapter 3]:

$$u^{n+1} = e^{-\sigma_0 k}\left(e^{\sqrt{\sigma_0^2 - \omega_0^2}k} + e^{-\sqrt{\sigma_0^2 - \omega_0^2}k}\right)u^n - e^{-2\sigma_0 k}u^{n-1}. \tag{3.36}$$

As in the undamped case, a full proof is beyond the scope of this work; for further details on this and initialisation strategies, interested readers may refer to [56, 57, 216].

3.4   Multiple degrees of freedom

A discrete version of scheme (2.52) can be written as:

$$\mathbf{M}\delta_{tt}\mathbf{u}^n = -\mathbf{K}\mathbf{u}^n, \tag{3.37}$$

where the vector $\mathbf{u}^n$ now contains the time series. By expanding the difference operators, one gets:

$$\mathbf{M}\mathbf{u}^{n+1} = (2\mathbf{M} - k^2\mathbf{K})\mathbf{u}^n - \mathbf{M}\mathbf{u}^{n-1}. \tag{3.38}$$

Scheme (3.37) may be proved to be second-order accurate and, since $\mathbf{M}$ is fully diagonal and not dependent on the system's state, it is explicit. An energy analysis is performed by taking an inner product with $\delta_{t\cdot}\mathbf{u}^n$. Using the usual discrete identities, one obtains the balance:

$$\delta_{t+}\mathfrak{h}^{n-1/2} = 0, \qquad \mathfrak{h}^{n-1/2} = \frac{1}{2}\left\langle \delta_{t-}\mathbf{u}^n, \mathbf{M}\delta_{t-}\mathbf{u}^n \right\rangle + \frac{1}{2}\left\langle \mathbf{u}^{n-1}, \mathbf{K}\mathbf{u}^n \right\rangle. \tag{3.39}$$

As in the single-mass case, there is no guarantee that the discrete energy is positive. While the kinetic energy is non-negative by definition, the potential energy has an indefinite sign. For the symmetric, non-negative matrix $\mathbf{K}$, a vector equivalent of the discrete-time identity (3.7f) can be given as:

$$\left\langle e_{t-}\mathbf{u}^n, \mathbf{K}\mathbf{u}^n \right\rangle = \left\langle \mu_{t-}\mathbf{u}^n, \mathbf{K}\mu_{t-}\mathbf{u}^n \right\rangle - \frac{k^2}{4}\left\langle \delta_{t-}\mathbf{u}^n, \mathbf{K}\delta_{t-}\mathbf{u}^n \right\rangle. \tag{3.40}$$

Substituting this into the energy expression one gets:

$$\mathfrak{h}^{n-1/2} = \frac{1}{2}\left(\left\langle \delta_{t-}\mathbf{u}^n, \mathbf{M}\delta_{t-}\mathbf{u}^n \right\rangle - \frac{k^2}{4}\left\langle \delta_{t-}\mathbf{u}^n, \mathbf{K}\delta_{t-}\mathbf{u}^n \right\rangle \right) + \frac{1}{2}\left\langle \mu_{t-}\mathbf{u}^n, \mathbf{K}\mu_{t-}\mathbf{u}^n \right\rangle. \tag{3.41}$$

Thus, non-negativity of the energy overall is guaranteed if:

$$\left\langle \delta_{t-}\mathbf{u}^n, \mathbf{M}\delta_{t-}\mathbf{u}^n \right\rangle - \frac{k^2}{4}\left\langle \delta_{t-}\mathbf{u}^n, \mathbf{K}\delta_{t-}\mathbf{u}^n \right\rangle = \left\langle \delta_{t-}\mathbf{u}^n, \mathbf{A}\delta_{t-}\mathbf{u}^n \right\rangle \geq 0, \tag{3.42}$$

where it was defined $\mathbf{A} \triangleq \left(\mathbf{M} - \frac{k^2}{4}\mathbf{K} \right)$. Following the bounds (2.51), this translates to:

$$\mathrm{eig}(\mathbf{A}) \geq 0, \tag{3.43}$$

meaning that $\mathbf{A}$ must be positive definite. As in equation (2.56), a modal expansion can be performed, resulting in a decoupled system

$$\delta_{tt}\mathbf{w}^n = -\mathbf{\Omega}^2\mathbf{w}^n, \tag{3.44}$$

where $\mathbf{\Omega}^2 = \mathbf{M}^{-1}\mathbf{K}$. The stability condition then becomes:

$$k \leq 2/\max(\omega_i), \qquad i = 1, 2, \ldots, N. \tag{3.45}$$

where ω_i are the eigenfrequencies stored into $\mathbf{\Omega}$. When (3.44) represents a modal system such as (2.101), the condition (3.45) sets a limit on the number of modes that can be simulated. As seen in Chapter 2, systems (3.37) or (3.44) may be easily integrated with loss and forcing terms.

It is important to note that when a continuous modal system (such as (2.101)) is simulated using the integrator (3.44), the previously discussed frequency warping effects arise. In particular, the simulated modal frequencies deviate from their analytical counterparts, especially at high frequencies, leading to mode mistuning and perceptual artefacts. This phenomenon is known as numerical dispersion. To account for such numerical dispersion, exact integrators of the kind (3.29) and (3.36) can be employed, as done in various works, see eg. Van Walstijn et al. [213, 211, 216]. Since these integrators are unconditionally stable, the number of simulated modes in these cases is typically limited by the hearing range, up to 20 kHz.

3.5 First-order ODEs

Many time-stepping schemes are designed for first-order ODEs. Thus, it is helpful to introduce the use of time difference operators in this context. Consider a generic IVP in the form:

$$\frac{d\mathbf{u}}{dt} + f(\mathbf{u}) = 0, \qquad \mathbf{u}(0) = \mathbf{u}_0, \tag{3.46}$$

where $\mathbf{u} = \mathbf{u}(t) : \mathbb{R}_0^+ \to \mathbb{R}^N$ is a N-elements vector representing the system's state as a function of time t, and $f = f(\mathbf{u})$ is a function that can be either linear or nonlinear.

The simplest numerical method for integrating this problem is the forward euler (FE) method, obtained by replacing the derivative with a forward difference operator:

$$\delta_{t+}\mathbf{u}^n + f(\mathbf{u}^n) = 0. \tag{3.47}$$

This method is only first-order accurate, and stability issues may arise, necessitating a stability condition. By rearranging the equation, the explicit update formula is obtained:

$$\mathbf{u}^{n+1} = -kf(\mathbf{u}^n) + \mathbf{u}^n. \tag{3.48}$$

Notice that here, only one previous value of the time series is required to step forward in time: this is a one-step method, contrary to scheme (3.15). One-step methods have the advantage of being self-starting, meaning they do not require the complex initialization strategies that multi-step methods often need. Consider the following:

$$\delta_{t+}\mathbf{u}^n + f(\mu_{t+}\mathbf{u}^n) = 0. \tag{3.49}$$

This is called Midpoint method. It is one-step and can be proved to be second-order accurate. Furthermore, it is unconditionally stable, meaning it does not require a stability condition. However, in this case, the function f is evaluated at time-step $n + 1$, making the method implicit. If f is nonlinear, the solution requires iterative methods such as Newton-Raphson.

Consider the oscillator in first-order form (2.30). A possible discretisation can be obtained as follows:

$$\delta_{t+}\mathbf{x}^n = \mathbf{J}(\nabla\mathfrak{h})^{n+1/2}, \qquad \mathfrak{h}(q^n, p^n) \triangleq \mathfrak{h}^n = \frac{(p^n)^2}{2} + \frac{(q^n)^2}{2}. \tag{3.50}$$

The partial derivative of $\mathfrak{h}$ with respect to q is given as:

$$\delta_{q+}\mathfrak{h}(q^n, p^n) = \frac{\mathfrak{h}(q^{n+1}, p^n) - \mathfrak{h}(q^n, p^n)}{q^{n+1} - q^n} = \mu_+q^n. \tag{3.51}$$

The partial derivative with respect to p can be defined analogously. Therefore, the gradient yields:

$$(\nabla\mathfrak{h})^{n+1/2} \triangleq \begin{bmatrix} \delta_{q+}\mathfrak{h}^n \\ \delta_{p+}\mathfrak{h}^n \end{bmatrix} = \mu_+ \begin{bmatrix} q^n \\ p^n \end{bmatrix} = \mu_+\mathbf{x}^n, \tag{3.52}$$

and scheme (3.50) is equivalent to the Midpoint method. The scheme may be initialised by simply setting $q^0 \triangleq \omega_0 u_0$ and $p^0 = v_0$ without reducing the accuracy order.

3.6   Spatial difference operators

Consider now a function defined on both time and space $u = u(x, t) : \mathcal{D} \times \mathbb{R}_0^+ \to \mathbb{R}$, where $\mathcal{D} \subseteq \mathbb{R}$. The spatial domain can be discretized like the time domain, using a finite grid spacing $h > 0$ at locations $x = lh$, $l \in \mathfrak{D} \subseteq \mathbb{Z}$, allowing the continuous function to be

approximated by a grid function: $u_l(t) \approx u(x,t)$. Correspondingly, discrete spatial operators, analogous to those in the time domain, can be defined as:

$$1u_l = u_l, \qquad e_{x+}u_l = u_{l+1}, \qquad e_{x-}u_l = u_{l-1}. \tag{3.53}$$

From here, the forward, backward and centred spatial difference operators (or FD operators in space) are defined as:

$$\delta_{x+} \triangleq \frac{e_{x+} - 1}{h} \approx \frac{\mathrm{d}}{\mathrm{d}x}, \qquad \delta_{t-} \triangleq \frac{1 - e_{x-}}{h} \approx \frac{\mathrm{d}}{\mathrm{d}x}, \qquad \delta_{t\cdot} \triangleq \frac{e_{x+} - e_{x-}}{2h} \approx \frac{\mathrm{d}}{\mathrm{d}x}. \tag{3.54}$$

When applied to a grid function, these operators provide different approximations to the first derivative:

$$\delta_{x+}u_l = \frac{u_{l+1} - u_l}{h}, \qquad \delta_{x-}u_l = \frac{u_l - u_{l-1}}{h}, \qquad \delta_{x\cdot}u_l = \frac{u_{l+1} - u_{l-1}}{2h}. \tag{3.55}$$

An approximation to the second spatial derivative is constructed as:

$$\delta_{xx} \triangleq \delta_{x+}\delta_{x-} = \frac{e_{x+} - 2 + e_{x-}}{h^2}. \tag{3.56}$$

Additionally, averaging operators can be defined as:

$$\mu_{x+} = \frac{e_{x+} + 1}{2} \approx 1, \quad \mu_{x-} = \frac{1 + e_{x-}}{2} \approx 1, \quad \mu_{x\cdot} = \frac{e_{x+} + e_{x-}}{2} \approx 1. \tag{3.57}$$

The Euler-Bernoulli stiff string equation involves a fourth-order spatial derivative, which can be approximated using a fourth-order difference operator defined as:

$$\delta_{xxxx} = \delta_{xx}\delta_{xx} \quad \Rightarrow \quad \delta_{xxxx}u_l = \frac{u_{l+2} - 4u_{l+1} + 6u_l - 4u_{l-1} + u_{l-2}}{h^4}. \tag{3.58}$$

Notice that this operator has a stencil of width 5. The same considerations regarding truncation error that apply to temporal operators also hold for spatial operators. Thus, the forward and backward difference and mean operators are first-order accurate, while the centred operators and the second and fourth difference operators are second-order accurate. Moreover, identities analogous to equations (3.6) and (3.7) exist in space as well. In addition, it is useful to write the following bounds explicitly:

$$|\delta_{x\pm}u_l| \leq 2|u_l|/h, \tag{3.59a}$$

$$|\delta_{xx}u_l| \leq 2|\delta_{x\pm}u_l|/h \leq 4|u_l|/h^2. \tag{3.59b}$$

3.6.1 Matrix form

Given that $u_l(t)$ is interpreted as a grid function, it can be condensed into a vector, referred to as the state vector:

$$\mathbf{u}(t) \triangleq [\ldots u_{l-1}, u_l, u_{l+1}, \ldots]^{\mathsf{T}}. \tag{3.60}$$

For now, the continuous function is considered defined over the entire real domain, meaning $\mathcal{D} = \mathbb{R}$ and $\mathfrak{D} = \mathbb{Z}$; therefore: $\mathbf{u} \in \mathbb{R}^{\infty}$. It is possible to define the application of the spatial difference operators acting element-wise over the entire state vector. For instance:

$$\delta_{x-}\mathbf{u} \triangleq [\ldots, \delta_{x-}u_{l-1}, \delta_{x-}u_l, \delta_{x-}u_{l+1}, \ldots]^{\mathsf{T}}. \tag{3.61}$$

The spatial difference operators can then be regarded as matrices acting on the state vector. Operators δ_{x+}, δ_{x-} and δ_{xx} may be expressed, respectively, as:

$$\mathbf{D}^+_{\cdot} = \frac{1}{h}\begin{bmatrix} \ddots & \ddots & & & \mathbf{0} \\ & -1 & 1 & & \\ & & -1 & 1 & \\ & & & -1 & \ddots \\ \mathbf{0} & & & & \ddots \end{bmatrix}, \qquad \mathbf{D}^-_{\cdot} = \frac{1}{h}\begin{bmatrix} \ddots & & & & \mathbf{0} \\ \ddots & 1 & & & \\ & -1 & 1 & & \\ & & -1 & 1 & \\ \mathbf{0} & & & \ddots & \ddots \end{bmatrix},$$

$$\mathbf{D}^2_{\cdot} = \mathbf{D}^+_{\cdot}\mathbf{D}^-_{\cdot} = \frac{1}{h^2}\begin{bmatrix} \ddots & \ddots & & & \mathbf{0} \\ \ddots & -2 & 1 & & \\ & 1 & -2 & 1 & \\ & & 1 & -2 & \ddots \\ \mathbf{0} & & & \ddots & \ddots \end{bmatrix}.$$

Here, the subscript $\cdot$ indicates that the boundaries of the matrices are not yet defined. Matrix representations of the mean and fourth-order difference operators can be constructed analogously, particularly $\mathbf{D}^4_{\cdot} = \mathbf{D}^2_{\cdot}\mathbf{D}^2_{\cdot}$.

3.6.2 Input and interpolation operators

Because much of the interaction between models is considered point-wise, it is important to introduce the notation used for discrete Dirac delta operators, which are also applicable beyond excitation, such as in modelling connections between distributed objects. There are various ways to discretize such a distribution. Consider the excitation location x_i, then, define $l_i \triangleq \lfloor x_i/h \rfloor$, where $\lfloor \cdot \rfloor$ indicates the flooring operation. Possible discretisations of the

Dirac delta operator can be represented by vectors defined as:

$$\mathbf{j}_1^{(x_i)} \triangleq \frac{1}{h} \begin{cases} 0, & l < l_i \\ (1 - \alpha_i), & l = l_i \\ \alpha_i, & l = l_i + 1 \\ 0, & l > l_i + 1 \end{cases} \qquad \mathbf{j}_3 = \frac{1}{h} \begin{cases} 0, & l < l_i - 1 \\ \alpha_i(\alpha_i - 1)(\alpha_i - 2)/ - 6, & l = l_i - 1 \\ (\alpha_i - 1)(\alpha_i + 1)(\alpha_i - 2)/2, & l = l_i \\ \alpha_i(\alpha_i + 1)(\alpha_i - 2)/ - 2, & l = l_i + 1 \\ \alpha_i(\alpha_i + 1)(\alpha_i - 1)/6, & l = l_i + 2 \\ 0, & l > l_i + 2, \end{cases}$$

where $\alpha_i = x_i/h - l_i$. Here, $\mathbf{j}_1$ uses linear interpolation between the neighbouring points, while $\mathbf{j}_3$ performs lagrange cubic interpolation.

Interpolation between points can be useful for evaluating the state of a grid function $\mathbf{u}$ at a specific point x_o. To achieve this, one may use the vectors defined above: $u(x_o) \approx h \left(\mathbf{j}^{(x_o)} \right)^{\mathsf{T}} \mathbf{u}$, where $\mathbf{j}^{(x_o)}$ is a generic input vector centred on x_o.

3.6.3   Preamble 3: discrete inner product and relations

Before proceeding, it is necessary to define a form for an inner product between grid functions. Consider now two grid functions a_l and b_l, defined over a finite domain $\mathfrak{D}$, so that $l \in \mathfrak{D} = [0, 1, \ldots, N]$. When condensed into vector form, these functions are denoted as $\mathbf{a}$ and $\mathbf{b}$ respectively. A discrete counterpart of the L^2 inner product may be defined as:

$$\sum_{l=0}^{N} h a_l b_l = h \left\langle \mathbf{a}, \mathbf{b} \right\rangle_{\mathfrak{D}}, \tag{3.62}$$

where the vector inner product is that defined in (2.47), and the subscript indicates the domain of definition of the inner product. The norm is then denoted as:

$$h \mathbf{a}^{\mathsf{T}} \mathbf{a} = h \|\mathbf{a}\|_{\mathfrak{D}}^2 \geq 0. \tag{3.63}$$

Consequently, the properties listed for the vector inner product also apply to grid functions.

The discrete analogous to integration by parts is summation by parts, which can be expressed in different variants, such as:

$$h \left\langle \mathbf{a}, \delta_{x-} \mathbf{b} \right\rangle_{\mathfrak{D}} = -h \left\langle \delta_{x+} \mathbf{a}, \mathbf{b} \right\rangle_{\mathfrak{D}} + a_{N+1} b_N - a_0 b_{-1}, \tag{3.64a}$$

$$= -h \left\langle \delta_{x+} \mathbf{a}, \mathbf{b} \right\rangle_{\underline{\mathfrak{D}}} + a_N b_N - a_0 b_{-1}. \tag{3.64b}$$

Another version, involving the forward difference operator, is given by:

$$h \langle \mathbf{a}, \delta_{x+}\mathbf{b} \rangle_{\mathfrak{D}} = -h \langle \delta_{x-}\mathbf{a}, \mathbf{b} \rangle_{\mathfrak{D}} + a_N b_{N+1} - a_{-1} b_0, \tag{3.65a}$$

$$= -h \langle \delta_{x-}\mathbf{a}, \mathbf{b} \rangle_{\overline{\mathfrak{D}}} + a_N b_{N+1} - a_0 b_0, \tag{3.65b}$$

where it was defined $\mathfrak{D} \triangleq [0, \ldots, N-1]$ and $\overline{\mathfrak{D}} \triangleq [1, \ldots, N]$. The expressions (3.64) and (3.65) can be obtained through algebraic manipulation. A detailed derivation of equations (3.64) is provided in [223]. By recalling that $\delta_{xx} = \delta_{x+}\delta_{x-}$, the above expressions can be combined to yield:

$$h \langle \mathbf{a}, \delta_{xx}\mathbf{b} \rangle_{\mathfrak{D}} = h \langle \delta_{xx}\mathbf{a}, \mathbf{b} \rangle_{\mathfrak{D}} + a_N \delta_{x+} b_N - b_N \delta_{x+} a_N - a_0 \delta_{x-} b_0 + b_0 \delta_{x-} a_0, \tag{3.66a}$$

$$= h \langle \delta_{xx}\mathbf{a}, \mathbf{b} \rangle_{\overline{\mathfrak{D}}} + a_N \delta_{x+} b_N - b_N \delta_{x-} a_N - a_0 \delta_{x-} b_0 + b_0 \delta_{x+} a_0, \tag{3.66b}$$

where $\overline{\mathfrak{D}} = [1, \ldots, N]$. Note that these expressions include grid points outside the domain of definition. This issue must be addressed by imposing appropriate discrete boundary conditions, as shown later on.

3.7 Discretisation of the 1-D wave equation

3.7.1 Semi-discretisation

Consider the ideal string equation (2.63), defined over the domain $\mathcal{D} = [0, L] \subset \mathbb{R}$. This domain is mapped onto the discrete grid $\mathfrak{D} = [0, N] \subset \mathbb{Z}$, with $N \triangleq \lfloor L/h \rfloor$, resulting in $N + 1$ discretisation points. The continuous function is then approximated by a grid function at these discretization points, and the semi-discretised equation can be expressed in vector form as:

$$\rho A \frac{\mathrm{d}^2 \mathbf{u}}{\mathrm{d}t^2} = T_0 \delta_{xx} \mathbf{u}. \tag{3.67}$$

Energy analysis begins by taking the inner product of equation (3.67) with $h\frac{\mathrm{d}\mathbf{u}}{\mathrm{d}t}$:

$$\rho A h \left\langle \frac{\mathrm{d}\mathbf{u}}{\mathrm{d}t}, \frac{\mathrm{d}^2 \mathbf{u}}{\mathrm{d}t^2} \right\rangle_{\mathfrak{D}} = T_0 h \left\langle \frac{\mathrm{d}\mathbf{u}}{\mathrm{d}t}, \delta_{xx}\mathbf{u} \right\rangle_{\mathfrak{D}}. \tag{3.68}$$

Noting that identities (2.4) hold for vectors as well, (2.4a) may be applied on the left-hand side. On the right-hand side, consider that $\delta_{xx} = \delta_{x+}\delta_{x-}$. Then, one may apply summation by parts as per (3.65b). Finally, using (2.4b), yields:

$$\frac{\mathrm{d}}{\mathrm{d}t}\mathcal{H} = T_0 \frac{\mathrm{d}u_N}{\mathrm{d}t}(\delta_{x+}u_N) - T_0 \frac{\mathrm{d}u_0}{\mathrm{d}t}(\delta_{x-}u_0). \tag{3.69}$$

Here, the semi-discrete energy $\mathcal{H}$ takes the form:

$$\mathcal{H} = \frac{\rho A h}{2} \left\| \frac{d\mathbf{u}}{dt} \right\|_{\mathfrak{D}}^2 + \frac{T_0 h}{2} \|\delta_{x-}\mathbf{u}\|_{\overline{\mathfrak{D}}}^2, \tag{3.70}$$

which clearly discretizes (2.78) in space. The two components can be identified as the kinetic and potential energies of the string. Note that the potential energy is defined over the reduced domain $\overline{\mathfrak{D}}$.

The energy is positive definite, while the boundary terms vanish under the conditions:

$$u_0 = 0; \qquad\qquad u_N = 0 \qquad \text{Dirichlet.} \tag{3.71a}$$

$$\delta_{x-}u_0 = 0; \qquad\qquad \delta_{x+}u_N = 0 \qquad \text{Neumann.} \tag{3.71b}$$

These are discrete versions of the boundary conditions (2.79) and (2.80), respectively; mixed boundaries are also possible. Note that the Neumann conditions involve first-order accurate operators: a version using a centred operator can also be implemented with a different inner product definition; further details can be found in [24, Chapter 5].

3.7.2 Dirichlet boundaries in matrix form

Boundary conditions can be incorporated into matrix operators. This discussion will focus on Dirichlet boundaries, which are the most commonly used in this work. Since the endpoints u_0 and u_N are always zero, one may completely avoid storing their values and redefine the state vector as its interior with dimension $N - 1$. Thus: $\mathbf{u} = [u_1, \ldots, u_{N-1}]$. Then, one has:

$$\mathbf{D}^- = \frac{1}{h} \begin{bmatrix} 1 & & & \mathbf{0} \\ -1 & 1 & & \\ & \ddots & \ddots & \\ \mathbf{0} & & & -1 \end{bmatrix}. \tag{3.72}$$

This matrix is rectangular, with dimensions $N \times (N - 1)$. The forward operator may be defined as: $\mathbf{D}^+ = -(\mathbf{D}^-)^\intercal$, and has dimension $(N-1) \times N$. The second difference operator

is then defined as:

$$\mathbf{D}^2 = \mathbf{D}^+\mathbf{D}^- = \frac{1}{h^2}\begin{bmatrix} -2 & 1 & & & \mathbf{0} \\ 1 & -2 & 1 & & \\ & \ddots & \ddots & \ddots & \\ & & 1 & -2 & 1 \\ \mathbf{0} & & & 1 & -2 \end{bmatrix}, \tag{3.73}$$

which is a square matrix of dimension $(N-1) \times (N-1)$. Note that the composition is not symmetric: reversing the product operation would result in a larger operator, conflicting with the dimensions of the state vector. Furthermore, $\mathbf{D}^+$ has a dimension incompatible with the state vector length and cannot be applied directly but only through composition with the backward operator. The semi-discretised wave equation in matrix form, with Dirichlet boundaries, is:

$$\rho A \frac{\mathrm{d}^2\mathbf{u}}{\mathrm{d}t^2} = T_0\mathbf{D}^2\mathbf{u}. \tag{3.74}$$

3.7.3   Eigenvalue decomposition of the second difference matrix

It is useful to explicitly write the eigenvalues and eigenvectors of the $\mathbf{D}^2$ matrix. The complete derivation may be found in [137, Chapter 2]. The eigenvalue problem relative to the m-th eigenvector $\hat{\mathbf{u}}_m$ is:

$$\mathbf{D}^2\hat{\mathbf{u}}_m - \lambda_m\hat{\mathbf{u}}_m = 0, \quad m = 1, 2, \dots, N-1. \tag{3.75}$$

The n-th component of the m-th eigenvector is:

$$(\hat{u}_n)_m = \sqrt{\frac{2}{N}}\sin(nh\beta_m), \quad n = 1, 2, \dots, N-1, \quad \beta_m = \frac{m\pi}{Nh}. \tag{3.76}$$

where β_m is the wavenumber, and $\sqrt{2/N}$ is a normalisation factor. The corresponding m-th eigenvalue is:

$$\lambda_m = -\frac{4}{h^2}\sin^2(\frac{m\pi}{2N}). \tag{3.77}$$

Thus, matrix $\mathbf{D}^2$ is negative definite, and equation (3.74) can be interpreted as a system of coupled oscillators, analogous to equation (2.52). Consequently, this system can be completely decoupled. Being negative definite, $\mathbf{D}^2$ and admits the diagonalisation:

$$\mathbf{D}^2 = -\mathbf{U}\boldsymbol{\Lambda}\mathbf{U}^\intercal, \tag{3.78}$$

where $\mathbf{\Lambda}$ is a diagonal matrix with elements λ_m, and the columns of $\mathbf{U}$ consist of the eigenvectors. Note that the following holds:

$$0 < \lambda_m < 4/h^2, \tag{3.79}$$

which implies that $\mathbf{\Lambda}$ is positive definite. Since the eigenvectors are normalised, $\mathbf{U}$ is orthonormal. Then, by left-multiplying equation (3.74) by $\frac{1}{\rho A}\mathbf{U}^{-1}$ and defining $\mathbf{w} \triangleq \mathbf{U}^{-1}\mathbf{u}$ one obtains:

$$\frac{\mathrm{d}^2\mathbf{w}}{\mathrm{d}t^2} = -c^2\mathbf{\Lambda}\mathbf{w}, \tag{3.80}$$

which is a system of decoupled oscillators. By defining $c^2\mathbf{\Lambda} \triangleq \mathbf{\Omega}^2$, one retrieves a form analogous to (2.101), which may be integrated in time as (3.44), or with the exact integrator (3.29).

3.7.4 Full discretisation

Time integration of system (3.74) can be performed through the time difference operators previously defined. To this end, the grid function $\mathbf{u}(t)$ is approximated by a time series vector $\mathbf{u}^n$. Then, a FD scheme is obtained by substituting the time derivative with a second-order difference operator in time:

$$\rho A \delta_{tt}\mathbf{u}^n = T_0\mathbf{D}^2\mathbf{u}^n. \tag{3.81}$$

3.7.5 Stability, consistency and convergence

Stability via energy analysis

An energy analysis is performed by taking an inner product of equation (3.81) with $h\delta_{t\cdot}\mathbf{u}^n$:

$$\rho A h\langle\delta_{t\cdot}\mathbf{u}^n, \delta_{tt}\mathbf{u}^n\rangle = T_0 h\langle\delta_{t\cdot}\mathbf{u}^n, \mathbf{D}^2\mathbf{u}^n\rangle. \tag{3.82}$$

Note that the subscript indicating the domain of the inner products has been omitted: since boundaries are now defined, the inner products and norms are understood to operate over the entire vector length $N-1$. One may consider that $\mathbf{D}^2 = \mathbf{D}^+\mathbf{D}^- = -(\mathbf{D}^-)^\mathsf{T}\mathbf{D}^-$. Utilizing the properties of the transposition operator and applying identities (3.7a) and (3.7b) (which hold for vectors), the following is obtained:

$$\delta_{t+}\mathfrak{h}^{n-1/2} = 0, \tag{3.83}$$

where the energy is written:

$$\mathfrak{h}^{n-1/2} = \frac{\rho A h}{2} \| \delta_{t-} \mathbf{u}^n \|^2 + \frac{T_0 h}{2} \left\langle \mathbf{D}^- \mathbf{u}^{n-1}, \mathbf{D}^- \mathbf{u}^n \right\rangle. \tag{3.84}$$

While the discrete energy balance is conservative, the discrete potential energy exhibits an indefinite sign. To ensure positivity, one may apply the identity (3.6f) and the bound (3.59a), which leads to:

$$\frac{\rho A h}{2} \| \delta_{t-} \mathbf{u}^n \|^2 + \frac{T_0 h}{2} \| \mu_{t-} \mathbf{D}^- \mathbf{u}^n \|^2 - \frac{T_0 h k^2}{8} \| \delta_{t-} \mathbf{D}^- \mathbf{u}^n \|^2 \geq h \left(\frac{\rho A}{2} - \frac{T_0 k^2}{2h^2} \right) \| \delta_{t-} \mathbf{u}^n \|^2.$$

Then, the discrete energy expression is non-negative if:

$$\left(\frac{\rho A}{2} - \frac{T_0 k^2}{2h^2} \right) \geq 0 \qquad \Rightarrow \qquad h^2 \geq \frac{T_0 k^2}{\rho A} = c^2 k^2. \tag{3.85}$$

This is referred to as the Courant-Fredrichs-Lewy (CFL) condition and links the space and time sampling steps.

Consistency

An analysis of the LTE may be performed by applying the difference operators to the continuous function $\bar{u}(x,t)$ (where the $\bar{\ }$ helps distinguish between the continuous function and the time series):

$$\tau_l^n = (\delta_{tt} - c^2 \delta_{xx}) \bar{u}(lh, nk). \tag{3.86}$$

by Taylor expanding the operators and factorising out the term $\partial_t^2 - c^2 \partial_x^2$, one gets:

$$\left(1 + \frac{k^2}{12} \left(\partial_t^2 + c^2 \partial_x^2 \right) + \frac{k^4}{360} \left(\partial_t^4 + c^4 \partial_x^4 + c^2 \partial_x^2 \partial_t^3 \right) + \dots \right) \left(\partial_t^2 - c^2 \partial_x^2 \right) \bar{u} = \tau_l^n.$$

Considering (2.63), the left-hand side vanishes, and one has $\tau_l^n = 0$. Thus, the scheme is exact.

Initialisation: global error

The global error for a space-time grid is defined as:

$$E_l^n = u(lh, nk) - u_l^n. \tag{3.87}$$

It has been established that the scheme (3.81) is both stable and consistent. Therefore, due to its linearity, it is also convergent, eliminating the need for further convergence analysis. However, the LTE is exactly zero when l is an inner point of the domain, and n is sufficiently far from the initial state. Indeed, the global error is influenced by both boundary and initial conditions. As previously discussed, the boundary conditions are discretized using the matrix $\mathbf{D}^2$. Now, appropriate initial conditions must be defined. The initial displacement can be set simply as:

$$u_l^0 = u_0(lh). \tag{3.88}$$

Similarly to what shown for the SHO, the next step can be initialised with different level of accuracy:

$$u_l^1 = u_l^0 + kv_0(lh) \tag{3.89a}$$

$$u_l^1 = u_l^0 + kv_0(lh) + \frac{k^2 c^2}{2}\delta_{xx}u_l^0, \tag{3.89b}$$

where the latter was derived using (3.6c) and the relation: $\delta_{tt}u_l^0 = c^2\delta_{xx}u_l^0$. These initializations are expected to yield first- and second-order accurate global errors, respectively. However, in the ideal string case only, the global error obtained with the second initialization is reduced to machine accuracy, making the scheme effectively exact. Note that this loses validity as soon as loss is introduced.

3.8 Discretisation of the complete linear string

3.8.1 Semi-discretisation

Consider now the full linear string model (2.135), defined over the domain $\mathcal{D} = [0, L]$. A discretisation of the spatial domain, with point-wise forcing centred on x_i, yields:

$$\rho A\frac{\mathrm{d}^2\mathbf{u}}{\mathrm{d}t^2} = T_0\delta_{xx}\mathbf{u} - EI_0\delta_{xxxx}\mathbf{u} - 2\rho A\left(\sigma_0 - \sigma_1\delta_{xx}\right)\frac{\mathrm{d}\mathbf{u}}{\mathrm{d}t} + \mathbf{j}^{(x_i)}F, \tag{3.90}$$

where the boundaries are not yet defined, and $\mathbf{u}$ is defined over the points $[0, N] \subset \mathbb{Z}$.

Energy analysis begins by taking the inner product of equation (3.90) with $h\frac{\mathrm{d}\mathbf{u}}{\mathrm{d}t}$ over the domain:

$$\rho Ah\left\langle \frac{\mathrm{d}\mathbf{u}}{\mathrm{d}t}, \frac{\mathrm{d}^2\mathbf{u}}{\mathrm{d}t^2}\right\rangle_{\mathfrak{D}} = h\left\langle \frac{\mathrm{d}\mathbf{u}}{\mathrm{d}t}, T_0\delta_{xx}\mathbf{u} - EI_0\delta_{xxxx}\mathbf{u} - 2\rho A\left(\sigma_0 - \sigma_1\delta_{xx}\right)\frac{\mathrm{d}\mathbf{u}}{\mathrm{d}t} + \mathbf{j}^{(x_i)}F\right\rangle_{\mathfrak{D}}.$$

The inertia and tension terms are treated as for the wave equation. For the stiffness term, one may consider that $\delta_{xxxx} = \delta_{xx}\delta_{xx}$ and apply summation by parts twice as per (3.66b), obtaining:

$$\frac{\mathrm{d}}{\mathrm{d}t}\mathcal{H} = \mathcal{B} - 2\rho Ah \left\langle \frac{\mathrm{d}\mathbf{u}}{\mathrm{d}t}, (\sigma_0 - \sigma_1\delta_{xx})\frac{\mathrm{d}\mathbf{u}}{\mathrm{d}t} \right\rangle_{\mathfrak{D}} + h \left\langle \frac{\mathrm{d}\mathbf{u}}{\mathrm{d}t}, \mathbf{j}^{(x_i)} \right\rangle_{\mathfrak{D}} F, \qquad (3.91)$$

where the boundary term is:

$$\begin{aligned}
\mathcal{B} = &-T_0 \left[T_0 \frac{\mathrm{d}u_0}{\mathrm{d}t}(\delta_{x-}u_0) - \frac{\mathrm{d}u_N}{\mathrm{d}t}(\delta_{x+}u_N) \right] \\
&- EI_0 \left[\frac{\mathrm{d}\delta_{x-}u_0}{\mathrm{d}t}\delta_{xx}u_0 - \frac{\mathrm{d}\delta_{x+}u_N}{\mathrm{d}t}\delta_{xx}u_N - \frac{\mathrm{d}u_0}{\mathrm{d}t}\delta_{x-}\delta_{xx}u_0 + \frac{\mathrm{d}u_N}{\mathrm{d}t}\delta_{x+}\delta_{xx}u_N \right].
\end{aligned} \qquad (3.92)$$

The semi-discrete energy $\mathcal{H}$ is clearly non-negative, taking the form:

$$\mathcal{H} = \frac{\rho Ah}{2}\left\| \frac{\mathrm{d}\mathbf{u}}{\mathrm{d}t} \right\|_{\mathfrak{D}}^2 + \frac{T_0 h}{2}\|\delta_{x-}\mathbf{u}\|_{\overline{\mathfrak{D}}} + \frac{EI_0 h}{2}\|\delta_{xx}\mathbf{u}\|_{\underline{\overline{\mathfrak{D}}}}. \qquad (3.93)$$

The boundary term vanishes under the following conditions:

$$u_0 = \delta_{x-}u_0 = u_N = \delta_{x+}u_N = 0 \qquad \text{clamped,} \qquad (3.94\mathrm{a})$$

$$u_0 = \delta_{xx}u_0 = u_N = \delta_{xx}u_N = 0 \qquad \text{simply supported,} \qquad (3.94\mathrm{b})$$

$$\left.\begin{aligned}
\delta_{xx}u_0 = -T_0\delta_{x-}u_0 + EI_0\delta_{x-}\delta_{xx}u_0 = 0 \\
\delta_{xx}u_N = -T_0\delta_{x+}u_N + EI_0\delta_{x+}\delta_{xx}u_N = 0
\end{aligned}\right\} \qquad \text{free.} \qquad (3.94\mathrm{c})$$

These are a discretisation of, respectively, the clamped, simply supported and free conditions (2.112), for both ends. Mixed boundaries are also possible.

3.8.2   Simply supported boundaries in matrix form

It is useful to express the finite difference operators in matrix form for simply supported boundary conditions. Similar to the Dirichlet case, the endpoints are always set to zero, allowing the state vector to be defined using only its interior points: $\mathbf{u} = [u_1, \ldots, u_{N-1}]$. The backward, forward, and second-order difference matrices are identical to those defined for Dirichlet conditions in equations (3.72) and (3.73). The fourth-order operator can be

represented as:

$$\mathbf{D}^4 = \mathbf{D}^2\mathbf{D}^2 = \frac{1}{h^4} \begin{bmatrix} 5 & -4 & 1 & & & & \mathbf{0} \\ -4 & 6 & -4 & 1 & & & \\ 1 & -4 & 6 & \ddots & \ddots & & \\ & 1 & \ddots & \ddots & & 1 \\ & & \ddots & & 6 & -4 \\ \mathbf{0} & & & 1 & -4 & 5 \end{bmatrix}. \tag{3.95}$$

This matrix is symmetric and positive definite, admitting an eigendecomposition with positive eigenvalues, though their explicit form will not be covered here.

Then, system (3.90), with simply supported boundaries, may be written:

$$\rho A \frac{\mathrm{d}\mathbf{u}}{\mathrm{d}t} = \mathfrak{L}\mathbf{u} + \mathbf{j}^{(x_i)}F, \quad \mathfrak{L} = (T_0\mathbf{D}^2 - EI_0\mathbf{D}^4) - 2\rho A(\sigma_0\mathbf{I} - \sigma_1\mathbf{D}^2)\frac{\mathrm{d}}{\mathrm{d}t}, \tag{3.96}$$

where $\mathbf{I}$ is the identity matrix of dimension $(N-1) \times (N-1)$, and $\mathfrak{L}$ is the semi-discretisation of the linear operator $\mathcal{L}$. Note that, since $\mathbf{D}^2$ is negative definite and $\mathbf{D}^4$ is positive definite, system (3.96) may be again interpreted as a system of coupled oscillators with loss and forcing.

3.8.3 Full discretisation

The linear string model can now be fully discretised. A FD scheme for equation (3.96) is written:

$$\rho A \delta_{tt}\mathbf{u}^n = \mathfrak{l}\mathbf{u}^n + \mathbf{j}^{(x_i)}F^n, \quad \mathfrak{l} = (T_0\mathbf{D}^2 - EI_0\mathbf{D}^4) - 2\rho A\left(\sigma_0\delta_{t\cdot} - \sigma_1\delta_{t-}\mathbf{D}^2\right), \tag{3.97}$$

where F^n is a time series sampling the input at time $F(nk)$, and $\mathfrak{l}$ is the fully discrete linear operator. This scheme is only first-order accurate due to the use of a backward operator for modelling the frequency-dependent damping term. Achieving second-order accuracy would require a centred time operator, resulting in an implicit scheme. However, since the frequency-dependent damping term is typically small, modelling it with a non-centred operator has only limited impact on accuracy [24, Chapter 7].

The discrete energy now takes the form:

$$
\begin{aligned}
\mathfrak{h}^{n-1/2} &= \frac{\rho A h}{2} \left\langle \delta_{t-}\mathbf{u}^n, \left(\mathbf{I} - k\sigma_1\mathbf{D}^2\right) \delta_{t-}\mathbf{u}^n \right\rangle \\
&+ \frac{T_0 h}{2} \left\langle \mathbf{D}^-\mathbf{u}^{n-1}, \mathbf{D}^-\mathbf{u}^n \right\rangle + \frac{E I_0 h}{2} \left\langle \mathbf{D}^2\mathbf{u}^{n-1}, \mathbf{D}^2\mathbf{u}^n \right\rangle,
\end{aligned}
\tag{3.98}
$$

where, once again, the subscript referring to the domain of the inner products is omitted, and the inner products and norms are understood to apply over the entire vector. The energy balance is expressed as:

$$
\delta_{t+}\mathfrak{h}^{n-\frac{1}{2}} = -Q^n + h\left\langle \delta_{t\cdot}\mathbf{u}^n, \mathbf{j}^{(x_i)} \right\rangle F^n,
\tag{3.99}
$$

where the loss term has the form:

$$
Q^n = 2\rho A h \left\langle \delta_{t\cdot}\mathbf{u}^n, \left(\sigma_0\mathbf{I} - k\sigma_1\mathbf{D}^2\right) \delta_{t\cdot}\mathbf{u}^n \right\rangle.
\tag{3.100}
$$

The stability condition for this scheme can be derived using discrete energy or frequency domain [223] arguments, and results in the following:

$$
h \geq \sqrt{\left(4\sigma_1 k + c^2 k^2 + \sqrt{\left(4\sigma_1 k + c^2 k^2\right)^2 + 16\kappa^2 k^2}\right)/2} \triangleq \bar{h},
\tag{3.101}
$$

where c and κ are defined in (2.84) and (2.114), respectively.

Notice that the scheme (3.97) suffers from numerical dispersion due to the finite difference approximation in space (unlike the scheme for the wave equation (3.81), which is exact). While this effect can be solved for modal systems by employing exact integrators for the modes, no equivalent solution exists for FDTD methods. The only option is to reduce the spatial sampling step; however, due to the stability condition (3.101), doing this requires increasing the sample rate, which is not always feasible in audio applications. Further discussion on numerical dispersion can be found in [24, Chapter 7].

3.8.4 Distributed bridge termination

In this paragraph, the eigenvalue problem of the model of a string coupled to a distributed bridge at the boundary, presented in Chapter 2, is solved numerically. To proceed, the spatial domain must be first discretized. A semi-discrete approximation of system (2.139) is given

by:

$$\rho_{\mathrm{s}} A_{\mathrm{s}} \frac{\mathrm{d}\mathbf{u}_{\mathrm{s}}}{\mathrm{d}t} = T_{\mathrm{s}}^2 \delta_{xx} \mathbf{u}_{\mathrm{s}} - E_{\mathrm{s}} I_{\mathrm{s}}^2 \delta_{xxxx} \mathbf{u}_{\mathrm{s}} \tag{3.102a}$$

$$\rho_{\mathrm{p}} A_{\mathrm{p}} \frac{\mathrm{d}\mathbf{u}_{\mathrm{p}}}{\mathrm{d}t} = -E_{\mathrm{p}} I_{\mathrm{p}} \delta_{zzzz} \mathbf{u}_{\mathrm{p}} + \mathbf{j}^{(z_s)} F. \tag{3.102b}$$

The string is simply supported at the left end, and the bar is simply supported at both ends; hence, $\mathbf{u}_{\mathrm{s}}$ is a state vector defined over a domain $\mathfrak{D}_{\mathrm{s}} = [1, N_{\mathrm{s}}] \subset \mathbb{Z}$, and $\mathbf{u}_{\mathrm{p}}$ is another state vector defined over $\mathfrak{D}_{\mathrm{p}} = [1, N_{\mathrm{p}} - 1] \subset \mathbb{Z}$. The input vector $\mathbf{j}^{(z_s)}$ is a discretisation of the Dirac delta operator centred on z_{s}. Next, discrete boundary conditions ensuring numerical stability are needed. A discretisation of (2.140), (2.141) and the contact condition (2.142) yields the complete set of discrete boundary conditions:

$$(u_{\mathrm{s}})_0 = \delta_{xx}(u_{\mathrm{s}})_0 = \delta_{xx}(u_{\mathrm{s}})_{N_{\mathrm{s}}} = 0, \tag{3.103a}$$

$$F(t) = -T_{\mathrm{s}} \delta_{x+}(u_{\mathrm{s}})_{N_{\mathrm{s}}} + E_{\mathrm{s}} I_{\mathrm{s}} \delta_{x+} \delta_{xx}(u_{\mathrm{s}})_{N_{\mathrm{s}}}, \tag{3.103b}$$

$$(u_{\mathrm{p}})_0 = \delta_{zz}(u_{\mathrm{p}})_0 = (u_{\mathrm{p}})_{N_{\mathrm{p}}} = \delta_{zz}(u_{\mathrm{p}})_{N_{\mathrm{p}}} = 0, \tag{3.103c}$$

$$h \left(\mathbf{j}^{(z_s)} \right)^{\mathsf{T}} \mathbf{u}_{\mathrm{p}} = (u_{\mathrm{s}})_{N_{\mathrm{s}}}, \tag{3.103d}$$

where the single grid points are denoted as: $(u_{\mathrm{s}})_l$ and $(u_{\mathrm{p}})_l$. An energy balance of the beam equation is obtained by taking an inner product of equation (3.102b) with $h\frac{\mathrm{d}\mathbf{u}_{\mathrm{p}}}{\mathrm{d}t}$, and yields:

$$\frac{\mathrm{d}}{\mathrm{d}t} \underbrace{\left(\frac{\rho_{\mathrm{p}} A_{\mathrm{p}}}{2} \left\| \frac{\mathrm{d}\mathbf{u}_{\mathrm{p}}}{\mathrm{d}t} \right\|_{\mathfrak{D}_{\mathrm{p}}}^2 + \frac{E_{\mathrm{p}} I_{\mathrm{p}}}{2} \|\delta_{zz}\mathbf{u}_{\mathrm{p}}\|_{\mathfrak{D}_{\mathrm{p}}}^2 \right)}_{\mathcal{H}_{\mathrm{p}}} = h \left(\mathbf{j}^{(z_s)} \right)^{\mathsf{T}} \frac{\mathrm{d}\mathbf{u}_{\mathrm{p}}}{\mathrm{d}t} F. \tag{3.104}$$

Analogously, the energy balance for the string equation is arrived at by taking an inner product of equation (3.102a) with $h\frac{\mathrm{d}\mathbf{u}_{\mathrm{s}}}{\mathrm{d}t}$. By employing summation by parts as per (3.64b) and (3.66a), and considering the boundary conditions one gets:

$$\frac{\mathrm{d}}{\mathrm{d}t} \underbrace{\left(\frac{\rho_{\mathrm{s}} A_{\mathrm{s}}}{2} \left\| \frac{\mathrm{d}\mathbf{u}_{\mathrm{s}}}{\mathrm{d}t} \right\|_{\mathfrak{D}_{\mathrm{s}}}^2 + \frac{T_{\mathrm{s}}}{2} \|\delta_{x+}\mathbf{u}_{\mathrm{s}}\|_{\underline{\mathfrak{D}}_{\mathrm{s}}}^2 + \frac{E_{\mathrm{s}} I_{\mathrm{s}}}{2} \|\delta_{xx}\mathbf{u}_{\mathrm{s}}\|_{\underline{\mathfrak{D}}_{\mathrm{s}}}^2 \right)}_{\mathcal{H}_{\mathrm{s}}} = \frac{\mathrm{d}(u_{\mathrm{s}})_{N_{\mathrm{s}}}}{\mathrm{d}t} F. \tag{3.105}$$

Then, through the contact condition (3.103d) one obtains: $\frac{\mathrm{d}}{\mathrm{d}t}(\mathcal{H}_{\mathrm{s}} + \mathcal{H}_{\mathrm{p}}) = 0$, and passivity is ensured.

By expanding the operators and applying the boundary and contact conditions, expressions for the points of the string outside the domain of definition, $(u_{\mathrm{s}})_{N_{\mathrm{s}}+1}$ and $(u_{\mathrm{s}})_{N_{\mathrm{s}}+2}$, can

be derived. Then, one may condense the state vectors into a vector $\mathbf{u} \triangleq [\mathbf{u}_{\mathrm{s}}^{\mathsf{T}}, \mathbf{u}_{\mathrm{p}}^{\mathsf{T}}]$, and write system (3.102) in compact form as:

$$\mathbf{M}\frac{\mathrm{d}\mathbf{u}}{\mathrm{d}t} = -\mathbf{K}\mathbf{u}. \tag{3.106}$$

The mass and stiffness matrices $\mathbf{M}$ and $\mathbf{K}$ are symmetric, positive definite block-matrices. $\mathbf{M}$ is defined as:

$$\mathbf{M} = \begin{bmatrix} \rho_{\mathrm{s}}A_{\mathrm{s}}\mathbf{I}_{\mathrm{s}} & \mathbf{0} \\ \mathbf{0} & \left(\rho_{\mathrm{p}}\mathbf{A}_{\mathrm{p}}\mathbf{I}_{\mathrm{p}} + \rho_{\mathrm{s}}A_{\mathrm{s}}h^2\mathbf{j}^{(z_s)}\left(\mathbf{j}^{(z_s)}\right)^{\mathsf{T}}\right) \end{bmatrix}. \tag{3.107}$$

Here, $\mathbf{I}_{\mathrm{s}}$ and $\mathbf{I}_{\mathrm{p}}$ are identity matrices, of dimension $(M_{\mathrm{s}} - 1) \times (M_{\mathrm{p}} - 1)$ and $(M_{\mathrm{p}} - 1) \times (M_{\mathrm{s}} - 1)$ respectively. $\mathbf{K}$ is defined as:

$$\mathbf{K} = \begin{bmatrix} -T_{\mathrm{s}}\mathbf{D}_{\mathrm{s}}^2 + E_{\mathrm{s}}I_{\mathrm{s}}\mathbf{D}_{\mathrm{s}}^4 & \mathbf{T}^{\mathsf{T}} \\ \mathbf{T} & E_{\mathrm{p}}I_{\mathrm{p}}\mathbf{D}_{\mathrm{p}}^4 + \left(T_0 + \frac{2E_sI_s}{h^2}\right)\mathbf{j}^{(z_s)}\left(\mathbf{j}^{(z_s)}\right)^{\mathsf{T}} \end{bmatrix}, \tag{3.108}$$

$$\mathbf{T} = \begin{bmatrix} \mathbf{0}, & +\frac{E_sI_s}{h^3}\mathbf{j}^{(z_s)}, & -\left(\frac{T_s}{h^2} + \frac{2E_sI_s}{h^3}\right)\mathbf{j}^{(z_s)} \end{bmatrix},$$

where $\mathbf{D}_{\mathrm{s}}^2$ and $\mathbf{D}_{\mathrm{s}}^4$ are difference operators of dimension $(N_{\mathrm{s}} - 1) \times (N_{\mathrm{s}} - 1)$, and $\mathbf{D}_{\mathrm{p}}^4$ has dimension $(N_{\mathrm{p}} - 1) \times (N_{\mathrm{p}} - 1)$. All three operators have simply supported boundaries. $\mathbf{T}$ has dimension $(N_{\mathrm{p}} - 1) \times (N_{\mathrm{s}} - 1)$, and is a composition of a zero-matrix of dimension $(N_{\mathrm{p}} - 1) \times (N_{\mathrm{s}} - 3)$ with two vectors.

To perform a modal expansion of system (3.106), a discrete eigenvalue problem is formulated as: $\mathbf{M}^{-1}\mathbf{K} = -\mathbf{U}\Omega^2\mathbf{U}$, where, as before, $\mathbf{U}$ is a matrix of real eigenvectors, and Ω^2 is a diagonal matrix of real, positive eigenvalues. Note that, altough both $\mathbf{K}$ and $\mathbf{M}$ are symmetric, the product $\mathbf{M}^{-1}\mathbf{K}$ generally is not. However, since $\mathbf{M}$ is positive definite, the eigenvalues of the product are then real [96], and they must also be non-negative since so are the eigenvalues of $\mathbf{K}$. The eigenvalue problem may be solved numerically using a fine grid h. Then, the modal expansion yields a system such as (2.56).

Figure 3.7 illustrates two comparisons of the eigenfrequencies of an isolated string versus those of the coupled string-bridge system, using different values of E_{p}. It is seen that reduced stiffness can shift the eigenfrequencies downwards by as much as two octaves in the lower frequency range. For materials with high E_{p}, like steel, the frequency gap is mostly confined around the fundamental frequency but can increase by up to two semitones for higher modes. Figure 3.7 shows the first four, the 10th and the 12th eigenmodes for a steel bridge. It can be observed that the bridge eigenmodes begin to show a third node only from the 10th mode onwards.
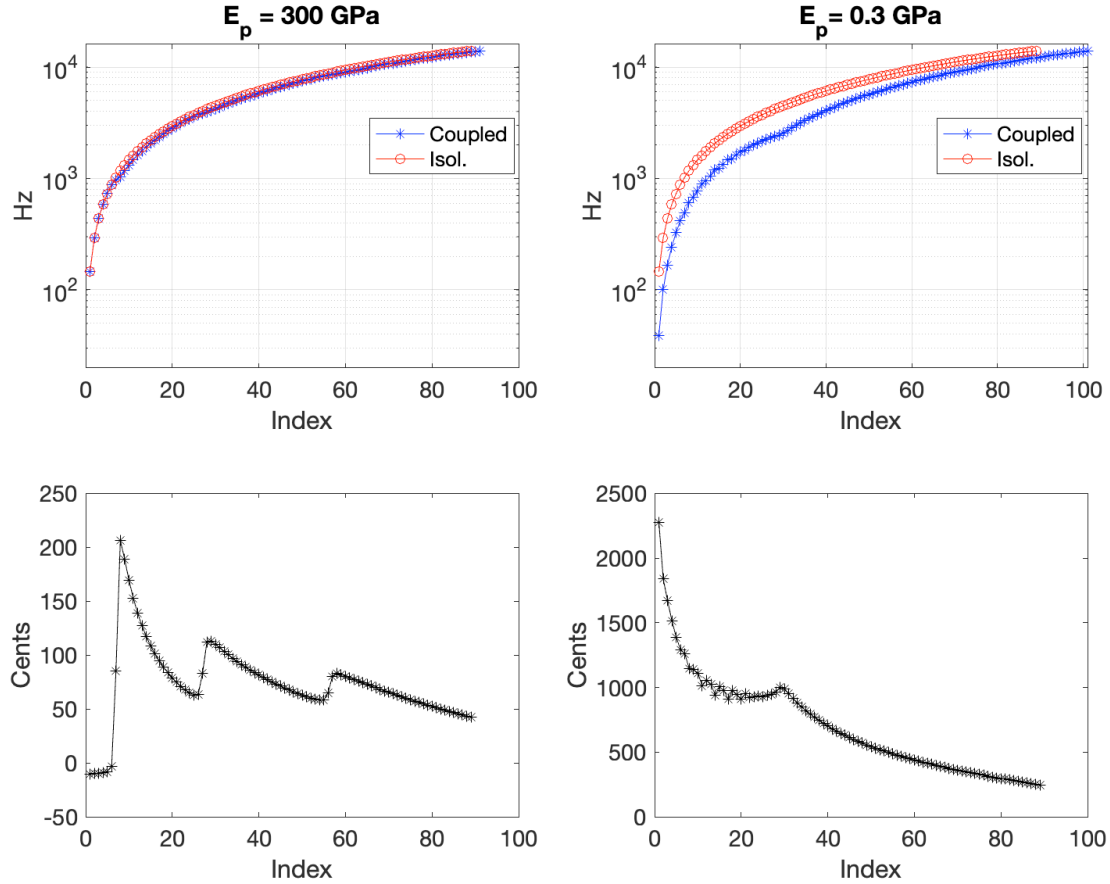
Fig. 3.6 Eigenfrequencies of the coupled system compared to those of an isolated simply supported stiff string, for two different values of E_p. The left value corresponds to typical steel, while the right value is chosen arbitrarily low for demonstration purposes. Other physical parameters in common between the two cases are $L_s = 0.69$ m; $T_s = 147.7$ N; $\rho_s A_s = 0.0063$ Kg m^{-1}; $E_s = 0.25$ GPa; $L_p = 0.07$ m; $\rho_p A_p = 0.0251$ Kg m^{-1}. The contact point is $z_s = 0.03$ m. Top figures show frequencies in log scale, while the bottom figures illustrate the frequency difference in cents for the same index. Reproduced from [181].
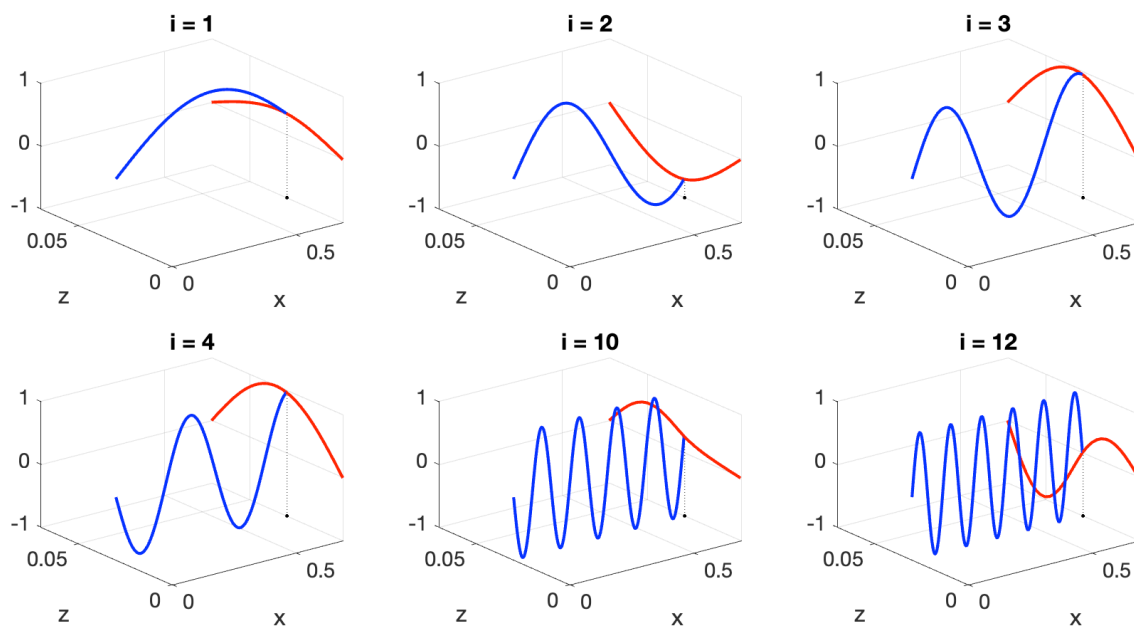
Fig. 3.7 Normalised modes of the coupled string-bridge system displayed and plotted orthogonally for visualization purposes. The mode index is indicated by the letter i. The blue line represents the string, while the red line represents the bridge. The contact point projection onto the z-axis is marked with a black dot. The physical parameters are consistent with those listed in Figure 3.6, using $E_{\mathrm{p}}I_{\mathrm{p}} = 300$ GPa. Reproduced from [181].

Chapter 4

Geometric nonlinearities

All the models presented in Chapter 2, along with the corresponding discretizations in Chapter 3, are linear. These are only approximations of the behaviour of vibrating systems and lose validity in cases of high-amplitude vibration. In this chapter, the linear models are extended to account for geometric nonlinearities, arising from large strains. First, the Duffing oscillator is introduced as a simple case study, extending the concept of the SHO. This is followed by a discussion on various nonlinear string models, where development proceeds differently from the rest of the work: starting with the most complex model and deriving simpler forms through simplifications. Finally, numerical integrators are presented; in particular, the SAV method will be introduced here.

4.1   The Duffing equation

The Duffing equation represents a linear oscillator with an added cubic restoring force. It arises in various scenarios, such as a pendulum with moderately large vibration amplitudes [231]. The equation is given by:

$$\frac{\mathrm{d}^2 u}{\mathrm{d}t^2} = -\omega_0^2 u - \gamma u^3, \tag{4.1}$$

where γ is a constant that controls the degree of nonlinearity in the restoring force. As outlined in Section 2.1, the potential is assumed non-negative; thus $\gamma \geq 0$, which defines a hardening nonlinearity. The softening case, where $\gamma < 0$, will not be addressed here. As for the SHO, an energy balance is computed by left-multiplying equation (4.1) by $m\frac{\mathrm{d}u}{\mathrm{d}t}$, leading to:

$$\frac{\mathrm{d}}{\mathrm{d}t}H = 0, \qquad H = \frac{m}{2}\left(\frac{\mathrm{d}u}{\mathrm{d}t}\right)^2 + \frac{Ku^2}{2} + \frac{m\gamma u^4}{4}. \tag{4.2}$$

The balance is passive; thus, the solution may be bounded with (2.9).

In the undamped, unforced case, with no initial velocity, the Duffing equation admits an analytic solution in terms of Jacobi elliptic functions:

$$\bar{u}(t) = u_0 \, \text{cn} \left(\sqrt{\omega_0^2 + \gamma u_0^2} t; \frac{\gamma u_0^2}{2\gamma u_0^2 + 2\omega_0^2} \right), \tag{4.3}$$

where $\text{cn}(z; a)$ is the Jacobi elliptic function of argument z and parameter a, and u_0 is the initial condition.

4.1.1 Potential quadratisation

Following (2.16), the potential in equation (4.2) may be written as:

$$V(u) = \frac{Ku^2}{2} + \phi_\text{d}(u), \qquad \phi_\text{d}(u) = \frac{\gamma u^4}{4} + \frac{\varepsilon}{2}. \tag{4.4}$$

Here, $\varepsilon > 0$ is an arbitrary constant that shifts the minimum of the potential without affecting the motion. Due to its non-negativity, the nonlinear part ϕ_d may be quadratised through an auxiliary variable ψ_d, as seen in equation (2.17). The energy can then be re-expressed as:

$$H = \frac{m}{2} \left(\frac{\text{d}u}{\text{d}t} \right)^2 + \frac{Ku^2}{2} + \frac{\psi_\text{d}^2}{2}, \tag{4.5}$$

and, using the definition of g from (2.18), the equation of motion (4.1) becomes the system of equations:

$$\frac{\text{d}^2 u}{\text{d}t^2} = -Ku - \psi_\text{d} g_\text{d}, \qquad \frac{\text{d}\psi_\text{d}}{\text{d}t} = g_\text{d} \frac{\text{d}u}{\text{d}t}, \qquad g_\text{d} = \frac{\gamma u^3}{\sqrt{\gamma u^4/2 + \varepsilon}}. \tag{4.6}$$

The system above is linear in u and ψ and can be solved efficiently using numerical methods, as will be shown later. The system can be extended to include loss and forcing terms, as was done for the SHO in Section 2.2.3. However, the analytic treatment of the lossy, forced Duffing oscillator is beyond the scope of this work; interested readers can refer to [148, Chapter 11] for further details.

4.1.2   Simulation

Three possible numerical schemes for the Duffing equation (4.1) are:

$$
\delta_{tt}u^n + \omega_0^2 u^n =
\begin{cases}
-\gamma(u^n)^3 \\
-\gamma(u^n)^2 \mu_{t.} u^n \\
-\gamma\mu_{t.}\left((u^n)^2\right)\mu_{t.} u^n
\end{cases} .
\tag{4.7}
$$

Through Taylor analysis, it may be proved that all three schemes are consistent and second-order accurate. When expanded, they become:

$$
u^{n+1} = \left(2 - k^2\omega_0^2 - k^2\gamma(u^n)^2\right)u^n - u^{n-1},
\tag{4.8a}
$$

$$
\left(1 + \frac{k^2\gamma(u^n)^2}{2}\right)u^{n+1} = \left(2 - k^2\omega_0^2\right)u^n - \left(1 + \frac{k^2\gamma(u^n)^2}{2}\right)u^{n-1},
\tag{4.8b}
$$

$$
g(u^{n+1}) = \left(2 - \omega_0^2 k^2\right)u^n - \left(1 + \frac{\gamma k^2}{4}(u^{n-1})^2\right)u^{n-1} \triangleq f(u^n, u^{n-1}),
\tag{4.8c}
$$

where

$$
g(u^{n+1}) \triangleq \frac{\gamma k^2}{4}(u^{n+1})^3 + \frac{\gamma k^2 u^{n-1}}{4}(u^{n+1})^2 + \left(1 + \frac{\gamma k^2(u^{n-1})^2}{4}\right)u^{n+1}.
$$

The first scheme is fully explicit. The second scheme is said to be linearly implicit, requiring division by a state-dependent coefficient at each time step. The third scheme is fully implicit, as it requires the solution of a nonlinear algebraic equation at each time step. In this simple case, the computational costs of the first two schemes are relatively comparable; however, in the distributed case linearly implicit schemes become significantly more computationally expensive than explicit ones. The third scheme requires substantially more computational effort, even in the lumped case, as solving it generally involves iterative methods, such as Newton-Raphson, which present various challenges, as discussed in Chapter 1. Through energy analysis, it can be shown [24, Chapter 4] that scheme (4.8a) does not possess a non-negative form of discrete energy and is thus prone to instability. In contrast, the other two schemes have a non-negative, nonlinear discrete energy, ensuring stability.

Consider now the quadratised system (4.6): following [28], a possible discretisation scheme is given by:

$$
\delta_{tt}u^n = -\omega_0^2 u^n - \mu_{t+}\psi_{\mathrm{d}}^{n-1/2} g_{\mathrm{d}}^n,
\tag{4.9a}
$$

$$
\delta_{t+}\psi_{\mathrm{d}}^{n-1/2} = g_{\mathrm{d}}^n \delta_{t.} u^n.
\tag{4.9b}
$$

Here, $\psi_{\mathrm{d}}^{n-1/2}$ is treated as an independent time series updated at each time step, defined on a staggered grid. This defines a three-step scheme, where g_{d}^n can be computed analytically from (4.6) as:

$$\bar{g}_{\mathrm{d}}^n = \begin{cases} \sqrt{2\gamma} u^n & : \; \varepsilon = 0 \\ \dfrac{\gamma \left(u^n\right)^3}{\sqrt{\gamma \left(u^n\right)^4 / 2 + \varepsilon}} & \text{otherwise} \end{cases} \tag{4.10}$$

where the $\bar{\cdot}$ indicates that the gradient has the analytic form (this notation will turn useful later on). The scheme is consistent and second-order accurate, as all operators are centred. A discrete energy balance is obtained by left-multiplying equation (4.9a) by $\delta_{t\cdot} u^n$:

$$\left(\delta_{t\cdot} u^n\right) \left(\delta_{tt} u^n\right) = -\omega_0^2 \left(\delta_{t\cdot} u^n\right) u^n - \left(\mu_{t+} \psi_{\mathrm{d}}^{n-1/2}\right) \left(\delta_{t\cdot} u_{\mathrm{d}}^n\right) g^n. \tag{4.11}$$

By substituting (4.9b) and using the usual discrete identities, one gets:

$$\delta_{t+}\mathfrak{h}^{n-1/2} = 0, \qquad \mathfrak{h}^{n-1/2} \triangleq \frac{\left(\delta_{t-} u^n\right)^2}{2} + \frac{\omega_0^2 \, u^n \, e_{t-} u^n}{2} + \frac{\left(\psi_{\mathrm{d}}^{n-1/2}\right)^2}{2}, \tag{4.12}$$

which has the dimension of energy scaled by the mass. Due to the quadratisation, the discrete nonlinear potential remains positive, and ensuring the positivity of the linear potential leads to the stability condition (3.20). Expanding out the operators in (4.9) and substituting the second equation into the first yields:

$$\left[\left(\frac{k g_{\mathrm{d}}^n}{2}\right)^2 + 1\right] u^{n+1} = \left(2 - \omega_0^2 k^2\right) u^n + \left[\left(\frac{k g_{\mathrm{d}}^n}{2}\right)^2 - 1\right] u^{n-1} - k^2 \psi_{\mathrm{d}}^{n-1/2} g_{\mathrm{d}}^n, \tag{4.13}$$

which forms a linearly implicit update procedure. Scheme (4.9) forms the core of the IEQ/SAV approaches, which coincide in the lumped case. The scheme must be integrated with suitable initial conditions, which in this case may be simply set using the true solution (4.3).

It was shown that the scheme (4.9) is consistent and stable; however, since it is nonlinear, this does not directly imply convergence. A detailed convergence analysis is provided in [231], where the convergence rate is examined for various values of ε. The study shows that the scheme converges when $\varepsilon \neq 0$. Moreover, when the shift is selected near certain numerically determined optimal values, local variations in the convergence rate are observed, reaching up to twelfth-order accuracy. In contrast, the scheme fails to converge when $\varepsilon = 0$. Figure 4.1 presents a comparison between the numerical solution obtained using the quadratised scheme (4.9) and the exact solution (4.3). The bottom panel displays the
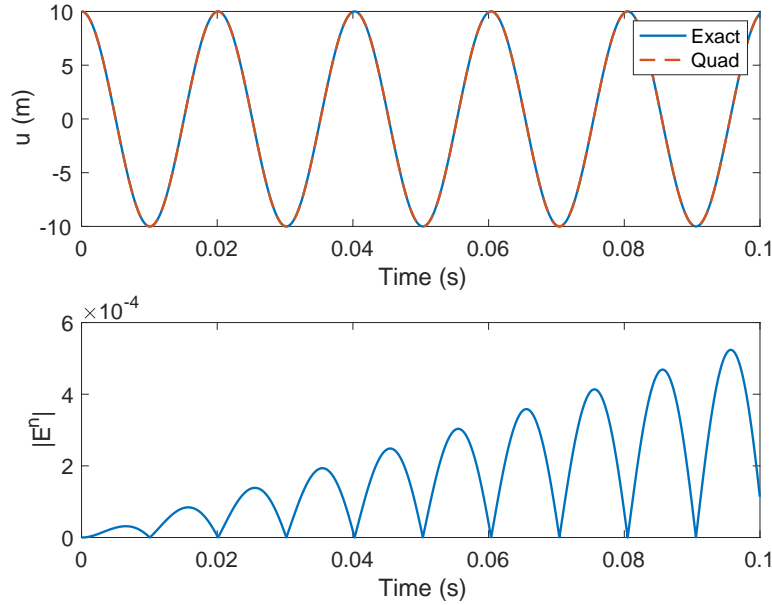
Fig. 4.1 Analytic and numerically computed solutions of the Duffing oscillator with parameters $\omega_0 = 300$ rad/s, $\gamma = 100$, $u_0 = 10$ m, and $v_0 = 0$ m/s. In the numerical scheme, $\varepsilon = \epsilon_m$, where ϵ_m denotes machine epsilon in double precision. In the top panel, the solid line represents the exact solution, while the dashed line shows the computed solution. The bottom panel illustrates the evolution of the global error over time.

evolution of the global error between the two solutions, highlighting discrepancies not visible in the top panel. The global error is defined as in (3.26), where now $\bar{u}(nk)$ represents the exact solution (4.3) at time nk. Although the error accumulates over time, testing reported in [231] ensures convergence.

It is important to note that the findings from [231] are empirical and specific to the Duffing equation. In particular, initial studies on PDEs suggest that simply adding a shift to the potential energy does not ensure convergence in all cases. An alternative method, based on constraining the auxiliary variable, will be presented later in this chapter.

4.2   Geometrically exact string

In Chapter 2, a model of linear string vibration, including the effects of stiffness following the Euler-Bernoulli theory of beams and frequency-dependent damping in the time domain, was presented. When the displacement increases, the deflection angle becomes large, and the linear model is no longer valid. In such cases, geometric nonlinearities arise, and an accurate model must account for the longitudinal displacement of the string along the x axis,
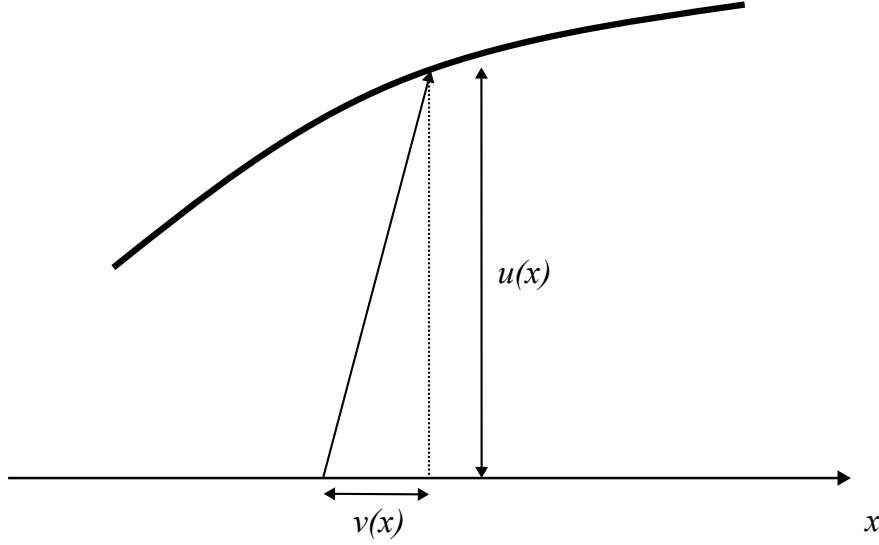
Fig. 4.2 Transversal and longitudinal displacements in a nonlinear string.

as illustrated in Figure 4.2. In [152, Chapter 14], Morse derives a model usually referred to as geometrically exact, taking into account motion in two polarisations in the transverse plane. It is common to restrict the motion to one polarisation only [24, Chapter 8]; in that case, the model, including loss and forcing in the transverse plane, may be written as [78]:

$$\left(\rho A \partial_t^2 - \mathcal{L}\right) u = \partial_x \partial_\zeta \phi_{\mathrm{G}} + \mathcal{F}_{\mathrm{e}}, \tag{4.14a}$$

$$\left(\rho A \partial_t^2 - \mathcal{L}_v\right) v = \partial_x \partial_\xi \phi_{\mathrm{G}}, \tag{4.14b}$$

where it was conveniently defined: $\zeta \triangleq \partial_x u$ and $\xi \triangleq \partial_x v$. Here, $u = u(x,t)$, $v = v(x,t)$: $[0, L] \times \mathbb{R}_0^+ \to \mathbb{R}$ represent the transverse and longitudinal displacements of the string, respectively. The linear transverse operator $\mathcal{L}$ was defined in equation (2.135), while the linear longitudinal operator $\mathcal{L}_v$ is given by:

$$\mathcal{L}_v = T_0 \partial_x^2 - 2\rho A \sigma_l \partial_t, \tag{4.15}$$

and includes a frequency-independent loss term regulated by a constant σ_l. The quantity $\phi_{\mathrm{G}} = \phi_{\mathrm{G}}(\zeta, \xi) : \mathbb{R} \times \mathbb{R} \to \mathbb{R}_0^+$ is the nonlinear potential density due to large strains, and is given by:

$$\phi_{\mathrm{G}} = \frac{EA - T_0}{2} \left(\sqrt{(1+\xi)^2 + \zeta^2} - 1\right)^2. \tag{4.16}$$

Note that this form differs slightly from the one derived by Morse; however, the two are mathematically equivalent, and one can switch between them through some algebra [28]. The potential density is non-negative under $EA \geq T_0$, which is always true for musical strings.

4.2.1 Energy analysis

An energy balance is obtained by taking an inner product of equation (4.14a) with $\partial_t u$ and equation (4.14b) with $\partial_t v$ over the string length:

$$\rho A \left\langle \partial_t u, \partial_t^2 u \right\rangle = \left\langle \partial_t u, \mathcal{L}u \right\rangle + \left\langle \partial_t u, \partial_x \partial_\zeta \phi_{\mathrm{G}} \right\rangle + \left\langle \partial_t u, \mathcal{F}_{\mathrm{e}} \right\rangle, \tag{4.17}$$

$$\rho A \left\langle \partial_t v, \partial_t^2 v \right\rangle = \left\langle \partial_t v, \mathcal{L}_v v \right\rangle + \left\langle \partial_t v, \partial_x \partial_\xi \phi_{\mathrm{G}} \right\rangle. \tag{4.18}$$

Summing the two equations, applying integration by parts, and using the chain rule

$$\frac{\mathrm{d}}{\mathrm{d}t} \phi_{\mathrm{G}} = \partial_t \zeta \partial_\zeta \phi_{\mathrm{G}} + \partial_t \xi \partial_\xi \phi_{\mathrm{G}}, \tag{4.19}$$

leads to the energy balance:

$$\frac{\mathrm{d}}{\mathrm{d}t} H = B_u + B_v - 2\rho A \left(\sigma_0 \|\partial_t u\|^2 + \sigma_1 \|\partial_t \zeta\|^2 + \sigma_l \|\partial_t v\|^2 \right) + P. \tag{4.20}$$

The boundary terms are given by:

$$B_u \triangleq \left[B + \partial_t u \partial_\zeta \phi_{\mathrm{G}} \right] \Big|_{x=0}^{x=L}, \qquad B_v \triangleq \left[T_0 \xi \partial_t v + \partial_t v \partial_\xi \phi_{\mathrm{G}} \right] \Big|_{x=0}^{x=L}, \tag{4.21}$$

where B is the linear boundary term obtained in (2.133). The total energy is expressed as:

$$H = \frac{\rho A}{2} \left(\|\partial_t u\|^2 + \|\partial_t v\|^2 \right) + \frac{T_0}{2} \left(\|\zeta\|^2 + \|\xi\|^2 \right) + \frac{EI_0}{2} \|\partial_x^2 u\|^2 + \Phi_{\mathrm{G}}, \tag{4.22}$$

where it was defined the total nonlinear potential energy as:

$$\Phi_{\mathrm{G}} \triangleq \left\| \sqrt{\phi_{\mathrm{G}}} \right\|^2 + \frac{\varepsilon}{2}. \tag{4.23}$$

Under simply supported boundary conditions for the transverse component and fixed conditions for the longitudinal component, the boundary terms vanish, making the balance (4.20) passive in the unforced case. Additionally, the energy remains positive and well-defined due to the non-negativity of the nonlinear potential density. Thus, bounds on the transverse solution size, analogous to (2.81) and (2.111) may be derived, with analogous bounds on the longitudinal component v following, where the initial energy $H_0 = H(0)$ is now computed

from (4.22). As in the linear case, under simply supported boundary conditions, bounds on the solution, as well as its derivatives, may be derived. The formulation of the quadratised equations of motion in the spatially distributed setting will be postponed until after spatial discretisation, to highlight the differences between the IEQ and SAV approaches.

4.3 Morse-Ingard strings

In the case of moderate amplitude motion, simpler forms of the nonlinear string equations can be obtained through potential density approximations. To illustrate this, it is convenient to rewrite equations (4.14) in the form provided by Morse:

$$\rho A \partial_t^2 u = EA \partial_x^2 u - EI_0 \partial_x^4 u - 2\rho A (\sigma_0 - \sigma_1 \partial_x^2)\partial_t u - (EA - T_0)\partial_x \partial_\zeta \phi_G' + \mathcal{F}_e, \quad \text{(4.24a)}$$

$$\rho A \partial_t^2 v = EA \partial_x^2 v - 2\rho A \sigma_l \partial_t v - (EA - T_0)\partial_x \partial_\xi \phi_G', \quad \text{(4.24b)}$$

where:

$$\phi_G' = \sqrt{(1 + \xi)^2 + \zeta^2} - 1 - \xi. \quad \text{(4.25)}$$

Since the elongation is small, the potential density can be expanded in a Taylor series around $\zeta = \xi = 0$. Truncating the series to the fourth order yields:

$$\phi_G' \approx \frac{\zeta^2}{2} - \frac{\xi \zeta^2}{2} - \frac{\zeta^4}{8} + \frac{\zeta^2 \xi^2}{2}. \quad \text{(4.26)}$$

This form is the standard approximation provided by Morse in [152, Chapter 14], and sometimes called MI string. Bank employed only the third-order term: $-\xi\zeta^2/2$ while retaining only the second-order term $\zeta^2/2$ decouples the motion. It was shown [23] that both forms, by Morse and Bank, yield energy with an indefinite sign, exposing the system to stability issues.

4.3.1 Anand's form

Anand's form is obtained by truncating the last term in (4.26):

$$\phi_G' \approx \frac{\zeta^2}{2} - \frac{\xi \zeta^2}{2} - \frac{\zeta^4}{8}. \quad \text{(4.27)}$$

It is accurate up to the third order and possesses non-negative energy. Substituting expression (4.27) in place of ϕ'_{G} in equations (4.24) yields:

$$\left(\rho A \partial_t^2 - \mathcal{L}\right) u = \frac{EA - T_0}{2} \partial_x \left(\zeta^3 + 2\zeta\xi\right) + \mathcal{F}_{\mathrm{e}}, \tag{4.28a}$$

$$\rho A \partial_t^2 v = EA \partial_x^2 v - 2\rho A \sigma_l \partial_t v + \frac{EA - T_0}{2} \partial_x \zeta^2. \tag{4.28b}$$

This system has been used in various works; see Chapter 1 for a comprehensive list. An energy analysis demonstrating stability may be found in [23].

4.3.2 Transverse-only system

An additional approximation involves considering only the transverse component of the system by assuming $v(x,t) = 0$. While this simplification is not physically motivated, the resulting system is a useful test case for numerical methods. In this case, the potential density simplifies to:

$$\phi_{\mathrm{T}} \triangleq \frac{\zeta^2}{2} - \frac{\zeta^4}{8}, \tag{4.29}$$

and the governing equation becomes:

$$\left(\rho A \partial_t^2 - \mathcal{L}\right) u = \partial_x \left(\frac{EA - T_0}{2}\zeta^3\right) + \mathcal{F}_{\mathrm{e}}. \tag{4.30}$$

This system will be referred to as "System T" in the rest of this work.

An energy analysis under simply supported boundary conditions can be derived by means of (2.4c), yielding a passive balance identical to (2.136), where the energy takes the form:

$$H = \frac{\rho A}{2} \|\partial_t u\|^2 + \frac{T_0}{2} \|\zeta\|^2 + \frac{EI}{2} \|\partial_x^2 u\|^2 + \Phi_{\mathrm{T}}. \tag{4.31}$$

The total nonlinear potential energy takes the form:

$$\Phi_{\mathrm{T}} = \frac{EA - T_0}{8} \|\zeta^2\|^2 + \frac{\varepsilon}{2}. \tag{4.32}$$

Thus, the energy is non-negative (under the condition $EA \geq T_0$), and the solution may be bounded in terms of the initial energy.

4.4 Kirchhoff-Carrier string

Consider again Anand's form in equations (4.28). When $T_0/EA \ll 1$, the inertial term $\partial_t^2 v$ may be neglected. Then, assuming fixed boundary conditions for the longitudinal motion, the system can be reduced to a single equation by integrating (4.28b) over the string length, yielding:

$$\left(\rho A \partial_t^2 - \mathcal{L}\right) u = \partial_x \left(\frac{EA}{2L}\|\zeta\|^2 \zeta\right) + \mathcal{F}_{\mathrm{e}}. \tag{4.33}$$

The full derivation can be found in [5]. This model is commonly referred to as Kirchhoff-Carrier string and will be called "System K" from now on. It is simpler than all those considered above, System T included. Here, the nonlinearity is averaged over the string length and thus represented as a scalar quantity. This nonlinear component links the wave speed to the total string length, resulting in pitch glide effects. An energy analysis, under simply supported boundary conditions, yields again the balance (2.136), with energy

$$H = \frac{\rho A}{2}\|\partial_t u\|^2 + \frac{T_0}{2}\|\zeta\|^2 + \frac{EI}{2}\|\partial_x^2 u\|^2 + \Phi_{\mathrm{K}}, \tag{4.34}$$

where:

$$\Phi_{\mathrm{K}} = \frac{EA}{8L}\|\zeta\|^4 + \frac{\varepsilon}{2}. \tag{4.35}$$

Again, the solution may be bounded in terms of the initial energy.

4.4.1 A modal form

As seen in Chapter 2, linear and time-invariant systems can be described in the frequency domain, where the motion is decomposed into independent contributions from various modes, each associated with a specific modal shape and eigenfrequency. However, as noted in Chapter 1, when a nonlinear system is projected onto a modal basis, such as those from Chapter 2, the resulting equations are typically densely coupled, impacting simulation efficiency. Nevertheless, a modal expansion can still be attempted on System K by leveraging the spatial invariance of the Kirchhoff-Carrier nonlinearity and using the modes of a simply supported linear string. To this end, consider a separable solution of the form: $u = \boldsymbol{\chi}^{\mathsf{T}}(x)\mathbf{w}(t)$, where $\boldsymbol{\chi}$ represents the normalised modes, as in (2.122). Substituting this separable solution into equation (4.33), with point-wise forcing centered on x_i, and taking an inner product with another set of modes $\boldsymbol{\chi}$ yields:

$$\frac{\mathrm{d}^2\mathbf{w}}{\mathrm{d}t^2} = -\boldsymbol{\Omega}^2\mathbf{w} - \mathbf{C}\frac{\mathrm{d}\mathbf{w}}{\mathrm{d}t} + \frac{E}{2L\rho}\langle\mathbf{w}, \mathbf{S}\mathbf{w}\rangle\,\mathbf{S}\mathbf{w} + \boldsymbol{\chi}(x_i)\frac{F}{\rho A}, \tag{4.36}$$

where F is a time-dependent forcing term as seen in equation (2.137). Here, $\boldsymbol{\Omega}^2$ is the eigenfrequencies matrix (2.123), $\mathbf{C}$ a diagonal damping matrix, and $\mathbf{S}$ is a diagonal matrix with elements:

$$S_{m,m} = \left(\frac{m\pi}{L}\right)^2, \tag{4.37}$$

where m is the mode index. An energy analysis is now performed by left-multiplying equation (4.36) by $\rho A \frac{\mathrm{d}\mathbf{w}^{\mathsf{T}}}{\mathrm{d}t}$, leading to:

$$\frac{\mathrm{d}}{\mathrm{d}t}H = -\rho A \left\langle \frac{\mathrm{d}\mathbf{w}}{\mathrm{d}t}, \mathbf{C}\frac{\mathrm{d}\mathbf{w}}{\mathrm{d}t} \right\rangle + \left\langle \frac{\mathrm{d}\mathbf{w}}{\mathrm{d}t}, \boldsymbol{\chi}(x_i) \right\rangle F. \tag{4.38}$$

The energy has the form:

$$H = \frac{\rho A}{2} \left\langle \frac{\mathrm{d}\mathbf{w}}{\mathrm{d}t}, \frac{\mathrm{d}\mathbf{w}}{\mathrm{d}t} \right\rangle + \frac{T_0}{2} \left\langle \mathbf{w}, \mathbf{S}\mathbf{w} \right\rangle + \frac{EI_0}{2} \left\langle \mathbf{w}, \mathbf{S}^2\mathbf{w} \right\rangle + \tilde{\Phi}_{\mathrm{K}}, \tag{4.39}$$

where the modal nonlinear potential is defined as:

$$\tilde{\Phi}_{\mathrm{K}} \triangleq \frac{EA}{8L} \left\langle \mathbf{w}, \mathbf{S}\mathbf{w} \right\rangle^2 + \frac{\varepsilon}{2}. \tag{4.40}$$

In the absence of external forcing, the energy balance is passive, and the energy remains positive, allowing for a bound on the solution. Thus, the system is stable.

4.4.2 Double polarisation

System (4.33) may be extended to account for motion in double polarisation. To this end, the two functions u_1 and u_2 are defined, representing the string motion along the y and z axis, respectively. Then, the equation reads:

$$\begin{bmatrix} (\rho A \partial_t^2 - \mathcal{L}) & 0 \\ 0 & (\rho A \partial_t^2 - \mathcal{L}) \end{bmatrix} \begin{bmatrix} u_1 \\ u_2 \end{bmatrix} = \partial_x \left(\frac{EA}{2L} \left\| \begin{bmatrix} \zeta_1 \\ \zeta_2 \end{bmatrix} \right\|^2 \begin{bmatrix} \zeta_1 \\ \zeta_2 \end{bmatrix} \right) + \boldsymbol{\mathcal{F}}_{\mathrm{e}}, \tag{4.41}$$

where $\zeta_{1,2} = \partial_x u_{1,2}$, $\boldsymbol{\mathcal{F}}_{\mathrm{e}}$ is a two-component vector directing the force in the two polarisations, and the inner product for vectors of functions was defined in (2.72).

A modal representation can be used for the double polarization system (4.41) as well, adopting the linear, simply supported modes for each polarization. Both functions can be written as $u_1 = \boldsymbol{\chi}^{\mathsf{T}}\mathbf{w}_1$ and $u_2 = \boldsymbol{\chi}^{\mathsf{T}}\mathbf{w}_2$, where $\mathbf{w}_1$ and $\mathbf{w}_2$ are two independent sets of functions describing the time evolution of motion in the modal domain for both polarizations.

Performing a modal expansion, with point-wise forcing, yields:

$$\frac{\mathrm{d}^2}{\mathrm{d}t^2} \begin{bmatrix} \mathbf{w}_1 \\ \mathbf{w}_2 \end{bmatrix} = - \begin{bmatrix} \mathbf{\Omega} & \mathbf{0} \\ \mathbf{0} & \mathbf{\Omega} \end{bmatrix} \begin{bmatrix} \mathbf{w}_1 \\ \mathbf{w}_2 \end{bmatrix} - \begin{bmatrix} \mathbf{C} & \mathbf{0} \\ \mathbf{0} & \mathbf{C} \end{bmatrix} \frac{\mathrm{d}}{\mathrm{d}t} \begin{bmatrix} \mathbf{w}_1 \\ \mathbf{w}_2 \end{bmatrix}$$
$$+ \frac{E}{2L\rho} [\mathbf{w}_1^{\mathsf{T}}, \mathbf{w}_2^{\mathsf{T}}] \begin{bmatrix} \mathbf{S} & \mathbf{0} \\ \mathbf{0} & \mathbf{S} \end{bmatrix} \begin{bmatrix} \mathbf{w}_1 \\ \mathbf{w}_2 \end{bmatrix} \begin{bmatrix} \mathbf{S} & \mathbf{0} \\ \mathbf{0} & \mathbf{S} \end{bmatrix} \begin{bmatrix} \mathbf{w}_1 \\ \mathbf{w}_2 \end{bmatrix} + \begin{bmatrix} F_1 \boldsymbol{\chi}(x_i) \\ F_2 \boldsymbol{\chi}(x_i) \end{bmatrix} \frac{1}{\rho A}, \tag{4.42}$$

where F_1, F_2 are time functions regulating the amount of force in both polarisations. The stability of both systems (4.41) and (4.42) may be confirmed through energy analysis.

4.5 Simulation of nonlinear transverse string vibration

The previous paragraphs introduced two models for nonlinear, transverse string vibration: System T (4.30) and System K (4.33). The literature presents two second-order accurate, conservative numerical schemes discretising these systems. The first, concerning System K, is described in [24, Chapter 8]. It involves an update relation requiring the inversion of a diagonal matrix with a rank-one perturbation, which can be solved efficiently using the Sherman-Morrison formula [189]. The second scheme, solving to System T, is detailed in [23] and results in a linearly implicit method that requires the inversion of a sparse, state-dependent matrix at each time step. However, both schemes are model-specific, meaning they had to be individually designed for each problem. In contrast, quadratised schemes offer a unified discretization approach, allowing for a highly efficient update process across different systems. Hence, it is interesting to explore the use of quadratised schemes to develop a general numerical framework for nonlinear transverse string vibration and compare their performance with existing reliable schemes. Note that this paragraph also serves as an introduction to the SAV quadratisation technique as applied to spatially distributed systems. The results presented here also apply to other types of nonlinearities, as will be demonstrated later.

First, the models may be expressed in a generic form:

$$(\rho A \partial_t^2 - \mathcal{L})u = \mathcal{F}_* + \mathcal{F}_{\mathrm{e}}, \tag{4.43}$$

where here $\mathcal{F}_* = \mathcal{F}_*(\zeta)$ is a force density representing the conservative nonlinear contribution. When $\mathcal{F}_*$ takes one of the following forms:

$$\mathcal{F}_{\mathrm{K}} = \partial_x \left(\frac{EA}{2L} \|\zeta\|^2 \zeta \right), \qquad \mathcal{F}_{\mathrm{T}} = \partial_x \left(\frac{EA - T_0}{2} \zeta^3 \right), \tag{4.44}$$

equation (4.43) corresponds to System K or System T, respectively.

A spatial discretisation of equation (4.43), with simply supported boundaries and point-wise forcing centred on x_i, can be performed using the operators outlined in Chapter 3. This results in a state vector $\mathbf{u}$ of dimension $N - 1$. It is useful to express the semi-discrete equation in terms of the nonlinear potential rather than the force density. By applying the chain rule and taking into account the transposition properties of the difference operator, the relation

$$\mathbf{D}^+\nabla_\zeta = -\nabla_\mathbf{u} \tag{4.45}$$

is obtained, leading to the following general form:

$$\left(\rho A\frac{\mathrm{d}^2}{\mathrm{d}t^2} - \mathfrak{L}\right)\mathbf{u} = \frac{1}{h}\mathbf{D}^+\nabla_\zeta\Phi_* + \mathbf{j}^{(x_i)}F, \tag{4.46}$$

where the discretised version of ζ, of size N, is given by: $\boldsymbol{\zeta} = \mathbf{D}^-\mathbf{u}$, and the gradient with respect to the vector $\boldsymbol{\zeta}$ is defined as:

$$\nabla_\zeta = [\partial_{\zeta_1}, \ldots, \partial_{\zeta_N}]. \tag{4.47}$$

The approximation of the linear operator, $\mathfrak{L}$, follows from equation (3.96), and Φ_* is a suitable spatial discretisation of the nonlinear potentials Φ_K, Φ_T. In particular, possible approximations of (4.35) and (4.32) are:

$$\Phi_\mathrm{K} = \frac{EAh^2}{8L}(\boldsymbol{\zeta}^\intercal\boldsymbol{\zeta})^2 + \frac{\varepsilon}{2} \tag{4.48a}$$

$$\Phi_\mathrm{T} = \frac{(EA - T_0)h}{8}(\boldsymbol{\zeta}^2)^\intercal\boldsymbol{\zeta}^2 + \frac{\varepsilon}{2}, \tag{4.48b}$$

where, in the latter equation, the power operator indicates element-wise raising.

A semi-discrete energy balance is obtained by taking an inner product of equation (4.46) with $h\frac{\mathrm{d}\mathbf{u}}{\mathrm{d}t}$. Using the chain rule and the definitions of the difference operators, the following relation is obtained:

$$\frac{\mathrm{d}\Phi_*}{\mathrm{d}t} = (\nabla_\zeta\Phi_*)^\intercal\frac{\mathrm{d}\boldsymbol{\zeta}}{\mathrm{d}t} = (-\mathbf{D}^+\nabla_\zeta\Phi_*)^\intercal\frac{\mathrm{d}\mathbf{u}}{\mathrm{d}t}. \tag{4.49}$$

By applying this result and integrating by parts, the energy balance (3.91) is obtained, which remains passive under simply supported boundaries and no external forcing. The

semi-discrete energy is now given by:

$$\mathcal{H} = \frac{\rho A h}{2} \left\| \frac{\mathrm{d}\mathbf{u}}{\mathrm{d}t} \right\|^2 + \frac{T_0 h}{2} \|\boldsymbol{\zeta}\| + \frac{EI_0 h}{2} \|\mathbf{D}^2 \mathbf{u}\| + \Phi_*. \tag{4.50}$$

where the norms are taken over the entire vector length.

4.5.1 Potential quadratisation in a distributed system

It is now possible to introduce quadratisation in the distributed setting. There are two distinct strategies available. Using the IEQ approach, one applies quadratisation to the discrete potential density. For example, in the case of System T, this density may be written as:

$$\frac{EA - T_0}{8} \boldsymbol{\zeta}^4,$$

where, again, the power operator indicates element-wise raising. Since this quantity is represented as a vector, the corresponding auxiliary variable is also a vector. This yields a linearly implicit scheme, which requires the inversion of a state-dependent matrix at each time step. Although this approach improves upon solving a fully implicit method, it still impacts efficiency. Alternatively, quadratisation can be performed through the following transformation:

$$\psi_* \triangleq \sqrt{2\Phi_*}, \tag{4.51}$$

which here is well defined, given the non-negativity of both Φ_K and Φ_T. This approach introduces a scalar auxiliary variable ψ_*, which forms the basis of the SAV approach. This lumped variable significantly improves the efficiency of the numerical solution, as will be seen shortly. After the quadratisation (4.51), equation (4.46) can be expressed in terms of ψ_*:

$$\left(\rho A \frac{\mathrm{d}^2}{\mathrm{d}t^2} - \mathfrak{L} \right) \mathbf{u} = -\frac{1}{h} \psi_* \mathbf{g}_* + \mathbf{j}^{(x_i)} F; \tag{4.52}$$

where it was used:

$$\mathbf{D}^+ \nabla_\zeta \Phi_* = -\nabla_\mathbf{u} \Phi_* = -\psi_* \nabla_\mathbf{u} \psi_* \triangleq -\psi_* \mathbf{g}_*. \tag{4.53}$$

The chain rule gives:

$$\frac{\mathrm{d}\psi_*}{\mathrm{d}t} = \mathbf{g}_*^\intercal \frac{\mathrm{d}\mathbf{u}}{\mathrm{d}t}. \tag{4.54}$$

The energy balance is unchanged, while the expression for conserved energy becomes:

$$\mathcal{H} = \frac{\rho A h}{2} \left\| \frac{d\mathbf{u}}{dt} \right\|^2 + \frac{T_0 h}{2} \|\boldsymbol{\zeta}\| + \frac{E I_0 h}{2} \|\mathbf{D}^2 \mathbf{u}\| + \frac{\psi_*^2}{2}, \tag{4.55}$$

which is clearly non-negative.

This procedure may be applied to the modal scheme (4.36) too, through the quadratisation of the potential (4.40):

$$\tilde{\psi}_{\mathrm{K}} \triangleq \sqrt{2\tilde{\Phi}_{\mathrm{K}}}. \tag{4.56}$$

Then, equation (4.36) becomes:

$$\frac{d^2 \mathbf{w}}{dt^2} = -\boldsymbol{\Omega}^2 \mathbf{w} - \mathbf{C} \frac{d\mathbf{w}}{dt} - \tilde{\psi}_{\mathrm{K}} \tilde{\mathbf{g}}_{\mathrm{K}} + \boldsymbol{\chi}(x_i) \frac{F}{\rho A}, \quad \tilde{\mathbf{g}}_{\mathrm{K}} \triangleq \nabla_{\mathbf{w}} \tilde{\psi}_{\mathrm{K}}, \tag{4.57}$$

which is analogous to (4.52). A non-negative energy follows also in this case.

4.5.2   Time discretisation: SAV update

A possible time discretisation of system (4.52), based on the SAV method, is a vector version of (4.9) and is written:

$$\left(\rho A \delta_{tt} \mathbf{I} - \mathfrak{l} \right) \mathbf{u}^n = -\frac{1}{h} \mu_{t+} \psi_*^{n-1/2} \mathbf{g}_*^n + \mathbf{j}^{(x_i)} F^n, \tag{4.58a}$$

$$\delta_{t+} \psi_*^{n-1/2} = (\mathbf{g}_*^n)^\mathsf{T} \delta_{t\cdot} \mathbf{u}^n. \tag{4.58b}$$

The second equation discretises the chain rule (4.54) and serves as the update for the auxiliary variable. Here, $\mathfrak{l}$ is a suitable discretisation of the linear operator, which can be implemented as in equation (3.97). The energy balance remains the same as obtained in equation (3.99), and the discrete energy now takes the form:

$$\begin{aligned} \mathfrak{h}^{n-1/2} = \frac{\rho A h}{2} \left\langle \delta_{t-} \mathbf{u}^n, \left(\mathbf{I} - k\sigma_1 \mathbf{D}^2 \right) \delta_{t-} \mathbf{u}^n \right\rangle \\ + \frac{T_0 h}{2} \left\langle \boldsymbol{\zeta}^{n-1}, \boldsymbol{\zeta}^n \right\rangle + \frac{E I_0 h}{2} \left\langle \mathbf{D}^2 \mathbf{u}^{n-1}, \mathbf{D}^2 \mathbf{u}^n \right\rangle + \frac{\left(\psi_*^{n-1/2} \right)^2}{2}. \end{aligned} \tag{4.59}$$

Since the nonlinear component only adds a non-negative term to the linear energy (3.98), the stability condition is governed by the linear part and remains the same as given in equation (3.101).

An update equation for scheme (4.58) is obtained by expanding the operators and substituting the second equation into the first one, obtaining:

$$\mathbf{A}_*^n \mathbf{u}^{n+1} = \mathbf{b}^n, \tag{4.60a}$$

$$\mathbf{b}^n = \mathbf{B}_* \mathbf{u}^n + \mathbf{C}_* \mathbf{u}^{n-1} + \frac{k^2}{\rho Ah(1+\sigma_0 k)} \left(\frac{1}{4} \mathbf{g}_*^n \left(\mathbf{g}_*^n\right)^\mathsf{T} \mathbf{u}^{n-1} - \mathbf{g}_*^n \psi_*^{n-1/2} \right) + \mathbf{j}^{(x_i)} F^n. \tag{4.60b}$$

The matrices take the form:

$$\mathbf{A}_*^n = \mathbf{I} + \frac{k^2}{4\rho Ah(1+\sigma_0 k)} \mathbf{g}_*^n \left(\mathbf{g}_*^n\right)^\mathsf{T}, \tag{4.61a}$$

$$\mathbf{B}_* = \frac{1}{1+\sigma_0 k} \left[2\mathbf{I} + \left(\frac{T_0 k^2}{\rho A} + 2\sigma_1 k \right) \mathbf{D}^2 - \frac{EI_0 k^2}{\rho A} \mathbf{D}^4 \right], \tag{4.61b}$$

$$\mathbf{C}_* = \frac{1}{1+\sigma_0 k} \left[(\sigma_0 k - 1)\mathbf{I} - 2\sigma_1 k \mathbf{D}^2 \right]. \tag{4.61c}$$

System (4.60) is linearly implicit, as solving it requires inverting a full, state-dependent matrix at each time step. However, the update matrix $\mathbf{A}_*^n$ is in the form of the identity matrix plus a rank-one perturbation, and it may be inverted through the Sherman-Morrison formula [189, 28]. Thus, the following update form is obtained:

$$\mathbf{u}^{n+1} = \mathbf{b}^n - \frac{\frac{k^2}{4\rho Ah(1+\sigma_0 k)} \mathbf{g}_*^n \left[\left(\mathbf{g}_*^n\right)^\mathsf{T} \mathbf{b}^n \right]}{1 + \frac{k^2}{4\rho Ah(1+\sigma_0 k)} \left(\mathbf{g}_*^n\right)^\mathsf{T} \mathbf{g}_*^n}, \tag{4.62}$$

which is fully explicit, allowing for a significant reduction in computation time. Once (4.62) is solved for $\mathbf{u}^{n+1}$, $\psi_*^{n+1/2}$ can be computed via (4.58b) as:

$$\psi_*^{n+1/2} = \psi_*^{n-1/2} + \frac{\mathbf{g}_*^n}{2} \left(\mathbf{u}^{n+1} - \mathbf{u}^{n-1} \right). \tag{4.63}$$

Note that, although this result was derived starting from Systems T and K, the update (4.62) is entirely independent of the specific form of the nonlinearity $\mathbf{g}_*^n$. Consequently, this formulation can serve as a numerical solver for any model of transverse string vibration where the linear part is time-invariant. The only system-specific variation lies in the discrete nonlinear potential, which can be computed at each time step n as

$$\bar{\mathbf{g}}_*^n = \nabla_{\mathbf{u}} \Phi_*^n / \sqrt{2\Phi_*^n}, \tag{4.64}$$

where the bar indicates that the gradient is computed analytically.

For Systems K and T, the analytic gradients take the forms:

$$\bar{\mathbf{g}}_{\mathrm{K}}^n = \sqrt{\frac{EA}{L}} h \mathbf{D}^2 \mathbf{u}^n, \tag{4.65a}$$

$$\bar{\mathbf{g}}_{\mathrm{T}}^n = -\frac{(EA - T_0) h \mathbf{D}^+ \left(\boldsymbol{\zeta}^n\right)^3}{2\sqrt{\frac{EA - T_0}{4} \left[(\boldsymbol{\zeta}^n)^2\right]^{\mathsf{T}} (\boldsymbol{\zeta}^n)^2 + \varepsilon}}. \tag{4.65b}$$

Note that, for System K, the denominator simplifies when $\varepsilon = 0$, which also eliminates the risk of division by zero. On the other hand, the potential cannot be simplified for System T, and a nonzero ε must be used. The system needs to be initialised by setting appropriate initial conditions. One may set $u^0 = u(0)$, and a technique for retrieving a second-order accurate value for u^1, based on Taylor arguments, is detailed in Chapter 3. The auxiliary variable can be then initialised at time-step $n = 1/2$ with: $\psi^{1/2} = \sqrt{2\Phi(\mu_{t+}\mathbf{u}^0)}$.

The modal system (4.57) may be integrated in time analogously, writing:

$$\left(\delta_{tt}\mathbf{I} - \tilde{\mathfrak{l}}\right) \mathbf{w}^n = -\mu_{t\cdot}\tilde{\psi}_{\mathrm{K}}^{n-1/2} \tilde{\mathbf{g}}_{\mathrm{K}}^n + \frac{1}{\rho A} \boldsymbol{\chi}(x_i) F^n, \tag{4.66a}$$

$$\delta_{t+}\tilde{\psi}_{\mathrm{K}}^{n-1/2} = (\tilde{\mathbf{g}}_{\mathrm{K}}^n)^{\mathsf{T}} \delta_{t\cdot}\mathbf{w}^n, \tag{4.66b}$$

where:

$$\tilde{\mathfrak{l}} = -\boldsymbol{\Omega}^2 - \mathbf{C}\delta_{t\cdot}, \tag{4.67}$$

and $\mathbf{I}$ is the identity matrix of size $M \times M$. The modal gradient $\tilde{\bar{\mathbf{g}}}^n$ can be computed analytically by evaluating the potential (4.40) at time step n as: $\tilde{\bar{\mathbf{g}}}^n = \nabla_{\mathbf{w}}\tilde{\Phi}_{\mathrm{K}}^n / \sqrt{2\tilde{\Phi}_{\mathrm{K}}^n}$. An energy analysis is run by taking an inner product of (4.66a) by $\rho A(\delta_{t\cdot}\mathbf{w}^n)$ and yields the stability condition (3.45), setting a limit on the maximum number of modes M. Alternatively, the exact scheme in (3.36) can be used to integrate the linear part, eliminating the need for a stability condition and avoiding numerical dispersion issues. In this case, a limit on the number of modes may be set up to the hearing range. A scheme of the form (4.66) can be expanded to obtain an update equation entirely equivalent to (4.60).

The same procedure can be applied to simulate the double-polarisation strings in (4.41) and (4.42).

4.5.3   Numerical testing

System K

Figure 4.3a displays the time solution, the energy error and the spectrogram of system (4.58), with potential (4.65a). Here, the energy error must be defined so that the total energy takes
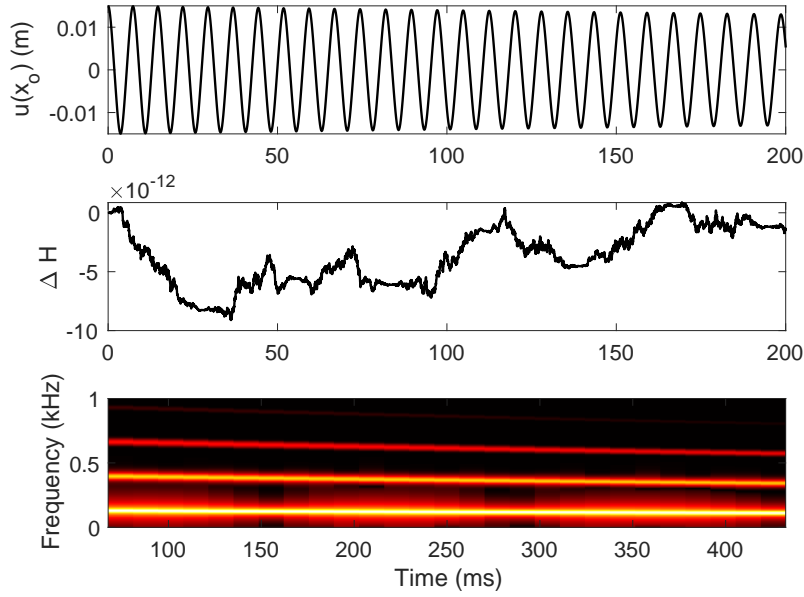
(a)
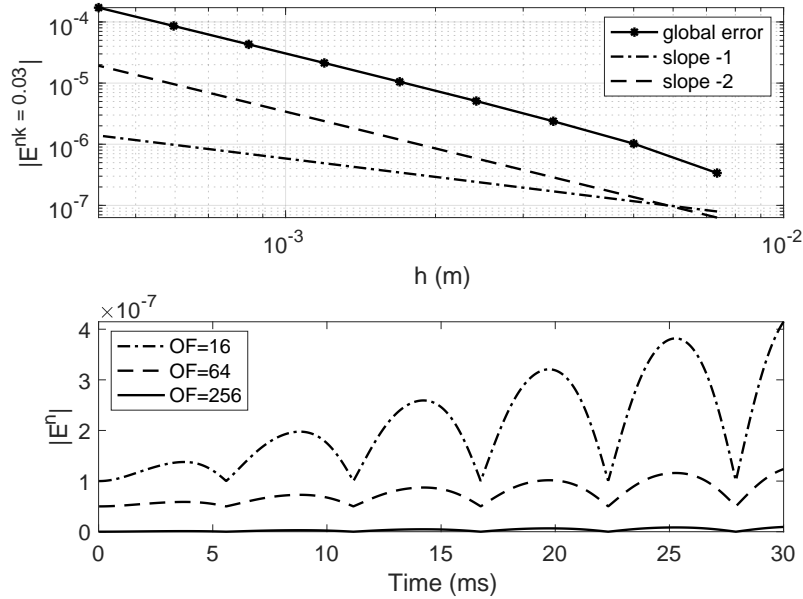
(b)

Fig. 4.3 (a) Waveform, energy error and spectrogram of system (4.58) with potential K. The algorithm is run at $OF = 10$.

(b) Convergence test for system K. The target solution is obtained at $OF = 512$. The SAV scheme is run at $OF = 2^a$, with $a = [0, 8]$ integer. Two reference lines are included for comparison: a dash-dotted line with a slope of -1 and a dashed line with a slope of -2. Physical parameters are: $\rho = 8 \times 10^3$ Kg/m^3, $T_0 = 75$ N, $A = 3.97 \times 10^{-7}$ m^2, $E = 174$ GPa, $\sigma_0 = 0.92$, $\sigma_1 = 2.86 \times 10^{-4}$. The output point $x_o = L/2$ is located at the midpoint of the string. The system is initialised in its first mode of vibration, with an amplitude of 1.5 cm.

into account the accumulated dissipated power; thus, it is expressed as:

$$\Delta H^{n+1/2} = 1 - (H_{\text{tot}}^{n+1/2})/(\mathfrak{h}^{1/2}), \qquad H_{\text{tot}}^{n+1/2} \triangleq \mathfrak{h}^{n-1/2} + \sum_{\nu=0}^{n} Q^{\nu} k. \qquad (4.68)$$

The second plot shows that the energy is indeed conserved, with an error within the order of machine accuracy. The different zooming times on the third panel highlight the pitch glide introduced by the nonlinear term, and the nonlinear behaviour is further emphasized by the appearance of two additional peaks in the spectrum.

A convergence test is performed similarly to that for the SHO in Chapter 3, and displayed in Figure 4.3b. Unlike the oscillator case, no analytical solution is available here. Instead, a target solution is computed using the integrator from [24, Chapter 8], with a high oversampling factor (OF). The OF is an integer number such that the final sample rate is OF $\times f_s$. Here, it was chosen $f_s = 44.1$ kHz. The global error is then calculated between the target solution and the solutions computed with system (4.58), run with an increasing OF. The first panel of Figure 4.3b represents the global error of scheme (4.58), computed at time $nk = 0.03$ s and plotted on a logarithmic scale with two reference lines of slope -1 and -2. The global error is defined in equation (3.87), where now $\bar{u}$ is the target solution, and $lh = x_o = L/2$. The second panel shows the evolution of the error over time for three solutions computed at different sample rates. An increasing offset of 5×10^{-8} is added to the plots for improved readability. Since the spatial sampling step is linked to the time step from the stability condition (3.101), the global error is plotted against h, which was chosen so that $h = 1.01\bar{h}$, following the rule of thumb #4 reported in [24, Chapter 8]. A comparison with the reference lines shows that the error decreases with order h^2, confirming that the scheme is convergent and second-order accurate. Similar results were obtained with the modal scheme (4.66). Note that, in this case, unlike the Duffing oscillator, convergence is achieved even with $\varepsilon = 0$.

System T

Figure 4.4a displays the time evolution, energy error and spectrogram of system (4.58), with potential (4.65b). This potential introduces stronger nonlinear behaviour, which is now clearly evident in the time domain plot. Energy is still conserved despite the error presenting more oscillations than in the previous case. The same convergence test used for System K is applied here. The target solution is computed using the integrator proposed in [23], run at a high OF. Results are displayed in Figure 4.4b. In the second panel, an increasing offset of 5×10^{-6} is added to the plots to improve readability. The time evolution of the error shows higher oscillations compared to System K. However, second-order accuracy is still evident in
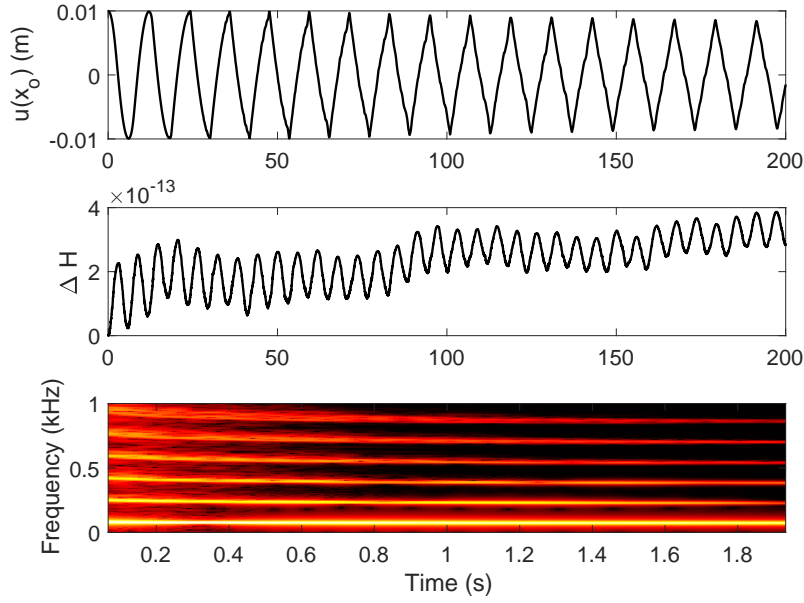
(a)
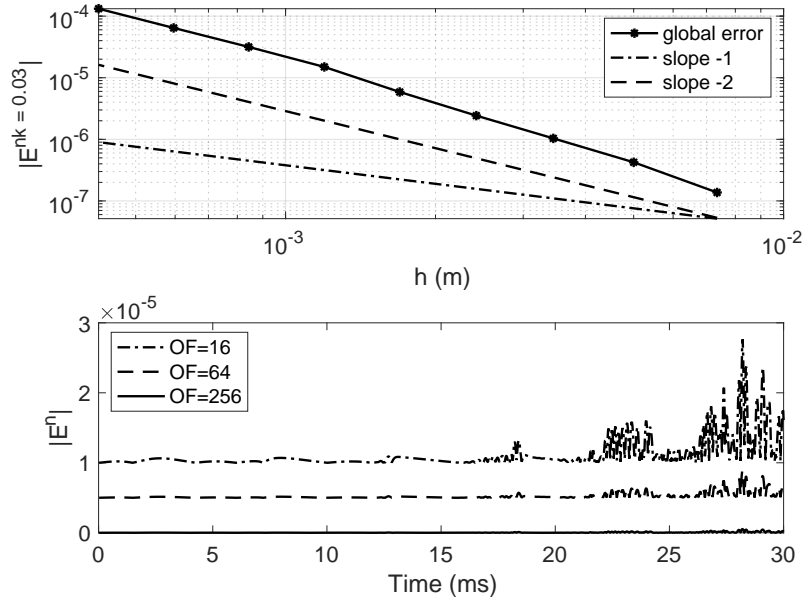
(b)

Fig. 4.4 (a) Waveform, energy error and spectrogram of system (4.58) with potential T. The algorithm is run at OF $= 10$.

(b) Convergence test for system T. The target solution and the SAV scheme are run at the same OFs listed in Figure 4.3b.

String parameters are as listed in Figure 4.3. The system is initialised in its first mode of vibration, with an amplitude of 1 cm.

the first panel, confirming the numerical convergence of the SAV algorithm. Note that an arbitrary potential shift $\varepsilon = 3 \times 10^{-5}$ was set in all tests.

During testing of System T, anomalous behaviour of the corresponding auxiliary variable, $\psi_{\mathrm{T}}^{n-1/2}$, was observed, which is reported in Figure 4.5a. In this test, System T was run with OF $= 10$ and initialized with two different amplitudes, using the same potential shift, now set as $\varepsilon = \epsilon_m$. It can be noted that $\mu_{t+}\psi_{\mathrm{T}}^{n-1/2}$ exhibits a sign flip and fails to decay to its theoretical minimum $\sqrt{\varepsilon}$ for the higher initial displacement, instead showing long-term drift. This leads to unnatural behaviour in longer simulations. The issue is significantly reduced when using higher oversampling factors. However, employing very high sample rates diminishes the advantage of the SAV approach, as it compromises real-time computation. Notably, this issue was not observed in System K.

4.5.4 Psi constraint

Problems similar to that observed in Figure 4.5a have been encountered in other studies [120, 216] when using SAV. Extensive research on this topic has been conducted, particularly in collision modelling. It is known that consistently using the analytic value $\bar{\mathbf{g}}_*^n$ can lead to anomalous behaviour in the auxiliary variable $\psi_*^{n-1/2}$, which, along with other problems, exhibits spurious sign flipping [216], causing the resulting force to be oriented incorrectly. In that study, which focuses on collisions, Van Walstijn et al. propose a solution by imposing the constraint $\psi_*^{n+1/2} \geq 0$. This results in a quadratic equation yielding a scaling factor for $\bar{\mathbf{g}}_*^n$. Here, in order to tackle the issue observed in Figure 4.5a, a similar method is developed, based on the constraint:

$$\mu_{t+}\psi_*^{n-1/2} \geq 0. \tag{4.69}$$

Indeed, from (4.58a), it can be noted that if $\mu_{t+}\psi_*^{n-1/2}$ remains positive, the sign of the force is determined solely by $\mathbf{g}_*^n$, ensuring the correct orientation of the nonlinear force density $\mathcal{F}_*$. By expanding the mean operator and considering equation (4.58b), the constraint becomes:

$$2\psi_*^{n-1/2} + \frac{1}{2}\left(\mathbf{g}_*^n\right)^{\mathsf{T}}\left(\mathbf{u}^{n+1} - \mathbf{u}^{n-1}\right) \geq 0. \tag{4.70}$$

Then, one may substitute the update form (4.62) in place of $\mathbf{u}^{n+1}$ and solve for $\mathbf{g}^n$, obtaining:

$$4\psi_*^{n-1/2} + \left(\mathbf{g}_*^n\right)^{\mathsf{T}}\left(\mathbf{B}\mathbf{u}^n + \mathbf{C}\mathbf{u}^{n-1} - \mathbf{u}^{n-1}\right) \geq 0. \tag{4.71}$$

Now, define

$$\mathbf{g}_*^n \triangleq \gamma\bar{\mathbf{g}}_*^n, \tag{4.72}$$
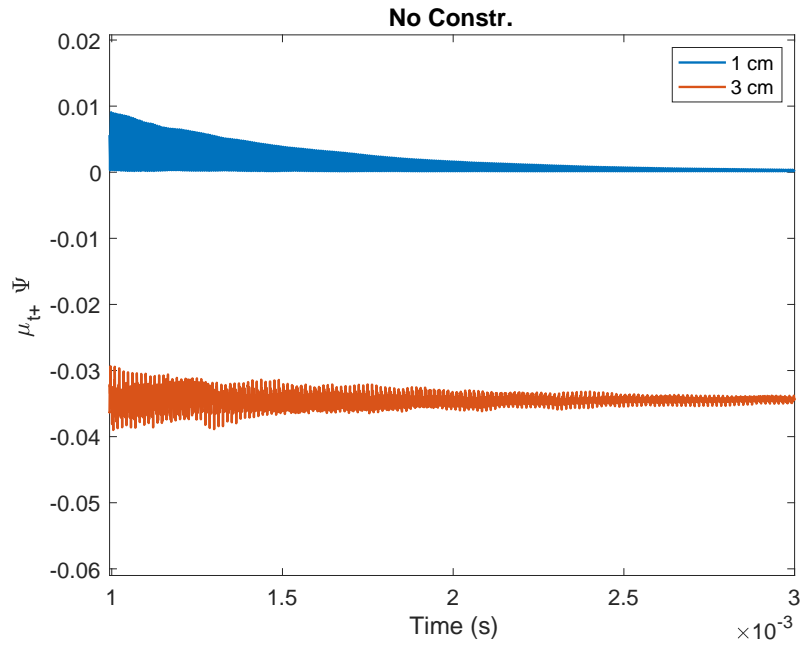
(a)
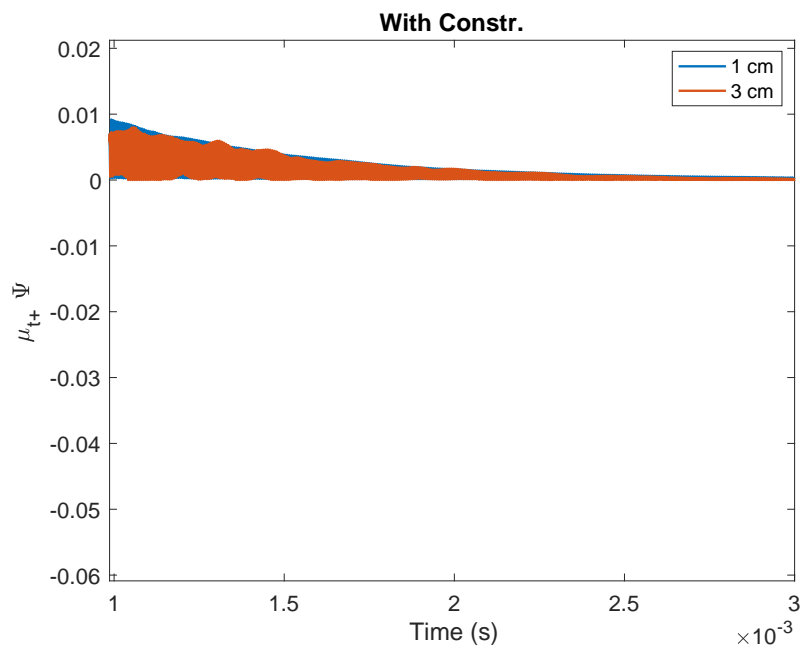
(b)

Fig. 4.5 (a) Decay of $\mu_{t+}\psi_{\mathrm{T}}^{n-1/2}$ over time for System T. The string was initialised with increasing amplitudes of 1 and 3 cm, and the scheme was run with OF $= 10$ and $\varepsilon = \epsilon_m$. The string physical values are as in Figure 4.3.

(b) Decay of $\mu_{t+}\psi_{\mathrm{T}}^{n-1/2}$ over time for System T with the constrained gradient (4.72).

(a)

(b)   (c)
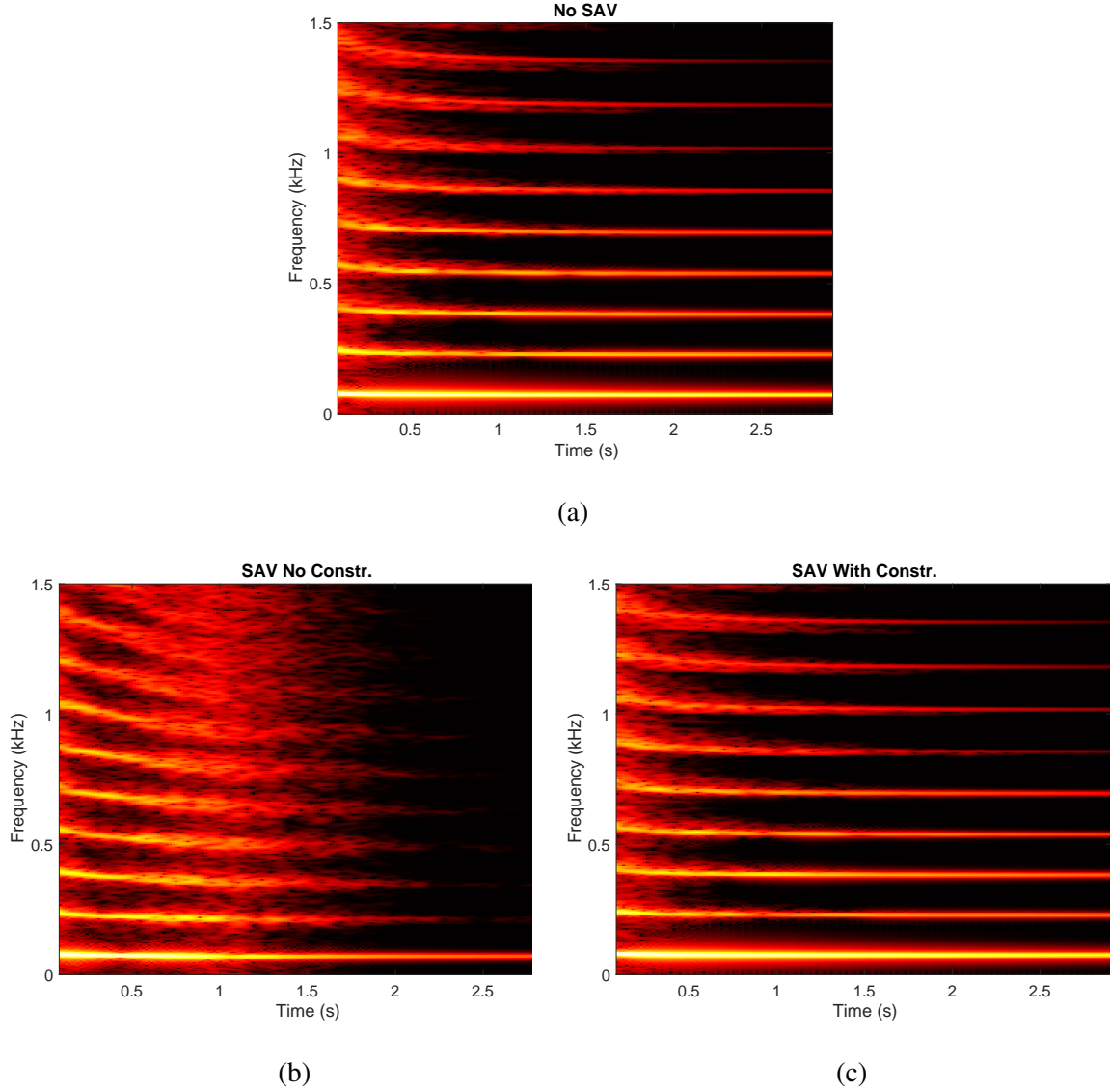
Fig. 4.6 Spectrograms resulting from the simulation of System T with external forcing, using (a) the integrator from [23], (b) SAV with the analytic gradient (4.65b) (c) SAV with the constrained gradient (4.72). The string physical parameters match those in Figure 4.3. The force amplitude and duration are set to $f_{\mathrm{amp}} = 5$ N and $\Delta = 2$ ms, respectively, with the input applied at $x_i = 0.8L$. The output point, $x_o = L/2$, is located at the string midpoint. The schemes are run with OF= 2, $\varepsilon = \epsilon_m$ and $h = 1.05\bar{h}$.

(a)

(b)
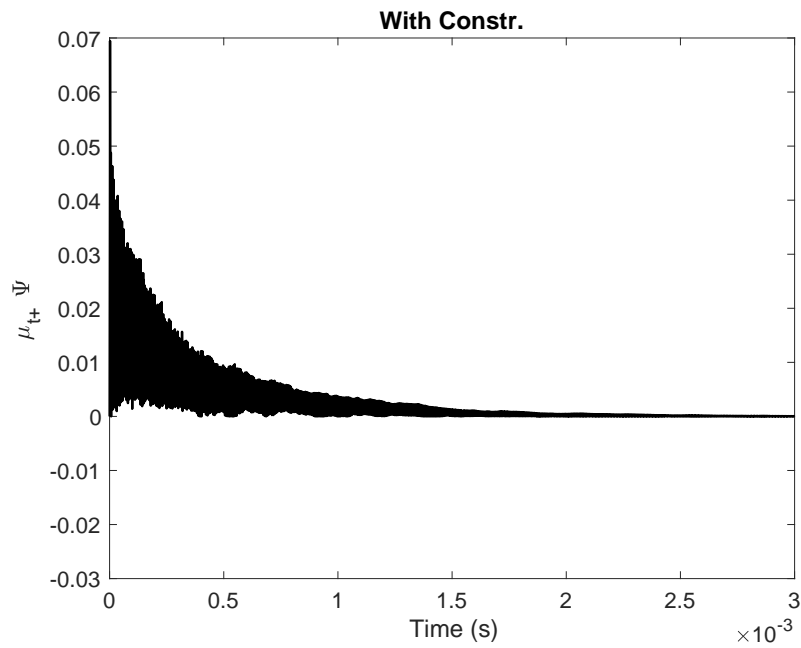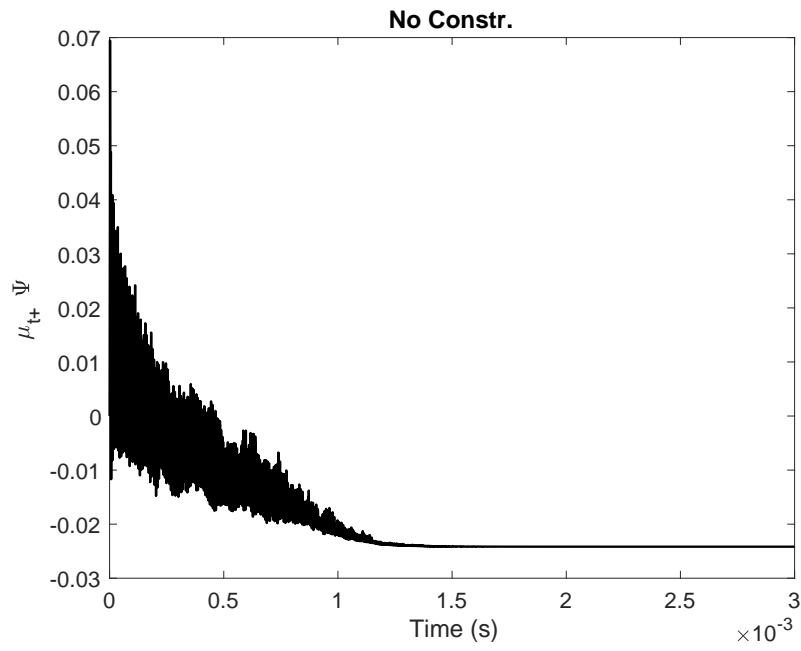
Fig. 4.7 Behaviour of $\mu_{t+}\psi_{\mathrm{T}}^{n-1/2}$ (a) without and (b) with the constraint applied, under external forcing. Simulation details match those described in Figure 4.6.

where γ is a scalar, and $\bar{\mathbf{g}}_*^n$ is the analytic gradient. Then, (4.71) becomes a first-order, scalar inequality in γ. The linearity of the expression guarantees a unique solution under the condition:

$$\gamma \geq -4\psi^{n-1/2}/\mathfrak{Z}, \qquad \mathfrak{Z} \triangleq (\bar{\mathbf{g}}_*^n)^\intercal \left(\mathbf{B}\mathbf{u}^n + \mathbf{C}\mathbf{u}^{n-1} - \mathbf{u}^{n-1} \right) \qquad (4.73)$$

Equation (4.73) yields a scalar multiplier for $\bar{\mathbf{g}}_*^n$, to be applied when (4.71) is not satisfied for $\mathbf{g}_*^n = \bar{\mathbf{g}}_*^n$. Thus, γ is set as:

$$\gamma = \begin{cases} -\dfrac{\vartheta 4\psi_*^{n-1/2}}{\mathfrak{Z}} & : \mathfrak{Z} \neq 0 \ \& \ \mathfrak{Z} < -4\psi_*^{n-1/2} \\ 1 & \text{otherwise,} \end{cases} \qquad (4.74)$$

where ϑ is a scalar multiplier that allows for shifting condition (4.73) away from the equality limit. Unless otherwise specified, it is set $\vartheta = 1$. Note that the second term in $\mathfrak{Z}$ corresponds to the linear string update minus the string state at time instant $n-1$, and it vanishes only when these two are equal.

Running the same test reported in Figure 4.5a on System T, using the constrained gradient form (4.72) yields the results illustrated in Figure 4.5b. It can be observed that the method effectively corrects the behaviour of the auxiliary variable.

As a second test, System T is excited by an external force and run with a lower OF to observe the effects of applying the constraint in a more typical simulation setting. The external force is pointwise, centred at x_i, with the time function modelled as a half raised cosine to simulate a pluck:

$$\mathcal{F}_e(x, t) = \delta(x - x_i)F(t), \qquad F(t) = \begin{cases} f_{\text{amp}} \sin^2\left(\frac{\pi(t-t_e)}{2\Delta} \right) & : t_e \leq t \leq t_e + \Delta \\ 0 & \text{otherwise} \end{cases} \qquad (4.75)$$

where here, f_{amp} is a maximum amplitude in N, t_e is the start time of the pulse in s, and Δ is the duration in s. The simulation is run first using the integrator from [23] as a reference, and then using SAV both with the analytic gradient form (4.65b) and the constrained form (4.72). The simulation results are presented as spectrograms, respectively, in Figures 4.6a, 4.6b and 4.6c. It is possible to observe that scalar auxiliary variable (SAV) with the analytic gradient fails to reproduce the behaviour from Figure 4.6a, while applying the constraint significantly improves the results. The behaviour of the auxiliary variable for System T, $\mu_{t+}\psi_{\text{T}}^{n-1/2}$, as shown in Figures 4.7a and 4.7b, reflects these results. Without the constraint, the mean of the auxiliary variable becomes negative, leading to an incorrect sign for the nonlinear force density. Conversely, Figure 4.7b demonstrates that the constraint effectively maintains a

positive sign for the mean of the auxiliary variable. Audio files for this test are available on the companion page.

Testing on the global error report similar results to those obtained without the constraint, indicating second-order convergence of the system with the constraint applied. Nevertheless, further evaluation is required to assess the performance of this technique in different scenarios. Particularly, two factors significantly influence the accuracy of the final result: the shift from the value $\bar{h}$ and the potential shift ε. Both were observed to play a major role in the final outcome but were chosen arbitrarily in these tests. Still, for System T, second-order convergence was observed across different values of ε and shifts from $\bar{h}$.

As mentioned earlier, a study by Zama et al. on the Duffing oscillator [231] demonstrated that adjustments to the potential shift can affect the algorithm's convergence properties; however, no constraint on the auxiliary variable was imposed in that case. Thus, further investigation of these aspects is left for future work.

4.6 Simulation of the geometrically exact string

A simulation of the GE string using IEQ [73, 78] and SAV [26, 77] was performed by Ducceschi and Bilbao. A summary is provided here. First, one may perform a spatial discretisation of equations (4.14), obtaining, with simply supported boundaries, two state vectors $\mathbf{u}$ and $\mathbf{v}$ of length $N - 1$. The semi-discrete transverse linear operator follows from equation (3.96), while an approximation of the longitudinal linear operator results in

$$\mathfrak{L}_v = T_0 \mathbf{D}^2 - 2\rho A \sigma_l \frac{\mathrm{d}}{\mathrm{d}t}. \tag{4.76}$$

The discrete version of ξ is given as the vector: $\boldsymbol{\xi} = \mathbf{D}^- \mathbf{v}$, of length N.

Again, there are two methods for quadratisation: in IEQ, one may quadratise the semi-discrete potential density

$$\frac{EA - T_0}{2} \left(\sqrt{(1 + \boldsymbol{\xi})^2 + \boldsymbol{\zeta}^2} - 1 \right)^2,$$

obtaining a vector auxiliary variable. This is the method employed in [73, 78]. Alternatively, in SAV, one can define a discrete form of the total nonlinear potential (4.23) as:

$$\Phi_{\mathrm{G}} = h \sum_{i=1}^{N} \frac{EA - T_0}{2} \left(\sqrt{(1 + \xi_i)^2 + \zeta_i^2} - 1 \right)^2. \tag{4.77}$$

Then, the semi-discretised equation may be written in vector form as:

$$
\begin{bmatrix} \rho A \frac{\mathrm{d}^2}{\mathrm{d}t^2}\mathbf{I} - \mathfrak{L} & \mathbf{0} \\ \mathbf{0} & \rho A \frac{\mathrm{d}^2}{\mathrm{d}t^2}\mathbf{I} - \mathfrak{L}_v \end{bmatrix} \begin{bmatrix} \mathbf{u} \\ \mathbf{v} \end{bmatrix} = \frac{1}{h} \begin{bmatrix} \mathbf{D}^+ \nabla_\zeta \Phi_{\mathrm{G}} \\ \mathbf{D}^+ \nabla_\xi \Phi_{\mathrm{G}} \end{bmatrix} + \begin{bmatrix} \mathbf{j}^{(x_i)} \\ \mathbf{0} \end{bmatrix} F,
\tag{4.78}
$$

where the nonlinear force was written in terms of the analytic potential gradients $\nabla_\zeta \Phi_{\mathrm{G}}$ and $\nabla_\xi \Phi_{\mathrm{G}}$. Quadratisation can now be performed by defining:

$$
\psi_{\mathrm{G}} \triangleq \sqrt{2\Phi_{\mathrm{G}}}.
\tag{4.79}
$$

Following the procedure outlined earlier, the quadratised system can be written as:

$$
\begin{bmatrix} \rho A \frac{\mathrm{d}^2}{\mathrm{d}t^2}\mathbf{I} - \mathfrak{L} & \mathbf{0} \\ \mathbf{0} & \rho A \frac{\mathrm{d}^2}{\mathrm{d}t^2}\mathbf{I} - \mathfrak{L}_v \end{bmatrix} \begin{bmatrix} \mathbf{u} \\ \mathbf{v} \end{bmatrix} = -\frac{1}{h}\psi_{\mathrm{G}} \begin{bmatrix} \mathbf{g}_{\mathrm{G}_u} \\ \mathbf{g}_{\mathrm{G}_v} \end{bmatrix} + \begin{bmatrix} \mathbf{j}^{(x_i)} \\ \mathbf{0} \end{bmatrix} F,
\tag{4.80}
$$

where the new gradients are defined as:

$$
\mathbf{g}_{\mathrm{G}_{u,v}} \triangleq -\mathbf{D}^+ \nabla_{\zeta,\xi}\psi = -\mathbf{D}^+ \nabla_{\zeta,\xi}\Phi_{\mathrm{G}}^n / \sqrt{2\Phi_{\mathrm{G}}^n + \varepsilon}.
\tag{4.81}
$$

Note that, unlike in the transverse system, the gradients are now given in terms of ζ and ξ: one may switch variables with (4.45). Application of the chain rule gives:

$$
\frac{\mathrm{d}\psi_{\mathrm{G}}}{\mathrm{d}t} = \begin{bmatrix} \mathbf{g}_{\mathrm{G}_u}^{\mathsf{T}}, & \mathbf{g}_{\mathrm{G}_v}^{\mathsf{T}} \end{bmatrix} \frac{\mathrm{d}}{\mathrm{d}t} \begin{bmatrix} \mathbf{u} \\ \mathbf{v} \end{bmatrix}.
\tag{4.82}
$$

An energy analysis, omitted here, may be obtained by taking an inner product with $h\frac{\mathrm{d}}{\mathrm{d}t}[\mathbf{u}^{\mathsf{T}}, \mathbf{v}^{\mathsf{T}}]^{\mathsf{T}}$, and yields a result analogous to that obtained for the transverse system.

Time integration can be performed with the SAV procedure, analogously to the transverse system. The time-stepping algorithm is now expressed as:

$$
\begin{bmatrix} \rho A \delta_{tt}\mathbf{I} - \mathfrak{l} & \mathbf{0} \\ \mathbf{0} & \rho A \delta_{tt}\mathbf{I} - \mathfrak{l}_v \end{bmatrix} \begin{bmatrix} \mathbf{u}^n \\ \mathbf{v}^n \end{bmatrix} = -\frac{1}{h}\mu_{t+}\psi_{\mathrm{G}}^{n-1/2} \begin{bmatrix} \mathbf{g}_{\mathrm{G}_u}^n \\ \mathbf{g}_{\mathrm{G}_v}^n \end{bmatrix} + \begin{bmatrix} \mathbf{j}^{(x_i)} \\ \mathbf{0} \end{bmatrix} F^n,
\tag{4.83a}
$$

$$
\delta_{t+}\psi_{\mathrm{G}}^{n-1/2} = \begin{bmatrix} \mathbf{g}_{\mathrm{G}_u}^{\mathsf{T}}, & \mathbf{g}_{\mathrm{G}_v}^{\mathsf{T}} \end{bmatrix} \delta_{t\cdot} \begin{bmatrix} \mathbf{u}^n \\ \mathbf{v}^n \end{bmatrix},
\tag{4.83b}
$$

where $\mathfrak{l}_v = T_0 \mathbf{D}^2 - 2\rho A \sigma_l \delta_{t\cdot}$. This defines a three-step scheme equivalent to (4.58). Expanding the operators allows for an efficient, explicit update by applying the Sherman-Morrison formula.

The energy analysis is run by taking an inner product with $h\delta_{t\cdot}\left[(\mathbf{u}^n)^\mathsf{T}, (\mathbf{v}^n)^\mathsf{T}\right]^\mathsf{T}$. As before, a passive energy balance is achieved in the unforced case, and the nonlinear component adds only a non-negative term to the total energy. Thus, a stability condition can be derived by examining the linear part alone, resulting in equation (3.101). However, as noted in [73, 77], applying this condition leads to aliasing issues due to the significant difference in wave speed between longitudinal and transverse motion. Instead, one can use $h = \sqrt{E/\rho k}$, the CFL condition associated with longitudinal motion, which is much less restrictive than the natural limit for transverse waves. This impacts the choice of the sample rate, which must be significantly higher than typical audio rates, with OFs of at least 12. In [78], longitudinal motion is spatially discretized using a modal expansion to address this issue. However, low OFs in this approach result in a minimal number of longitudinal modes that can be represented.

The behaviour of $\mu_{t+}\psi_\mathrm{G}^{n-1/2}$ in this system has not been analyzed, and the effects of applying the constraint have not been observed yet. It is possible that the high oversampling required for longitudinal motion may reduce the need for a constraint on the auxiliary variable. However, further investigation is necessary to confirm this.

Chapter 5

Collisions

Collisions play a fundamental role in musical acoustics. In the context of strings, collisions occur in various scenarios, such as in hammered strings (e.g., in pianos) or in the interaction between the string and the fretboard of guitars. As discussed in Chapter 1, two primary approaches exist for mathematically modelling collisions. The first models rigid contact, while the second, known as the penalty method, is based on Hertz's contact formulation. In this work, the second approach is employed, as it allows for the modelling of object compression by permitting a degree of mutual interpenetration. As in previous chapters, the discussion begins with a simple case study, a mass-barrier collision, and then extends to the spatially distributed case of string-fretboard interaction.

5.1   Collision of a mass against a rigid barrier

Though not directly related to a musical instrument, the mass-barrier collision provides a useful introductory test case for evaluating numerical schemes. The system can be represented by a SHO with an additional nonlinear forcing term. It is more practical to express the system in mass-stiffness form as:

$$m\frac{\mathrm{d}^2 u}{\mathrm{d}t^2} = -Ku - \frac{\mathrm{d}\phi_{\mathrm{b}}}{\mathrm{d}u}. \tag{5.1}$$

The collision potential is written:

$$\phi_{\mathrm{b}} = \frac{K_{\mathrm{b}}}{\alpha_{\mathrm{b}}+1}[b-u]_+^{\alpha_{\mathrm{b}}+1} + \frac{\varepsilon}{2}, \tag{5.2}$$

where $[\cdot]_+$ indicates the "positive part of", defined as $[x]_+ = (x+|x|)/2$. Here, $K_{\mathrm{b}} \geq 0$ is a constant representing the barrier's stiffness, $\alpha_{\mathrm{b}} \geq 1$ is the nonlinearity exponent, which controls the degree of interpenetration between the objects, and $b \leq 0$ is a constant offset
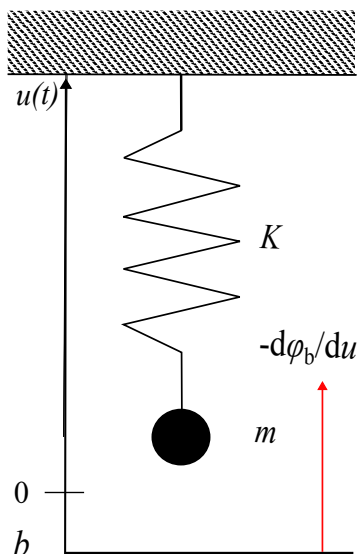
Fig. 5.1 Schematic of system (5.1) with potential (5.2). The red arrow indicates the direction of the collision force $-\frac{\mathrm{d}\phi_{\mathrm{b}}}{\mathrm{d}u}$.

representing the barrier position, which lies below the mass. The collision force is thus active only when the mass is in contact with the barrier and is otherwise zero. Thus, the potential is non-negative. A schematic of the system is depicted in Figure 5.1. The energy analysis is obtained by left-multiplying equation (5.1) by $m\frac{\mathrm{d}u}{\mathrm{d}t}$. Using the chain rule:

$$\frac{\mathrm{d}\phi_{\mathrm{b}}}{\mathrm{d}u} = \frac{\mathrm{d}\phi_{\mathrm{b}}/\mathrm{d}t}{\mathrm{d}u/\mathrm{d}t},\tag{5.3}$$

one gets:

$$\frac{\mathrm{d}}{\mathrm{d}t}H = 0, \qquad H = \frac{m}{2}\left(\frac{\mathrm{d}u}{\mathrm{d}t}\right)^2 + \frac{Ku^2}{2} + \phi_{\mathrm{b}}.\tag{5.4}$$

Thus, the energy balance is passive, and the solution may again be bounded in terms of the initial energy.

5.1.1   Potential quadratisation

Potential quadratisation can now be performed analogously to the Duffing oscillator, using an auxiliary variable ψ_{b}. The energy may be then written accordingly as:

$$H = \frac{m}{2}\left(\frac{\mathrm{d}u}{\mathrm{d}t}\right)^2 + \frac{Ku^2}{2} + \frac{\psi_{\mathrm{b}}^2}{2}\tag{5.5}$$

Next, using the definition of g from (2.18), equation (5.1) is re-written as:

$$\frac{\mathrm{d}^2 u}{\mathrm{d}t^2} = -Ku - \psi_\mathrm{b} g_\mathrm{b}, \qquad \frac{\mathrm{d}\psi_\mathrm{b}}{\mathrm{d}t} = g_\mathrm{b} \frac{\mathrm{d}u}{\mathrm{d}t}, \qquad g_\mathrm{b} = \frac{-K_\mathrm{b}[b - u]_+^{\alpha_\mathrm{b}}}{\sqrt{\frac{2K_\mathrm{b}}{\alpha_\mathrm{b}+1}[b - u]_+^{\alpha_\mathrm{b}+1} + \varepsilon}}. \tag{5.6}$$

Note that this equation has the same form of (4.6), the only difference being the form of g, and it can be integrated in time using the same method.

5.1.2   Simulation

As discussed in the introduction, developing energy-conserving schemes for collisions modelled using the penalty method has gained significant attention in recent years. For mass-barrier interactions, fully implicit approaches have been explored in [53, 34], though these will not be covered here. Recently, there has been growing interest in using linearly implicit or fully explicit methods by discretizing the quadratised equations through IEQ/SAV techniques. In particular, a discrete version of the quadratised scheme (5.6) is derived analogously to the Duffing oscillator case, as:

$$m\delta_{tt}u^n = -Ku^n - \mu_{t+}\psi_\mathrm{b}^{n-1/2}g_\mathrm{b}^n, \tag{5.7a}$$

$$\delta_{t+}\psi_\mathrm{b}^{n-1/2} = g_\mathrm{b}^n \delta_{t\cdot}u^n. \tag{5.7b}$$

As with the nonlinear oscillator, the discrete energy balance is conservative, with the discrete energy now given as:

$$\mathfrak{h}^{n-1/2} \triangleq \frac{m(\delta_{t-}u^n)^2}{2} + \frac{K\,u^n\,e_{t-}u^n}{2} + \frac{\left(\psi_\mathrm{b}^{n-1/2}\right)^2}{2}. \tag{5.8}$$

The scheme is second-order accurate, as all the operators are centred. Expanding the operators yields the explicit update:

$$\left[\left(\frac{kg_\mathrm{b}^n}{2m}\right)^2 + 1\right]u^{n+1} = \left(2 - \omega_0^2 k^2\right)u^n + \left[\left(\frac{kg_\mathrm{b}^n}{2m}\right)^2 - 1\right]u^{n-1} - \frac{k^2}{m}\psi_\mathrm{b}^{n-1/2}g_\mathrm{b}^n. \tag{5.9}$$

Testing conducted in [81] reports convergence of this numerical scheme, although convergence of the auxiliary variable was not examined.

5.1.3 Gradient calculation

As discussed in Chapter 4, significant effort has been devoted in recent years to optimizing the computation of the potential gradient in collision modelling. The analytic form can be computed at time-step n as:

$$\bar{g}_\text{b}^n = \begin{cases} -\sqrt{\dfrac{K_\text{b}(\alpha_\text{b}+1)}{2}[b-u^n]_+^{\alpha_\text{b}-1}} & : \ \varepsilon = 0 \\[4mm] -\dfrac{K_\text{b}[b-u^n]_+^{\alpha_\text{b}}}{\sqrt{\frac{2K_\text{b}}{\alpha_\text{b}+1}[b-u^n]_+^{\alpha_\text{b}+1}+\varepsilon}} & \text{otherwise.} \end{cases} \tag{5.10}$$

However, consistently applying this analytic expression leads to two main issues: (a) the auxiliary variable experiences sign flipping, resulting in incorrect force orientation, and (b) the contact energy remains non-zero after contact [216]. While the first problem has already been encountered in Chapter 4, the latter is specific to collisions, where the nonlinear force is not always active, unlike in the geometric nonlinearity case. In [81], Ducceschi et al. introduced conditional branching for gradient computation. This form is defined here $g_{\text{b},1}$ and expressed as:

$$g_{\text{b},1}^n = \begin{cases} g_{\text{b},*}^n & : \ (b-u^n) \geq 0 \ \& \ \frac{1}{4}g_{\text{b},*}^n(b-u^{n-1}) \geq \psi_\text{b}^{n-1/2} \\[2mm] 0 & : \ (b-u^n) \geq 0 \ \& \ \frac{1}{4}g_{\text{b},*}^n(b-u^{n-1}) < \psi_\text{b}^{n-1/2} \\[2mm] \dfrac{-2\psi_\text{b}^{n-1/2}}{\left(2-\omega_0^2 k^2\right)u^n - 2u^{n-1}} & : \ (b-u^n) < 0, \end{cases} \tag{5.11}$$

with

$$g_{\text{b},*}^n = \begin{cases} \bar{g}_\text{b}^n \ : \ \psi_\text{b}^{n-1/2} \geq 0 \\[2mm] -\bar{g}_\text{b}^n \ : \ \psi_\text{b}^{n-1/2} < 0. \end{cases}$$

This approach effectively address the second issue, eliminating spurious energy after contact. However, as noted in [216], the contact energy does not always have the correct sign. In that study, Van Walstijn et al. propose to enforce the constraint $\psi_\text{b}^{n+1/2} > 0$ to ensure proper force orientation during collisions. This leads to the quadratic constraint equation:

$$\frac{k^2}{4m}\psi_\text{b}^{n-1/2}\left(g_\text{b}^n\right)^2 + g_\text{b}^n \underbrace{\left[u^{n-1}-\left(1-\frac{1}{2}\omega_0^2 k^2\right)u\right]}_{a} - \psi_\text{b}^{n-1/2} \leq 0. \tag{5.12}$$

Following [216], solving for g_b^n yields the roots:

$$\dot{g}_{b,\pm}^n = 2 \frac{-a \pm \sqrt{a^2 + \frac{k^2}{m}\left(\psi_b^{n-1/2}\right)^2}}{\sqrt{\frac{k^2}{m}\varepsilon a^2 + \frac{k^4}{m^2}\left(\psi_b^{n-1/2}\right)^4}}, \tag{5.13}$$

(note that the dot does not indicate time differentiation here). The gradient, defined here $g_{b,2}$, is then set as follows:

$$g_{b,2}^n = \begin{cases} \max(\bar{g}_b^n, \dot{g}_{b,-}^n) & : (b - u^n) > 0 \\ \dot{g}_{b,-}^n & : (b - u^n) = 0 \ \& \ (b - u^{n-1}) > 0 \\ 0 & \text{otherwise.} \end{cases} \tag{5.14}$$

In this formulation, the first branch ensures the auxiliary variable remains positive, while the second branch sets the contact force to zero after the contact event. Note that Van Walstijn et al. [216] employ the exact integrator in equation (3.36); the constraint was here re-derived for the second-order accurate integrator.

Finally, the technique described in Chapter 4 is adapted here to handle collisions. The idea is to impose again the constraint $\mu_{t+}\psi_b^{n-1/2} \geq 0$. By expanding the mean operator and using (5.7a), equation (4.70) simplifies in the lumped case to:

$$4\psi_b^{n-1/2} + g_b^n\left(u^{n+1} - u^{n-1}\right) \geq 0. \tag{5.15}$$

where the form for g_b^n is still undefined. Substituting the expression for u^{n+1} (5.9) yields the inequality:

$$4\psi_b^{n-1/2} + g_b^n\left[\left(2 - \omega_0^2 k^2\right)u^n - 2u^{n-1}\right] = 4\psi_b^{n-1/2} - 2g_b^n a \geq 0, \tag{5.16}$$

where a is the quantity defined in equation (5.12). As in the distributed case discussed in Chapter 4, the term $\left(2 - \omega_0^2 k^2\right)u^n - 2u^{n-1} = -2a$ corresponds to the difference between the linear update and the mass state at time step $n - 1$, vanishing only when these two are equal. Finally, the gradient (defined here $g_{b,3}$) is set as:

$$g_{b,3}^n = \begin{cases} -\vartheta\dfrac{4\psi_b^{n-1/2}}{-2a} & : (b - u^n) > 0 \ \& \ 4\psi_b^{n-1/2} + \mathfrak{z} < 0 \ \& \ a \neq 0 \\[2ex] -\vartheta'\dfrac{4\psi_b^{n-1/2}}{-2a} & : (b - u^n) = 0 \ \& \ (b - u^{n-1}) > 0 \ \& \ a \neq 0 \\[2ex] \bar{g}_b^n & \text{otherwise} \end{cases} \tag{5.17}$$
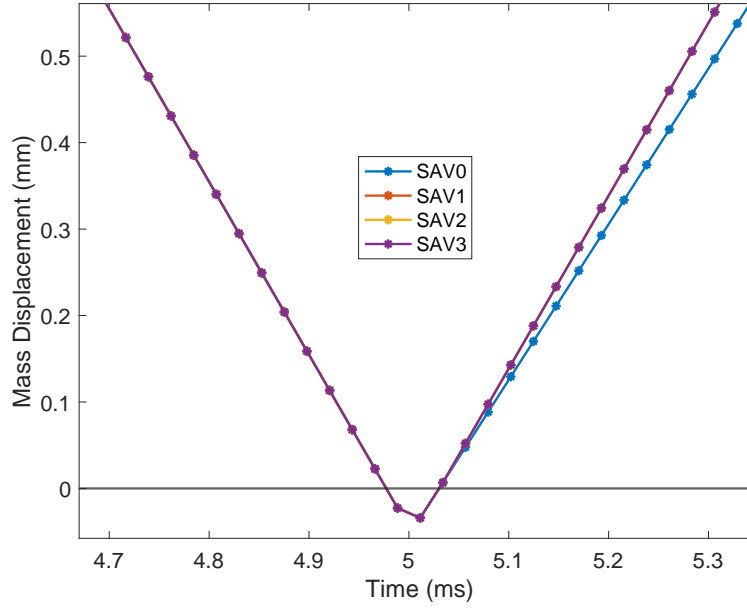
Fig. 5.2 Single collision event simulated using the scheme (5.9), with gradients (5.10), (5.11), (5.14) and (5.17), referred to as SAV0, SAV1, SAV2 and SAV3, respectively. The sample rate is $f_s = 44100$ Hz. Physical parameters are: $m = 0.01$ Kg, $K = 0$ rad/s, $K_{\mathrm{b}} = 10^9$, $\alpha_{\mathrm{b}} = 1.3$. The barrier is positioned at $b = 0$ and is represented by the black horizontal line. The mass is initialised with $u_0 = 0.01$m and $v_0 = -2$ m/s, and it is used $\varepsilon = 0$.

where it was defined:

$$\mathfrak{z} \triangleq \bar{g}_{\mathrm{b}}^n \left[\left(2 - \omega_0^2 k^2 \right) u^n - 2u^{n-1} \right] = -2\bar{g}_{\mathrm{b}}^n a, \tag{5.18}$$

and, as before, ϑ and ϑ' are scalar multipliers shifting the constraint from the equality. In the first branch, if equation (5.16) is not satisfied with $g_{\mathrm{b}}^n = \bar{g}_{\mathrm{b}}^n$, the gradient is adjusted to enforce the inequality (5.16). The second branch ensures that the contact force is set to zero immediately after the contact event. Otherwise, the analytic gradient is applied. Additionally, verifying that $a \neq 0$ in the first two branches serves as an extra safeguard against division by zero. Note that setting $\vartheta' \neq 0$ means the nonlinear energy is not reduced to zero immediately after contact but takes a few samples. Consequently, the natural choice would be to set $\vartheta' = 1$ in all cases. However, this approach leads to spurious oscillations of the auxiliary variable around the Nyquist frequency. It was observed that introducing a scalar to relax the condition helped mitigate these oscillations.
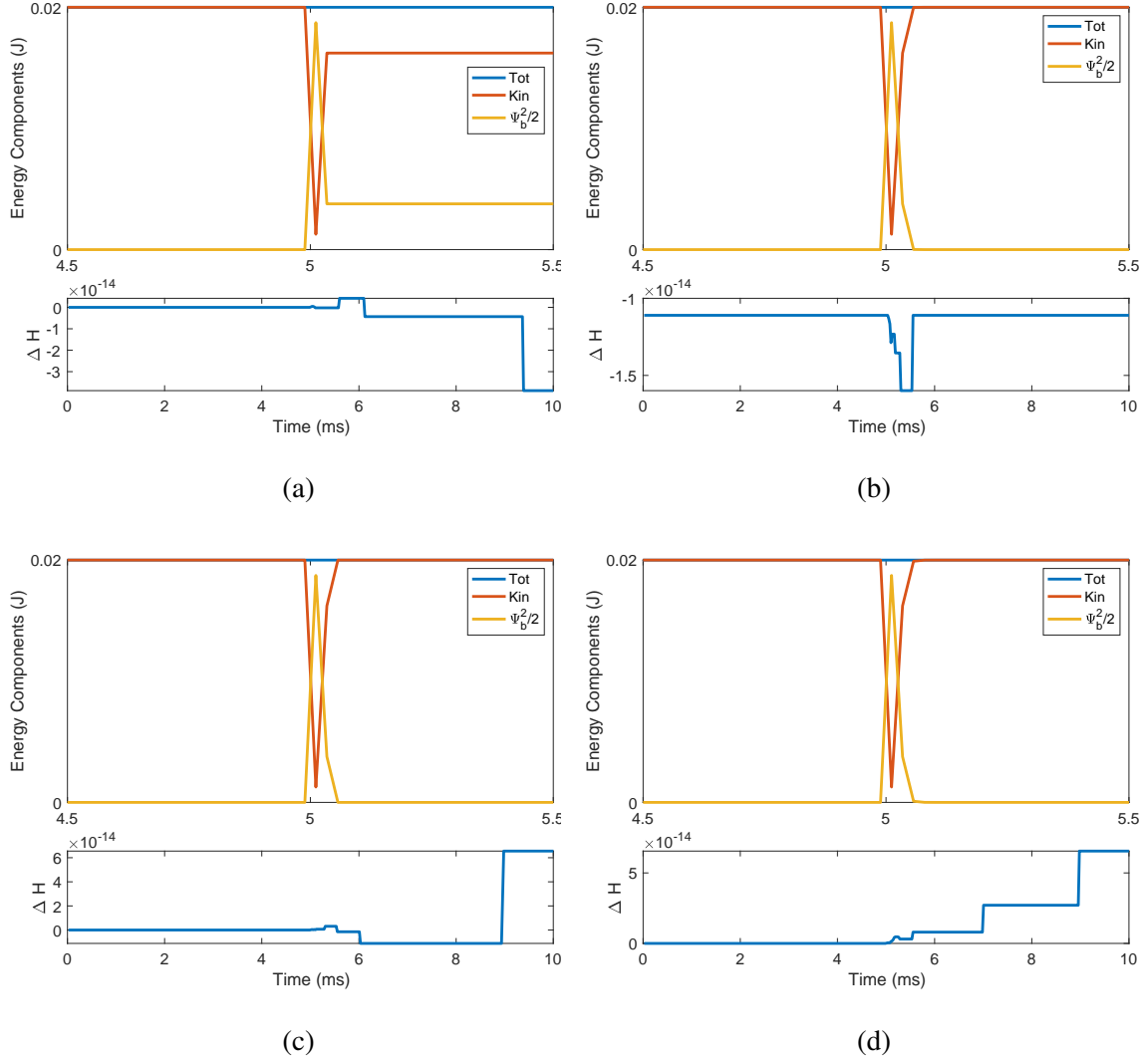
Fig. 5.3 Energy plots for the collision event shown in Figure 5.2 for (a) scheme SAV0, (b) scheme SAV1, (c) scheme SAV2, and (d) scheme SAV3. The top plots display the total energy $\mathfrak{h}^{n-1/2}$ in blue (from (5.8)), kinetic energy $(\delta_{t-}u^n)^2/2$ in red, and nonlinear potential energy $\left(\psi_{\mathrm{b}}^{n-1/2}\right)^2/2$ in yellow. Note that since $K=0$, the linear potential energy is zero. The bottom plots show the energy error, computed as $\Delta H = \mathfrak{h}^{n-1/2}/\mathfrak{h}^{1/2} - 1$.
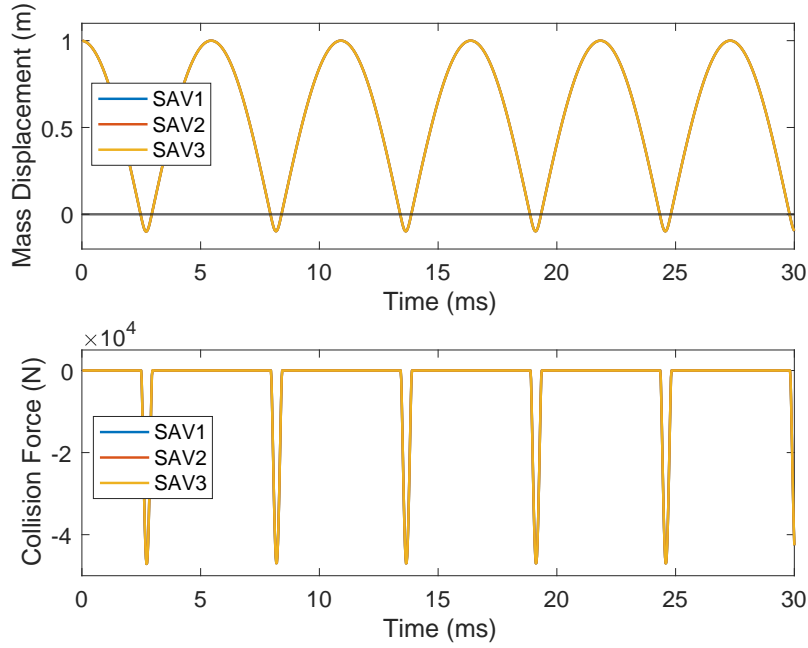
(a)
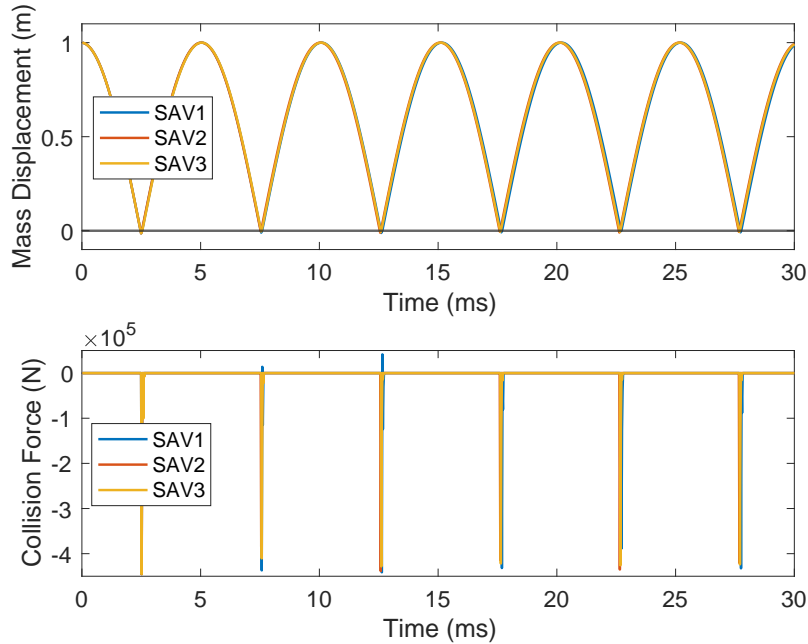
(b)

Fig. 5.4 Multi-collision event simulated using the scheme (5.9), with gradients (5.11), (5.14) and (5.17), referred to as SAV1, SAV2 and SAV3, respectively. The stiffness is set to $K = 3.95 \times 10^3$ N/m (giving a linear eigenfrequency of 100 Hz). The mass is initialised with $u_0 = 1$m and $v_0 = -2$ m/s. Other parameters match those in Figure 5.2. In (a), the barrier stiffness is $K_{\mathrm{b}} = 10^6$, and in (b), $K_{\mathrm{b}} = 10^9$. The top plots show the solution, while the bottom plots display (the negative of) the collision force, computed as $g_{\mathrm{b}}^n \mu_{t+} \psi^{n-1/2}$. The sample rate is $f_s = 44100$ Hz.
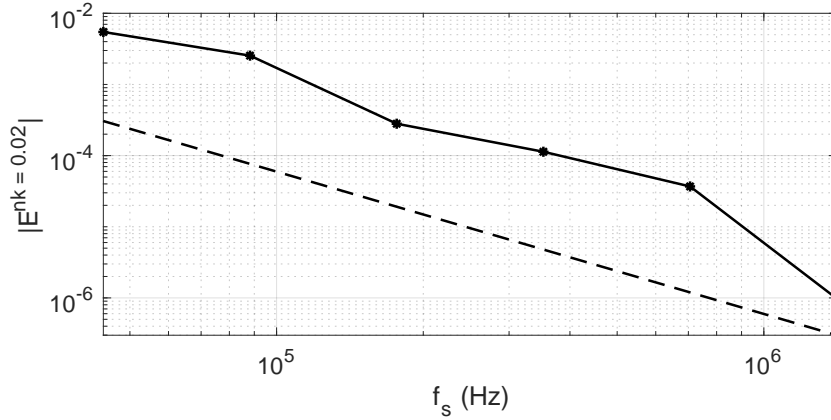
Fig. 5.5 Convergence test for scheme SAV3. The target solution is generated by running SAV2 with OF $= 512$. Scheme SAV3 is run with OF $= 2^a$, with $a = [0, 5]$ integer. The dashed line represents a slope of -2 for comparison.

5.1.4 Numerical testing

As a first experiment, the quadratised scheme (5.9) is tested using the four gradients (5.10), (5.11), (5.14) and (5.17), referred to as SAV0, SAV1, SAV2 and SAV3, respectively, in a single collision event. The results are presented in Figures 5.2 and 5.3. It is observed that the trajectories of SAV1-3 are nearly identical after the collision, while the analytic scheme SAV0 exhibits a noticeable deviation. This discrepancy is explained by the energy plots in Figure 5.3, which show the discrete energy components and the energy error for each system. In SAV0, the auxiliary variable does not return to zero after the collision, leading to a non-zero nonlinear potential energy even during non-collision periods. This is the anomalous behaviour reported by [74], [81] and [216]. Since the total numerical energy is conserved, as shown in the bottom plot, this numerical anomaly manifests as a reduction in kinetic energy after the collision, resulting in an altered trajectory. In contrast, SAV1-3 produce correct energy behaviour. In particular, the correction for g_b^n can be observed, taking effect in the sample immediately after the collision, at which point the energy components assume their correct values. In case of the gradient SAV3, it is set $\vartheta = 1$ and $\vartheta' = 0.5$ if $\frac{-4\psi_b^{n-1/2}}{-2a} < 0$, $\vartheta' = 1$ otherwise. As noted earlier, spurious high-frequency oscillations in the auxiliary variable were observed when $\vartheta' = 1$ was used consistently.

A second test, shown in Figure 5.4, involves a multiple collision event. Since previous testing has demonstrated that system SAV0 is unreliable, only the remaining systems, SAV1, SAV2, and SAV3, are considered here. Figure 5.4 presents the mass displacement and collision force for two different barrier stiffness values. The initial displacement was set

particularly high to test the schemes under more stressful conditions. It is observed that, with lower stiffness, all schemes produce comparable results. However, as stiffness increases, differences between the solutions emerge. Notably, Figure 5.4b shows that the SAV1 scheme produces incorrectly oriented forcing in some instances, as predicted by [216]. Figure 5.5 shows a convergence test for scheme SAV3, using the same parameters as those in Figure 5.4b. The reference solution was obtained by running scheme SAV2 with an OF of 512. A comparison with a line of slope -2 confirms that the scheme achieves second-order accuracy. The value $\varepsilon = \epsilon_m$ is used when computing equation (5.13) in all tests.

Additional investigation is needed to assess how well the constrained form SAV3 performs compared to SAV2 for different physical parameters. Moreover, further research is needed on the effects of the scaling coefficients ϑ and ϑ' and is left for future work.

5.2 Lumped collision: finger or hammer against a string

One common example of a collision in musical instruments is a stopping finger pressing the string. In this case, the interpenetration represents the compression of the finger during contact with the string. This concept has been applied in guitar models to simulate finger articulation [32], typically in conjunction with a fretboard model. The same model is often used to simulate hammer-string interactions [81], with the difference being that the hammer is usually provided with an initial velocity rather than an externally applied force. For simplicity, no geometric nonlinearity will be considered here, and the string will be treated as linear. The model can be expressed as:

$$\left(\rho A \partial_t^2 - \mathcal{L}\right) u = -\delta(x - x_{\mathrm{H}}) \partial_u \phi_{\mathrm{H}} \tag{5.19a}$$

$$m_{\mathrm{H}} \frac{\mathrm{d}^2 U_{\mathrm{H}}}{\mathrm{d}t^2} = -\partial_{U_{\mathrm{H}}} \phi_{\mathrm{H}} + F_{\mathrm{H}}, \tag{5.19b}$$

where external forces on the string are omitted. The second equation models the dynamics of the hammer (though the term "hammer" is used here, this model is completely analogous to that of a finger), where m_{H} is the hammer mass, U_{H} is a function representing its vertical displacement, and $F_{\mathrm{H}} = F_{\mathrm{H}}(t)$ is an externally supplied driving force, employed to keep a finger pressed against the string. Typically, this force is not applied to the hammer, which instead rebounds off the string. The hammer contact is modelled as lumped and located at a point x_{H} along the string. The potential $\phi_{\mathrm{H}} = \phi_{\mathrm{H}}(u, U_{\mathrm{H}})$ has the form:

$$\phi_{\mathrm{H}} = \frac{K_{\mathrm{H}}}{\alpha_{\mathrm{H}} + 1} [u(x_{\mathrm{H}}, t) - U_{\mathrm{H}}]_+^{\alpha_{\mathrm{H}} + 1}. \tag{5.20}$$

Consider the string to have simply supported boundaries. An energy balance can be obtained by taking the inner product of the first equation with $\partial_t u$, left-multiplying the second equation by $\frac{\mathrm{d}U_{\mathrm{H}}}{\mathrm{d}t}$ and summing. Using the chain rule, this yields:

$$\frac{\mathrm{d}}{\mathrm{d}t}H = -Q(t) + \frac{\mathrm{d}U_{\mathrm{H}}}{\mathrm{d}t}F_{\mathrm{H}}, \tag{5.21}$$

where Q is as defined in (2.134), and:

$$H = \frac{\rho A}{2}\|\partial_t u\|^2 + \frac{m_{\mathrm{H}}}{2}\left(\frac{\mathrm{d}U_{\mathrm{H}}}{\mathrm{d}t}\right)^2 + \frac{T_0}{2}\|\partial_x u\|^2 + \frac{EI_0}{2}\|\partial_x^2 u\|^2 + \phi_{\mathrm{H}}. \tag{5.22}$$

The energy now includes the kinetic term associated with the hammer and the lumped nonlinear potential. Without an external force applied, the system is passive.

5.2.1 Simulation

A simulation of system (5.19) will now be performed using a quadratised approach. First, a spatial discretisation of the potential (5.20) can be expressed as:

$$\Phi_{\mathrm{H}} = \frac{K_{\mathrm{H}}}{\alpha_{\mathrm{H}}+1}\left[\left(\mathbf{j}^{(x_{\mathrm{H}})}\right)^{\mathsf{T}}\mathbf{u} - U_{\mathrm{H}}\right]_+^{\alpha_{\mathrm{H}}+1}, \tag{5.23}$$

and a semi-discrete version of equation (5.19) can be written:

$$\left(\rho A\frac{\mathrm{d}^2}{\mathrm{d}t^2} - \mathfrak{L}\right)\mathbf{u} = -\frac{1}{h}\mathbf{j}^{(x_{\mathrm{H}})}\nabla_{\mathbf{u}}\Phi_{\mathrm{H}} \tag{5.24a}$$

$$m_{\mathrm{H}}\frac{\mathrm{d}^2 U_{\mathrm{H}}}{\mathrm{d}t^2} = -\partial_{U_{\mathrm{H}}}\Phi_{\mathrm{H}} + F_{\mathrm{H}}. \tag{5.24b}$$

Next, quadratisation is performed by defining:

$$\psi_{\mathrm{H}} \triangleq \sqrt{2\Phi_{\mathrm{H}}}, \tag{5.25}$$

and the quadratised system can now be written as:

$$\left(\rho A\frac{\mathrm{d}^2}{\mathrm{d}t^2} - \mathfrak{L}\right)\mathbf{u} = -\frac{1}{h}\psi_{\mathrm{H}}\mathbf{g}_{\mathrm{H}} \tag{5.26a}$$

$$m_{\mathrm{H}}\frac{\mathrm{d}^2 U_{\mathrm{H}}}{\mathrm{d}t^2} = \psi_{\mathrm{H}}g_{\mathrm{H}} + F_{\mathrm{H}}, \tag{5.26b}$$

where, following the definition in the final step of (4.53):

$$\mathbf{g}_{\mathrm{H}} = \nabla_{\mathbf{u}} \psi_{\mathrm{H}}, \qquad g_{\mathrm{H}} = \partial_{U_{\mathrm{H}}} \psi_{\mathrm{H}}. \tag{5.27}$$

The chain rule gives:

$$\frac{\mathrm{d}\psi_{\mathrm{H}}}{\mathrm{d}t} = \mathbf{g}_{\mathrm{H}}^{\mathsf{T}} \frac{\mathrm{d}\mathbf{u}}{\mathrm{d}t} + g_{\mathrm{H}} \frac{\mathrm{d}U_{\mathrm{H}}}{\mathrm{d}t}. \tag{5.28}$$

An energy analysis, omitted here, can be carried out by taking the inner product of the first equation with $h\frac{\mathrm{d}u}{\mathrm{d}t}$ and of the second equation with $\frac{\mathrm{d}U_{\mathrm{H}}}{\mathrm{d}t}$, and summing.

A time integrator based on SAV may now be written as:

$$(\rho A \delta_{tt} - \mathfrak{l}) \, \mathbf{u}^n = -\frac{1}{h} \psi_{\mathrm{H}}^{n-1/2} \mathbf{g}_{\mathrm{H}}^n \tag{5.29a}$$

$$m_{\mathrm{H}} \delta_{tt} U_{\mathrm{H}} = \psi_{\mathrm{H}}^{n-1/2} g_{\mathrm{H}}^n + F_{\mathrm{H}}^n, \tag{5.29b}$$

$$\delta_{t+} \psi_{\mathrm{H}}^{n-1/2} = (\mathbf{g}_{\mathrm{H}}^n)^{\mathsf{T}} \delta_{t\cdot} \mathbf{u}^n + g_{\mathrm{H}}^n \delta_{t\cdot} U_{\mathrm{H}}. \tag{5.29c}$$

The energy analysis takes an inner product of the first equation with $h\delta_{t\cdot} \mathbf{u}^n$ and the second by $\delta_{t\cdot} U_{\mathrm{H}}^n$. Summing yields the energy balance:

$$\delta_{t+} \mathfrak{h}^{n-\frac{1}{2}} = -Q^n + \delta_{t\cdot} U_{\mathrm{H}}^n F_{\mathrm{H}}^n, \tag{5.30}$$

where the loss term is as in equation (3.100). The discrete energy includes the hammer kinetic term and takes the form:

$$\begin{aligned}
\mathfrak{h}^{n-1/2} = {}& \frac{\rho A h}{2} \left\langle \delta_{t-} \mathbf{u}^n, \left(\mathbf{I} - k\sigma_1 \mathbf{D}^2 \right) \delta_{t-} \mathbf{u}^n \right\rangle + \frac{m_{\mathrm{H}}}{2} \left(\delta_{t-} U_{\mathrm{H}}^n \right)^2 \\
& + \frac{T_0 h}{2} \left\langle \mathbf{D}^- \mathbf{u}^{n-1}, \mathbf{D}^- \mathbf{u}^n \right\rangle + \frac{E I_0 h}{2} \left\langle \mathbf{D}^2 \mathbf{u}^{n-1}, \mathbf{D}^2 \mathbf{u}^n \right\rangle + \frac{\left(\psi_{\mathrm{H}}^{n-1/2} \right)^2}{2}.
\end{aligned} \tag{5.31}$$

Ensuring the positivity of the energy leads to the stability condition (3.101).

By expanding the operator and combining the two states into a single vector, the system can be expressed in matrix form as:

$$\begin{aligned}
\mathbf{A}^n \begin{bmatrix} \mathbf{u}^n \\ U_{\mathrm{H}}^n \end{bmatrix} = {}& \mathbf{B} \begin{bmatrix} \mathbf{u}^n \\ U_{\mathrm{H}}^n \end{bmatrix} + \mathbf{C} \begin{bmatrix} \mathbf{u}^{n-1} \\ U_{\mathrm{H}}^{n-1} \end{bmatrix} \\
& + \frac{1}{4} \mathbf{D} \begin{bmatrix} \mathbf{g}_{\mathrm{H}}^n \\ g_{\mathrm{H}}^n \end{bmatrix} \begin{bmatrix} \mathbf{g}_{\mathrm{H}}^n \\ g_{\mathrm{H}}^n \end{bmatrix}^{\mathsf{T}} \begin{bmatrix} \mathbf{u}^{n-1} \\ U_{\mathrm{H}}^{n-1} \end{bmatrix} - \mathbf{D} \begin{bmatrix} \mathbf{g}_{\mathrm{H}}^n \\ g_{\mathrm{H}}^n \end{bmatrix} \psi_{\mathrm{H}}^{n-1/2} + \begin{bmatrix} \mathbf{0} \\ \frac{k^2}{m_{\mathrm{H}}} \end{bmatrix} F_{\mathrm{H}}^n,
\end{aligned} \tag{5.32}$$

where the matrices take the following form:

$$\mathbf{A}^n = \begin{bmatrix} \mathbf{I} & 0 \\ 0 & 1 \end{bmatrix} + \frac{1}{4}\mathbf{D} \begin{bmatrix} \mathbf{g}_H^n \\ g_H^n \end{bmatrix} \begin{bmatrix} \mathbf{g}_H^n \\ g_H^n \end{bmatrix}^\intercal, \qquad \mathbf{B} = \begin{bmatrix} \mathbf{B}_* & 0 \\ 0 & 2 \end{bmatrix},$$

$$\mathbf{D} = \begin{bmatrix} \frac{k^2}{\rho A h(1+\sigma_0 k)}\mathbf{I} & 0 \\ 0 & \frac{k^2}{m_H} \end{bmatrix}, \qquad \mathbf{C} = \begin{bmatrix} \mathbf{C}_* & 0 \\ 0 & -1 \end{bmatrix}.$$

Here, $\mathbf{I}$ is the $(N-1) \times (N-1)$ identity matrix and $\mathbf{B}_*$ and $\mathbf{C}_*$ have the form (4.61). The update matrix retains the structure of an identity matrix with a rank-one perturbation, allowing for an efficient, explicit update via the Sherman-Morrison formula.

Here, the analytic form of the gradient was employed, and a thorough study of constrained gradient forms is left for future work. Thus, it is set:

$$g_H^n = -\frac{K_H \left[\left(\mathbf{j}^{(x_H)}\right)^\intercal \mathbf{u}^n - U_H^n \right]_+^{\alpha_H}}{\sqrt{\frac{2K_H}{\alpha_H + 1} \left[\left(\mathbf{j}^{(x_H)}\right)^\intercal \mathbf{u}^n - U_H^n \right]_+^{\alpha_H + 1} + \varepsilon}}, \qquad \mathbf{g}_H^n = -\mathbf{j}^{(x_H)} g_H^n. \tag{5.34}$$

Figure 5.6 presents an illustrative example of a hammer striking the string. The hammer is given an initial velocity with no external forcing applied. As no restoring force acts on the hammer, it continues moving at a constant positive velocity after contact while the string is set into vibration. No comparative study has been conducted to assess the performance of SAV for this case, thus, the test primarily serves to illustrates the system functionality. An animation of the hammer-string collision can be found on the companion page.

5.3 Distributed collisions: fretboard and frets

As with geometric nonlinearities, the nonlinear potential becomes a potential density when collisions are distributed in space. Thus, the model of a string undergoing distributed collisions is quite similar to the case of transverse nonlinear motion. The continuous equation remains identical to (4.43), where now $\mathcal{F}_* = \partial_u \phi_*$ represents a collision force density based on a generic potential density ϕ_*. Two specific systems are examined here: string-fretboard and string-frets collisions, common in guitars. For these cases, it is often simpler to express the total nonlinear potentials directly. To this end, the energy analysis is first performed using the usual approach, taking the inner product of equation (4.43) with the velocity. Applying the chain rule to the nonlinear potential results in a conservative energy balance analogous to
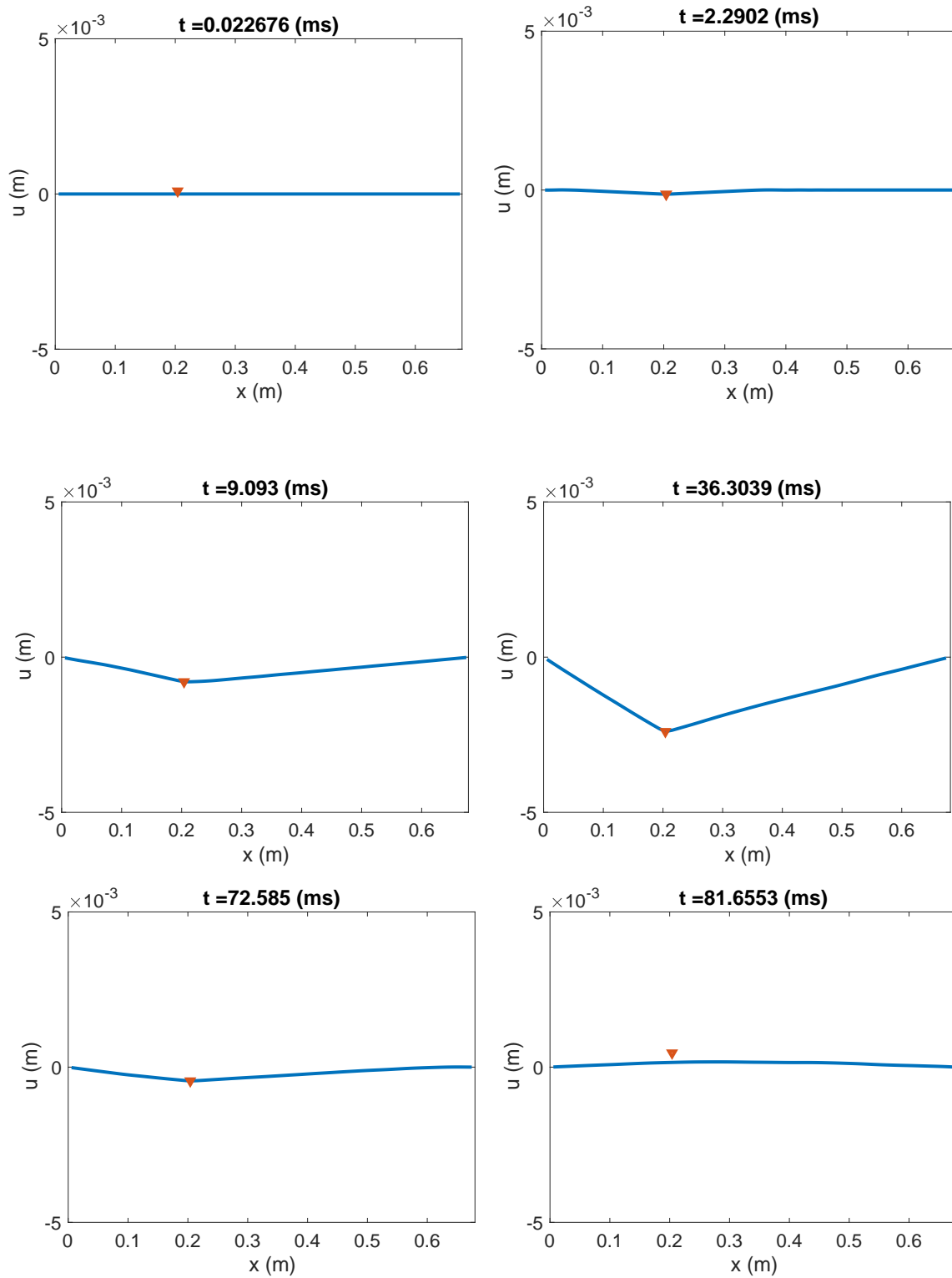
Fig. 5.6 Snapshots of the hammer-string collision at the indicated times. The string physical parameters are: $L = 0.68$ m, $E = 2e11$ GPa, $T_0 = 12.1$ N, $A = 1.26 \times 10^{-7}$, $\rho = 8 \times 10^3$ Kg/m^3, $\sigma = 0.92$, $\sigma_1 = 6.1 \times 10^{-4}$. The hammer physical parameters are: $m_{\mathrm{H}} = 0.05$ Kg, $K_{\mathrm{H}} = 10^{10}$, $\alpha_{\mathrm{H}} = 1.3$. The hammer has an initial displacement of 0.1 mm and an initial velocity of -0.1 m/s. The input point is located at $x_{\mathrm{H}} = 0.3L$. The sample rate is $f_s = 44100$ Hz.
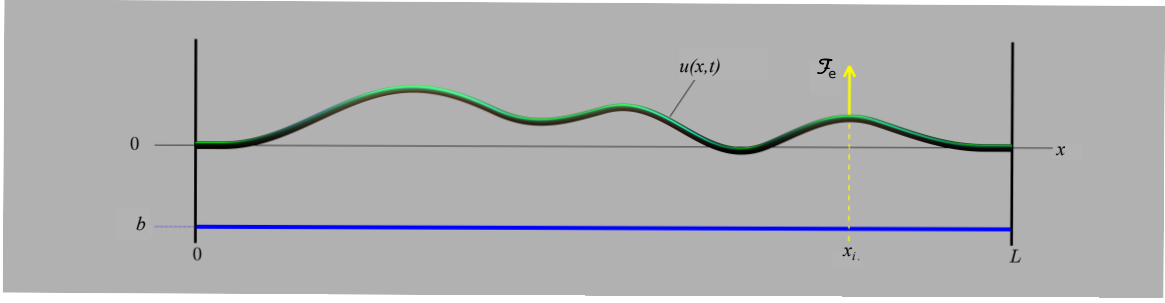
Fig. 5.7 Model of a string (in green) with a fretboard (in blue). External excitation is shown in yellow.

equation (2.136), and the energy is now expressed as:

$$H = \frac{\rho A}{2} \|\partial_t u\|^2 + \frac{T_0}{2} \|\partial_x u\|^2 + \frac{EI_0}{2} \|\partial_x^2 u\|^2 + \Phi_*, \tag{5.35}$$

where the total nonlinear potential energy was defined:

$$\Phi_* \triangleq \left\| \sqrt{\phi_*} \right\|^2 + \frac{\varepsilon}{2}. \tag{5.36}$$

The fretboard (in the absence of frets) is modelled as a smooth function $b(x)$, with $b(x) \leq 0$, so that the fretboard lies below the rest position of the string. In the simplest case, one may assume $b(x) = b_0$, representing a constant offset. This situation is depicted in Figure 5.7. The collision potential in this case is given by:

$$\Phi_{\mathrm{B}} = \frac{K_{\mathrm{B}}}{\alpha_{\mathrm{B}} + 1} \int_0^L [b - u]_+^{\alpha_{\mathrm{B}}+1} \mathrm{d}x, \tag{5.37}$$

where K_{B} represents the fretboard stiffness and $\alpha_{\mathrm{B}} \geq 1$ is the nonlinearity exponent.

Now, assume there are R frets located at coordinates $x = x_1, \ldots, x_R$ (R typically ranges from 19 to 24 for standard guitars). Interactions of the string with the frets are assumed to occur at the tips, located at a vertical height m_0, with $m_0 \leq 0$ so that the rest position of the string lies above the fret tip. Additionally, $m_0 \geq b(x_r)$ for $r = 1, \ldots, R$, meaning that the frets protrude above the fretboard. The resulting collision potential for the frets is:

$$\Phi_{\mathrm{F}} = \frac{K_{\mathrm{F}}}{\alpha_{\mathrm{F}} + 1} \sum_{r=1}^{R} [m_0 - u(x_r, t)]_+^{\alpha_{\mathrm{F}}+1}, \tag{5.38}$$

where as before K_F and α_F are constants regulating the nonlinearity. The eventual algorithm design is insensitive to the placement of frets: for standard semitone tuning, frets should be located at coordinates $x_r = L\left(1 - 2^{-r/12}\right)$.

5.3.1 Simulation

A spatial discretisation of a distributed collision system follows analogously to the approach presented in Chapter 4, with the difference that now the potential depends on the state, rather than its derivative. Therefore, considering relation, (4.45), the semi-discrete equation (4.46) may be re-written as:

$$\left(\rho A \frac{d^2}{dt^2} - \mathfrak{L}\right)\mathbf{u} = -\frac{1}{h}\nabla_{\mathbf{u}}\Phi_* + \mathbf{j}^{(x_i)}F, \tag{5.39}$$

where the semi-discrete linear operator $\mathfrak{L}$ is as defined in equation (3.96). Here, Φ_* is a suitable discretisation of the nonlinear potentials (5.37) and (5.38), taking the forms

$$\Phi_B = \frac{K_B h}{\alpha_B + 1}\sum_{l=1}^{N-1}[b_l - u_l]_+^{\alpha_B+1} + \frac{\varepsilon}{2} \tag{5.40a}$$

$$\Phi_F = \frac{K_F}{\alpha_F + 1}\sum_{r=1}^{R}\left[m_0 - \left(\mathbf{j}^{(x_r)}\right)^\intercal\mathbf{u}\right]_+^{\alpha_F+1} + \frac{\varepsilon}{2}, \tag{5.40b}$$

where $b_1, \ldots, b_{N-1}$ is the fretboard profile sampled at the $N-1$ interior grid locations. As mentioned earlier, one may choose a flat barrier with an offset so that $b_l = b_0 \forall l \in [1, N-1]$.

Quadratisation can be performed in the same manner as in Chapter 4, by introducing an auxiliary variable as defined in (4.51). This leads to the quadratised equation of motion (4.52), and the chain rule (4.54), which will serve as the update equation for the auxiliary variable. The energy analysis yields the same results, with semi-discrete energy taking the form (4.55).

Time discretisation proceeds in the same way, resulting in the fully discrete system (4.58), leading to the update form (4.62), and the update for the auxiliary variable follows from (4.63).

As for the other systems, the calculation of the potential gradients needs to be handled carefully. The analytic forms, following from equation (4.64), are:

$$\bar{\mathbf{g}}_{\mathrm{B}}^n = -\frac{hK_{\mathrm{B}}[\mathbf{b} - \mathbf{u}^n]_+^{\alpha_{\mathrm{B}}}}{\sqrt{\frac{2K_{\mathrm{B}}h}{\alpha_{\mathrm{B}}+1}\sum_{l=1}^{N-1}[b_l - u_l^n]_+^{\alpha_{\mathrm{B}}+1} + \varepsilon}} \tag{5.41a}$$

$$\bar{\mathbf{g}}_{\mathrm{F}}^n = -\frac{K_{\mathrm{F}}\left[m_0 - \mathfrak{d}^\mathsf{T}\mathbf{u}^n\right]^{\alpha_{\mathrm{F}}}}{\sqrt{\frac{2K_{\mathrm{F}}}{\alpha_{\mathrm{F}}+1}\sum_{r=1}^{R}\left[m_0 - (\mathbf{j}^{(x_r)})^\mathsf{T}\mathbf{u}^n\right]_+^{\alpha_{\mathrm{F}}+1} + \varepsilon}}, \tag{5.41b}$$

where $\mathfrak{d}$ is a $(N-1) \times R$ matrix whose columns are the fret interpolators $\mathbf{j}^{(x_r)}$.

Applying the constraint to distributed collisions is somewhat more complex than in the case of geometric nonlinearities. In [216], the constraint (5.12) is extended to handle the distributed case. Similarly, the constraint (4.69), already adapted for lumped collisions, is modified here by incorporating a branched form of the gradient, following the approach in [216]. The constraint equation is then derived in the same way as for the geometric nonlinearity case, resulting in equation (4.71). A scalar multiplier γ is then defined, as in equation (4.72), to scale the analytic gradient such that $\mathbf{g}_*^n = \gamma\bar{\mathbf{g}}_*^n$. This is set as follows:

$$\gamma = \begin{cases} -\dfrac{\vartheta 4\psi_*^{n-1/2}}{\mathfrak{Z}} & : \ \mathfrak{Z} \neq 0 \ \& \ \mathfrak{Z} < -4\psi_*^{n-1/2} \\ -\dfrac{\vartheta' 4\psi_*^{n-1/2}}{\mathfrak{Z}'} & : \ \mathfrak{Z} = 0 \ \& \ \mathfrak{Z}' \neq 0 \\ 1 & \text{otherwise,} \end{cases} \tag{5.42}$$

where $\mathfrak{Z}$ is defined in equation (4.73) and:

$$\mathfrak{Z}' \triangleq \left(\bar{\mathbf{g}}_*^{n-1}\right)^\mathsf{T}\left(\mathbf{B}\mathbf{u}^n + \mathbf{C}\mathbf{u}^{n-1} - \mathbf{u}^{n-1}\right). \tag{5.43}$$

Note that the equation for γ includes an additional branch compared to (4.74). The upper condition ensures the non-negativity of $\mu_{t+}\psi_*^{n-1/2}$, functioning analogously to what was seen in Chapter 4, and activates when (4.71) is not satisfied for $\mathbf{g}_*^n = \bar{\mathbf{g}}_*^n$. The middle branch condition is satisfied only during the initial instants without contact. Using the gradient from the previous time step enforces $\mu_{t+}\psi_*^{n-1/2} = 0$, ensuring no residual energy is stored during non-contact periods. As before, ϑ and ϑ' are scalars shifting the constraint away from the equality limit.

5.3.2 Numerical testing

The system, with the analytic potential (5.41a), is now tested by initialising it in its first mode of vibration. Figure 5.8a shows the time solution and spectrogram, while Figure 5.8b presents the different energy components and the energy error, computed as in (4.68). The spectrogram reveals significant noise as the time solution remains "trapped" below the barrier, causing continuous collisions. This behaviour is further explained by the energy plots, where the nonlinear energy is always active and fails to decay to zero, even though the total discrete energy is conserved. In contrast, Figures 5.9a and 5.9b show the same data for the system under identical conditions, but with the constraint (5.42) applied. In this case, the time solution and spectrogram are much cleaner, as collisions only occur in the initial moments. This is also reflected in the energy plots, showing that the string collides a few times before the vibration diminishes, preventing further contact with the barrier. The energy behaviour is paired by the trend of the auxiliary variable $\mu_{t+}\psi_{\mathrm{B}}^{n-1/2}$, reported in Figure 5.10 both with and without the constraint applied. In the first case, the auxiliary variable drops below zero and oscillates with a noisy behaviour. When the constraint is applied, the trend becomes much more regular, and the variable remains constrained. It can be seen that it assumes negative values only for one sample after the collision and then returns to zero. This is the result of the parameter choice for ϑ', which was set, as in the lumped case, $\vartheta' = 0.5$ if $\frac{-4\psi_*^{n-1/2}}{3'} < 0$, $\vartheta' = 1$ otherwise. Figure 5.11 shows the same data as the other figures but with $\vartheta' = 1$. In this case, the auxiliary variable remains properly constrained, never becoming negative, but there is an unusual response in the nonlinear potential, as seen in Figure 5.11b. Additionally, the energy error drops to the order of 10^{-8}. This is likely due to high-frequency oscillations in the auxiliary variable: while the mean remains zero, ψ_{B}^n oscillates between two opposing values at Nyquist frequency. Note that similar results were obtained with the potential (5.41b) but are not shown here to avoid redundancy. Audio files relative to this test are available on the companion page.

   This preliminary test suggests that the constraint (5.42) yields promising results in handling collisions. However, further study is needed. Convergence must be verified, and an investigation into the role of the parameter ϑ' is required. Additionally, a comparison with the constraint developed in [216] is necessary. These tasks are left for future work.

(a)

(b)
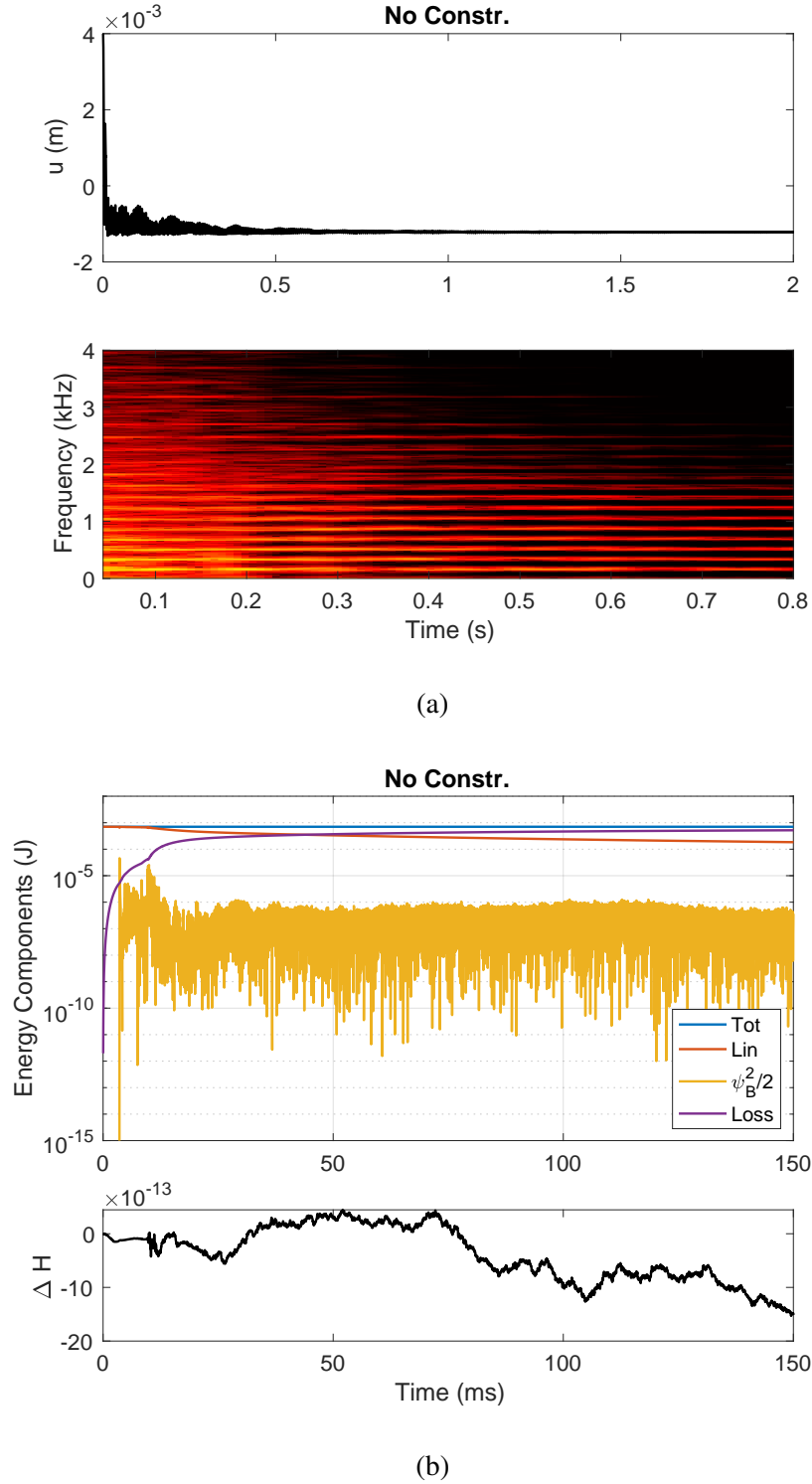
Fig. 5.8 (a) Time domain solution and spectrogram, (b) evolution of the energy components and energy error for the system (5.41a) without the constraint (5.42) applied. The system is initialised in its first mode of vibration, with an amplitude of 4 mm. The string parameters are as specified in Figure 5.6, and the barrier parameters are $K_{\mathrm{B}} = 10^{13}, \alpha_{\mathrm{B}} = 2.3$. The string rest position is set to zero, with a flat barrier positioned at $b_0 = -1$ mm. The output point $x_o = L/2$ is located at the string midpoint. The sample rate is $f_s = 44100$ Hz. The value $\varepsilon = \epsilon_m$ is used throughout the test.
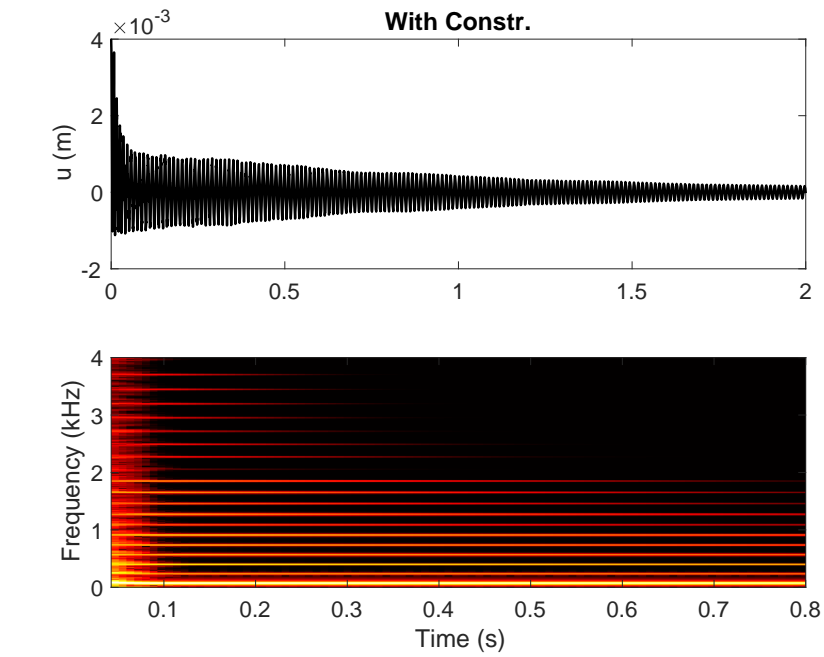
(a)
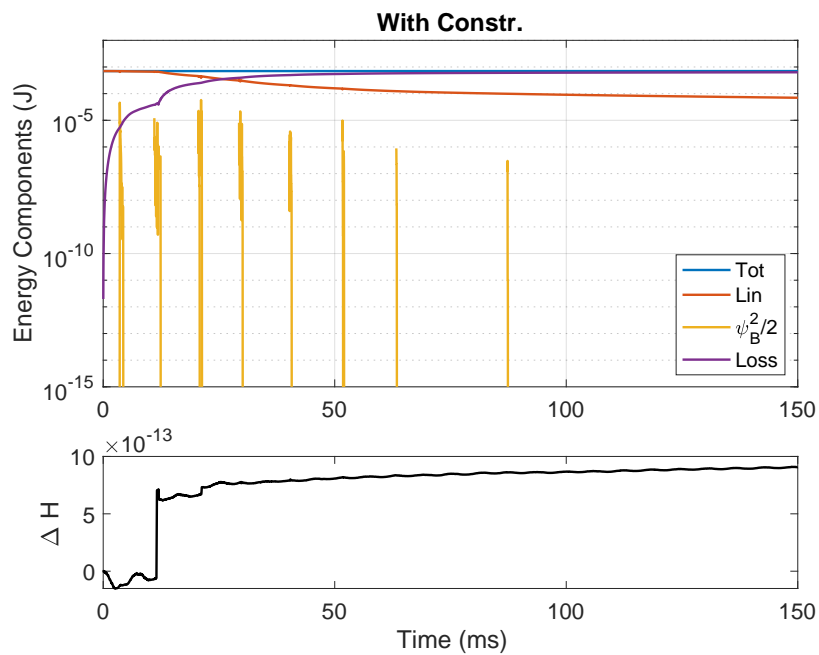
(b)

Fig. 5.9 (a) Time domain solution and spectrogram, (b) evolution of the energy components and energy error for the system (5.41a) with the constraint (5.42) applied. Other details are as provided in Figure 5.8.
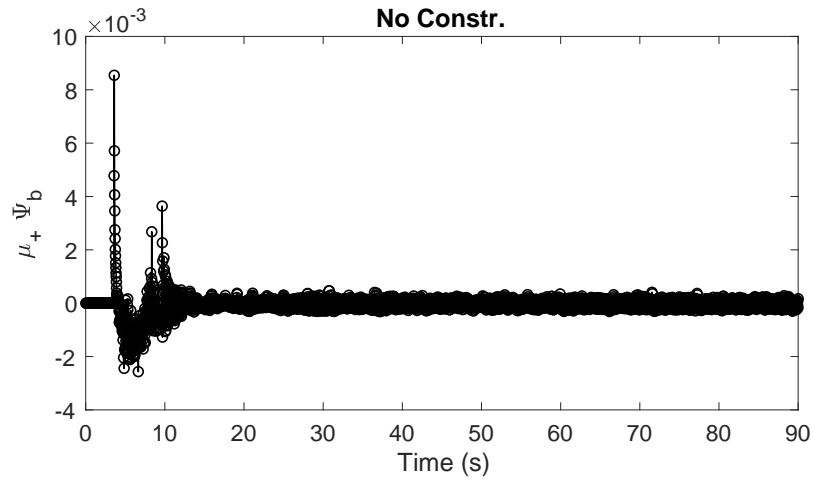
(a)
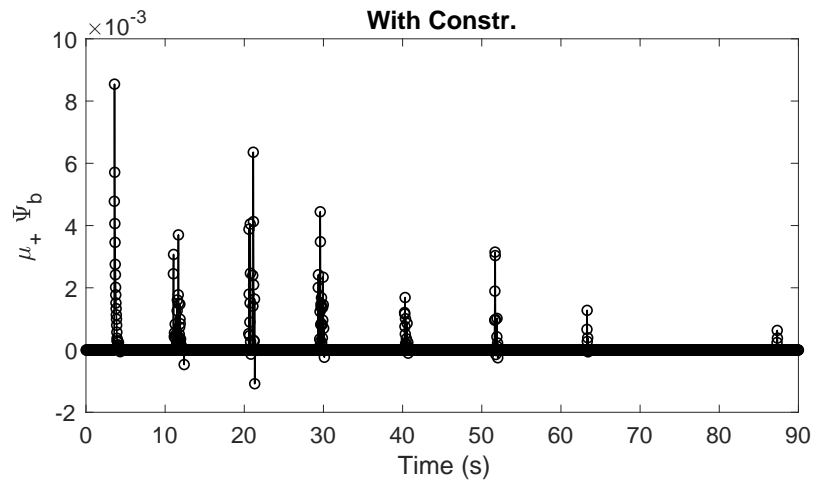
(b)

Fig. 5.10 Behaviour of the auxiliary variable $\mu_{t+}\psi_{\mathrm{B}}^{n-1/2}$ for the test reported in Figures 5.8 and 5.9: (a) without and (b) with the constraint (5.42) applied.
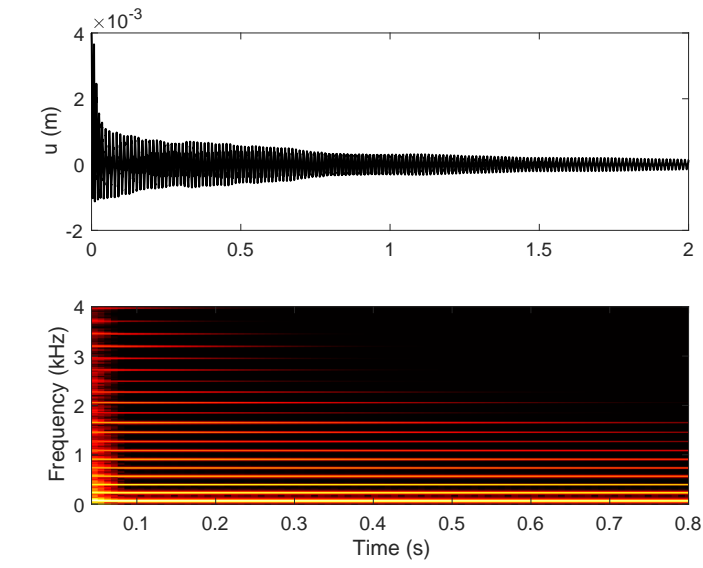
(a)
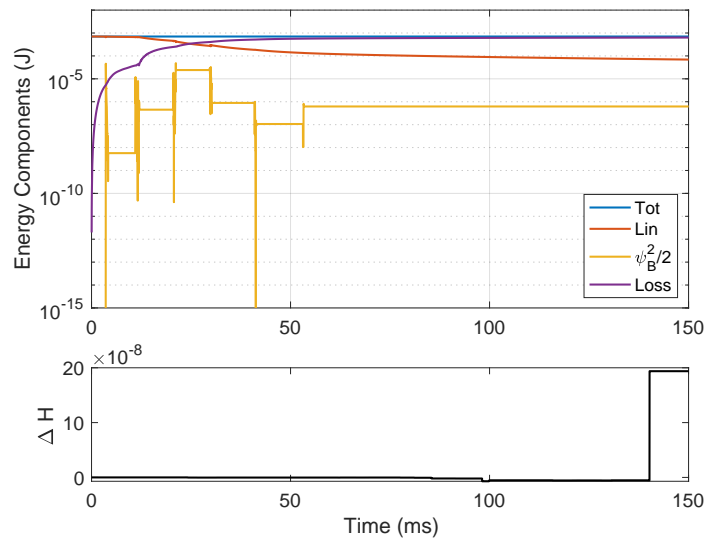
(b)
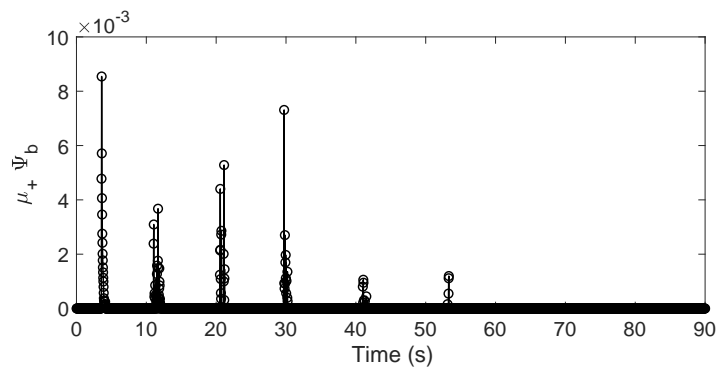
(c)

Fig. 5.11 Results of the test reported in Figure 5.9, with $\vartheta' = 1$ throughout.

Chapter 6

Friction: the bow

As discussed in Chapter 1, friction in stringed instruments is predominantly associated with the bowing mechanism. When a string is bowed to produce musical tones, it exhibits Helmholtz motion, alternating sticking and slipping phases. This motion is typically modelled by a force that depends on the relative velocity between the string and the bow at the bowing point. The force is thus represented by a friction curve, which varies nonlinearly with the relative velocity. Several models exist for this friction coefficient, some of which are illustrated in Figure 6.1. The discussion here begins with the case of a bowed mass and later extends to spatially distributed cases.

Audio files and code for this chapter are available on the companion page.

6.1   Bowed mass

As in previous chapters, the lumped system serves as an introductory example for numerical methods. A system with two degrees of freedom, consisting of a SHO excited by a bow, can be described by two coupled ODEs as [24, Chapter 4]:

$$\frac{\mathrm{d}^2 u}{\mathrm{d}t^2} = -\omega_0^2 u - F_\mathrm{C}\phi_\mathrm{C}(\eta) \tag{6.1a}$$

$$\eta = \frac{\mathrm{d}u}{\mathrm{d}t} - v_\mathrm{C} \tag{6.1b}$$

Here, the function $v_\mathrm{C}(t)$ is the bow velocity in m/s, while $F_\mathrm{C}(t) > 0$ is the bow force normalised by the object mass ("C" here stands for "Cello"). Both are assumed to be known. Here, the "soft" friction characteristic illustrated in panel (d) of Figure 6.1 is employed. It is expressed as:

$$\phi_\mathrm{C}(\eta) = \sqrt{2a}\,\eta\,e^{-a\eta^2 + 1/2}, \tag{6.2}$$
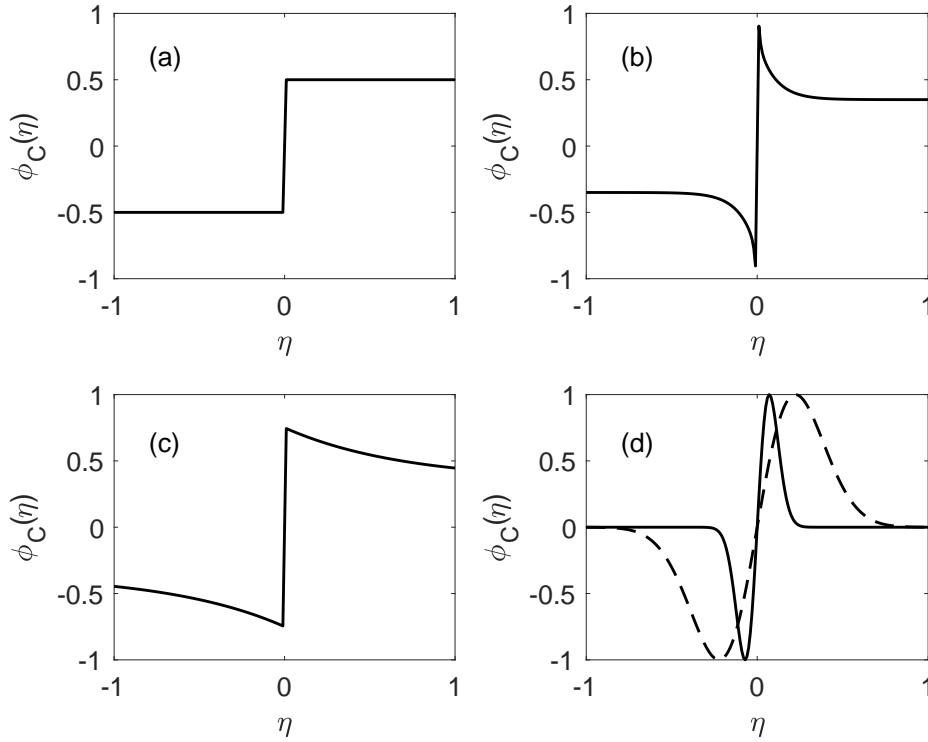
Fig. 6.1 Various friction characteristics: (a) Coulomb dry friction, with equation $\phi_C(\eta) = \text{sgn}(\eta)/2$; (b) the "classical" curve by Woodhouse and Smith [192], with the form $\phi_C(\eta) = \text{sgn}(\eta)(0.4e^{-|\eta|/0.01} + 0.45e^{-|\eta|/0.1} + 0.35)$; (c) the reconstructed curve by Galluzzo [98], defined by $\phi_C(\eta) = \text{sgn}(\eta)(0.4e^{-|\eta|/0.7} + 0.35)$; (d) the continuous approximation defined in equation 6.2, with $a = 10$ (dashed) and $a = 100$ (solid). Here, $\eta(t)$ is the relative velocity between the bow and the mass in m/s, and the function $\phi_C = \phi_C(\eta) : \mathbb{R} \to \mathbb{R}$ is a dimensionless friction coefficient, expressed as a function of the relative velocity only. Since $\text{sgn}(\eta) = 0$, curves (a), (b) and (c) are defined for nonzero values of η only. The vertical portion of these curves shows the range of possible values during the sticking phase [98]. Specifically, this can be expressed as: $\min \phi_C \leq \phi_C(0) \leq \max \phi_C$.

where a is a free parameter. Note that ϕ_C satisfies:

$$\eta \, \phi_C(\eta) \geq 0, \tag{6.3a}$$

$$\lim_{|\eta| \to 0} \phi_C(\eta)/\eta = \sqrt{2ae} < \infty . \tag{6.3b}$$

Property (6.3a) is referred to as sector-boundedness, here to sector $[0, \infty]$. Both this and property (6.3b) are fundamental for numerical discretisation. As noted in Chapter 1, the friction curve (6.2) was not designed on physical principles. However, since the focus here is on the efficiency of the numerical algorithm, this characteristic was used for convenience. Any other curve may be used instead, provided it satisfies properties (6.3a) and (6.3b).

An energy balance is obtained by multiplying equation (6.1a) by the velocity $\frac{du}{dt}$, yielding:

$$\frac{d}{dt}H = -F_C(\eta + v_C)\phi_C(\eta),\qquad(6.4)$$

where H corresponds to the energy of a SHO scaled by the mass, already seen in equation (2.25). In the zero-velocity case ($v_C = 0$), owing to the property (6.3a), the system is dissipative. Since the nonlinear force is non-conservative, there is no nonlinear potential to quadratise in this case.

In preparation for time discretisation, it is helpful to express the equation of motion (6.1) in first-order form. As shown in Chapter 2, this can be done by defining the generalised coordinates q and p as $q \triangleq \omega_0 u$ and $p \triangleq du/dt$, resulting in:

$$\frac{d\mathbf{x}}{dt} = \mathbf{J}\nabla_{\mathbf{x}}H - \mathbf{i}F_C\phi_C(\eta)\qquad(6.5a)$$

$$\eta = \mathbf{i}^\mathsf{T}\mathbf{x} - v_C,\qquad(6.5b)$$

with $\mathbf{i} = [0, 1]^\mathsf{T}$, and other terms as defined in Chapter 2. The energy balance is obtained by left-multiplying (6.5a) by $(\nabla H)^\mathsf{T}$. Owing to the skew-symmetry of $\mathbf{J}$, and by applying the chain rule, one obtains the passive balance (in the zero-velocity case):

$$\frac{d}{dt}H = -F_C\, p\, \phi_C(p) \le 0.\qquad(6.6)$$

Note that system (6.5a) retains the structure of a PHS, now including dissipation induced by the bow. As in the linear case, system (6.5) and equation (6.1) are equivalent in the continuous domain.

6.1.1 Iterative discretisation of the second-order system

A possible discretisation of equation (6.1), referred to here as SOIT, is given by:

$$\delta_{tt}u^n = -\omega_0^2 u^n - F_C^n\phi_C(\delta_{t\cdot}u^n - v_C^n),\qquad(6.7)$$

where F_C^n and v_C^n are time series representing the bow force and velocity, allowed to vary over time. A discrete energy balance, in the zero-velocity case, is obtained by left-multiplying by $\delta_{t\cdot}u^n$, yielding:

$$\delta_{t+}\mathfrak{h}^{n-1/2} = -F_C^n\,\delta_{t\cdot}u^n\phi_C(\delta_{t\cdot}u^n) \le 0,\qquad(6.8)$$

where the energy has the form (3.17), divided by the mass. The balance is dissipative, and ensuring energy positivity leads to the stability condition (3.20). Alternatively, an exact integrator may be employed to avoid stability conditions and frequency warping issues.

Scheme (6.7) can be written as:

$$2k\delta_{t.}u^n + 2u^{n-1} - 2u^n + \omega_0^2 k^2 u^n + k^2 F_C^n \phi_C(\delta_{t.}u^n - v_C^n) = 0. \tag{6.9}$$

This is a nonlinear algebraic equation, solvable for $\delta_{t.}u^n$ with a nonlinear root finder such as Newton-Raphson. Then, u^{n+1} may be retrieved by simply applying the centred operator definition. Notice that a condition on the existence and uniqueness of the solution of (6.9) must be given, and this appears as an additional constraint on the time step k. Further details can be found in [24, Chapter 4]. Alternatively, the "Friedlander construction" [227] may be used to explicitly lock the string and bow velocities during the sticking phase, thus preventing the need for bounds on the time step.

6.1.2 Iterative discretisation of the first-order system

A possible discretisation of the first-order system (6.5) can be obtained using the midpoint method detailed in equation (3.5). The resulting scheme is:

$$\delta_{t+}\mathbf{x}^n = \mathbf{J}\nabla\mathfrak{h}^{n+1/2} - \mathbf{i}F_C\phi_C(\mu_{t+}\eta^n), \quad \eta^n = \mathbf{i}^\intercal\mathbf{x}^n - v_C^n, \tag{6.10}$$

where the form of the discrete gradient is as given in equation (3.52). This scheme is referred to here as FOIT. The discrete energy balance is obtained by left-multiplying (6.10) by $\nabla\mathfrak{h}^\intercal$, yielding, in the zero-velocity case:

$$\delta_{t+}\mathfrak{h}^n = -F_C^n \mu_{t+}p^n \phi_C(\mu_{t+}p^n) \leq 0. \tag{6.11}$$

Thus, the system is dissipative. Note that, in this case, the scheme is unconditionally stable due to the non-negativity of the discrete energy. The update equation of (6.10) is:

$$\left(\frac{\mathbf{I}}{k} - \frac{\mathbf{J}}{2}\right)\mathbf{x}^{n+1} - \left(\frac{\mathbf{I}}{k} + \frac{\mathbf{J}}{2}\right)\mathbf{x}^n + \mathbf{i}F_C^n\phi_C(\mu_+\eta^n) = 0, \tag{6.12}$$

where $\mathbf{I}$ here indicates the 2×2 identity matrix. Scheme (6.16) forms a nonlinear algebraic system due to the implicit definition of $\mathbf{x}^{n+1}$ appearing in the argument of the nonlinear function ϕ_C. Therefore, an iterative root-finding method is required.

6.1.3   Non-iterative discretisation of the first-order system

The quadratisation techniques employed in the previous chapters are not applicable in this case, as the nonlinear force is non-conservative. Therefore, an alternative discretization of the first-order system (6.5) is provided, adapted from [80, 76], where a family of non-iterative schemes is introduced in the context of stiff nonlinear ODEs modelling audio circuits. These schemes demonstrate good numerical behaviour without requiring iterative techniques, as shown in the examples below. The discretization is given by:

$$\boldsymbol{\sigma}^{(P)}\delta_{t+}\mathbf{x}^n = \mathbf{J}\nabla\mathfrak{h}^{n+1/2} - \mathbf{i}F_{\mathrm{C}}^n\xi^n\mu_{t+}\eta^n. \tag{6.13}$$

Here, $\boldsymbol{\sigma}^{(P)} = \boldsymbol{\sigma}^{(P)}(\mathbf{x}^n)$ is a factor taking the form of a perturbation expansion, which can be set to yield a truncation error with an accuracy of order $(P+1)$. Its expression is:

$$\boldsymbol{\sigma}^{(P)}(\mathbf{x}^n) = \sum_{p=0}^{P} k^p \boldsymbol{\zeta}^{(p)}(\mathbf{x}^n). \tag{6.14}$$

The functions $\boldsymbol{\zeta}^{(p)}(\mathbf{x}^n)$ are obtained through Taylor expansion by means of a technique which has strong links to the modified equation method [Chapter 10][137]. The first two terms are here given explicitly as:

$$\boldsymbol{\zeta}^{(0)}(\mathbf{x}^n) = \mathbf{I} \tag{6.15a}$$

$$\boldsymbol{\zeta}^{(1)}(\mathbf{x}^n) = \frac{kF_{\mathrm{C}}}{2}(\lambda^n - \xi^n)\mathbf{i}\mathbf{i}^\mathsf{T} \tag{6.15b}$$

where it was defined:

$$\lambda^n \triangleq \left.\frac{\mathrm{d}\phi_{\mathrm{C}}}{\mathrm{d}\eta}\right|_{\eta=\eta^n}, \qquad \xi^n \triangleq \left.\frac{\phi_{\mathrm{C}}}{\eta}\right|_{\eta=\eta^n}. \tag{6.16}$$

Note that both λ and ξ are well-defined due to properties (6.3a) and (6.3b). The definition of η is as in (6.10), and the discrete gradient is as in (3.52). With $P=1$, one gets a factor:

$$\boldsymbol{\sigma}^{(1)}(\mathbf{x}^n) = \mathbf{I} + \frac{kF_{\mathrm{C}}}{2}(\lambda^n - \xi^n)\mathbf{i}\mathbf{i}^\mathsf{T}, \tag{6.17}$$

which allows the formulation of the second-order accurate numerical scheme:

$$\mathbf{A}^n\mathbf{x}^{n+1} = \mathbf{B}^n\mathbf{x}^n + \mathbf{i}F_{\mathrm{C}}^n\xi^n\mu_{t+}v_{\mathrm{C}}^n, \tag{6.18}$$

where the matrices have the form:

$$\mathbf{A}^n \triangleq \frac{\mathbf{I}}{k} + \frac{F_C \lambda^n}{2} \mathbf{i} \mathbf{i}^\mathsf{T} - \frac{\mathbf{J}}{2}, \qquad \mathbf{B}^n \triangleq \frac{\mathbf{I}}{k} + F_C \left(\frac{\lambda^n}{2} - \xi^n \right) \mathbf{i} \mathbf{i}^\mathsf{T} + \frac{\mathbf{J}}{2}, \qquad (6.19)$$

and $\mathbf{I}$ again indicates the 2×2 identity matrix. Note that both $\mathbf{A}^n$ and $\mathbf{B}^n$ are computed using values from previous time steps, allowing the update to be expressed as the solution of a single linear system, making the scheme linearly implicit. Proof of the accuracy order may be obtained through Taylor series arguments, as shown in Chapter 3. Ensuring numerical passivity for schemes like (6.13) is more challenging than the iterative discretisations shown earlier. Partial results are available in [76]. However, numerical testing provides insights into the stability properties of these schemes compared to the iterative discretisations and a standard explicit integrator. In particular, since the linear part is unconditionally stable, no stability conditions are required for it, and the scheme remained stable in all simulations performed.

6.1.4   Numerical testing

Figure 6.2 presents the results computed with different solvers for two empirically chosen values of F_C, representing force normalized by mass. A reference solution is obtained running scheme (6.7) with an OF $= 30$ and a base sample rate $f_s = 44100$ Hz. Then, schemes (6.7), (6.10) and (6.13) are run with OF $= 2$, and the global error is computed as in equation (3.26). Newton-Raphson is used with a 10^{-9} threshold. Additionally, the forward euler (FE) integrator, detailed in equation (3.47), is included in the test. For the lower bowing pressure ($F_C = 100$), FE yields an error three orders of magnitude larger than the other schemes. More notably, for the larger bowing pressure ($F_C = 4000$) FE exhibits instability. In contrast, the FONIT scheme displays robust numerical behaviour, comparable to the iterative schemes.

6.2   The bowed ideal string

As an extension to a spatially distributed case, consider a bowed ideal string without stiffness or damping, where the bowing force is assumed to act pointwise at the bowing location. The string-bow system is described by:

$$\partial_t^2 u = c^2 \partial_x^2 u - F_C \delta(x - x_C) \phi_C(\eta), \qquad (6.20a)$$

$$\eta = \partial_t u |_{x_C} - v_C, \qquad (6.20b)$$
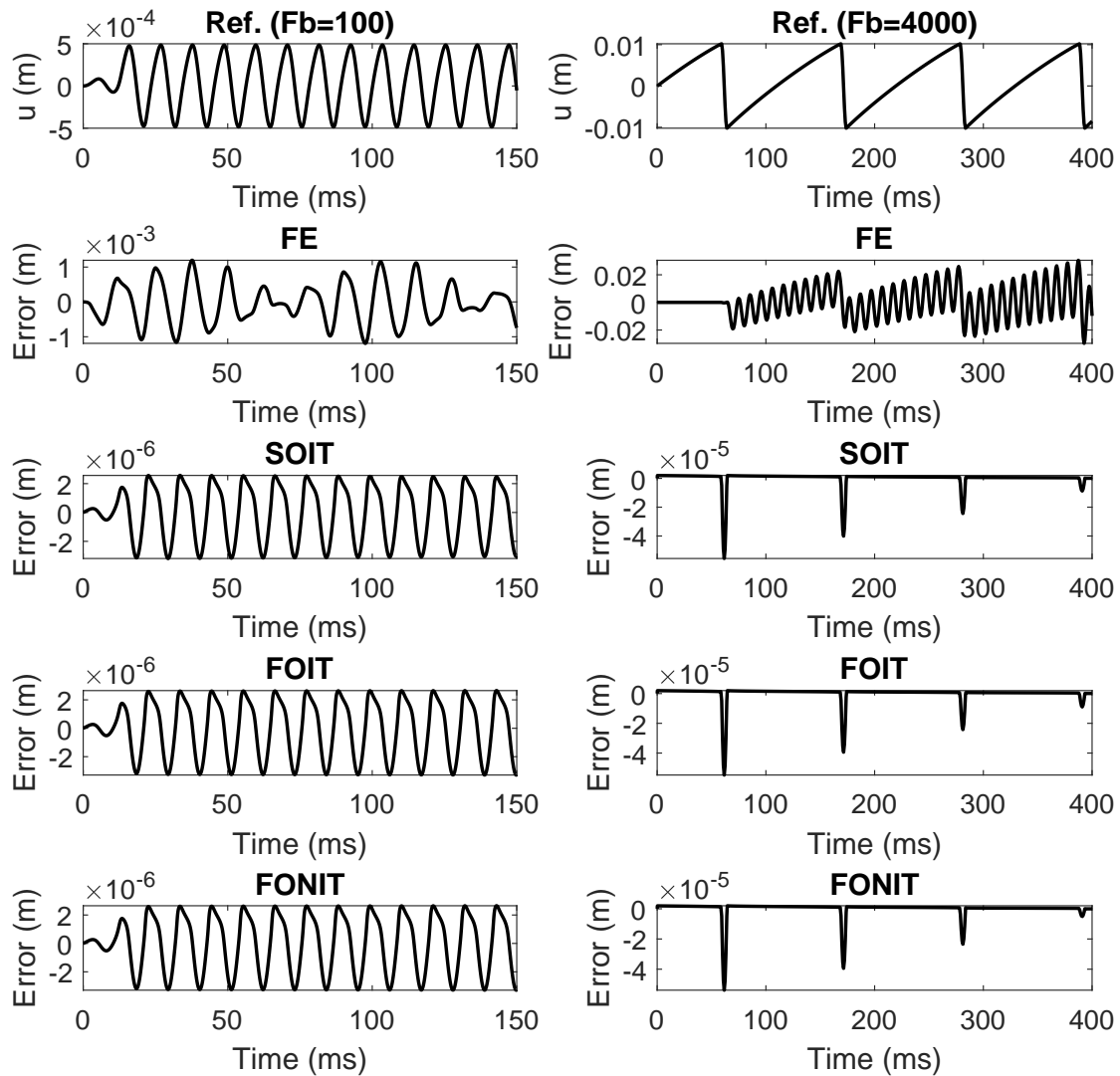
Fig. 6.2 Comparison between the different bowed mass simulations, using the friction function (6.2). All cases used: $a = 100$, $f_0 = \omega_0/2\pi = 100$ Hz, $v_C = 0.2$ m/s. "Ref." indicates the reference solution. Reproduced from [180].

where the wave speed c is defined in equation (2.84), and F_C is the bow force normalised by the string linear mass ρA. Here, $\eta = \eta(t) \in \mathbb{R}$ represents the relative velocity of the bow and the string at the bowing location x_C. The energy balance is obtained by taking the inner product of equation (6.20a) with $\rho A \frac{\mathrm{d}u}{\mathrm{d}t}$. With Dirichlet boundary conditions, the energy balance in the zero-velocity case is given by:

$$\frac{\mathrm{d}}{\mathrm{d}t}H = -\rho A F_C \, \partial_t u(x_C, t) \, \phi_C \left(\partial_t u(x_C, t) \right) \leq 0, \tag{6.21}$$

where H has the form (2.78).

As in the case of the mass, it is convenient to express the system in first-order form. First, one defines the generalised coordinate and momentum:

$$q \triangleq c \, \partial_x u, \quad p \triangleq \partial_t u. \tag{6.22}$$

The energy may be then re-written in terms of the energy density H as:

$$H = \int_0^L \mathrm{H} \, \mathrm{d}x; \qquad \mathrm{H} = \frac{p^2}{2} + \frac{q^2}{2}. \tag{6.23}$$

The equations of motion in first-order form then are:

$$\partial_t \mathbf{x} = \mathbf{J}\nabla\mathrm{H} - \begin{bmatrix} 0 \\ \delta(x - x_C) \end{bmatrix} F_C \phi_C(\eta), \tag{6.24a}$$

$$\eta = \int_0^L [0, \delta(x - x_C)]\mathbf{x} \, \mathrm{d}x - v_C, \tag{6.24b}$$

where:

$$\mathbf{x} = \begin{bmatrix} q \\ p \end{bmatrix}, \qquad \mathbf{J} = c \begin{bmatrix} 0 & \partial_x \\ \partial_x & 0 \end{bmatrix}.$$

The energy balance is obtained by left-multiplying (6.24a) by $\nabla\mathrm{H}^\intercal$, and integrating. Considering Dirichlet boundary conditions and using the identity: $\int_0^L \nabla\mathrm{H}^\intercal \partial_t \mathbf{x}\mathrm{d}x = \frac{\mathrm{d}}{\mathrm{d}t}H$, one obtains again the energy balance (6.21).

6.2.1 Simulation of the second-order system

Following the definitions in Chapter 3, a spatial discretisation of system (6.20), with Dirichlet boundary conditions, is given by:

$$\frac{\mathrm{d}^2\mathbf{u}}{\mathrm{d}t^2} = c^2\mathbf{D}^2\mathbf{u} - \mathbf{j}^{(x_\mathrm{C})}F_\mathrm{C}\phi_\mathrm{C}(\eta) \tag{6.25a}$$

$$\eta = h\left(\mathbf{j}^{(x_\mathrm{C})}\right)^\mathsf{T}\frac{\mathrm{d}\mathbf{u}}{\mathrm{d}t} - v_\mathrm{C}. \tag{6.25b}$$

Time integration can then be performed as follows:

$$\delta_{tt}\mathbf{u}^n = c^2\mathbf{D}^2\mathbf{u}^n - \mathbf{j}^{(x_\mathrm{C})}F_\mathrm{C}\phi_\mathrm{C}(\eta^n) \tag{6.26a}$$

$$\eta^n = h\left(\mathbf{j}^{(x_\mathrm{C})}\right)^\mathsf{T}\delta_{t\cdot}\mathbf{u}^n - v_\mathrm{C} \tag{6.26b}$$

A discrete energy balance is obtained by taking an inner product of equation (6.26a) with $\rho A h \delta_{t\cdot}\mathbf{u}^n$. In the zero-velocity case, this results in:

$$\delta_{t+}\mathfrak{h}^{n-1/2} = -\rho A F_\mathrm{C}^n\left[h\left(\mathbf{j}^{(x_\mathrm{C})}\right)^\mathsf{T}\delta_{t\cdot}\mathbf{u}^n\right]\phi_\mathrm{C}\left(h\left(\mathbf{j}^{(x_\mathrm{C})}\right)^\mathsf{T}\delta_{t\cdot}\mathbf{u}^n\right) \leq 0, \tag{6.27}$$

where the discrete energy is as per (3.84). Ensuring the energy positivity leads to the stability condition (3.85). However, ensuring the existence and uniqueness of a solution leads to a further constraint, as discussed in [24, Chapter 7]. Since the update $\mathbf{u}^{n+1}$ appears implicitly in the argument of ϕ_C, the scheme is fully implicit, and a solution may be found using a suitable iterative routine in vector form. System (6.26) will be referred to as SOIT.

6.2.2 Simulation of the first order system

Iterative discretisation

A spatially discretized version of the generalized coordinates and momenta can be expressed as:

$$\mathbf{q} = c\,\mathbf{D}^-\mathbf{u}, \quad \mathbf{p} = \frac{\mathrm{d}\mathbf{u}}{\mathrm{d}t}, \tag{6.28}$$

and the energy is now given by:

$$H = \frac{h\mathbf{p}^\mathsf{T}\mathbf{p}}{2} + \frac{h\mathbf{q}^\mathsf{T}\mathbf{q}}{2}. \tag{6.29}$$

The equations of motion in semi-discrete form are then written as:

$$\frac{\mathrm{d}\mathbf{x}}{\mathrm{d}t} = \boldsymbol{\mathcal{J}}\nabla H - \mathbf{d}F_{\mathrm{C}}\phi_{\mathrm{C}}(\eta), \tag{6.30a}$$

$$\eta = h\,\mathbf{d}^{\mathsf{T}}\,\mathbf{x} - v_{\mathrm{C}}. \tag{6.30b}$$

where:

$$\mathbf{x} = \begin{bmatrix} \mathbf{q} \\ \mathbf{p} \end{bmatrix}, \qquad \mathbf{d} = \begin{bmatrix} \mathbf{0} \\ \mathbf{j}^{(x_{\mathrm{C}})} \end{bmatrix}, \qquad \boldsymbol{\mathcal{J}} = c\begin{bmatrix} \mathbf{0} & \mathbf{D}^{-} \\ \mathbf{D}^{+} & \mathbf{0} \end{bmatrix}. \tag{6.31}$$

Note that $\boldsymbol{\mathcal{J}}$ is a square, skew-symmetric matrix, retaining the structure characteristic of PHS.

One possible time integrator for system (6.30) is the Midpoint method, applied as follows:

$$\delta_{tt}\mathbf{x}^n = \boldsymbol{\mathcal{J}}\nabla\mathfrak{h}^{n+1/2} - \mathbf{d}F_{\mathrm{C}}\phi_{\mathrm{C}}(\mu_{t+}\eta^n), \tag{6.32a}$$

$$\mu_{t+}\eta^n = h\mathbf{d}^{\mathsf{T}}\mu_{t+}\mathbf{x}^n - \mu_{t+}v_{\mathrm{C}}^n, \tag{6.32b}$$

Here, the discrete energy is:

$$\mathfrak{h}^n = \frac{h(\mathbf{p}^n)^{\mathsf{T}}\,\mathbf{p}^n}{2} + \frac{h(\mathbf{q}^n)^{\mathsf{T}}\,\mathbf{q}^n}{2}, \tag{6.33}$$

and the discrete gradient results:

$$\nabla\mathfrak{h}^{n+1/2} = \begin{bmatrix} \mu_{t+}\mathbf{q}^n \\ \mu_{t+}\mathbf{p}^n \end{bmatrix} = \mu_{t+}\mathbf{x}^n. \tag{6.34}$$

As mentioned in Chapter 3, the Midpoint method is unconditionally stable. Indeed, it can be noticed that the discrete energy here remains non-negative $\forall\,\mathbf{p}^n, \mathbf{q}^n$. Scheme (6.32), referred to here as FOIT, is fully implicit, and an iterative root-finding method is required for its solution.

Non-ierative discretisation

Alternatively, the non-iterative method proposed for the bowed mass can be extended to the spatially distributed case. This is achieved with:

$$\boldsymbol{\sigma}^{(P)}(\mathbf{x}^n)\delta_{tt}\mathbf{x}^n = \boldsymbol{\mathcal{J}}\nabla\mathfrak{h}^{n+1/2} - \mathbf{d}F_{\mathrm{C}}^n\xi^n\mu_{t+}\eta^n. \tag{6.35}$$

The definitions of λ and ξ are given in (6.16), while $\mu_{t+}\eta^n$ is defined in (6.32b). The operator $\mathcal{J}$ is described in (6.31), and the energy gradient follows from (6.34). Choosing $P = 1$, one has

$$\boldsymbol{\sigma}^{(1)} = \mathbf{I} + \frac{kh}{2}F_{\mathrm{C}}(\lambda^n - \xi^n)\mathbf{dd}^{\mathsf{T}} \tag{6.36}$$

and a second-order accurate discretisation arises. Isolating the state vector $\mathbf{x}^{n+1}$ results in the linearly implicit update:

$$\mathbf{A}^n\mathbf{x}^{n+1} = \mathbf{B}^n\mathbf{x}^n + F_{\mathrm{C}}^n\xi^n\mathbf{d}\mu_{t+}v_{\mathrm{C}}^n, \tag{6.37}$$

where the matrices have the form:

$$\mathbf{A}^n = \frac{\mathbf{I}}{k} + \frac{F_{\mathrm{C}}^n\lambda^n}{2}\mathbf{dd}^{\mathsf{T}} - \frac{\mathcal{J}}{2}, \qquad \mathbf{B}^n = \frac{\mathbf{I}}{k} + F_{\mathrm{C}}^n\left(\frac{\lambda^n}{2} - \xi^n\right)\mathbf{dd}^{\mathsf{T}} + \frac{\mathcal{J}}{2}. \tag{6.38}$$

Scheme (6.37) will be referred to here as FONIT.

6.2.3   Modal form

As an alternative approach, the continuous equations (6.20) are now semi-discretised using a modal approach. Consider a separable solution of the form: $u = \boldsymbol{\chi}^{\mathsf{T}}(x)\mathbf{w}(t)$ with M modes, where $\boldsymbol{\chi}$ represents the normalised modes from (2.94). Substituting this solution form into equation (6.20) and performing a modal projection yields:

$$\frac{\mathrm{d}^2\mathbf{w}}{\mathrm{d}t^2} = -\boldsymbol{\Omega}^2\mathbf{w} - F_{\mathrm{C}}\boldsymbol{\chi}(x_{\mathrm{C}})\phi_{\mathrm{C}}(\eta) \tag{6.39a}$$

$$\eta = \boldsymbol{\chi}^{\mathsf{T}}(x_{\mathrm{C}})\frac{\mathrm{d}\mathbf{w}}{\mathrm{d}t} - v_{\mathrm{C}}, \tag{6.39b}$$

where $\boldsymbol{\Omega}^2$ is as defined in (2.101).

For a non-iterative discretization it is necessary to express the equation of motion (6.39) in first-order form. First, define:

$$\tilde{\mathbf{q}} \triangleq \boldsymbol{\Omega}_0\mathbf{w}, \qquad \tilde{\mathbf{p}} \triangleq \frac{\mathrm{d}\mathbf{w}}{\mathrm{d}t}, \qquad \tilde{\mathbf{x}} \triangleq \begin{bmatrix} \tilde{\mathbf{q}} \\ \tilde{\mathbf{p}} \end{bmatrix}. \tag{6.40}$$

Then, the energy takes the form:

$$\tilde{H} = \frac{\tilde{\mathbf{p}}^{\mathsf{T}}\tilde{\mathbf{p}}}{2} + \frac{\tilde{\mathbf{q}}^{\mathsf{T}}\tilde{\mathbf{q}}}{2}, \tag{6.41}$$

and system (6.39) can be re-written as:

$$\frac{\mathrm{d}^2\tilde{\mathbf{x}}}{\mathrm{d}t^2} = \tilde{\mathbf{J}}\nabla\tilde{H} - \tilde{\mathbf{d}}\,F_{\mathrm{C}}\phi_{\mathrm{C}}(\tilde{\eta}) \tag{6.42a}$$

$$\tilde{\eta} = \tilde{\mathbf{d}}^{\mathsf{T}}\tilde{\mathbf{x}} - v_{\mathrm{C}}, \tag{6.42b}$$

where:

$$\tilde{\mathbf{J}} = \begin{bmatrix} \mathbf{0} & \mathbf{\Omega} \\ -\mathbf{\Omega} & \mathbf{0} \end{bmatrix}, \quad \tilde{\mathbf{d}} = \begin{bmatrix} \mathbf{0} \\ \boldsymbol{\chi}(x_{\mathrm{C}}) \end{bmatrix}, \quad \nabla\tilde{H} = \begin{bmatrix} \tilde{\mathbf{q}} \\ \tilde{\mathbf{p}} \end{bmatrix}. \tag{6.43}$$

Note that $\tilde{\mathbf{J}}$ retains the typical stricture of a PHS.

The non-iterative solver can be used for the integration of the modal system 6.42, resulting in a fully discrete form analogous to (6.35). Expanding out the operators gives the update:

$$\tilde{\mathbf{A}}^n\tilde{\mathbf{x}}^{n+1} = \tilde{\mathbf{B}}^n\tilde{\mathbf{x}}^n + F_{\mathrm{C}}^n\xi^n\tilde{\mathbf{d}}\mu_+v_{\mathrm{C}}^n, \tag{6.44}$$

and the system matrices in the modal case take the form:

$$\tilde{\mathbf{A}}^n = \frac{\mathbf{I}}{k} + \frac{F_{\mathrm{C}}^n\lambda^n}{2}\tilde{\mathbf{d}}\tilde{\mathbf{d}}^{\mathsf{T}} - \frac{\tilde{\mathbf{J}}}{2}, \qquad \tilde{\mathbf{B}}^n = \frac{\mathbf{I}}{k} + F_{\mathrm{C}}^n\left(\frac{\lambda^n}{2} - \xi^n\right)\tilde{\mathbf{d}}\tilde{\mathbf{d}}^{\mathsf{T}} + \frac{\tilde{\mathbf{J}}}{2}. \tag{6.45}$$

By defining:

$$\mathbf{T} \triangleq \frac{\mathbf{I}}{k} - \frac{\tilde{\mathbf{J}}}{2} = \begin{bmatrix} \mathbf{I}/k & -\mathbf{\Omega}_0/2 \\ \mathbf{\Omega}_0/2 & \mathbf{I}/k \end{bmatrix}. \tag{6.46}$$

The matrix $\tilde{\mathbf{A}}^n$ can be expressed as the sum of $\mathbf{T}$ plus a rank-1 perturbation, allowing its inversion using the Sherman-Morrison formula [189]:

$$(\tilde{\mathbf{A}}^n)^{-1} = \mathbf{T}^{-1} - \frac{F_B^n\lambda^n}{2}\frac{\mathbf{T}^{-1}\tilde{\mathbf{d}}\tilde{\mathbf{d}}^{\mathsf{T}}\mathbf{T}^{-1}}{1 + \frac{F_B^n\lambda^n}{2}\tilde{\mathbf{d}}^{\mathsf{T}}\mathbf{T}^{-1}\tilde{\mathbf{d}}}. \tag{6.47}$$

Furthermore, $\mathbf{T}$ is block-diagonal, which allows for efficient decomposition using a block LUD factorisation [38]:

$$\mathbf{T} = \begin{bmatrix} \mathbf{T}_{11} & \mathbf{T}_{12} \\ \mathbf{T}_{21} & \mathbf{T}_{22} \end{bmatrix} = \begin{bmatrix} \mathbf{I} & \mathbf{0} \\ \mathbf{T}_{21}\mathbf{T}_{11}^{-1} & \mathbf{I} \end{bmatrix} \begin{bmatrix} \mathbf{T}_{11} & \mathbf{0} \\ \mathbf{0} & \mathbf{\Xi} \end{bmatrix} \begin{bmatrix} \mathbf{I} & \mathbf{T}_{11}^{-1}\mathbf{T}_{12} \\ \mathbf{0} & \mathbf{I} \end{bmatrix}, \tag{6.48}$$

and the inverse is computed as:

$$\mathbf{T}^{-1} = \begin{bmatrix} \mathbf{I} & -\mathbf{T}_{11}^{-1}\mathbf{T}_{12} \\ \mathbf{0} & \mathbf{I} \end{bmatrix} \begin{bmatrix} \mathbf{T}_{11}^{-1} & \mathbf{0} \\ \mathbf{0} & \mathbf{\Xi}^{-1} \end{bmatrix} \begin{bmatrix} \mathbf{I} & \mathbf{0} \\ -\mathbf{T}_{21}\mathbf{T}_{11}^{-1} & \mathbf{I} \end{bmatrix}$$
$$= \begin{bmatrix} \mathbf{T}_{11}^{-1} + \mathbf{T}_{11}^{-1}\mathbf{T}_{12}\mathbf{\Xi}^{-1}\mathbf{T}_{21}\mathbf{T}_{11}^{-1} & -\mathbf{T}_{11}^{-1}\mathbf{T}_{12}\mathbf{\Xi}^{-1} \\ -\mathbf{\Xi}^{-1}\mathbf{T}_{21}\mathbf{T}_{11}^{-1} & \mathbf{\Xi}^{-1} \end{bmatrix}. \tag{6.49}$$

Here, $\mathbf{\Xi} \triangleq \mathbf{T}_{22} - \mathbf{T}_{21}\mathbf{T}_{11}^{-1}\mathbf{T}_{12}$ is the Schur complement, which is diagonal due to algebraic operations between diagonal matrices. This decomposition allows for efficient matrix-vector multiplication involving $\mathbf{T}$ by breaking down the operation into serial steps involving diagonal matrices. Furthermore, since $\mathbf{T}$ is composed entirely of constant values, the factorisation components can be precomputed offline, significantly reducing compute time. Note that the same approach can be applied to system (6.37). In this case, however, the components $\mathbf{T}_{12}$ and $\mathbf{T}_{21}$ are tridiagonal, making multiplication of $\mathbf{T}$ with vectors less efficient due to the additional non-zero off-diagonal elements that need to be handled during the operation.

6.2.4   Numerical testing

Figure 6.3 reports the output displacement $u(t, x_o)$ of the string computed using schemes (6.26), (6.32), (6.35) and (6.44), under two values of F_B. All schemes were run with OF = 2 at a base sample rate $f_s = 44100$ Hz. As described previously, both SOIT and FOIT require the Newton-Raphson algorithm in vector form, including Jacobian inversion at each iteration; this was achieved using Matlab's backslash function, with a tolerance set to 10^{-9}. The backslash function was also employed for the non-iterative FONIT scheme, whereas the modal system used the efficient inversion technique detailed above. The two chosen values of F_B yield different motion types. When $F_B = 1$, the resulting motion is steady but not Helmholtz-like. Increasing the bowing pressure to $F_B = 5$ leads to fully developed Helmholtz motion. This change of motion regime with bowing pressure is consistent with the typical behaviour of musical strings, as represented by diagrams like Schelleng's [184] mentioned in Chapter 1. All solvers produce comparable results.

Table 6.1 presents the run-time/real-time ratio for the solvers and, for the iterative schemes, the average number of iterations per time-step at two different sample rates under different values of F_B. Run-times were measured using the Matlab `tic toc` function. As expected, the number of iterations rises with F_B as the system becomes "stiffer". On the other hand, the run-time for non-iterative schemes remains unaffected by F_B. The modal algorithm is the fastest among all the solvers. In contrast, the non-modal first-order systems are the slowest due to the explicit inversion of non-diagonal matrices (the Jacobian for FOIT
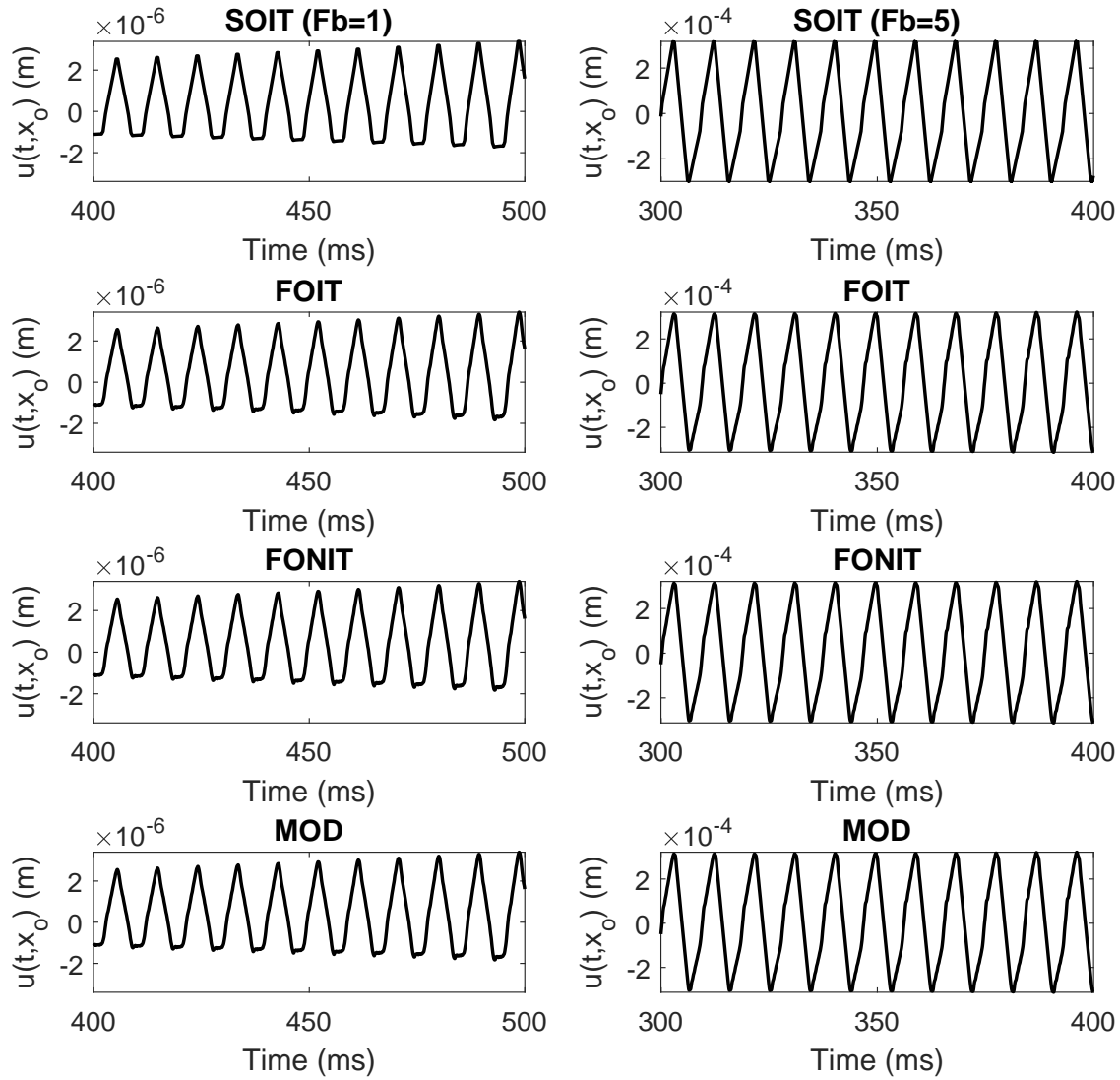
Fig. 6.3 Ideal string simulation. Both cases used: $c = 150$ m/s, $L = 0.7$ m, $v_B = 0.2$ m/s, $a = 100$. The input and output positions were, respectively, $0.633L$ and $0.33L$. Reproduced from [180].

OF	F_B	SOIT	FOIT	FONIT	MOD
	1	3.91 (3.00)	33.46 (3.00)	16.97	0.69
1	5	4.89 (3.61)	47.39 (3.83)	17.05	0.88
	30	6.45 (4.58)	54.26 (4.28)	16.86	0.87
	1	9.95 (3.00)	106.66 (3.00)	54.48	2.51
2	5	12.21 (3.48)	144.99 (3.72)	54.72	2.47
	30	25.14 (6.34)	167.38 (4.15)	54.90	2.58

Table 6.1 Run-time/real-time ratio for the different schemes with two OFs, under different values of F_B The string parameters are the same as in Figure 6.3. The average number of iterations per time step requested by Newton-Raphson to converge is reported in brackets for the iterative schemes. Reproduced from [180].

and $\mathbf{A}$ for FONIT), both of which are twice the size of the SOIT Jacobian. It should be noted that no specific optimizations were applied for SOIT, FOIT, or FONIT. In particular, efficient matrix inversion is also possible for the FONIT scheme, as described earlier. The results in Table 6.1 highlight the importance of optimizing linear system solvers, particularly in cases involving structured matrices, which are often overlooked by compilers.

As in the lumped case, analysing the energy behaviour of systems FONIT (in the distributed case) and MOD is complex. A case study can be found in [76]. Notably, the midpoint method eliminates the need for stability conditions on the linear parts, and these schemes remained stable in all simulations.

Since the focus here was on algorithmic optimization, the second-order integrator (3.14) was used for the modes. Employing the exact integrator (3.29) would have helped reduce dispersion issues without impacting the system's performance; this is left for future work.

6.3   Addition of stiffness and damping

The addition of stiffness and damping terms can be achieved directly in the modal domain. When considering a stiff string with simply supported boundaries, the mode shapes remain unchanged, while the eigenfrequencies are adjusted to include stiffness, as discussed in Chapter 2. To account for damping, a diagonal damping matrix can be introduced, with each diagonal element representing the damping coefficient for a specific mode, thereby enabling the modelling of complex damping profiles, such as that proposed by Valette and Cuesta [206]. The resulting system is:

$$\frac{\mathrm{d}^2\mathbf{w}}{\mathrm{d}t^2} = -\mathbf{\Omega}^2\mathbf{w} - \mathbf{C}\frac{\mathrm{d}\mathbf{w}}{\mathrm{d}t} - F_\mathrm{C}\boldsymbol{\chi}(x_\mathrm{C})\phi_\mathrm{C}(\eta), \qquad (6.50)$$

where Ω^2 now stores the eigenfrequencies as given by equation (2.123). The resulting system can be simulated with an algorithm analogous to that used for the ideal string, the only difference being that the matrices $\mathbf{T}$ and $\mathbf{B}$ are now augmented by the diagonal matrix $\mathbf{C}$. Since these can be computed offline, the efficiency of the algorithm is unaffected.
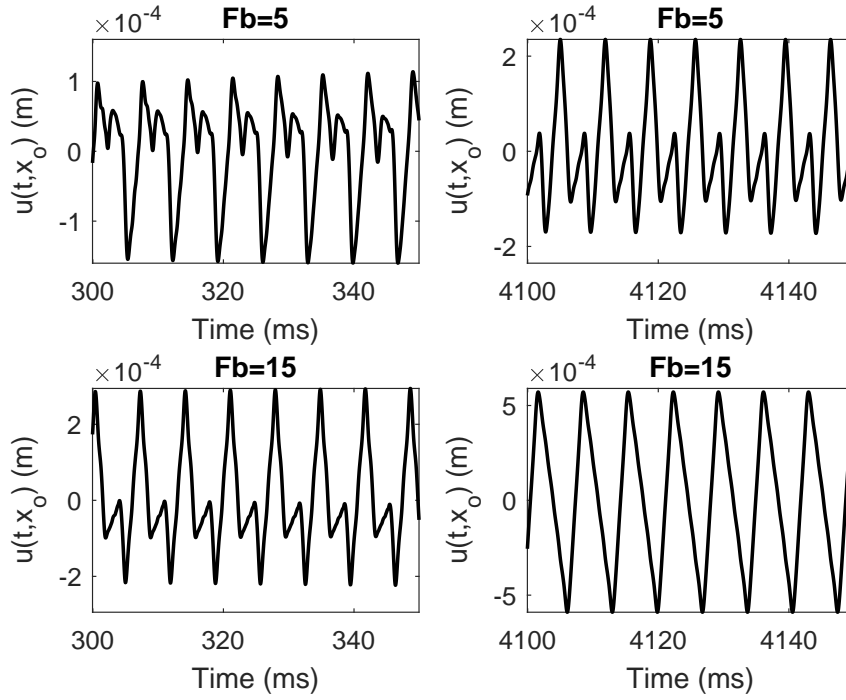
Fig. 6.4 Vibration regimes of the stiff string under two values of F_B. Plots on the same row are snapshots of the same waveform, taken in different time instants. String parameters were the ones of a D3 cello string, taken from [67]. Bowing parameters, input and output positions are as in Figure 6.3. Reproduced from [180].

Figure 6.4 illustrates different vibration regimes of the stiff string for two values of F_B, selected empirically to achieve specific types of string excitation. The plots in each row show snapshots of the same waveform at different times, capturing the string motion both at the onset of excitation and after reaching steady state. When $F_B = 5$, the string exhibits a multi-slip motion, whereas for $F_B = 15$ it reaches Helmholtz motion after a few seconds. Table 6.2 presents the run-time/real-time ratio for the stiff string simulations, demonstrating that the algorithm can achieve real-time performance even at high sample rates in Matlab. Notably, including string stiffness reduces the number of degrees of freedom (i.e., the number of harmonics in the audible range), thereby decreasing computational load compared to the simple wave equation.

OF $= 1$	OF $= 2$	OF $= 5$
0.19	0.39	0.91

Table 6.2 Run-time/real-time ratio for the stiff string, tested with different OF values. The base sampling frequency is $f_s = 44100$ Hz. Reproduced from [180].

While adding stiffness and damping significantly improves the realism of the string model, several approximations remain in the bowing mechanism. One such simplification, as previously mentioned, is the use of a non-physical friction curve; another is the reliance on a second-order integrator, which introduces frequency warping. Additionally, the bow-string interaction is modelled as a point-wise contact. In reality, a bow has a finite width, with multiple hairs touching the string simultaneously, and previous works have addressed this aspect, see, e.g. [186]. In principle, the non-iterative method presented here imposes no restrictions on incorporating this effect. However, further investigation is needed in this sense.

Chapter 7

Case studies

This chapter presents two papers that serve as musical case studies for the techniques introduced in the preceding chapters. All bibliographic references are provided within this chapter rather than at the end of the manuscript. Audio examples related to these papers are available on the companion page.

7.1 Physical modelling of the guitar

This section corresponds to a paper presented at the International Conference on Digital Audio Effects (DAFx) in 2024 [30]. It introduces a comprehensive guitar fretboard model incorporating the Kirchhoff-Carrier geometric nonlinearity for the string, along with three distinct collision nonlinearities representing the fretboard, individual frets, and a moving finger. Collisions are modelled using the SAV approach, resulting in a system involving three auxiliary variables and four nonlinear gradients (including the geometric nonlinearity). An important contribution of this work is the demonstration of a method for solving multiple nonlinearities altogether using SAV, achieved by employing multiple auxiliary variables. The paper's conclusion states: "A better approach would be to consolidate all of the nonlinear dynamics into a single scalar potential". Here, "better" refers to algorithmic efficiency. This approach necessitates inverting a small matrix with dimensions corresponding to the number of nonlinear gradients. In contrast, previous methods, such as that in [77], combined multiple nonlinearities into a single scalar auxiliary variable, enabling a fully explicit solver. However, the technique presented below offers greater control over the algorithmic design and flexibility for managing individual nonlinearities. For instance, as demonstrated in the paper, individual constraints may be introduced for each auxiliary variable, something impossible with the approach developed in [77].

REAL-TIME GUITAR SYNTHESIS

Stefan Bilbao

Acoustics and Audio Group
University of Edinburgh
Edinburgh, UK
sbilbao@ed.ac.uk

Riccardo Russo, Craig J. Webb and Michele Ducceschi *

Department of Industrial Engineering
University of Bologna
Bologna, Italy
riccardo.russo19@unibo.it,
craigjonathan.webb@unibo.it,
michele.ducceschi@unibo.it

ABSTRACT

The synthesis of guitar tones was one of the first uses of physical modeling synthesis, and many approaches (notably digital waveguides) have been employed. The dynamics of the string under playing conditions is complex, and includes nonlinearities, both inherent to the string itself, and due to various collisions with the fretboard, frets and a stopping finger. All lead to important perceptual effects, including pitch glides, rattling against frets, and the ability to play on the harmonics. Numerical simulation of these simultaneous strong nonlinearities is challenging, but recent advances in algorithm design due to invariant energy quadratisation and scalar auxiliary variable methods allow for very efficient and provably numerically stable simulation. A new design is presented here that does not employ costly iterative methods such as the Newton-Raphson method, and for which required linear system solutions are small. As such, this method is suitable for real-time implementation. Simulation and timing results are presented.

1. INTRODUCTION

Sound synthesis based on physical models of stringed instruments is a very old topic, with its origins in the quasi-physical feedback delay model of Karplus and Strong [1, 2]. Major advances followed from the physical interpretation of the bidirectional delay-line pair or digital waveguide [3, 4] in terms of traveling waves—opening the door to physical modeling for a wide array of instrument types, including the guitar [5, 6], the subject of this paper.

More recently, increasingly sophisticated models of the guitar have seen investigation. One avenue has been pure musical acoustics research, where full three-dimensional modeling of the interaction of the guitar body with the acoustic field is incorporated [7, 8]. Another, geared towards synthesis applications, has been the investigation of interactions between the string, finger and fretboard, allowing for a great deal of gestural control and nuance in performance. Various techniques have been employed, including digital waveguides [9], modal methods [10] and time-stepping methods such as the finite difference time domain (FDTD) method [11, 12], which have their roots in very early attempts at synthesis [13]. Here, we adopt the latter approach, due to the very general

flexibility of FDTD in handling multiple nonlinearities simultaneously. Such methods capture many subtle musical effects, including tapping, the rattling of strings against the frets and fretboard, and also the ability to play on string harmonics. See [14].

Such brute-force simulation methods are computationally intensive, and the move to real time is non-trivial. This expense stems from the strong collision nonlinearities, and the need for provably stable numerical methods (such as those ensuring energy conservation) for robust behaviour. These nonlinearities have been dealt with previously using iterative methods, such as Newton-Raphson, which are computationally intensive, and inherently serial. Recent algorithmic advances, based on invariant energy quadratisation (IEQ) [15, 16] and scalar auxiliary variable (SAV) [17, 18] approaches offer a means of sidestepping iterative methods entirely, and have been employed previously in order to accelerate physical modeling synthesis for strongly nonlinear instruments to the real-time threshold [19]. In particular, IEQ/SAV have seen use in modeling collisions within the context of musical acoustics [20, 21, 22]. In these studies, it was noted that computing the nonlinear collision force directly as the analytic potential energy gradient produced spurious oscillations, causing anomalous results in simulation, and various solutions have been proposed. Here, we present a variation of that in [22].

This paper can thus be viewed as a belated follow-up to a DAFx paper [11] from 2014, which outlined a full synthesis model of the finger/string/fretboard interaction—though well out of real time. Applying IEQ and SAV approaches allows for real-time performance for a full model of guitar string vibration for multiple strings, including four simultaneous nonlinearities: a) the distributed geometric nonlinearity in a string vibrating at high amplitudes; b) the interaction between a string with a smooth fretboard; c) the interaction between a string and an array of point-like obstacles (frets), and d) the interaction between the finger and string.

A complete model of transverse string vibration in a single polarization, including the various nonlinearities listed above, is described in Section 2, followed by a spatially semi-discrete form in Section 3, and a fully time-discrete algorithm in Section 4. Real-time implementation details and timing results follow in Section 5. and some numerical illustrations appear in Section 6. Some concluding remarks are offered in Section 7. Sound examples are available at the companion page [1].

2. MODEL SYSTEM

The model employed here appeared previously, with some minor alterations, in [11, 12], and will be presented in condensed form

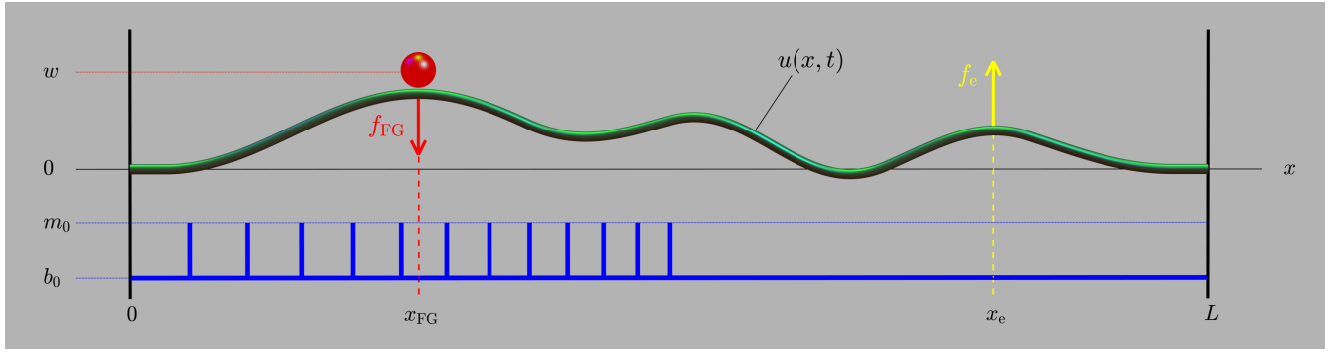[1] https://physicalaudio.co.uk/guitar/

Figure 1: *Guitar model, illustrating the string (in green), the fretboard and frets (in blue), the finger (in red), and plucking excitation force (in yellow).*

here. See Figure 1. The general equation of motion is

$$\mathcal{L} = \mathcal{F}_e + \mathcal{F}_{KC} + \mathcal{F}_B + \mathcal{F}_F + \mathcal{F}_{FG} . \tag{1}$$

The terms above are differential operators applied to $u = u(x,t)$, which represents the transverse displacement of a string in a single polarization (generally taken here to be perpendicular to the fretboard), and depends on spatial coordinate $x \in [0, L]$, for a string length L in m, and time t in s. Boundary conditions are assumed to be of simply supported type at the string endpoints, so that

$$u(0,t) = \partial_x^2 u(0.t) = u(L,t) = \partial_x^2 u(L,t) = 0 . \tag{2}$$

Output is assumed drawn directly from the string displacement at $x = x_o$ as $y(t) = u(x_o, t)$.

The linear free vibration of the string is encapsulated in the standard term $\mathcal{L}(u)$, defined as

$$\mathcal{L} = \rho A \partial_t^2 u - T_0 \partial_x^2 u + EI \partial_x^4 u + 2\rho A \sigma_0 \partial_t u - 2\rho A \sigma_1 \partial_t \partial_x^2 u \tag{3}$$

where ∂_t and ∂_x indicate partial differentiation with respect to t and x, respectively. The various parameters that appear here are: ρ, the mass density in kg· m^{-3}; $A = \pi r^2$, the string cross-sectional area in m^2 for a string of radius r m; T_0, the string tension in N; E, Young's modulus for the string, in Pa; $I = \pi r^4/4$, the moment of inertia of the string; and $\sigma_0 \geq 0$ and $\sigma_1 \geq 0$, two parameters that give frequency-dependent control over decay time—see [23] for a means of calibrating these values against 60 dB decay times.

The remaining terms in (1) are force densities, defined over the domain $x \in [0, L]$, and are presented consecutively below.

2.1. Plucking Excitation

$\mathcal{F}_e = \mathcal{F}_e(x,t)$ constitutes the pointwise external forcing of the string due to a single upward pluck, and may be modelled as

$$\mathcal{F}_e = \delta(x - x_e) f_e(t) . \tag{4}$$

Here, $\delta(x - x_e)$ is a Dirac delta function selecting the plucking location $x = x_e$, and $f_e(t)$ is a parameterized function of the form

$$f_e(t) = \begin{cases} f_{amp} \sin^2 \left(\frac{\pi(t-t_e)}{2\Delta} \right) & \text{when} \quad t_e \leq t \leq t_e + \Delta \\ 0 & \text{otherwise} \end{cases} \tag{5}$$

where here, f_{amp} is a maximum amplitude in N, t_e is the start time of the pulse in s, and Δ is the duration in s.

2.2. Geometric Nonlinearity

There are many possible models of geometric nonlinearity in strings [24]—most important here is the pitch glide effect, audible in guitar plucks at high amplitudes. This is most easily modeled through the simple Kirchhoff-Carrier model [25, 26], for which the additional force density $\mathcal{F}_{KC}$ is defined as

$$\mathcal{F}_{KC} = \frac{EA}{2L} \left(\int_0^L (\partial_x u)^2 \, dx \right) \partial_x^2 u . \tag{6}$$

The Kirchhoff-Carrier model has been used extensively in sound synthesis algorithms—see, e.g., [27, 23].

2.3. Fretboard Interaction

The fretboard (in the absence of frets) is modeled as a smooth function $b(x)$, with $b(x) \leq 0$ (so that the fretboard lies below the rest position of the string). In the simplest case, one may simply take $b(x) = b_0$, for a constant offset. The collision force density may be modelled through a penalty potential as

$$\mathcal{F}_B = K_B[b - u]_+^{\alpha_B} \tag{7}$$

where here $[\cdot]_+$ indicates the "positive part of," so $[\eta]_+ = (\eta + |\eta|)/2$. Here, $K_B \geq 0$ is the fretboard stiffness, and $\alpha_B \geq 1$ is the nonlinearity exponent. This collision force density is active only when the string is in contact with the barrier, and is otherwise zero. We employ a simple Hertzian model of contact, in line with models used in, e.g., piano hammer modelling [28], and in other models of string-barrier interaction [29, 30].

2.4. Fret Interaction

Assume that there are M frets, located at coordinates $x = x_1, \ldots, x_M$. (M is normally between 19 and 24 for standard guitars.) Interactions of the string with the frets is assumed to occur at their tips located at vertical height m_0—again with $m_0 \leq 0$, so that the rest position of the string lies above the fret tip. In addition, $m_0 \geq b(x_q)$, $q = 1, \ldots, M$, so that the frets themselves protrude from the fretboard. The resulting force density is

$$\mathcal{F}_F = \sum_{q=1}^{M} K_F[m_0 - u(x_q, t)]_+^{\alpha_F} \delta(x - x_q) . \tag{8}$$

As in the case of the barrier, $K_F \geq 0$ is the fret stiffness, and $\alpha_F \geq 1$ is the nonlinearity exponent. The eventual algorithm design is insensitive to the placement of frets—for standard semitone tuning, frets should be located at coordinates $x_q = L\left(1 - 2^{-q/12}\right)$.

2.5. Finger Interaction

The finger interaction must also be modelled as a collision, but in this case has its own dynamics to account for, as well as external forcing. The finger, of mass M_{FG} in kg is assumed to act at location $x = x_{FG}$. It is defined by

$$\mathcal{F}_{FG} = -f_{FG}\delta(x - x_{FG}) \quad f_{FG} = K_{FG}[u(x_{FG}, t) - w(t)]_+^{\alpha_{FG}} . \quad (9)$$

Here, $w(t)$ is the vertical displacement of the finger—its dynamics are governed by

$$M_{FG}\ddot{w} = f_{FG} + f_{e,FG} , \quad (10)$$

where dots indicate ordinary time differentiation. Here, $f_{e,FG}(t)$ is an externally-supplied driving force, employed in order to trap the string against the fretboard and frets. (Though we assume x_{FG} to be constant in this paper, it will ultimately be allowed to vary over time, in order to effect pitch changes.)

2.6. Energy Balance

The governing equation (1), accompanied by the definitions of the various force densities in Sections 2.1 to 2.5, satisfies an energy balance of the following form:

$$\dot{H} + Q = P . \quad (11)$$

Here, H is the total stored energy in the system in J, Q and P are the power loss and supplied power, respectively, in W. Furthermore, the stored energy may be decomposed into components representing the various storage mechanisms:

$$H = T_L + V_L + V_{KC} + V_B + V_F + T_{FG} + V_{FG} , \quad (12)$$

where components T and V indicate kinetic and potential energy, respectively. The constituent energy components and power terms are defined as follows:

$$T_L = \frac{\rho A}{2}\int_0^L (\partial_t u)^2 \, dx \quad (13a)$$

$$V_L = \frac{T_0}{2}\int_0^L (\partial_x u)^2 \, dx + \frac{EI}{2}\int_0^L (\partial_x^2 u)^2 \, dx \quad (13b)$$

$$V_{KC} = \frac{EA}{8L}\left(\int_0^L (\partial_x u)^2 \, dx\right)^2 \quad (13c)$$

$$V_B = \frac{K_B}{\alpha_B + 1}\int_0^L [b - u]_+^{\alpha_B + 1} dx \quad (13d)$$

$$V_F = \frac{K_F}{\alpha_F + 1}\sum_{q=1}^M [m_0 - u(x_q, t)]_+^{\alpha_F + 1} \quad (13e)$$

$$T_{FG} = \frac{M_{FG}}{2}\dot{w}^2 \quad (13f)$$

$$V_{FG} = \frac{K_{FG}}{\alpha_{FG}+1}[u(x_{FG}, t) - w]_+^{\alpha_{FG} + 1} \quad (13g)$$

$$Q = 2\rho A\left(\int_0^L \sigma_0 (\partial_t u)^2 + \sigma_1 (\partial_t \partial_x u)^2 \, dx\right) \quad (13h)$$

$$P = f_e\partial_t u(x_e, t) + f_{e,FG}\dot{w} . \quad (13i)$$

Note that $H \geq 0$ and $Q \geq 0$, implying that the system is dissipative in the absence of external forcing, or that $H(0) \geq H(t) \geq 0$.

3. SEMI-DISCRETE FORM

It is useful, as an intermediate step, to perform a spatial semi-discretisation of the system defined in the previous section. Suppose that the domain $[0, L]$ has been discretised with a grid spacing h, for integer $N = L/h$. Under supported boundary conditions in (2), a semi-discrete approximation to $u(x, t)$ may then be written as the $(N - 1) \times 1$ column vector $\mathbf{u}(t)$, where

$$\mathbf{u} = [u_1, \ldots, u_{N-1}]^T , \quad (14)$$

where ^{T} indicates transposition. In the vectorised setting, the second spatial derivative ∂_x^2 may be approximated by the $(N - 1) \times (N - 1)$ negative-definite matrix $\mathbf{D}$, which is of the form

$$\mathbf{D} = \frac{1}{h^2}\begin{bmatrix} \text{-2} & 1 & & & \\ 1 & \text{-2} & 1 & & \\ & \ddots & \ddots & \ddots & \\ & & 1 & \text{-2} & 1 \\ & & & 1 & \text{-2} \end{bmatrix} .$$

Consider a Dirac delta function selecting the location $x = x_c$. It may be approximated as

$$\delta(x - x_c) \quad \rightarrow \quad \frac{1}{h}\mathbf{j}^{(x_c)} , \quad (15)$$

where $\mathbf{j}^{(x_c)}$ is an $(N-1) \times 1$ column vector. It may be constructed by a variety of means using, perhaps, Lagrange interpolation. In general, it will be sparse and must satisfy the first moment condition [31], or that $\mathbf{1}^T\mathbf{j}^{(x_c)} = 1$, where $\mathbf{1}$ is an $(N - 1) \times 1$ vector consisting of ones (mirroring the property of the delta function that it integrates to unity). See [23]. Such a representation here can be used directly in order to simulate a pointwise forcing (as in (4), (8) or (9)), or as an interpolant, as in (8) or (9), so that

$$u(x_c, t) \rightarrow \left(\mathbf{j}^{(x_c)}\right)^T \mathbf{u}(t) . \quad (16)$$

The object here is to arrive at a semi-discrete form of (1):

$$\mathcal{L}^{(s)} = \mathcal{F}_e^{(s)} + \mathcal{F}_{KC}^{(s)} + \mathcal{F}_B^{(s)} + \mathcal{F}_F^{(s)} - \mathcal{F}_{FG}^{(s)} . \quad (17)$$

Distinct approaches to semi-discretisation will be taken for the different components of the model, grouped into categories as below.

3.1. Linear Operator and Excitation

The linear operator (3) may be semi-discretised immediately as

$$\mathcal{L}^{(s)} = \rho A\ddot{\mathbf{u}} - T_0\mathbf{D}\mathbf{u} + EI\mathbf{D}^2\mathbf{u} + 2\rho A\sigma_0\dot{\mathbf{u}} - 2\rho A\sigma_1\mathbf{D}\dot{\mathbf{u}} . \quad (18)$$

Using an approximation to a delta function as in (15), centered at x_e, the excitation force density (4) may be semi-discretised as

$$\mathcal{F}_e^{(s)} = \frac{1}{h}\mathbf{j}^{(x_e)}f_e(t) . \quad (19)$$

3.2. Geometric Nonlinearity

For the geometric nonlinearity, with force density as defined in (6), a semi-discrete form follows, using summation by parts, as

$$\mathcal{F}_{KC}^{(s)} = -\frac{EAh}{2L}\left(\mathbf{u}^T\mathbf{D}\mathbf{u}\right)\mathbf{D}\mathbf{u} . \quad (20)$$

3.3. Fretboard and Frets

For the fretboard and frets, a different approach is taken here, following the SAV methodology. Here, beginning from a semi-discrete potential energy term $V_*^{(s)}(\mathbf{u})$, one may write

$$V_*^{(s)} = \tfrac{1}{2}\psi_*^2 , \qquad (21)$$

where here, ψ is a scalar auxiliary variable—the key here is that the potential energy contribution has been quadratised. At this point, semi-discrete force densities follow as

$$\mathcal{F}_*^{(s)} = -\tfrac{1}{h}\nabla_{\mathbf{u}}V_*^{(s)} = -\tfrac{1}{h}\psi_*\underbrace{\nabla_{\mathbf{u}}\psi_*}_{\mathbf{g}} , \qquad (22)$$

where $\nabla_{\mathbf{u}}$ is a gradient with respect to the dependent variable $\mathbf{u}$. ψ becomes a new state variable, to be updated in an eventual discrete-time implementation. To this end, note that one may write

$$\dot{\psi}_* = (\nabla_{\mathbf{u}}\psi_*)^T \dot{\mathbf{u}} = \mathbf{g}_*^T \dot{\mathbf{u}} . \qquad (23)$$

The relevant semi-discrete potential energy terms, corresponding to the fretboard and frets are:

$$V_{\mathrm{B}}^{(s)} = \tfrac{K_{\mathrm{B}}h}{\alpha_{\mathrm{B}}+1}\mathbf{1}^T[\mathbf{b}-\mathbf{u}]_+^{\alpha_{\mathrm{B}}+1} \qquad (24a)$$

$$V_{\mathrm{F}}^{(s)} = \tfrac{K_{\mathrm{F}}}{\alpha_{\mathrm{F}}+1}\sum_{q=1}^{M}\left[m_0 - \left(\mathbf{j}^{(x_q)}\right)^T\mathbf{u}\right]_+^{\alpha_{\mathrm{F}}+1} . \qquad (24b)$$

Here, $\mathbf{b} = [b_1,\dots,b_{N-1}]^T$ is the fretboard profile sampled at the $N-1$ interior grid locations.

3.4. Finger

The case of the finger is similar to that of the frets and fretboard outlined above, but now the potential energy must include contributions from both the string and finger. Now, one may write

$$V_{\mathrm{FG}}^{(s)} = \frac{K_{\mathrm{FG}}}{\alpha_{\mathrm{FG}}+1}\left[\left(\mathbf{j}^{(x_{\mathrm{FG}})}\right)^T\mathbf{u} - w\right]_+^{\alpha_{\mathrm{FG}}+1} = \frac{1}{2}\psi_{\mathrm{FG}}^2 \qquad (25)$$

and thus

$$\mathcal{F}_{\mathrm{FG}}^{(s)} = -\tfrac{1}{h}\psi_{\mathrm{FG}}\underbrace{\nabla_{\mathbf{u}}\psi_{\mathrm{FG}}}_{\mathbf{g}_{\mathrm{FG}}} \quad\text{and}\quad f_{\mathrm{FG}}^{(s)} = -\psi_{\mathrm{FG}}\underbrace{\frac{\partial\psi_{\mathrm{FG}}}{\partial w}}_{g'_{\mathrm{FG}}} . \qquad (26)$$

The defining equation for w remains as in (10). It also follows that

$$\dot{\psi}_{\mathrm{FG}} = \mathbf{g}_{\mathrm{FG}}^T\dot{\mathbf{u}} + g'_{\mathrm{FG}}\dot{w} . \qquad (27)$$

The computation of $\mathbf{g}_*$ and g'_{FG} needs to be handled carefully—see Section 4.7 for details.

3.5. Energy Balance

An energy balance in the semi-discrete case is of the form of (11):

$$\dot{H}^{(s)} + Q^{(s)} = P^{(s)} , \qquad (28)$$

where $H^{(s)}$ has the same decomposition as in the continuous case in (12). For the linear system,

$$T_{\mathrm{L}}^{(s)} = \frac{\rho A h}{2}\|\dot{\mathbf{u}}\|^2 \quad V_{\mathrm{L}}^{(s)} = -\frac{T_0 h}{2}\mathbf{u}^T\mathbf{D}\mathbf{u} + \frac{EIh}{2}\mathbf{u}^T\mathbf{D}^2\mathbf{u} \quad (29)$$

where for a vector $\mathbf{f}$, $\|\mathbf{f}\|^2 = \mathbf{f}^T\mathbf{f}$. For the nonlinearities,

$$V_{\mathrm{KC}}^{(s)} = \frac{EAh^2}{8L}\left(\mathbf{u}^T\mathbf{D}\mathbf{u}\right)^2 \quad V_{\mathrm{B,F,FG}}^{(s)} = \tfrac{1}{2}\psi_{\mathrm{B,F,FG}}^2 . \qquad (30)$$

The kinetic energy for the finger, from (13f) remains unchanged under discretisation, and the loss and power terms become

$$Q^{(s)} = 2\rho A h\left(\sigma_0\|\dot{\mathbf{u}}\|^2 - \sigma_1\dot{\mathbf{u}}^T\mathbf{D}\dot{\mathbf{u}}\right) \qquad (31a)$$

$$P^{(s)} = f_e\left(\mathbf{j}^{(x_e)}\right)^T\dot{\mathbf{u}} + f_{\mathrm{FG}}^{(\mathrm{ext})}\dot{w} . \qquad (31b)$$

The non-negativity property of $H^{(s)}$ and $Q^{(s)}$ persists in the semi-discrete case (note that $\mathbf{D}$ is negative definite by construction).

4. FULLY DISCRETE FORM

First define a time step $k = 1/f_s$ in terms of a specified audio sample rate f_s in Hz. The $(N-1)\times 1$ vector $\mathbf{u}^n$ represents an approximation to $\mathbf{u}(t)$ at $t = nk$, for integer n. The excitation force signals $f_e(t)$ and $f_{\mathrm{FG}}(t)$ may be sampled as f_e^n and f_{FG}^n, respectively. For auxiliary variables $\psi_*(t)$, as defined in (21), an interleaved approximation $\psi_*^{n+1/2}$ is employed, representing an approximation to $\psi_*(t)$ at $t = (n+1/2)k$ for integer n.

Basic shifts e_+ and e_-, applied to a time series ζ^ν, where ν is either integer, or half-integer, are defined as

$$e_+\zeta^\nu = \zeta^{\nu+1} \qquad e_-\zeta^\nu = \zeta^{\nu-1} . \qquad (32)$$

Forward, backward and centered difference approximations to a first time derivative follow as

$$D_\pm = \pm\tfrac{1}{k}\left(e_\pm - 1\right) \quad D_\circ = \tfrac{1}{2k}\left(e_+ - e_-\right) \qquad (33)$$

and averaging operators $M_\pm$ and $M_\circ$ as

$$M_\pm = \tfrac{1}{2}\left(1 + e_\pm\right) \qquad M_\circ = \tfrac{1}{2}\left(e_+ + e_-\right) . \qquad (34)$$

An approximation to a second time derivative follows as

$$D_2 = D_+D_- = \tfrac{1}{k^2}\left(e_+ - 2 + e_-\right) . \qquad (35)$$

As in the semi-discrete case, we proceed through the various components of the full model.

4.1. Linear Operator and Excitation

The linear semi-discrete operator defined in (18) may be discretised as follows

$$\mathcal{L}^{(d),n} = \rho A D_2\mathbf{u}^n - T_0\mathbf{D}\mathbf{u}^n + EI\mathbf{D}^2\mathbf{u}^n \qquad (36)$$
$$+ 2\rho A\sigma_0 D_\circ\mathbf{u}^n - 2\rho A\sigma_1 D_-\mathbf{D}\mathbf{u}^n .$$

This is the standard "explicit" discretisation of the linear stiff string [23]. The semi-discrete form of the excitation force density from (19) remains the same, under the replacement of $f_e(t)$ by f_e^n.

4.2. Geometric Nonlinearity

Following early work on energy-conserving numerical methods for the Kirchhoff-Carrier string [32], the fully discrete form of the force density is chosen to be

$$\mathcal{F}_{\mathrm{KC}}^{(d),n} = -\frac{EAh}{2L}\left((\mathbf{u}^n)^T\mathbf{D}M_\circ\mathbf{u}^n\right)\mathbf{D}\mathbf{u}^n . \qquad (37)$$

Note the appearance of the additional time-averaging operation $M_\circ$, as defined in (34). A scalar auxiliary variable is not necessary in the discretisation of this nonlinearity.

4.3. Collisions: Fretboard and Frets

For the fretboard and frets, one may begin from the semi-discrete forms in (22) and (23), which may be discretized [18] as

$$\mathcal{F}_*^{(d),n} = -\frac{1}{h}\left(M_- \psi_*^{n+1/2}\right)\mathbf{g}_*^n \tag{38a}$$

$$D_-\psi_*^{n+1/2} = (\mathbf{g}_*^n)^T D_\circ \mathbf{u}^n . \tag{38b}$$

4.4. Collisions: Finger

Finally, the dynamics of the finger are discretised as

$$M_{\text{FG}} D_2 w^n = f_{\text{FG}}^{(d),n} + f_{e,\text{FG}}^n \tag{39}$$

where f_{FG}^n is sampled from $f_{e,\text{FG}}(t)$. The force density and force may be written as

$$\mathcal{F}_{\text{FG}}^{(d),n} = -\frac{1}{h}\left(M_- \psi_{\text{FG}}^{n+1/2}\right)\mathbf{g}_{\text{FG}} \quad f_{\text{FG}}^{(d),n} = -\left(M_- \psi_{\text{FG}}\right)g_{\text{FG}}'^{,n} . \tag{40}$$

It also follows that

$$D_-\psi_{\text{FG}}^{n+1/2} = (\mathbf{g}_{\text{FG}}^n)^T D_\circ \mathbf{u}^n + g_{\text{FG}}'^{,n} D_\circ w^n . \tag{41}$$

4.5. Energy Balance and Stability Condition

A discrete-time energy balance follows from the scheme above as

$$D_- H^{(d)} + Q^{(d)} = P^{(d)} , \tag{42}$$

where the decomposition of $H^{(d)} = H^{(d),n+1/2}$ is as in the continuous and semi-discrete cases, with all terms now assumed defined at time step $n + 1/2$. For the linear system,

$$T_{\text{L}}^{(d)} = \frac{\rho A h}{2}(D_-\mathbf{u}^{n+1})^T \left(\mathbf{I}_{N-1} + \sigma_1 k \mathbf{D}\right) D_-\mathbf{u}^{n+1} \tag{43a}$$

$$V_{\text{L}}^{(d)} = \frac{h}{2}(\mathbf{u}^n)^T \left(-T_0 \mathbf{D} + EI\mathbf{D}^2\right)\mathbf{u}^{n+1} . \tag{43b}$$

For the nonlinearities,

$$V_{\text{KC}}^{(d)} = \frac{EAh^2}{8L}\left((\mathbf{u}^{n+1})^T \mathbf{D}\mathbf{u}^n\right)^2 \quad V_{\text{B,F,FG}}^{(d)} = \frac{1}{2}\left(\psi_{\text{B,F,FG}}^{n+1/2}\right)^2 . \tag{44}$$

For the finger inertia, one has

$$T_{\text{FG}}^{(d)} = \frac{M_{\text{FG}}}{2}(D_- w^{n+1})^2 . \tag{45}$$

The loss and power terms, defined at time step n, become

$$Q^{(d)} = 2\rho A h \left(\sigma_0\|D_\circ \mathbf{u}^n\|^2 - \sigma_1 (D_\circ \mathbf{u}^n)^T \mathbf{D} D_\circ \mathbf{u}^n\right) \tag{46a}$$

$$P^{(d)} = f_e^n \left(\mathbf{j}^{(x_e)}\right)^T D_\circ \mathbf{u}^n + f_{e,\text{FG}}^n D_\circ w^n . \tag{46b}$$

For stability, note first that $Q^{(d)} \geq 0$. It remains to find conditions under which the stored energy $H^{(d)} \geq 0$. Given that the nonlinear potential energy contributions from (44) are all nonnegative, all that is necessary is to find a non-negativity condition on the linear potential and kinetic energy terms, from (43). This leads, ultimately, to the bound $h \geq h_{\min}$, where

$$h_{\min}^2 = \frac{k}{2}\left(\frac{T_0 k}{\rho A} + 4\sigma_1 + \sqrt{\left(\frac{T_0 k}{\rho A} + 4\sigma_1\right)^2 + \frac{16EI}{\rho A}}\right) . \tag{47}$$

This serves as a numerical stability condition for the scheme [11].

4.6. Condensed Vector-matrix Update Form

The scheme presented in the previous sections is undeniably complex—mainly because of the use of disparate discretisation approaches for different parts of the problem—all in the interest of maximizing efficiency. The key feature is that in all the updates presented, the unknown appears linearly, meaning that iterative methods such as Newton-Raphson are not needed. What is perhaps less obvious is that the algorithm is mainly explicit, with only a small (size four) linear system solution required. It is thus useful to see the ultimate form of the update.

First, define a combined state $\mathbf{z}^n = [(\mathbf{u}^n)^T, w^n]^T$, including both the string displacement and finger displacement in a single $N \times 1$ column vector. Furthermore, one may also consolidate the three scalar potentials into a single 3×1 column vector as $\boldsymbol{\Psi}^{n+1/2} = [\psi_{\text{B}}^{n+1/2}, \psi_{\text{F}}^{n+1/2}, \psi_{\text{FG}}^{n+1/2}]^T$, and the two input force signals into a 2×1 vector $\mathbf{f}^n = [f_e^n, f_{e,\text{FG}}^n]^T$. Given $\mathbf{z}^n$ and $\mathbf{z}^{n-1}$, as well as $\boldsymbol{\Psi}^{n-1/2}$, it is possible to write the entire update as the sequence of operations

$$\mathbf{A}^n \mathbf{z}^{n+1} = \mathbf{b}^n \quad \boldsymbol{\Psi}^{n+1/2} = \boldsymbol{\Psi}^{n-1/2} + \frac{1}{2}\left(\mathbf{G}^n\right)^T \left(\mathbf{z}^{n+1} - \mathbf{z}^{n-1}\right) . \tag{48}$$

In the primary update of $\mathbf{z}^{n+1}$, $\mathbf{A}^n$ and $\mathbf{b}^n$ are an $N \times N$ matrix and $N \times 1$ vector, respectively; both must be constructed anew at each time step. The vector $\mathbf{b}^n$ may be written as

$$\begin{aligned}\mathbf{b}^n =\ & \mathbf{B}\mathbf{z}^n + \mathbf{C}\mathbf{z}^{n-1} + \mathbf{E}\mathbf{f}^n \\ & -\boldsymbol{\Lambda}\mathbf{G}^n \boldsymbol{\Psi}^{n-1/2} + \frac{1}{4}\boldsymbol{\Lambda}\mathbf{G}^n (\mathbf{G}^n)^T \mathbf{z}^{n-1} - \mathbf{k}^n (\mathbf{k}^n)^T \mathbf{z}^{n-1} . \end{aligned} \tag{49}$$

Here, $\mathbf{B}$ and $\mathbf{C}$ are $N \times N$ constant matrices, and $\mathbf{E}$ is an $N \times 2$ constant matrix, defined by

$$\mathbf{B} = \begin{bmatrix} \frac{1}{1+\sigma_0 k}\left(2\mathbf{I}_{N-1} + \frac{T_0 k^2}{\rho A}\mathbf{D} - \frac{EIk^2}{\rho A}\mathbf{D}^2 + 2\sigma_1 k \mathbf{D}\right) & \mathbf{0} \\ \mathbf{0} & 2 \end{bmatrix} \tag{50a}$$

$$\mathbf{C} = \begin{bmatrix} \frac{1}{1+\sigma_0 k}\left((\sigma_0 k - 1)\mathbf{I}_{N-1} - 2\sigma_1 k \mathbf{D}\right) & \mathbf{0} \\ \mathbf{0} & -1 \end{bmatrix} \tag{50b}$$

$$\mathbf{E} = \begin{bmatrix} \frac{k^2}{\rho A h (1+\sigma_0 k)}\mathbf{j}_e & \mathbf{0} \\ 0 & \frac{k^2}{M_{\text{FG}}} \end{bmatrix} \tag{50c}$$

that represent the linear dynamics of the string simulation, where $\mathbf{I}_{N-1}$ is the $(N-1) \times (N-1)$ identity matrix. All are extremely sparse. The term involving the $N \times 3$ matrix $\mathbf{G}^n$ and $N \times N$ constant diagonal scaling matrix $\boldsymbol{\Lambda}$, defined by

$$\mathbf{G}^n = \begin{bmatrix} \mathbf{g}_{\text{B}}^n & \mathbf{g}_{\text{F}}^n & \mathbf{g}_{\text{FG}}^n \\ 0 & 0 & g_{\text{FG}}'^{,n} \end{bmatrix} \quad \boldsymbol{\Lambda} = \begin{bmatrix} \frac{k^2}{\rho A h (1+\sigma_0 k)}\mathbf{I}_{N-1} & \mathbf{0} \\ \mathbf{0} & \frac{k^2}{M_{\text{FG}}} \end{bmatrix} \tag{51}$$

follow from the collision model. Notice that the same matrix $\mathbf{G}^n$ is used in the update of $\boldsymbol{\Psi}^{n+1/2}$, from (48). The $N \times 1$ vector $\mathbf{k}^n$ follows from the Kirchhoff-Carrier model, and is defined as

$$\mathbf{k}^n = \frac{k}{2}\sqrt{\frac{Eh}{\rho L (1+\sigma_0 k)}}[(\mathbf{D}\mathbf{u}^n)^T, 0]^T . \tag{52}$$

Finally, the matrix $\mathbf{A}$ is defined as

$$\mathbf{A} = \mathbf{I}_N + \frac{1}{4}\boldsymbol{\Lambda}\mathbf{G}^n (\mathbf{G}^n)^T + \mathbf{k}^n (\mathbf{k}^n)^T . \tag{53}$$

In terms of computational cost, the main nontrivial operations are the calculations of the vectors $\mathbf{g}_*$—see the next section for

more details. Beyond this, all other operations are sparse. An exception is the need for a linear system solution in (48) involving the $N \times N$ matrix $\mathbf{A}^n$ in (53). But $\mathbf{A}^n$ is in the form of a low-rank (four) perturbation of the identity, and thus very efficient resolution methods such as the Woodbury identity [33] can be employed. This avoids both the computational expense of iterative methods, and of fully linearly-implicit methods, where in general one would require the resolution of a full linear system of size N, and thus is the key to real-time performance.

Audio output y^n is drawn from the string as $y^n = (\mathbf{j}^{(x_\circ)})^T \mathbf{u}^n$, where $\mathbf{j}^{(x_\circ)}$ is an interpolant selecting the location $x = x_\circ$.

4.7. Calculation of Potential Gradients

Vectors of the form $\mathbf{g}_*^n$, which scale with the gradient of a potential, and as defined in (22), play a central role in the operation of the scheme described above. The simplest choice for computing the nonlinear potential gradients is using the analytic expressions:

$$\tilde{\mathbf{g}}_*^n = \frac{(\nabla_{\mathbf{u}} V_*)^n}{\sqrt{2 V_*^n + \epsilon}} \quad \tilde{g}_{\mathrm{FG}}^{\prime,n} = \frac{(\partial V_{\mathrm{FG}}/\partial w)^n}{\sqrt{2 V_{\mathrm{FG}}^n + \epsilon}} \qquad (54)$$

where ϵ is a small gauge constant [18], in this case set as machine epsilon. Here, the values V_*^n are obtained by evaluating equations (24) and (25) at time step n, and the gradients take the form:

$$(\nabla_{\mathbf{u}} V_{\mathrm{B}})^n = -h K_{\mathrm{B}} [\mathbf{b} - \mathbf{u}^n]_+^{\alpha_{\mathrm{B}}} \qquad (55a)$$

$$(\nabla_{\mathbf{u}} V_{\mathrm{F}})^n = -K_{\mathrm{F}} [m_0 - \mathbf{J}^\mathsf{T} \mathbf{u}^n]^{\alpha_{\mathrm{F}}} \qquad (55b)$$

$$(\partial V_{\mathrm{FG}}/\partial w)^n = -K_{\mathrm{FG}} \left[\left(\mathbf{j}^{(x_{\mathrm{FG}})} \right)^T \mathbf{u}^n - w^n \right]_+^{\alpha_{\mathrm{FG}}} \qquad (55c)$$

$$(\nabla_{\mathbf{u}} V_{\mathrm{FG}})^n = -\mathbf{j}^{(x_{\mathrm{FG}})} (\partial V_{\mathrm{FG}}/\partial w)^n \qquad (55d)$$

where $\mathbf{J}$ is a $(N-1) \times M$ matrix whose columns are the fret interpolators $\mathbf{j}^{(x_q)}$.

It is known, however, that simply using the analytic values produces an anomalous behaviour of the auxiliary variable $\psi^{n-1/2}$, that a) can exhibit long-term drift [34], and b) exhibits spurious sign flipping, meaning that the resulting force may be oriented incorrectly. The solution proposed in [22] is to impose the constraint $\psi^{n+1/2} \geq 0$. This results in a quadratic equation to be solved during contact times, yielding a scaling factor for $\tilde{\mathbf{g}}_*^n$. In this work, we propose a similar method, applied here to the computation of $\tilde{\mathbf{g}}_B^n$ and $\tilde{\mathbf{g}}_F^n$ (and not to the finger, which exhibited less drift than in the case of the fretboard or frets). The technique described here is based on the constraint: $M_- \psi_*^{n+1/2} \geq 0$. In fact, from (38a), it is apparent that if $M_- \psi_*^{n+1/2}$ remains positive, the sign of the expression is determined only by $\mathbf{g}_*^n$, which is negative by definition. This ensures that the force $\mathcal{F}_*^{(\mathrm{s})}$ is oriented upwards. By considering equation (38b), the constraint becomes:

$$2 \psi_*^{n-1/2} + \frac{1}{2} (\mathbf{g}_*^n)^T (\hat{\mathbf{u}}^{n+1} - \mathbf{u}^{n-1}) \geq 0 . \qquad (56)$$

Here, $\hat{\mathbf{u}}^{n+1}$ is the update of the system with no external forcing, and in presence of only the relevant nonlinearity (from the fretboard or frets). In this case, the Woodbury identity reduces to the Sherman-Morrison formula [35], and one has:

$$\hat{\mathbf{u}}^{n+1} = \hat{\mathbf{b}}^n - \frac{\frac{1}{4} \hat{\mathbf{\Lambda}} \mathbf{g}_*^n (\mathbf{g}_*^n)^\mathsf{T} \hat{\mathbf{b}}^n}{1 + \frac{1}{4} (\mathbf{g}_*^n)^\mathsf{T} \hat{\mathbf{\Lambda}} \mathbf{g}_*^n} , \qquad (57)$$

with

$$\hat{\mathbf{b}}^n = \hat{\mathbf{B}} \mathbf{u}^n + \hat{\mathbf{C}} \mathbf{u}^{n-1} - \hat{\mathbf{\Lambda}} \mathbf{g}_*^n \psi_*^{n-1/2} + \frac{1}{4} \hat{\mathbf{\Lambda}} \mathbf{g}_*^n (\mathbf{g}_*^n)^\mathsf{T} \mathbf{u}^{n-1} . \qquad (58)$$

Here, $\hat{\mathbf{B}}$, $\hat{\mathbf{C}}$, $\hat{\mathbf{\Lambda}}$ are the upper left-hand $(N-1) \times (N-1)$ blocks of (50a), (50b) and $\mathbf{\Lambda}$ in (51) respectively. By inserting (57) and (58) into (56) and solving for $\mathbf{g}_*^n$ one gets:

$$4 \psi_*^{n-1/2} + \underbrace{(\mathbf{g}_*^n)^\mathsf{T} (\hat{\mathbf{B}} \mathbf{u}^n + \hat{\mathbf{C}} \mathbf{u}^{n-1} - \mathbf{u}^{n-1})}_{\xi^n} \geq 0 . \qquad (59)$$

Now, as in [22], let $\mathbf{g}_*^n \triangleq \gamma \tilde{\mathbf{g}}_*^n$, where γ is a scalar. Then, (59) becomes a first-order, scalar inequality in γ. The linearity of the expression guarantees a unique solution under the condition:

$$\gamma \geq -4 \psi_*^{n-1/2} / \xi^n . \qquad (60)$$

Equation (60) yields a scalar multiplier for $\tilde{\mathbf{g}}_*^n$, to be applied when (59) is not satisfied for $\mathbf{g}_*^n = \tilde{\mathbf{g}}_*^n$. Thus, we set γ as:

$$\gamma = \begin{cases} -\frac{4 \psi_*^{n-1/2}}{\xi^n}, & \text{if } \xi^n \neq 0 \text{ and } \xi^n < -4 \psi_*^{n-1/2} \\ -\frac{\lambda 4 \psi_*^{n-1/2}}{\xi^{n-1}}, & \text{if } \xi^n = 0 \text{ and } \xi^{n-1} \neq 0 \\ 1, & \text{otherwise} \end{cases} . \qquad (61)$$

While the upper condition is designed to ensure the non-negativity of $M_- \psi_*^{n+1/2}$, the purpose of the middle condition is perhaps less obvious. Here, $\xi^{n-1} = (\tilde{\mathbf{g}}_*^{n-1})^\mathsf{T} (\hat{\mathbf{B}} \mathbf{u}^n + \hat{\mathbf{C}} \mathbf{u}^{n-1} - \mathbf{u}^{n-1})$, and the condition is satisfied only at the first instants without contact. Using the gradient from the previous time-step enforces $M_- \psi^{n+1/2} = 0$, meaning that no residual energy is stored during non-contact periods. Finally, λ is a scalar multiplier that allows the condition (60) to be satisfied away from the equality. Here, it was set $\lambda = 0.5$ if $-4 \psi^{n-1/2} / \xi^{n-1} < 0$ and $\lambda = 1.5$ if $-4 \psi^{n-1/2} / \xi^{n-1} \geq 0$.

5. REAL-TIME IMPLEMENTATION AND TIMING RESULTS

The algorithm was prototyped initially in the Matlab environment, and then ported to offline C++ in order to gauge the CPU performance on a number of different machines. Whilst the vector-matrix form described in Section 4.6 is algebraically compact and efficient for prototyping in Matlab, for high performance C++ the sparse matrix operations are unrolled into their equivalent vector updates. The core elements of the algorithm that are performed at each time step are as follows: a) compute the linear update to the string and finger, for the terms in (49) employing the matrices $\mathbf{B}$, $\mathbf{C}$ and $\mathbf{E}$; b) compute $\mathbf{k}^n$ from (52), and the accompanying term in (49); compute the columns of $\mathbf{G}^n$ from (51) corresponding to c) the fretboard, d) the frets and e) the finger, and the accompanying term in (49); and f) perform the linear system solution required in (48), using the construction of $\mathbf{A}^n$ from (53) and the Woodbury identity, and the update of $\Psi^{n+1/2}$ from (48). Final steps of negligible computational cost are the reading the output and a pointer swap of the state vectors. With attention to the content and data arrangement in the FOR loops being used, the Clang compiler at -Ofast was able to fully vectorise all of the core updates of the algorithm without the use of manual intrinsics.

Performance testing was carried out on a model containing a single string with 20 frets on the fretboard and a single finger. The

tension and radius of the string were varied to give results for a typical set of acoustic guitar strings from low E to top E tuning. Test machines were a Mac Pro with a Xeon E5 processor, a Mac mini with Apple Silicon M1 processor, and MacBook Pro with an M2 Pro. Table 1 shows the resulting computation times for simulations of 44100 timesteps.

Table 1: *Computation times for C++ over 44100 time-steps.*

String	Xeon E5	Apple M1	Apple M2 Pro
1 (low E)	0.18s	0.13s	0.11s
2	0.18s	0.13s	0.11s
3	0.15s	0.11s	0.10s
4	0.13s	0.09s	0.08s
5	0.12s	0.08s	0.06s
6 (top E)	0.09s	0.06s	0.04s

These results show that it is possible to run a 6-voice model for a full guitar simulation within the necessary bounds for a real-time instrument. Examining the CPU usage for the various elements of the time-loop computation gives a breakdown as shown in Table 2 for a low E string (the worst case in terms of compute time).

Table 2: *Computation breakdown for optimised C++ for a low E string.*

Section	Compute %
a) Linear update	2.3%
b) Kirchhoff-Carrier	1.9%
c) Fretboard	19.1%
d) Frets	7.7%
e) Finger	5.1%
f) SAV update and solver	63.9%

6. SIMULATION RESULTS

6.1. Numerical Energy Balance

The numerical energy balance (42) is easily demonstrated under unforced conditions. In order to incorporate the effects of loss, it is direct to define a total energy $E^{(d)}$, including stored energy $H^{(d)}$ and accumulated dissipated energy $Q^{(d)}$ as in Section 4.5, as

$$E^{(d),n+1/2} = H^{(d),n+1/2} + \sum_{\nu=0}^{n} kQ^{(d),\nu} . \tag{62}$$

This quantity should be conserved to near machine precision. See Figure 2, illustrating the time evolution of the various components of the discrete energy, as well as the relative deviation, defined as: $\Delta E^n = \frac{E^{(d),n+1/2} - E^{(d),n-1/2}}{\lfloor H^{(d),1/2} \rfloor_2}$, where the operator $\lfloor \eta \rfloor_2$ indicates the nearest power of two to η, rounding towards zero.

6.2. Audio Simulations

Figure 3 displays the spectrograms of the output signals in three different situations: a) the string is plucked with force of $f_e = 5N$, at $x_e = 0.8L$, and only the geometric nonlinearity is active. A pitch glide is clearly observable; b) the string is plucked as in
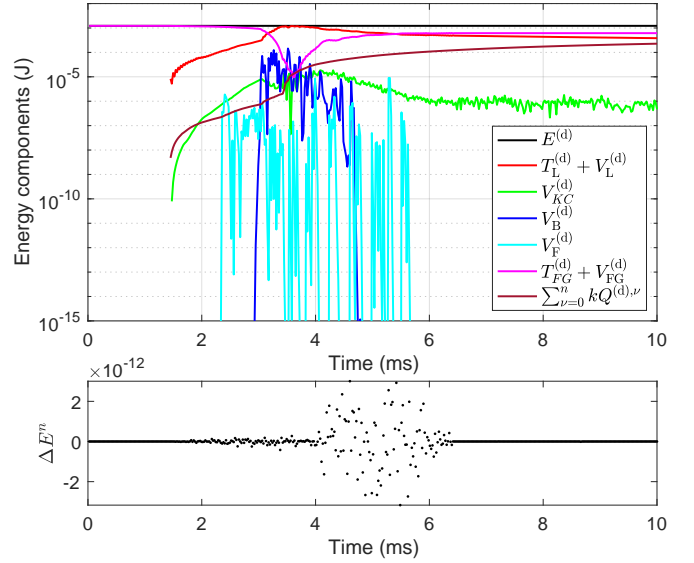

Figure 2: *Numerical energy balance. The upper panel displays the evolution of the discrete energy components over time. The string is at rest, while the finger is initially positioned above the string, with a starting velocity of -0.7 m/s. The second panel represents the relative energy deviation in the same situation, as defined in Section 6.1.*

(a), and all nonlinearities but the finger are active. The rattling of the string against the fretboard and the frets is evident at the first instants; c) all nonlinearities are active, and the string is not plucked, but the finger is excited with a constant force of $f_{e,FG} = 0.9$ N, the result is similar to a finger tap sound.

7. CONCLUDING REMARKS

An efficient method for the simulation of complex dynamics of the guitar string has been presented here. In terms of efficiency, it is near to the "baseline" cost of the simulation of a string under linear conditions, while retaining the feature of an energy balance, leading to a stable algorithm. Simulation in real time for a full six-string acoustic guitar is comfortably within the capability of modest commercially-available hardware.

This good performance relies on judicious choices of discretisation strategies for the different parts of the problem—explicit methods for the linear part of the problem, coupled with specialised energy-based discretisation methods for the nonlinear components of the dynamics. Here, we have chosen to attack the four distinct nonlinearities separately, leading to a 4×4 linear system—which is not expensive. A better approach would be to consolidate all of the nonlinear dynamics into a single scalar potential, eliminating the need for any linear system solution, at the expense of less algorithmic control (and in particular the distinct approaches to the calculation of the potential gradients, as discussed in Section 4.7.

Many features have not been included here. Most important are: a) string motion in distinct polarisations, and b) the modeling of the coupling to the body and radiation. Incorporating a) is certainly possible, and would roughly double computational cost,
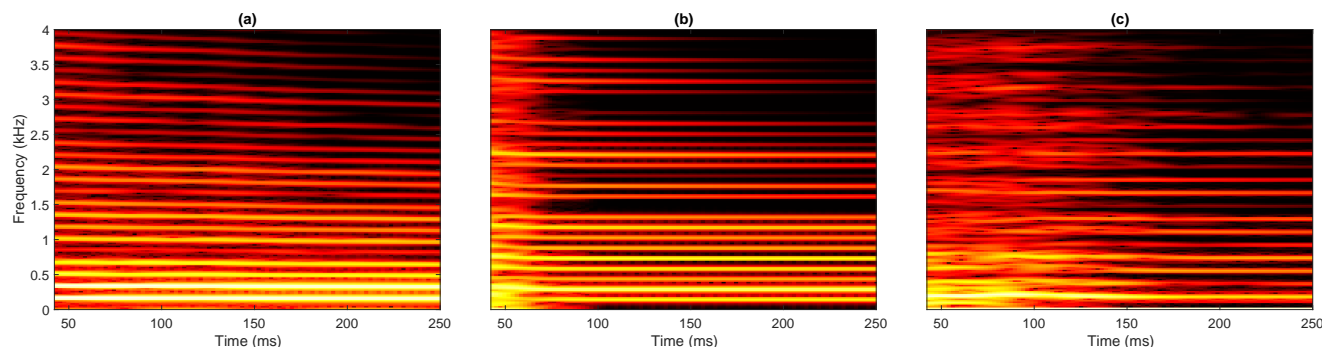
Figure 3: *Audio simulations: a) plucked string with geometric nonlinearity alone; b) plucked string with geometric, fretboard and frets nonlinearities; c) finger tap simulation. These spectrograms correspond to a guitar D string, with parameters as given in [11].*

and introduce a wider sound palette, through the angle of plucking relative to the fretboard (and the accompanying additional control complexity). Incorporating b) through a full physical model is infeasible, though such effects can be approximated through the use of measured body responses. Further work in the very near future will include plugin development, and examining the very large problem of instrument control—not addressed here.

8. REFERENCES

[1] K. Karplus and A. Strong, "Digital synthesis of plucked-string and drum timbres," *Comp. Music J.*, vol. 7, no. 2, pp. 43–55, 1983.

[2] D. Jaffe and J. O. Smith III, "Extensions of the Karplus-Strong plucked string algorithm," *Comp. Music J.*, vol. 7, no. 2, pp. 56–68, 1983.

[3] J. O. Smith III, "Efficient simulation of the reed-bore and bow-string mechanisms," in *Proc. of Int. Comp. Music Conf.*, The Hague, The Netherlands, October 1986, pp. 275–280.

[4] J. O. Smith III, "Physical modelling using digital waveguides," *Comp. Music J.*, vol. 16, no. 4, pp. 74–91, 1992.

[5] M. Karjalainen, V. Välimäki, and Z. Janosy, "Towards high-quality sound synthesis of the guitar and string instruments," in *Proc. Int. Comp. Music Conf.*, Tokyo, Japan, September 1993, pp. 56–63.

[6] M. Laurson, C. Erkut, V. Välimäki, and M. Kuuskankare, "Methods for modeling realistic playing in acoustic guitar synthesis," *Comp. Music J.*, vol. 25, no. 3, pp. 38–49, 2001.

[7] G. Derveaux, A. Chaigne, P. Joly, and E. Bécache, "Time-domain simulation of a guitar: Model and method," *J. Acoust. Soc. Am.*, vol. 114, no. 6, pp. 3368–3383, 2003.

[8] R. Bader, *Computational Mechanics of the Classical Guitar*, Springer-Verlag, Berlin Heidelberg, 2005.

[9] G. Evangelista and F. Eckerholm, "Player instrument interaction models for digital waveguide synthesis of guitar: Touch and collisions," *IEEE Trans. Audio Speech Language Proces.*, vol. 18, no. 4, pp. 822–832, 2010.

[10] V. Debut and J. Antunes, "Physical synthesis of six-string guitar plucks using the Udwadia-Kalaba modal formulation," *J. Acoust. Soc. Am.*, vol. 148, no. 2, pp. 575–587, 2020.

[11] S. Bilbao and A. Torin, "Numerical modeling of string/barrier collisions: The fretboard," in *Proc. 17th Int. Conf. Digital Audio Effects*, Erlangen, Germany, Sept. 2014.

[12] S. Bilbao and A. Torin, "Numerical modeling and sound synthesis for articulated string/fretboard interactions," *J. Audio Eng. Soc.*, vol. 63, no. 5, pp. 336–347, 2015.

[13] L. Hiller and P. Ruiz, "Synthesizing musical sounds by solving the wave equation for vibrating objects: Part I," *J. Audio Eng. Soc.*, vol. 19, no. 6, pp. 462–70, 1971.

[14] S. Bilbao, C. Desvages, M. Ducceschi, B. Hamilton, R. Harrison, A. Torin, and C. Webb, "Physical modeling, algorithms and sound synthesis: The NESS project," *Comp. Music J.*, vol. 43, no. 2/3, pp. 15–30, 2020.

[15] X. Yang and D. Han, "Linearly first- and second-order, unconditionally energy stable schemes for the phase field crystal model," *J. Comp. Phys.*, vol. 330, pp. 1116–1134, 2016.

[16] X. Yang, J. Zhao, and Q. Wang, "Numerical approximations for the molecular beam epitaxial growth model based on the invariant energy quadratization method," *J. Comp. Phys.*, vol. 333, pp. 104–127, 2017.

[17] J. Shen, J. Xu, and J. Yang, "The scalar auxiliary variable (SAV) approach for gradient flows," *J. Comp. Phys.*, vol. 353, pp. 407–416, 2018.

[18] S. Bilbao, M. Ducceschi, and F. Zama, "Explicit exactly energy-conserving methods for hamiltonian systems," *J. of Comp. Phys.*, vol. 472, pp. 111697, 2023.

[19] M. Ducceschi and S. Bilbao, "Simulation of the geometrically exact nonlinear string via energy quadratisation," *J. Sound Vib.*, vol. 534, pp. 117021, 2022.

[20] M. Ducceschi and S. Bilbao, "Real-time simulation of the struck piano string with geometrically exact nonlinearity via novel quadratic hamiltonian method," in *Proc. 10th Eur. Nonlinear Dynamics Conf.*, Lyon, France, July 2022.

[21] M. Ducceschi, S. Bilbao, S. Willemsen, and S. Serafin, "Linearly-implicit schemes for collisions in musical acoustics based on energy quadratisationa)," *J. Acoust. Soc. Am.*, vol. 149, no. 5, pp. 3502–3516, 05 2021.

[22] M. van Walstijn, V. Chatziioannou, and A. Bhanuprakash, "Implicit and explicit schemes for energy-stable simulation of string vibrations with collisions: Refinement, analysis, and comparison," *J. Sound Vib.*, vol. 569, pp. 117968, 2024.

[23] S. Bilbao, *Numerical Sound Synthesis: Finite Difference Schemes and Simulation in Musical Acoustics*, John Wiley and Sons, Chichester, UK, 2009.

[24] P. Morse and U. Ingard, *Theoretical Acoustics*, Princeton University Press, Princeton, NJ, USA, 1968.

[25] G. Kirchhoff, *Vorlesungen über Mechanik*, Tauber, Leipzig, 1883.

[26] G. F. Carrier, "On the non-linear vibration problem of the elastic string," *Q. Appl. Math.*, vol. 3, no. 2, pp. 157–165, 1945.

[27] T Tolonen, V. Välimäki, and M. Karjalainen, "Modelling of tension modulation nonlinearity in plucked strings," *IEEE Trans. Speech Audio Proces.*, vol. 8, pp. 300–310, 2000.

[28] A. Chaigne and A. Askenfelt, "Numerical simulations of struck strings. I. A physical model for a struck string using finite difference methods," *J. Acoust. Soc. Am.*, vol. 95, no. 2, pp. 1112–1118, 1994.

[29] S. Bilbao, A. Torin, and V. Chatziioannou, "Numerical modeling of collisions in musical instruments," *Acta Acustica u. Acustica*, vol. 101, no. 1, pp. 155–1731, 2015.

[30] V. Chatziioannou and M. van Walstijn, "Energy conserving schemes for the simulation of musical instrument contact dynamics," *J. Sound Vib.*, vol. 339, pp. 262–279, 2015.

[31] B. Hosseini, N. Nigam, and J. Stockie, "On regularizations of the Dirac delta distribution," *J. Comp. Phys.*, vol. 305, pp. 423–447, 2016.

[32] S. Bilbao and J. O. Smith III, "Energy conserving finite difference schemes for nonlinear strings," *Acustica*, vol. 91, pp. 299–311, 2005.

[33] M Woodbury, "Inverting modified matrices," Tech. Rep., Princeton, New Jersey, USA, 1950, Statistical Research Group, Memo. Rep. no. 42.

[34] R. Russo, S. Bilbao, and M. Ducceschi, "Scalar auxiliary variable techniques for nonlinear transverse string vibration," *IFAC-PapersOnLine*, Accepted for publication, IFAC Workshop on Lagrangian and Hamiltonian Methods for Nonlinear Control LHMNC.

[35] J. Sherman and W. J. Morrison, "Adjustment of an inverse matrix corresponding to a change in one element of a given matrix," *Ann. Math. Stat.*, vol. 21, pp. 124–127, 1950.

[36] G. Evangelista and J. O. Smith, "Structurally passive scattering element for modeling guitar pluck action," in *Proc. 13th Int. Conf. Digital Audio Effects*, Graz, Austria, Sept. 2010, pp. 10–17.

7.2   Physical modelling of the yaybahar

This section is based on a paper presented at the International Conference on Digital Audio Effects (DAFx) in 2023 [181]. It introduces the physical model of the yaybahar, a recently invented acoustic musical instrument. The model uses a modal approach featuring a bowed string connected to a distributed bridge at the boundary. Springs are attached to the bridge, set in motion by its vibrations, and are connected, at the opposite end, to a tensioned membrane. The elements are interconnected using an energy-consistent framework through boundary forces. Additionally, a modal model of a thin spring is presented, utilizing analytic modes. This specific model is not detailed elsewhere in the thesis.

The springs and the membranes are treated here as feed-forward elements, as discussed in Section 2 of the paper. This approximation significantly simplifies the modal approach and allows for the formulation of a set of boundary conditions for the spring that yield a closed-form expression for the mode shape functions, similar to that of the linear string discussed in Chapter 2. The simplification has little impact on the instrument sound when the excitation originates from the string. However, the yaybahar was also designed to be excited from the membranes and springs, producing echo and reverb effects [59, Instrumental Interlude 2]: this part of the dynamics cannot be captured with the simplified inter-object connections. Future work should incorporate physically motivated boundary conditions for the spring, along with a fully coupled model with bi-directional connections.

Additionally, in the original yaybahar design, the springs were attached to the strings near the bridge, whereas other iterations of the instrument have them attached directly to the bridge. The latter approach was adopted in this work.

Paper errata

The curve in Figure 3(c) of the paper, along with the corresponding formula in the caption, is incorrect. The correct version is presented in Figure 6.1 of this thesis.

EFFICIENT SIMULATION OF THE YAYBAHAR USING A MODAL APPROACH

Riccardo Russo, Michele Ducceschi

Department of Industrial Engineering
University of Bologna
Viale Risorgimento 2, Bologna, Italy
riccardo.russo19@unibo.it
michele.ducceschi@unibo.it

Stefan Bilbao

Acoustics & Audio Group
University of Edinburgh
Edinburgh, UK
sbilbao@ed.ac.uk

ABSTRACT

This work presents a physical model of the yaybahar, a recently invented acoustic instrument. Here, output from a bowed string is passed through a long spring, before being amplified and propagated in air via a membrane. The highly dispersive character of the spring is responsible for the typical synthetic tonal quality of this instrument. Building on previous literature, this work presents a modal discretisation of the full system, with fine control over frequency-dependent decay times, modal amplitudes and frequencies, all essential for an accurate simulation of the dispersive characteristics of reverberation. The string-bow-bridge system is also solved in the modal domain, using recently developed non-iterative numerical methods allowing for efficient simulation.

1. INTRODUCTION

The yaybahar is an acoustic musical instrument, recently invented by Turkish artist Görkem Şen [1]. It consists of a neck, with two strings and a fretboard, to which two long springs are attached; each spring is in turn connected, on its opposite end, to a tensioned membrane. The instrument, depicted in Figure 1, is played by either bowing and plucking the strings, or by hitting the springs and the membranes with a mallet. The yaybahar can be described as a cello-like instrument, where amplification is provided by springs and membranes, and not by a resonant body. This structure provides a distinctive reverberant sound, mainly due to the characteristic sound transmission of springs [1]. Given its modular design, the yaybahar lends itself well to physical modeling simulation: in fact, all its components are widely studied systems in physical modeling literature [1, 2, 3]; therefore, a model can be implemented by first simulating the different modules, and by then connecting them together appropriately. A first physical model of the yaybahar was recently proposed by Christensen et al. [4]. There, the strings and membranes are described by the Kirchhoff-Carrier and the Berger models respectively [2, Chapters 8, 13], thus incorporating mild nonlinear effects, while the spring is modeled by a linear stiff bar, following [5]. The components are then coupled by lumped, spring-like connections, and the full model is simulated by using finite-difference-time-domain (FDTD) methods.

---

[1] https://www.gorkemsen.com/gorkem-sen-s-yaybahar

[2] https://commons.wikimedia.org/wiki/File:Yaybahar.jpg

Figure 1: *The yaybahar (Source [2])*

In this work, a different approach is proposed, based on a modal decomposition of the subsystems. The bowed string, in particular, is simulated in the modal domain following the non-iterative procedure developed in [6], and building on the results presented in [7]. The spring and the membrane, acting as reverberation units, can be simulated efficiently in the modal domain, incorporating refined loss profiles for realistic reverberation [8, 9]. Here, the interconnection between subsystems is performed in an energy-consistent framework via boundary forces, rather than using additional spring-like connections as in [4]. To this end, a novel model for the coupling between a vibrating string and a distributed bridge is presented, in the modal domain, which serves as an emulation for the neck. Given the low amplitude of vibration in the subsystems, linear models for the resonators are adopted without compromising the realism of the sound synthesis overall, as the nonlinear bowing mechanism is largely responsible for the typical drone-like sound of the instrument.

The paper is structured as follows: Section 2 presents the mathematical models of the instrument subcomponents, Section 3 describes the semi-discretisation in the modal domain, Section 4 illustrates the time-stepping algorithms, Section 5 presents the results of a case study and, finally, Section 6 concludes the paper.

2. MODELS

In this section, continuous models for the various components of the yaybahar are presented. A diagram of the instrument's subsystems (bow, string and bridge) and their couplings is as shown in Figure 2. The resulting bridge force is fed to the spring, and the spring sets the membrane into vibration. As shown below,
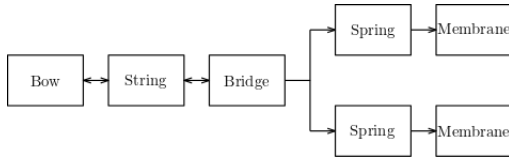
Figure 2: *A scheme of the instrument model and the elements connections.*

the string-bridge coupling modifies significantly the distribution of the eigenfrequencies compared to the isolated string. On the other hand, the spring and the membrane, acting as reverberant units characterised by a large modal density, are less affected by couplings at the boundaries. This justifies their inclusion as non-interacting subsystems, thus considerably simplifying the modal approach. This design shares some similarities with the commuted synthesis approach [10].

For simplicity, in this section, the models are presented here with no damping, except for friction losses induced by the bow. Viscous-type and radiation damping will be introduced in a frequency-dependent manner in the modal domain, as illustrated in Section 3.4.

2.1. Bowed Stiff String and Distributed Bridge

The equations for the coupled bowed string/bridge system are given here as follows:

$$\rho_s \partial_t^2 u_s = T_s \partial_x^2 u_s - \kappa_s^2 \partial_x^4 u_s - F_b \delta(x - x_b)\phi(\eta), \quad (1a)$$

$$\rho_p \partial_t^2 u_p = -\kappa_p^2 \partial_z^4 u_p + \delta(z - z_s)F_s(t). \quad (1b)$$

Here, subscripts s, p, b refer, respectively, to the string, the bridge ("ponticello") and the bow. In the system above assumes that the string and the bridge vibrate in a single, vertical polarisation, thus neglecting the rocking motion observed in instruments such as the violin [11]. In (1a), $u_s = u_s(x, t) : [0, L_s] \times \mathbb{R}_0^+ \to \mathbb{R}$ represents
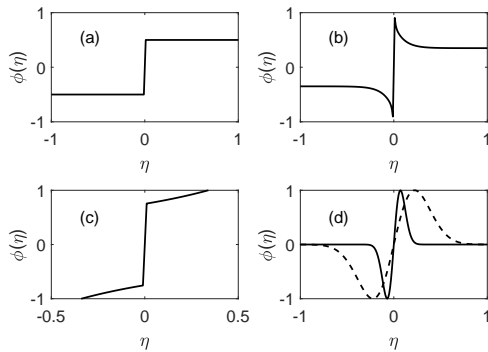

Figure 3: *Some friction characteristics: (a) Coulomb dry friction; (b) the curve by Woodhouse and Smith [12]; (c) the curve by Galluzzo [13]; (d) the continuous curve defined in equation 3, with $a = 10$ (dashed line) and $a = 100$ (solid line). For the mathematical expressions of the four friction characteristics refer to [6].*

the transverse displacement of a string of length L_s in a single polarisation, as a function of spatial coordinate x and time t. ρ_s is the string linear density in kg m^{-1}; T_s is the string tension in N, and κ_s is a rigidity constant in N$^{1/2}$m (κ_s^2 is typically given

as the product of Young's modulus times the moment of inertia). Analogous definitions hold for (1b), the equation describing the displacement $u_p = u_p(z, t) : [0, L_p] \times \mathbb{R}_0^+ \to \mathbb{R}$ of the bridge. Here and elsewhere the nth partial derivative with respect to the variable α is denoted by ∂_α^n.

In (1a), the string is coupled with a bow model, following [6]. The bow excitation is assumed to act pointwise downward at x_b, according to the dimensionless friction coefficient ϕ, as seen in [14]. Various choices for this coefficient are available, see e.g. [12, 13, 2] and also Figure 3. Note that all the four curves displayed in Figure 3 satisfy:

$$\eta \, \phi(\eta) \geq 0, \quad \lim_{|\eta| \to 0} \phi(\eta)/\eta < \infty, \quad (2)$$

allowing a non-iterative time stepping procedure to be used, following recent results in [7]. Here, for illustrative purposes, the "soft" characteristic defined in [2] was chosen, defined as:

$$\phi(\eta) = \sqrt{2a} \, \eta \, e^{-a\eta^2 + \frac{1}{2}}, \quad \eta := \partial_t u(x_b, t) - v_b. \quad (3)$$

The input bow parameters are the bow force F_b, in N, and the bow velocity v_b in m s^{-1}. Furthermore, in (3), a is a free parameter of the model adjusting the slope of the curve.

The coupling between the string and the bridge takes place at the string's right boundary, and is expressed as an input force F_s in the bridge equation (1b). The string is assumed to be in contact with the bridge at z_s along the bridge's domain. The string's left boundary, as well as the bridge's endpoints, are all assumed to be simply-supported. The complete set of boundary conditions to be imposed is:

$$u_p(0, t) = \partial_z^2 u_p(0, t) = u_p(L_p, t) = \partial_z^2 u_p(L_p, t) = 0, \quad (4a)$$

$$u_s(0, t) = \partial_x^2 u_s(0, t) = \partial_x^2 u_s(L_s, t) = 0, \quad (4b)$$

$$F_s(t) = -T_0 \partial_x u_s(L_s, t) + \kappa_s^2 \partial_x^3 u_s(L_s, t), \quad (4c)$$

$$u_p(z_s, t) = u_s(L_s, t). \quad (4d)$$

The relations above are assumed to hold $\forall t \geq 0$. Note that (4d) represents a rigid contact condition between the string and the bridge.

2.1.1. Energy Balance

An energy balance for the bridge is obtained after multiplying (1b) by $\partial_t u_p$ and integrating over $[0, L_p]$. After integration by parts, and owing to (4a), one obtains:

$$\frac{d}{dt} \int_0^{L_p} \underbrace{\left(\frac{\rho_p}{2}(\partial_t u_p)^2 + \frac{\kappa_p^2}{2}(\partial_z^2 u_p)^2 \right)}_{\mathcal{H}_p} dz = \dot{u}_p(z_s, t)F_s. \quad (5)$$

The string energy balance is obtained analogously, by multiplying equation (1a) by $\partial_t u_s$ and integrating. After suitable integration by parts, and taking into account the boundary conditions (4b) and (4c), one obtains:

$$\frac{d}{dt} \int_0^{L_s} \underbrace{\left(\frac{\rho_s}{2}(\partial_t u_s)^2 + \frac{T_s}{2}(\partial_x u_s)^2 + \frac{\kappa_s^2}{2}(\partial_x^2 u_s)^2 \right)}_{\mathcal{H}_s} dx =$$

$$= -F_s \dot{u}_s(L_s, t) - F_b \, \dot{u}(x_b, t) \, \phi(\dot{u}(x_b, t)). \quad (6)$$

Finally, owing to the contact condition (4d), and by means of (5), one may express (6) as:

$$\frac{\mathrm{d}}{\mathrm{d}t}\left(\int_0^{L_s}\mathcal{H}_s\,\mathrm{d}x + \int_0^{L_p}\mathcal{H}_p\,\mathrm{d}z\right) = -\mathcal{Q} + \mathcal{P}, \qquad (7)$$

where the dissipated and supplied power are defined as, respectively, $\mathcal{Q} := F_b\,\eta\,\phi(\eta)$, $\mathcal{P} := -F_b\,v_b\,\phi(\eta)$. Owing to property (2), in the combined system the energy is non-increasing when the bow velocity v_b (and, therefore, the supplied power $\mathcal{P}$) is identically zero, leading to boundedness of the solutions.

Finally, the output force exerted by the bridge onto the spring is then computed at the desired location z_o as:

$$F_p(t) = -\kappa_p^2\partial_z^3 u_p(z_o, t). \qquad (8)$$

2.2. Spring

A model of a thin spring that takes into account the helical structure is here implemented, following [3]. In fact, the "bar" model of a spring holds for specific geometries [5], and cuts the low-frequency echoes that are characteristic of spring reverberators [1]. The system is developed starting from Wittrick's equations [15], under the assumption that the wire radius-helix radius ratio r_c/R_c is small [16] (see Figure 4). This allows the model to be reduced to a system of four equations, which relate the displacement in the transverse and longitudinal directions to the moments along the same directions:

$$\mathbf{A}\partial_t^2\mathbf{v} = \mathbf{R}\,\partial_s\mathbf{m} + \delta(s - s_p)\boldsymbol{\alpha}_p F_p, \quad \mathbf{Dm} = \mathbf{R}\partial_s\mathbf{v}. \qquad (9)$$

Here, $\mathbf{v} := [v_\tau(s,t), v_\lambda(s,t)]^\mathsf{T} : [0, L_c] \times \mathbb{R}_0^+ \to \mathbb{R}^2$ is the vector of displacements, where the subscripts τ and λ refer to the transverse and longitudinal directions, respectively. Analogously, $\mathbf{m} := [m_\tau, m_\lambda]^\mathsf{T}$ is the vector of moments. Above, s expresses the arclength of the coil, such that $0 \le s \le L_c$. The input force F_p, computed in equation (8), is applied pointwise at $s = s_p$, while the vector $\boldsymbol{\alpha}_p$ is a unit vector that indicates the amount of force exerted in both polarisations. The matrices $\mathbf{A}, \mathbf{D} \in \mathbb{R}^{2\times2}$ are diagonal, and given by:

$$\mathbf{A} = \rho_c\begin{bmatrix}1 & 0 \\ 0 & 1 - l^2\partial_s^2\end{bmatrix}, \quad \mathbf{D} = \kappa_c^{-2}\begin{bmatrix}1 & 0 \\ 0 & 1 + \nu_c - l^2\partial_s^2\end{bmatrix}. \qquad (10)$$

Above, ρ_c is the linear density of the coil, in kg m^{-1}, κ_c is a rigidity constant in N$^{1/2}$m, and ν_c is the Poisson ratio of the coil. $\mathbf{R} \in \mathbb{R}^{2\times2}$ is a symmetric matrix, of the form:

$$\mathbf{R} = \begin{bmatrix}-2\mu/l & (1-\mu^2)/l + l\partial_s^2 \\ 0 & 2\mu(l\partial_s^2 + 1/l)\end{bmatrix}. \qquad (11)$$

The symbol l denotes the ratio $R_c/\cos^2(\theta)$, where θ is the pitch angle, R_c the coil radius, and μ is shorthand for $\tan(\theta)$. A graphical representation of the spring physical quantities is provided in Figure 4.

2.2.1. Energy Analysis

The energy balance and boundary conditions may be obtained, in the zero-input ($F_p = 0$) case, as follows. First, left-multiply the first equation in (9) by $\partial_t\mathbf{v}^\mathsf{T}$. Then, take a time derivative of the
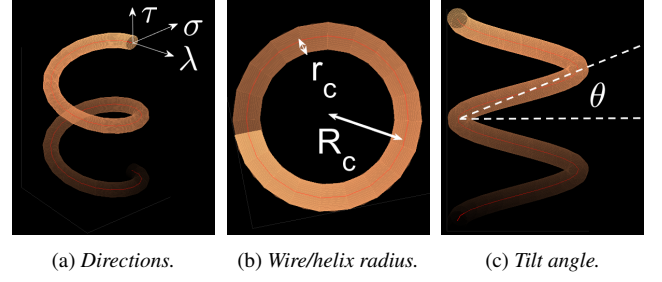

(a) *Directions.*   (b) *Wire/helix radius.*   (c) *Tilt angle.*

Figure 4: *Spring physical quantities.*

second equation in (9), and left-multiply by $\mathbf{m}^\mathsf{T}$, where T is the transposition operator. Integrating the resulting equations gives:

$$\int_0^{L_c}\partial_t\mathbf{v}^\mathsf{T}\mathbf{A}\,\partial_t^2\mathbf{v}\,\mathrm{d}s = \int_0^{L_c}\partial_t\mathbf{v}^\mathsf{T}\mathbf{R}\,\partial_s\mathbf{m}\,\mathrm{d}s, \qquad (12a)$$

$$\int_0^{L_c}\mathbf{m}^\mathsf{T}\mathbf{D}\,\partial_t\mathbf{m}\,\mathrm{d}s = \int_0^{L_c}\mathbf{m}^\mathsf{T}\mathbf{R}(\partial_s\partial_t\mathbf{v})\,\mathrm{d}s. \qquad (12b)$$

Integrating by parts to the right-hand side of (12b), one is able to express the right-hand side of (12a), which, in turn, can be rewritten as:

$$\int_0^{L_c}\left(\partial_t\mathbf{v}^\mathsf{T}\mathbf{A}\,\partial_t^2\mathbf{v} + \mathbf{m}^\mathsf{T}\mathbf{D}\,\partial_t\mathbf{m}\right)\mathrm{d}s = (\mathcal{B}_0 + \mathbf{m}^\mathsf{T}\mathbf{R}\,\partial_t\mathbf{v})\big|_0^{L_c}.$$

Here

$$\mathcal{B}_0 := l\partial_s\partial_t v_\lambda\,(\partial_s m_\tau + 2\mu\partial_s m_\lambda) + \partial_t v_\lambda(2\mu l\partial_s^2 m_\lambda - l\partial_s^2 m_\tau)$$
$$- l\partial_s\partial_t v_\tau(\partial_s m_\lambda) - \partial_t v_\tau(l\partial_s^2 m_\lambda). \qquad (13)$$

By further applying integration by parts, one derives the energy balance:

$$\frac{\mathrm{d}}{\mathrm{d}t}\int_0^{L_c}\mathcal{H}_c\,\mathrm{d}s = (\mathcal{B}_0 + \mathcal{B}_1 + \mathbf{m}^\mathsf{T}\mathbf{R}\,\partial_t\mathbf{v})\big|_0^{L_c} := \mathcal{B}_c\big|_0^{L_c}. \qquad (14)$$

Here, the energy density is:

$$\mathcal{H}_c = \frac{\rho_c}{2}\left((\partial_t v_\tau)^2 + (\partial_t v_\lambda)^2 + l^2(\partial_t\partial_s v_\lambda)^2\right) +$$
$$+ \frac{\kappa_c^{-2}}{2}\left(m_\tau^2 + (1 + \nu_c)m_\lambda^2 + l^2(\partial_s m_\lambda)^2\right); \qquad (15)$$

while $\mathcal{B}_1$ is:

$$\mathcal{B}_1 = l^2\rho_c(\partial_t v_\lambda)(\partial_s\partial_t^2 v_\lambda) + l^2\kappa_c^{-2}m_\lambda(\partial_s\partial_t m_\lambda). \qquad (16)$$

It is useful to write the boundary terms in terms of the conjugate variables forces / velocities and moments / angular velocities [3]. To that end, rearranging the boundary terms in (14) allows to write:

$$\mathcal{B}_c = F_\tau\partial_t v_\tau + F_\lambda\partial_t v_\lambda + F_\sigma\partial_t v_\sigma + m_\tau\phi_\tau + m_\lambda\phi_\lambda + m_\sigma\phi_\sigma.$$

Here, the σ denotes the direction perpendicular to the (τ, λ)-plane. Denoting $g := -\frac{\mu^2}{l} + \frac{1}{l} + l\partial_s^2$, one has

$$F_\tau = g\, m_\lambda - 2\mu m_\tau / l, \tag{17a}$$

$$F_\lambda = g\, m_\tau + 2\mu \left(l\partial_s^2 + 1/l\right) m_\lambda + l^2 \rho_c \partial_s \partial_t^2 v_\lambda, \tag{17b}$$

$$F_\sigma = -\partial_s (m_\tau + 2\mu m_\lambda), \tag{17c}$$

$$\phi_\tau = l\partial_s^2 \partial_t v_\lambda, \tag{17d}$$

$$\phi_\lambda = 2\mu l\partial_s^2 \partial_t v_\lambda + l^2 \kappa_c^{-2} \partial_s \partial_t m_\lambda + l\partial_s^2 \partial_t v_\tau, \tag{17e}$$

$$\phi_\sigma = -\partial_s \partial_t v_\tau, \tag{17f}$$

$$m_\sigma = l\partial_s m_\lambda, \tag{17g}$$

$$v_\sigma = l\partial_s v_\lambda. \tag{17h}$$

Setting boundary displacements, forces and moments to zero leads to a generalisation of the classic beam boundary conditions of free, simply-supported or clamped type. Here, a variant of free boundary conditions along τ, λ will be used, combined with clamped conditions along σ. Hence:

$$F_\tau = F_\lambda = m_\tau = m_\lambda = v_\sigma = \phi_\sigma = 0. \tag{18}$$

These are intended to hold at the boundary points $s = \{0, L_c\}$, and $\forall t \geq 0$. An output signal $F_c(t)$ may be then be extracted by computing the sum of the forces F_τ, F_λ, F_σ at a s_o, close, but not equal, to the boundary L_c. Thus:

$$F_c(t) = F_\tau(s_o, t) + F_\lambda(s_o, t) + F_\sigma(s_o, t). \tag{19}$$

2.3. Membrane

A model for the membrane is given by the 2D wave equation [2, Chapter 11]:

$$\rho_m \partial_t^2 w = T_m \nabla^2 w + \delta(X - X_c)\delta(Y - Y_c)F_c(t). \tag{20}$$

In the above, the two dimensional Laplacian was introduced as $\nabla^2 := \partial_X^2 + \partial_Y^2$. For simplicity, and to avoid the introduction of further symbols, the membrane is supposed to be defined over a square, of side length L_m. Thus, $w = w(X, Y, t) : [0, L_m] \times [0, L_m] \times \mathbb{R}^+ \to \mathbb{R}$ describes the displacement of the membrane in the transversal direction, ρ_m is the material surface density in kg m^{-2}, and T_m is the tension applied at the edges in N m^{-1}. An energy analysis for this system can be found in [2, Chapter 11]. Boundary conditions of fixed type will be considered here, such that:

$$w(0, Y) = w(L_m, Y) = w(X, 0) = w(X, L_m) = 0. \tag{21}$$

3. SEMI-DISCRETISATION

The equations presented in Section 2 will be now semi-discretised in space using a modal approach. While the spring and the membrane possess an analytical form for the modes of vibration, this is not true in the case of a string coupled with a distributed bridge on one end. For this reason, the modal expansion for the latter system will be performed by solving the eigenvalue problem numerically.

3.1. Bowed Stiff String and Distributed Bridge

First, it is convenient to introduce spatial difference operators. The string domain is divided into M_s subintervals of length h, the grid spacing. This yields $M_s + 1$ discretisation points, including the

end points. Analogously, the bridge is divided into M_p subintervals of length h. The continuous functions $u_s(x, t)$ and $u_p(z, t)$ are then approximated by grid functions $u_s^m(t) \approx u_s(mh, t)$ and $u_p^n(t) \approx u_p(nh, t)$, for integer m, n. In light of the numerical boundary conditions given below, one has $m \in [1, ..., M_s - 1]$, $n \in [1, ..., M_p - 1]$. In vector notation, the grid functions will be denoted $\mathbf{u}_s$, $\mathbf{u}_p$.

Basic forward and backward difference operators, approximating the first spatial derivative, and acting on u_s^m, are:

$$\delta_x^\pm u_s^m = \pm(u_s^{m\pm 1} - u_s^m)/h. \tag{22}$$

Analogous definitions hold for the grid function u_p^n, thus, for instance, $\delta_z^+ u_p^n = (u_p^{n+1} - u_p^n)/h$. The second and fourth spatial derivatives are approximated by difference operators obtained by combining the operators above, as:

$$\delta_x^2 := \delta_x^+ \delta_x^-, \qquad \delta_x^4 := \delta_x^2 \delta_x^2, \tag{23}$$

with similar definitions holding for δ_z^2, δ_z^4. Discrete versions of the Dirac deltas in (1) are also needed. To that end, $\delta(x - x_b)$ in (1a) is approximated by the column vector $\mathbf{d}_b$, of length $M_s - 1$, as:

$$d_b^\nu = (1 - \alpha)/h, \qquad d_b^{\nu+1} = \alpha/h, \tag{24}$$

where $\nu := \text{floor}(x_b/h)$, $\alpha := x_b/h - \nu$. An analogous definition holds for $\mathbf{d}_s$, approximating $\delta(z - z_s)$ in (1b).

3.1.1. Semi-Discrete Formulation

Given the definitions above, a semi-discrete approximation of (1) is given as:

$$\rho_s \ddot{u}_s^m = T_s \delta_x^2 u_s^m - \kappa_s^2 \delta_x^4 u_s^m - F_b d_b^m \phi(\eta), \tag{25a}$$

$$\rho_p \ddot{u}_p^n = -\kappa_b^2 \delta_z^4 u_p^n + d_s^n f_s(t). \tag{25b}$$

Here, $\eta = h\mathbf{d}_b^\mathsf{T} \dot{\mathbf{u}}_s - v_b$. A discrete version of the boundary conditions and contact condition (4) ensuring numerical stability is:

$$u_p^0 = \delta_z^2 u_p^0 = u_p^{M_p} = \delta_z^2 u_p^{M_p} = 0, \tag{26a}$$

$$u_s^0 = \delta_x^2 u_s^0 = \delta_x^2 u_s^{M_s} = 0, \tag{26b}$$

$$f_s(t) = -T_s \delta_x^+ u_s^{M_s} + \kappa_s^2 \delta_x^+ \delta_x^2 u_s^{M_s}, \tag{26c}$$

$$h\mathbf{d}_s^\mathsf{T} \mathbf{u}_p = u_s^{M_s}. \tag{26d}$$

By expanding the operators and applying the boundary conditions, the semi-discrete equations can be arranged in vector form. To that end, define $\mathbf{u}^\mathsf{T} := [\mathbf{u}_s^\mathsf{T}, \mathbf{u}_p^\mathsf{T}]$. System (25) can be then written in compact form as:

$$\mathbf{M}\ddot{\mathbf{u}} = -\mathbf{K}\mathbf{u} - F_b \mathbf{J}_b \phi(\eta). \tag{27}$$

Here, $\mathbf{J}_b$ is a vector obtained by concatenating $\mathbf{d}_b$ with a zero-vector of dimension M_{p-1}, and $\eta = h\mathbf{J}_b^\mathsf{T} \dot{\mathbf{u}} - v_b$. $\mathbf{M}$ is positive-definite, symmetric, square diagonal block matrix, with diagonal blocks given as:

$$\mathbf{M}_{11} = \rho_s \mathbf{I}_s, \ \mathbf{M}_{22} = \left(\rho_p \mathbf{I}_p + \rho_s h^2 \mathbf{d}_s \mathbf{d}_s^\mathsf{T}\right). \tag{28}$$

Here, $\mathbf{I}_s$ and $\mathbf{I}_p$ are identity matrices, of dimension $(M_s - 1) \times (M_p - 1)$ and $(M_p - 1) \times (M_s - 1)$ respectively. Furthermore,

the stiffness matrix is a positive-definite, square block matrix, with blocks:

$$\mathbf{K}_{11} = -T_{\mathrm{s}}\mathbf{D}_x^2 + \kappa_{\mathrm{s}}^2\mathbf{D}_x^2\mathbf{D}_x^2,$$

$$\mathbf{K}_{12} = \mathbf{K}_{21}^{\mathsf{T}} \quad \mathbf{K}_{21} = \left[\mathbf{0}, \frac{\kappa_{\mathrm{s}}^2}{h^3}\mathbf{d}_{\mathrm{s}}, -\left(\frac{T_{\mathrm{s}}}{h^2} + \frac{2\kappa_{\mathrm{s}}^2}{h^3}\right)\mathbf{d}_{\mathrm{s}}\right], \quad (29)$$

$$\mathbf{K}_{22} = \kappa_{\mathrm{p}}^2\mathbf{D}_z^2\mathbf{D}_z^2 + \left(T_{\mathrm{s}} + \frac{2\kappa_{\mathrm{s}}^2}{h^2}\right)\mathbf{d}_{\mathrm{s}}\mathbf{d}_{\mathrm{s}}^{\mathsf{T}},$$

where $\mathbf{D}_x^2$ and $\mathbf{D}_z^2$ are the second difference operators with Dirichlet end conditions of dimensions, respectively, $(M_{\mathrm{s}} - 1) \times (M_{\mathrm{s}} - 1)$, and $(M_{\mathrm{p}} - 1) \times (M_{\mathrm{p}} - 1)$ (for the explicit form of these matrices, see [2, Chapter 5]). $\mathbf{K}_{21}$ has dimension $(M_{\mathrm{p}} - 1) \times (M_{\mathrm{s}} - 1)$, and is a composition of a zero-matrix of dimension $(M_{\mathrm{p}} - 1) \times (M_{\mathrm{s}} - 3)$ with two vectors.

An energy balance in the modal domain is readily available from (27), after left-multiplying by $h\dot{\mathbf{u}}^{\mathsf{T}}$. When $v_{\mathrm{b}} = 0$, one has:

$$\frac{\mathrm{d}}{\mathrm{d}t}\left(\frac{h}{2}\dot{\mathbf{u}}^{\mathsf{T}}\mathbf{M}\dot{\mathbf{u}} + \frac{h}{2}\mathbf{u}^{\mathsf{T}}\mathbf{K}\mathbf{u}\right) = -\eta\phi(\eta) \leq 0. \quad (30)$$

Since both $\mathbf{M}, \mathbf{K}$ are non-negative, the energy is non-negative, and decays over time.
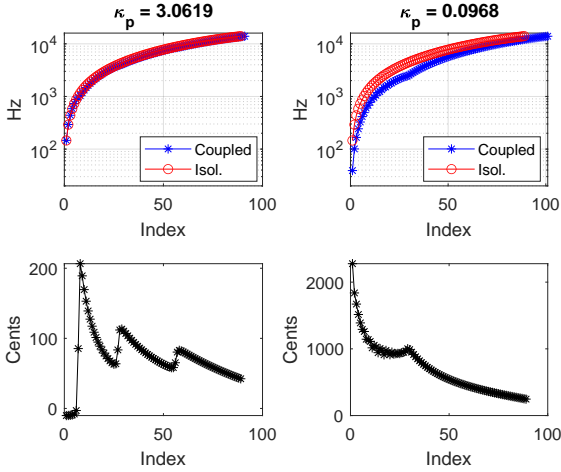

Figure 5: *Eigenfrequencies of the coupled system and the ones of a simply supported stiff string in isolation, under two different values of κ_{p}. The left value is typical of steel, while the right one was chosen arbitrarily low for demonstration purposes. Other physical parameters, on common between the two cases, were: $L_{\mathrm{s}} = 0.69$ m; $T_{\mathrm{s}} = 147.7$ N; $\rho_{\mathrm{s}} = 0.0063$ Kg m^{-1}; $\kappa_{\mathrm{s}} = 0.4835$ N$^{1/2}$ m; $L_{\mathrm{p}} = 0.07$ m; $\rho_{\mathrm{p}} = 0.0251$ Kg m^{-1}. The contact point was set to: $z_{\mathrm{s}} = 0.03$ m. The top figures report the frequencies in log scale, while the bottom figures display the difference in cents between frequencies with the same index.*

3.1.2. Modal Expansion

A modal expansion of system (27) is now performed by solving the generalised eigenvalue problem. For that, consider the following:

$$\mathbf{K}\mathbf{U} = \mathbf{M}\mathbf{U}\mathbf{\Omega}_{\mathfrak{u}}^2. \quad (31)$$
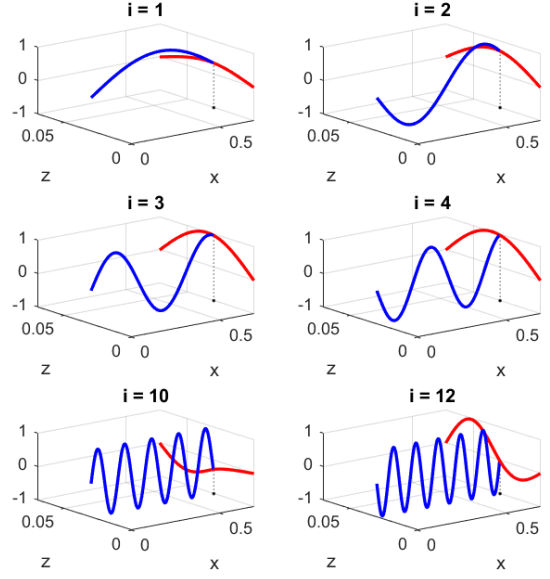

Figure 6: *Modes of the coupled string-bridge system, which were normalized, and plotted orthogonal one to another for visualisation purposes. The letter i gives the mode index. The blue line represents the string, and red one the bridge, while the projection of the contact point on the z-axis is highlighted with a black dot. The physical parameters were the same listed in Figure 5, with $\kappa_{\mathrm{p}} = 3.0619$ N$^{1/2}$ m.*

Here, $\mathbf{U}$ is a matrix of real eigenvectors, and $\mathbf{\Omega}^2$ is a diagonal matrix of real, positive eigenvalues. Note that, while both $\mathbf{K}$ and $\mathbf{M}$ are symmetric, the product $\mathbf{M}^{-1}\mathbf{K}$ generally will not be. However, since $\mathbf{M}$ is positive definite, the eigenvalues are then real [17], and they must also be non-negative since so are the eigenvalues of $\mathbf{K}$. Then, define $\mathfrak{u} = \mathbf{U}^{-1}\mathbf{u}$. System (27) may then be written as:

$$\ddot{\mathfrak{u}} = -\mathbf{\Omega}_{\mathfrak{u}}^2\mathfrak{u} - F_{\mathrm{b}}\boldsymbol{\xi}_{\mathrm{b}}\phi(\eta), \quad \eta = \boldsymbol{\xi}_{\eta}^{\mathsf{T}}\dot{\mathfrak{u}} - v_{\mathrm{b}}, \quad (32)$$

with $\boldsymbol{\xi}_{\eta}^{\mathsf{T}} := h\mathbf{J}_{\mathrm{b}}^{\mathsf{T}}\mathbf{U}$, $\boldsymbol{\xi}_{\mathrm{b}} := (\mathbf{M}\mathbf{U})^{-1}\mathbf{J}_{\mathrm{b}}$. This a modal system with a diagonal linear part, with modal coordinates $\mathfrak{u}$. One may of course solve the numerical eigenvalue problem (31) using a very fine grid (i.e., using a small grid spacing h), though only a number $N_{\mathfrak{u}}$ is kept in (32), fixed by Nyquist requirements.

Before proceeding, it is useful to compare the eigenfrequencies of the string in isolation against those of the coupled string-bridge system. Figure 5 shows two such comparisons, under two different values of κ_{p}. These are computed for a bar of circular cross section, with a diameter of 5 mm. The first value ($\kappa_{\mathrm{p}} \approx 3$) is typical of steel, while the second value ($\kappa_{\mathrm{c}} \approx 0.1$) was selected to artificially amplify the effects of the coupling. The top panels report the frequencies in a log scale: it is seen that the reduced stiffness shifts the eigenfrequencies downwards by up to two octaves in the lowest range, as seen in the bottom panels. With sufficiently large values of κ_{p}, as is the case of steel, the frequency gap remains contained around the fundamental, as expected, but it increases up to two semitones for larger modal indices. These results underline the importance of considering the string-bridge coupling for in the distribution of the eigenfrequencies.

The eigenmodes are represented in Figure 6, for a steel bridge. Here, the first four modes are displayed, along with the 10th and the 12th. It is possible to see that the bridge eigenmodes start exhibiting a third node only after the 10th mode.

3.2. Spring

A modal version of the thin spring model was originally proposed by van Walstijn [18]. In van Walstijn's model, the modal expansion is carried out numerically, by first performing a semi-discretisation in space, and then computing the eigenvalues of the resulting matrix. Such model found practical application in [19], where a virtual analogue simulation of a spring reverb is developed. In this work an analytic form for the modes is available under a choice of the boundary conditions as per (18). To that end, consider the following:

$$\mathbf{v}(s,t) = \sqrt{2/L_c}\cos(\gamma s)\,\bar{\mathbf{v}}(t),$$
$$\mathbf{m}(s,t) = \sqrt{2/L_c}\sin(\gamma s)\,\bar{\mathbf{m}}(t), \tag{33}$$

where $\bar{\mathbf{v}}$, $\bar{\mathbf{m}}$ are the time modal coordinates, and the factor $\sqrt{2/L_c}$ is just a useful normalisation constant. It is immediate to see that these satisfy the boundary conditions (18) when $\gamma = \{\pi/L_c, 2\pi/L_c, ..., n\pi/L_c, ...\}$.

Let now $\gamma_n := n\pi/L_c$, for integer n. A solution to the equation of motion is obtained using the quantised expressions of the modes to solve an eigenvalue problem. Left-multiplying the first equation in (9) by $\sqrt{2/L_c}\cos(\gamma_n s)$, and the second by $\sqrt{2/L_c}\sin(\gamma_n s)$ and integrating, one is able to express (9) as:

$$\bar{\mathbf{A}}\ddot{\bar{\mathbf{v}}} = \gamma_n\bar{\mathbf{R}}\bar{\mathbf{m}} + \sqrt{2/L_c}\cos(\gamma_n s_p)\boldsymbol{\alpha}_p F_p(t), \tag{34a}$$
$$\bar{\mathbf{D}}\bar{\mathbf{m}} = -\gamma_n\bar{\mathbf{R}}\bar{\mathbf{v}}. \tag{34b}$$

Here, the transformed matrices are obtained by applying the derivatives to the modal functions, and have the form (10), (11) under the replacement of ∂_s^2 by $-\gamma_n^2$. Then, (34b) is used to express $\bar{\mathbf{m}}$ is terms of $\bar{\mathbf{v}}$, and this is substituted in (34a). One gets:

$$\ddot{\bar{\mathbf{v}}} = -\mathbf{V}\boldsymbol{\Omega}_n^2\mathbf{V}^{-1}\bar{\mathbf{v}} + \sqrt{2/L_c}\cos(\gamma_n s_p)\bar{\mathbf{A}}^{-1}\boldsymbol{\alpha}_p F_p.$$

where it was set:

$$\mathbf{V}\boldsymbol{\Omega}_n^2\mathbf{V}^{-1} := \gamma_n^2\bar{\mathbf{A}}^{-1}\bar{\mathbf{R}}\bar{\mathbf{D}}^{-1}\bar{\mathbf{R}}. \tag{35}$$

Here $\mathbf{V}$ is a 2×2 matrix of eigenvectors for the wavenumber γ_n, and $\boldsymbol{\Omega}_n$ is a diagnoal 2×2 matrix of eigenfrequencies. Figure 7 reports the solution to the eigenvalue problem for a typical spring. The eigenfrequencies lay on the yellow an purple lines.

Then, define $\mathfrak{v}_n := (\mathbf{V})^{-1}\bar{\mathbf{v}}$. Thus, one gets:

$$\ddot{\mathfrak{v}}_n = -\boldsymbol{\Omega}_n^2\mathfrak{v} + \sqrt{2/L_c}\cos(\gamma_n s_p)(\bar{\mathbf{A}}\mathbf{V})^{-1}\boldsymbol{\alpha}_p F_p(t). \tag{36}$$

Assume now $n = 1, ..., N_\mathfrak{v}$. The modal equations for the spring are then a system of $2N_\mathfrak{v}$ equations, of the form:

$$\ddot{\mathfrak{v}} = -\boldsymbol{\Omega}_\mathfrak{v}^2\mathfrak{v} + \boldsymbol{\xi}_p F_p(t), \tag{37}$$

where $\mathfrak{v}$ is a vector of length $2N_\mathfrak{v}$, $\boldsymbol{\Omega}_\mathfrak{v}$ is a $2N_\mathfrak{v} \times 2N_\mathfrak{v}$ diagonal matrix, whose diagonal elements are the 2×2 diagonal blocks $\boldsymbol{\Omega}_n$, $n = 1, ... N_\mathfrak{v}$ defined in (35), and $\boldsymbol{\xi}_p$ is a $2N_\mathfrak{v}$ vector made composed by stacking the 2×1 blocks: $\sqrt{2/L_c}\cos(\gamma_n s_p)(\bar{\mathbf{A}}\mathbf{V})^{-1}\boldsymbol{\alpha}_p$, $n = 1, ..., N_\mathfrak{v}$.

Output (19) is extracted by substituting the solution (33) into the boundary forces (17c) (17b) and (17a) computed at a position close to L_c.
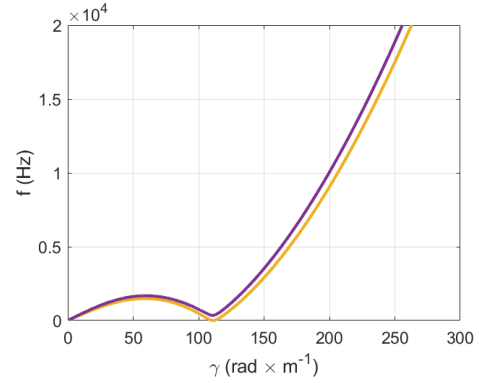

Figure 7: *Plot of the dispersion relation of a thin spring. Physical parameters were chosen to be coherent with a possible yaybahar spring: $R_c = 9$ mm, $r_c = 1$ mm, $\theta = 2°$, $L_c = 40$ m, $\kappa_c = 9.9$ and $\nu_c = 0.3$. These values yield $N_\mathfrak{v} = 2812$ within the hearing range.*

3.3. Membrane

A particular solution to equation (20) with fixed boundary conditions (21) is given by:

$$w(X,Y,t) = \frac{2}{L_m}\sin\frac{\beta_X^j\pi X}{L_m}\sin\frac{\beta_Y^j\pi Y}{L_m}\mathfrak{w}_j(t), \tag{38}$$

for integers β_X^j, β_Y^j [20]. The associated modal frequency is:

$$\omega_j = \frac{\pi}{L_m}\sqrt{\frac{T_m}{\rho_m}\left((\beta_X^j)^2 + (\beta_Y^j)^2\right)}. \tag{39}$$

The modal system for the membrane is then given by:

$$\ddot{\mathfrak{w}} = -\boldsymbol{\Omega}_\mathfrak{w}^2\mathfrak{w} + \boldsymbol{\xi}_c F_c(t), \tag{40}$$

where $\mathfrak{w}$ is a $N_\mathfrak{w} \times 1$ vector, $\boldsymbol{\Omega}_\mathfrak{w}$ is a $N_\mathfrak{w} \times N_\mathfrak{w}$ diagonal matrix where the jth diagonal element is ω_j given above. The frequencies should here be sorted in ascending order, such that $\omega_{j-1} \leq \omega_j \leq \omega_{j+1}$, $j = 2, ..., N_\mathfrak{w} - 1$. This allows to find the corresponding modal indices β_X^j, β_Y^j. Above, $\boldsymbol{\xi}_c$ is a $N_\mathfrak{w} \times 1$ vector whose jth component is $\frac{2}{L_m\rho_m}\sin\frac{\beta_X^j\pi X_c}{L_m}\sin\frac{\beta_Y^j\pi Y_c}{L_m}$.

Output is extracted as:

$$w_o(t) = \sum_{j=1}^{N_\mathfrak{w}}\frac{2}{L_m}\sin\frac{\beta_X^j\pi X_o}{L_m}\sin\frac{\beta_Y^j\pi Y_o}{L_m}\mathfrak{w}_j(t), \tag{41}$$

though for synthesis purposes it may be convenient to use $\dot{w}_o(t)$ instead.

3.4. Modal Equations of the Full System with Loss

The full system in the modal domain can thus be written as an augmented version of (32), (37) and (40). This is:

$$\ddot{\mathfrak{u}}(t) = -\boldsymbol{\Omega}_\mathfrak{u}^2\mathfrak{u}(t) - \mathbf{C}_\mathfrak{u}\dot{\mathfrak{u}}(t) - \boldsymbol{\xi}_b F_b\phi(\eta), \tag{42a}$$
$$\ddot{\mathfrak{v}}(t) = -\boldsymbol{\Omega}_\mathfrak{v}^2\mathfrak{v}(t) - \mathbf{C}_\mathfrak{v}\dot{\mathfrak{v}}(t) + \boldsymbol{\xi}_p F_p(t), \tag{42b}$$
$$\ddot{\mathfrak{w}}(t) = -\boldsymbol{\Omega}_\mathfrak{w}^2\mathfrak{w}(t) - \mathbf{C}_\mathfrak{w}\dot{\mathfrak{w}}(t) + \boldsymbol{\xi}_c F_c(t), \tag{42c}$$

where $\mathbf{C}_\mathfrak{u}$, $\mathbf{C}_\mathfrak{v}$, $\mathbf{C}_\mathfrak{w}$ are, respectively, $N_\mathfrak{u} \times N_\mathfrak{u}$, $2N_\mathfrak{v} \times 2N_\mathfrak{v}$, $N_\mathfrak{w} \times N_\mathfrak{w}$ positive, diagonal matrices containing the modal loss coefficients in s^{-1}. System (42) depends on time only, and a suitable time stepping routine is offered below. Here, the input parameters are the bow force F_b, velocity v_b and position along the string x_b, which may be time-varying. The output is given by the membrane displacement at the output location, as per (41).

4. TIME DISCRETISATION

Now, time is discretised with a time step k, yielding a sample rate $f_s = 1/k$. Then, a continuous function $u(t)$ is approximated at time step $t = nk$ by the time series u^n. Time difference operators are then introduced, as:

$$\delta_t^\pm u^n := \pm(u^{n\pm1} - u^n)/k, \; \delta_t^\circ u^n := (u^{n+1} - u^{n-1})/2k. \quad (43)$$

The second time difference is defined by combining the operators above: $\delta_t^2 u^n := \delta_t^+ \delta_t^- u^n$. Finally, a time averaging operator is defined as:

$$\mu_t^+ u^n := (u^{n+1} + u^n)/2. \quad (44)$$

4.1. String-Bridge System

It is now possible to adapt the numerical solver proposed in [7, 6] to numerically integrate equation (42a) in time. To that end, (42a) is first turned into a $2N_\mathfrak{u} \times 2N_\mathfrak{u}$ system of first-order-in-time equations. Thus, define $\mathfrak{q} := \mathbf{\Omega}_\mathfrak{u}\mathbf{u}$, $\mathfrak{p} := \dot{\mathbf{u}}$. Therefore, (42a) becomes:

$$\begin{bmatrix} \dot{\mathfrak{q}} \\ \dot{\mathfrak{p}} \end{bmatrix} = \underbrace{\begin{bmatrix} \mathbf{0} & \mathbf{\Omega}_\mathfrak{u} \\ -\mathbf{\Omega}_\mathfrak{u} & -\mathbf{\Omega}_\mathfrak{u}^{-1}\mathbf{C}_\mathfrak{u} \end{bmatrix}}_{\mathbf{G}} \begin{bmatrix} \mathfrak{q} \\ \mathfrak{p} \end{bmatrix} - \begin{bmatrix} \mathbf{0} \\ \mathbf{\Omega}_\mathfrak{u}^{-1}\boldsymbol{\xi}_\text{b} \end{bmatrix} F_\text{b}\phi(\eta),$$

$$\eta = \begin{bmatrix} \mathbf{0}, \boldsymbol{\xi}_\eta^\mathsf{T} \end{bmatrix} \begin{bmatrix} \mathfrak{q} \\ \mathfrak{p} \end{bmatrix} - v_\text{b}. \quad (45)$$

A second-order accurate, non-iterative numerical scheme is given as:

$$\boldsymbol{\sigma}^n \begin{bmatrix} \delta_t^+ \mathfrak{q}^n \\ \delta_t^+ \mathfrak{p}^n \end{bmatrix} = \mathbf{G} \begin{bmatrix} \mu_t^+ \mathfrak{q}^n \\ \mu_t^+ \mathfrak{p}^n \end{bmatrix} - \begin{bmatrix} \mathbf{0} \\ \mathbf{\Omega}_\mathfrak{u}^{-1}\boldsymbol{\xi}_\text{b} \end{bmatrix} F_\text{b} \frac{\phi(\eta^n)}{\eta^n}\mu_{t+}\eta^n. \quad (46)$$

The form of $\boldsymbol{\sigma}^n$, adapted from [6], is:

$$\boldsymbol{\sigma}^n = \mathbf{I} + \frac{kF_\text{b}}{2}\left(\frac{d\phi}{d\eta} - \frac{\phi}{\eta}\right)_{t=kn} \begin{bmatrix} \mathbf{0} \\ \mathbf{\Omega}_\mathfrak{u}^{-1}\boldsymbol{\xi}_\text{b} \end{bmatrix} \begin{bmatrix} \mathbf{0}, \boldsymbol{\xi}_\eta^\mathsf{T} \end{bmatrix}, \quad (47)$$

and is well-defined, owing to (2). Here, $\mathbf{J}_\text{b}$ and $\mathbf{U}$ are as per Section 3.1.1 and 3.1.2, respectively. Expanding out the operators in (46), one is able to compute $\mathfrak{q}^{n+1}$, $\mathfrak{p}^{n+1}$ as the solution of a single linear system, thus avoiding entirely the need for iterative nonlinear root finders. The update equation in this case is:

$$\left(\mathbf{I} + \frac{kF_\text{b}}{2}\left(\frac{d\phi}{d\eta}\right) \begin{bmatrix} \mathbf{0} \\ \mathbf{\Omega}_\mathfrak{u}^{-1}\boldsymbol{\xi}_\text{b} \end{bmatrix} \begin{bmatrix} \mathbf{0}, \boldsymbol{\xi}_\eta^\mathsf{T} \end{bmatrix} - \frac{k}{2}\mathbf{G}\right) \begin{bmatrix} \mathfrak{q}^{n+1} \\ \mathfrak{p}^{n+1} \end{bmatrix} = \mathbf{b}^n,$$

where $\mathbf{b}^n$ is known from previous time steps. It is seen that the update matrix is in the form of a block matrix with fully diagonal blocks, plus a rank-1 perturbation. This can be solved efficiently, via the Sherman-Morrison formula [21], as detailed in [6].

Stability of scheme (46) is somewhat harder to prove, though partial results are available in [7]. Provided one chooses a number $N_\mathfrak{u}$ of modes lower than the Nyquist limit, empirical evidence

suggests that the proposed scheme greatly outperforms simpler explicit designs such as forward Euler or Runge-Kutta-type algorithms [22] in terms of stability, while keeping compute times within reference bounds for efficient simulation.

4.2. Spring & Membrane

The numerical integration of (42b), (42c) may be performed simply as:

$$\delta_t^2 \mathfrak{v}^n = -\mathbf{\Omega}_\mathfrak{v}^2 \mathfrak{v}^n - \mathbf{C}_\mathfrak{v}\delta_t^\circ \mathfrak{v}^n + \boldsymbol{\xi}_\text{p}F_\text{p}^n, \quad (48a)$$

$$\delta_t^2 \mathfrak{w}^n = -\mathbf{\Omega}_\mathfrak{w}^2 \mathfrak{w}^n - \mathbf{C}_\mathfrak{w}\delta_t^\circ \mathfrak{w}^n + \boldsymbol{\xi}_c F_c^n. \quad (48b)$$

Various other designs are possible, varying greatly in terms of stability and spectral accuracy. An attractive alternative is represented by exact integrators [23, 2], though the schemes above yield a perceptually reasonable reverberation characteristic [8]. Note that stability conditions arise as: $\mathbf{\Omega}_{\mathfrak{v},\mathfrak{w}} < 2/k$. These set upper limits for the modal frequencies.

5. OUTPUT SIGNALS

Figure 8 displays the spectrograms of the normalised signals extracted from the three subsystems. The string physical values were the ones of a C2 cello string, taken from [14], while the bridge parameters were the same listed in Figure 5. The bow pressure was $F_\text{b} = 0.02$ N, and the input and output positions were set to $0.73 \cdot L_\text{s}$ and $0.34 \cdot L_\text{p}$ respectively. The latter values were chosen empirically to obtain a Helmholtz motion-shaped output sound [2, Chapter 7]. The damping profile applied was the one proposed by Valette [24]. The spring parameters were the ones detailed in Figure 7. Finally, the membrane physical values were: $L_m = 0.5$ m, $T_m = 3000$ N m^{-1} and $\rho_m = 1.26$ Kg m^{-2}, and the output point was $(X_\text{o}, Y_\text{o}) = (0.47, 0.62) \cdot L_m$. A damping profile was chosen, for the spring and the membrane, which consists of a frequency-independent (F-I) and a frequency-dependent (F-D) part; as proposed by Bilbao [2, Chapter 7] the latter depends on the square of the mode number. The damping coefficients for the spring were taken from [18]; in the mebrane case, the F-I coefficient was set to 10, while the F-D one to 5×10^{-5}, both chosen empirically. Only a few seconds-long portion of data was analysed, in order to avoid including too many signal variations. The spring and the membrane act here as reverberant components. Panel (b) from Figure 8 clearly exhibits cross stripes which correspond to the spring chirps. The membrane, on the other hand, introduces a broadband signal, which mimics late reflections. This is clearly visible in Panel (c) from Figure 8. Sound samples can be found at the following Github link[3].

6. CONCLUSION

This paper presented a physical model of the yaybahar in the modal domain. To this end, a modal decomposition of its subcomponents was offered, including a model for the coupling between a vibrating string and a distributed bridge, and the analytic modal expansion of a helical spring. In addition, an energy-consistent method for connecting the instrument components was here presented, making use of boundary forces.

This work focused on the development of a yaybahar physical model; nevertheless, different aspects were overlooked, and will be
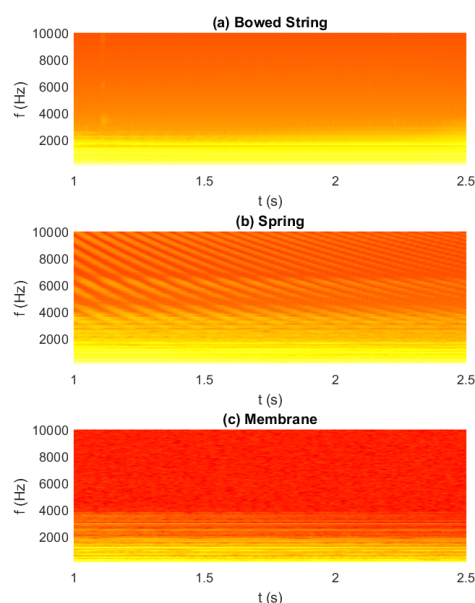
---

[3] https://github.com/Nemus-Project/yaybahar-nit

Figure 8: *Spectrograms of the three subsystems outputs after the initial transient. Panel (a) displays the spectrogram of the extracted force F_p, panel (b) shows the spectrogram of the force signal F_c, and panel (c) represents the output signal $\dot{w}_\mathrm{o}$ at the output position $(X_\mathrm{o}, Y_\mathrm{o})$.*

subject of future work. The physical values for the spring and the membrane were empirically tuned, while running proper measurements on a real instrument would significantly improve the sound quality. This is valid for the damping profiles as well. In addition, the membrane was considered to be rectangular, while an accurate reproduction would employ a circular model. Further future work will also include a real-time implementation.

7. ACKNOWLEDGMENTS

8. REFERENCES

[1] J Parker and S. Bilbao, "Spring reverberation: A physical perspective," in *Proc. Digital Audio Effects (DAFx-09)*, Como, Italy, 09 2009.

[2] S. Bilbao, *Numerical Sound Synthesis*, John Wiley & Sons, Ltd, Chichester, UK, 2009.

[3] S. Bilbao, "Numerical simulation of spring reverberation," in *Proc. Digital Audio Effects (DAFx-13)*, Maynooth, Ireland, 09 2013.

[4] P.J. Christensen, S. Willemsen, and S. Serafin, "Applied Physical Modeling for Sound Synthesis: the Yaybahar," in *Proc. 2nd Nordic SMC Conf.*, Online, 11 2021.

[5] J. Parker, H. Penttinen, S. Bilbao, and J.S. Abel, "Modeling methods for the highly dispersive slinky spring: A novel mu-

[6] Riccardo Russo, Michele Ducceschi, and Stefan Bilbao, "Efficient simulation of the bowed string in modal form," in *Proc. Digital Audio Effects (DAFx-2022), Vienna*, 09 2022.

[7] M. Ducceschi and S. Bilbao, "Non-iterative simulation methods for virtual analog modelling," *IEEE/ACM Trans. Audio Speech Lang. Process.*, vol. 30, pp. 3189–3198, 2022.

[8] M. Ducceschi and C.J. Webb, "Plate reverberation: Towards the development of a real-time plug-in for the working musician," in *Proc. Int. Conf. Acoust. (ICA 2016)*, Buenos Aires, Argentina, 09 2016.

[9] R. Russo, "Physical modeling and optimisation of a emt 140 plate reverb," M.S. thesis, Aalborg University Copenhagen, Copenhagen, Denmark, 2021.

[10] J.O. Smith, *Physical Audio Signal Processing*, `https://ccrma.stanford.edu/~jos/pasp/pasp.html`, accessed April 2023, online book, 2010 edition.

[11] J. Woodhouse, "On the "bridge hill" of the violin," *Acta Acust. united Acust.*, vol. 91, pp. 155–165, 2005.

[12] J.H. Smith and J. Woodhouse, "The tribology of rosin," *J. Mech. Phys. Solids*, vol. 48, pp. 1633–1681, 08 2000.

[13] P. Galluzzo, J. Woodhouse, and H. Mansour, "Assessing friction laws for simulating bowed-string motion," *Acta Acust. united Acust.*, vol. 103, pp. 1080–1099, 11 2017.

[14] C. Desvages, *Physical modelling of the bowed string and applications to sound synthesis*, Ph.D. thesis, The University of Edinburgh, 2018.

[15] W.H. Wittrick, "On elastic wave propagation in helical springs," *Int. J. Mech. Sci.*, vol. 8, no. 1, pp. 25–47, 1966.

[16] L. Della Pietra and S. della Valle, "On the dynamic behaviour of axially excited helical springs," *Meccanica*, vol. 17, pp. 31–43, 1982.

[17] J.N. Franklin, *Matrix Theory*, Dover Publications, Mineola, NY, USA, 2000.

[18] M. Van Walstijn, "Numerical calculation of modal spring reverb parameters," in *Proc. Digital Audio Effects (DAFx-2020), Online*, 09 2020.

[19] J. McQuillan and M. Van Walstijn, "Modal spring reverb based on discretisation of the thin helical spring model," in *Proc. Digital Audio Effects (DAFx-2021), Online*, 09 2021, vol. 2.

[20] L.E. Kinsler, A.R. Frey, A.B. Coppens, and J.V. Sanders, *Fundamentals of Acoustics, 4th Edition*, Wiley, Hoboken, NJ, USA, 1999.

[21] J. Sherman and W.J. Morrison, "Adjustment of an inverse matrix corresponding to a change in one element of a given matrix," *Ann. Math. Stat.*, vol. 21, pp. 124–127, 1950.

[22] R.J. LeVeque, *Finite Difference Methods for Ordinary and Partial Differential Equations. Steady State and Time Dependent Problems*, SIAM, Philadelphia, USA, 2007.

[23] J. Cieslinski, "On the exact discretization of the classical harmonic oscillator equation," *J. Differ. Equ. Appl.*, vol. 17, no. 11, pp. 1673–1694, 2009.

[24] C. Valette and C. Cuesta, *Mécanique de la corde vibrante*, Hermès, Paris, 1993.

Chapter 8

Conclusion and perspectives

This chapter provides a summary of the content and results of each chapter, followed by concluding remarks and directions for future research.

8.1 Summary

Chapter 1 serves as a broad introduction to musical string vibration modelling. It reviews the most significant mathematical models, starting from linear ones and extending to geometric nonlinearities, collisions, and friction, while presenting fundamental numerical techniques. Following this review, an examination of state-of-the-art frameworks for the efficient simulation of nonlinear systems is included, and the specific objectives of the thesis are outlined.

Chapters 2 and 3 cover linear vibration and introduce the mathematical tools and notation used throughout the text. Chapter 2 focuses on the continuous domain: it begins with the concept of potential quadratisation in the lumped case and proceeds with the presentation of the linear oscillator. It extends to systems of coupled oscillators; then, linear strings are introduced. This chapter also details modal techniques, including refined, finite-impedance boundary conditions. Chapter 3 illustrates numerical simulation techniques, starting with time-stepping methods for both first- and second-order ODEs, discussing differences between one-step and two-step methods, and introducing the fundamental concepts of stability (achieved through energy analysis), consistency, and convergence. The FD method is then discussed for spatial domain discretisation and is applied to linear string models. An original contribution of these chapters is the development of a model for a linear stiff string terminating with a spatially distributed boundary condition, serving as a model for a bridge within an energy-consistent framework. The eigenfrequencies and vibration modes are derived by solving a discrete eigenvalue problem.

Chapter 4 discusses geometric nonlinearities. It begins with the lumped case of the Duffing oscillator. Then, it extends to nonlinear string models, concluding with the KC string, which is also presented in a modal form and with double polarisation. Quadratisation-based approaches are first examined in the lumped case, followed by a description of the SAV procedure for general spatially distributed nonlinear systems. The chapter includes an in-depth analysis of the performance of SAV in the context of nonlinear transverse string vibration, including a study on the global error demonstrating convergence. An issue arising at lower sample rates, linked to anomalous behaviour of the auxiliary variable, is reported. Finally, a technique based on a physical constraint is presented to mitigate this anomalous behaviour while maintaining convergence. The chapter concludes with a brief discussion on applying SAV to the GE string, building on prior work.

Chapter 5 focuses on simulating collisions using penalty models. The discussion begins with the lumped case of a mass-barrier collision: the performance of a quadratised method is here evaluated, confirming earlier observations of anomalous behaviour. Three techniques are compared to address this issue: two from previous works and one adapted from the constraint introduced in Chapter 4. Convergence is reported for the latter. The discussion then extends to collisions involving strings, considering both lumped and distributed scenarios. These cases are solved using SAV, and the constraint technique presented in Chapter 4 is further adapted to handle distributed collisions. It is demonstrated that this approach effectively helps in improving the simulation results. However, an open question remains regarding the role of a shift constant, which must be non-zero to ensure the correct behaviour of the simulation.

Chapter 6 deals with nonlinear friction induced by a bow. Here, a different non-iterative approach is utilised, adapted from virtual-analogue modelling. The chapter begins by discussing a lumped, bowed mass-spring system. Then, the analysis of a spatially distributed case is examined, by considering the bowed ideal string, which is spatially discretised using both FD and modal methods. A comprehensive comparison is made between traditional iterative methods and newly developed non-iterative approaches for both the lumped and distributed systems. The proposed schemes are shown to produce results comparable to those obtained with fully implicit methods, while avoiding the need for iterative routines. Moreover, they demonstrate robust numerical behaviour, outperforming classic explicit integrators, such as forward Euler, in terms of stability. Yet, the stability properties of these new schemes still require further study.

Chapter 7 proposes two case studies of physical models of musical instruments using the techniques and models detailed in previous chapters. It corresponds to two papers presented at the International Conference on Digital Audio Effects (DAFx). The first study shows the

simulation of a guitar fretboard. A novel approach is here introduced for solving multiple nonlinearities simultaneously using SAV, which involves distinct auxiliary variables. This approach differs from previous works and requires the inversion of a small matrix whose size matches the number of nonlinear gradients. This method offers more flexibility in algorithm design, allowing for the application of the constraint equations developed in earlier chapters. The second study makes use of a bowed string coupled to a distributed bridge, as seen in Chapter 3, solved through the non-iterative method presented in Chapter 6, combined with a modal spring model employing analytic modes, to implement a physical model of the yaybahar.

8.2 Concluding remarks

The aim of this thesis was to explore and advance the use of FDTD and modal methods for simulating nonlinear string vibration, emphasising the perceptual accuracy of the synthesis and efficiency of the algorithms. This work encompasses different nonlinearities typically occurring in strings, employing newly developed non-iterative methods. In particular, quadratisation-based techniques are used for conservative nonlinear forces, enabling a unified time-stepping procedure. It is demonstrated here that these non-iterative methods significantly reduce the computational load required to solve nonlinear systems, allowing for real-time simulation of physical models that were previously far from achieving real-time performance. This is the case, for instance, of the guitar fretboard presented in Chapter 7. Comparisons with classic iterative methods show that these non-iterative techniques overcome common challenges, such as variable compute times and issues related to the existence and uniqueness of solutions. Additionally, while a formal mathematical proof of convergence is not yet available, numerical testing strongly suggests convergence for these methods, indicating that the simulation results are reliable at sufficiently high sample rates.

Despite these promising results, some issues remain unresolved. One of the goals of this thesis was to formulate a general framework for the sound synthesis of nonlinear strings. It was observed that the quality of the simulations is still highly dependent on careful discretisation choices, particularly regarding the implementation of the nonlinear potential gradients. This means the algorithm must still be tailored to each specific problem. These issues are primarily linked to the behaviour of the auxiliary variable, which, if not properly constrained, does not behave as its continuous counterpart at lower sample rates, leading to inaccurate simulation results. While solutions were proposed for distinct nonlinearities, a universal procedure for regularising the auxiliary variable's behaviour has yet to be established. An attempt was made here to extend a single technique to address two different nonlinearities, but

its correct functioning in cases involving collisions requires further investigation. Moreover, the results are still partial, as a convergence test was not performed for distributed collisions with constraints applied. Further studies on these techniques will represent an important direction for future research.

Some systems still require thorough exploration. For instance, while a SAV implementation of the GE string has been developed recently, no detailed study exists on the behaviour of the auxiliary variable, nor is there an established technique to address the grid spacing issue mentioned in Chapter 4. Future work will focus on employing modal techniques to spatially discretize both transverse and longitudinal motion while also investigating the behaviour of the auxiliary variable.

Additional research is needed to determine the best strategy for handling multiple nonlinearities. Consolidating all the nonlinear dynamics into a single scalar potential, thereby eliminating the need to solve any linear system, would result in a much more efficient procedure. However, studies on auxiliary variable behaviour remain necessary in this case.

Another unresolved issue concerns the stability properties of the non-iterative method presented for the bow, which requires additional investigation. Furthermore, an important research direction is extending this method to account for finite-width bow interaction. Other potential directions for future work include unifying the two numerical methods by developing a non-iterative procedure to handle both conservative and non-conservative nonlinear forces simultaneously and incorporating complex boundary conditions in cases involving geometric nonlinearities and collisions.

References

[1] Adrien, J.-M. (1991). The missing link: modal synthesis. *Representations of Musical Signals*, pages 269–297.

[2] Adrien, J.-M. and Rodet, X. (1985). Physical models of instruments: A modular approach, application to strings. In *Proceedings of the International Computer Music Conference*, pages 85–89, Vancouver, Canada.

[3] Amerio, L. (1978). Continuous solutions of the problem of a string vibrating against an obstacle. *Rendiconti del Seminario Matematico della Università di Padova*, 59:67–96.

[4] Anand, G. V. (1966). Nonlinear resonance in stretched strings with viscous damping. *The Journal of the Acoustical Society of America*, 40(6):1517–1528.

[5] Anand, G. V. (1969). Large-amplitude damped free vibration of a stretched string. *The Journal of the Acoustical Society of America*, 45(5):1089–1096.

[6] Antunes, J. and Debut, V. (2017). Dynamical computation of constrained flexible systems using a modal Udwadia-Kalaba formulation: Application to musical instruments. *The Journal of the Acoustical Society of America*, 141(2):764–778.

[7] Arosio, A. (1999). On the nonlinear Timoshenko-Kirchhoff beam equation. *Chinese Annals of Mathematics*, 20(04):495–506.

[8] Arosio, A. (2001). A geometrical nonlinear correction to the Timoshenko beam equation. *Nonlinear Analysis: Theory, Methods & Applications*, 47(2):729–740.

[9] Avanzini, F., Marogna, R., and Bank, B. (2012). Efficient synthesis of tension modulation in strings and membranes based on energy estimation. *The Journal of the Acoustical Society of America*, 131(1):897–906.

[10] Bacon, R. A. and Bowsher, J. M. (1978). A discrete model of a struck string. *Acta Acustica united with Acustica*, 41(1):21–27.

[11] Bader, R. (2005). *Computational mechanics of the classical guitar*. Springer-Verlag, Berlin Heidelberg, Germany.

[12] Bank, B. (2006). *Physics-based sound synthesis of string instruments including geometric nonlinearities*. PhD thesis, Department of Measurement and Information Systems, Budapest University of Technology and Economics.

[13] Bank, B. and Sujbert, L. (2003). Modeling the longitudinal vibration of piano strings. In *Proceedings of the Stockholm Musical Acoustic Conference (SMAC)*, pages 143–146, Stockholm, Sweden.

[14] Bank, B. and Sujbert, L. (2004). A piano model including longitudinal string vibrations. In *Proceedings of the International Conference on Digital Audio Effects (DAFx)*, pages 89–94, Naples, Italy.

[15] Bank, B. and Sujbert, L. (2005). Generation of longitudinal vibrations in piano strings: From physics to sound synthesis. *The Journal of the Acoustical Society of America*, 117(4):2268–2278.

[16] Bank, B., Zambon, S., and Fontana, F. (2010). A modal-based real-time piano synthesizer. *IEEE Transactions on Audio, Speech, and Language Processing*, 18(4):809–821.

[17] Bensa, J., Bilbao, S., Kronland-Martinet, R., Smith, J., and Voinier, T. (2005). Computational modeling of stiff piano strings using digital waveguides and finite differences. *Acta Acustica united with Acustica*, 91:289–298.

[18] Bensa, J., Bilbao, S., Kronland-Martinet, R., and Smith, J. O. (2003). The simulation of piano string vibration: From physical models to finite difference schemes and digital waveguides. *The Journal of the Acoustical Society of America*, 114(2):1095–1107.

[19] Betsch, P. and Steinmann, P. (2002). Frame-indifferent beam finite elements based upon the geometrically exact beam theory. *International Journal for Numerical Methods in Engineering*, 54(12):1775–1788.

[20] Bhanuprakash, A., Van Walstijn, M., and Stapleton, P. (2020). A finite difference model for articulated slide-string simulation. In *Proceedings of the International Conference on Digital Audio Effects (DAFx)*, pages 195–202, Vienna, Austria.

[21] Bhargava, S. and Ghosh, R. (1924). Elastic impact of pianoforte hammer. *The London, Edinburgh, and Dublin Philosophical Magazine and Journal of Science*, 47(282):1141–1148.

[22] Bilbao, S. (2004). Modal type synthesis techniques for nonlinear strings with an energy conservation property. In *Proceedings of the International Conference on Digital Audio Effects (DAFx)*, pages 119–124, Naples, Italy.

[23] Bilbao, S. (2005). Conservative numerical methods for nonlinear strings. *The Journal of the Acoustical Society of America*, 118(5):3316–3327.

[24] Bilbao, S. (2009). *Numerical sound synthesis*. John Wiley & Sons, Ltd, Chichester, UK.

[25] Bilbao, S., Desvages, C., Ducceschi, M., Hamilton, B., Harrison-Harsley, R., Torin, A., and Webb, C. (2020). Physical modeling, algorithms, and sound synthesis: The ness project. *Computer Music Journal*, 43(2-3):15–30.

[26] Bilbao, S. and Ducceschi, M. (2022). Fast explicit algorithms for hamiltonian numerical integration. In *Proceedings of 2020 the European Nonlinear Dynamics Conference*, Lyon, France.

[27] Bilbao, S., Ducceschi, M., and Webb, C. (2019). Large-scale real-time modular physical modeling sound synthesis. In *Proceedings of the International Conference on Digital Audio Effects (DAFx)*, pages 128–135, Birmingham, UK.

[28] Bilbao, S., Ducceschi, M., and Zama, F. (2023). Explicit exactly energy-conserving methods for hamiltonian systems. *Journal of Computational Physics*, 472:111697.

[29] Bilbao, S., Hamilton, B., Torin, A., Webb, C., Graham, P., Gray, A., Kavoussanakis, K., and Perry, J. (2013). Large scale physical modeling sound synthesis. In *Proceedings of the Stockholm Musical Acoustics Conference/Sound and Music Computing Conference (SMAC/SMC)*, pages 593–600, Stockholm, Sweden.

[30] Bilbao, S., Russo, R., Webb, C., and Ducceschi, M. (2024). Real-time guitar synthesis. In *Proceedings of the International Conference on Digital Audio Effects (DAFx)*, pages 163–170, Guildford, UK.

[31] Bilbao, S. and Smith, J. O. (2005). Energy-conserving finite difference schemes for nonlinear strings. *Acta Acustica*, 91(2):299–311.

[32] Bilbao, S. and Torin, A. (2014). Numerical simulation of string/barrier collisions: The fretboard. In *Proceedings of the International Conference on Digital Audio Effects (DAFx)*, pages 137–144, Erlangen, Germany.

[33] Bilbao, S. and Torin, A. (2015). Numerical modeling and sound synthesis for articulated string/fretboard interactions. *Journal of the Audio Engineering Society*, 63(5):336–347.

[34] Bilbao, S., Torin, A., and Chatziioannou, V. (2015). Numerical modeling of collisions in musical instruments. *Acta Acustica united with Acustica*, 101(1):155–173.

[35] Boutillon, X. (1988). Model for piano hammers: Experimental determination and digital simulation. *The Journal of the Acoustical Society of America*, 83(2):746–754.

[36] Bridges, J. and Van Walstijn, M. (2015). Investigation of tanpura string vibrations using a two-dimensional time-domain model incorporating coupling and bridge friction. *Proceedings of the Vienna Talk on Music Acoustics*, pages 126–131.

[37] Bruyns, C. (2006). Modal synthesis for arbitrarily shaped objects. *Computer Music Journal*, 30(3):22–37.

[38] Bunch, J. R. and Hopcroft, J. E. (1974). Triangular factorization and inversion by fast matrix multiplication. *Mathermatics of Computation*, 28(125):231–236.

[39] Burridge, R., Kappraff, J., and Morshedi, C. (1982). The sitar string, a vibrating string with a one-sided inelastic constraint. *SIAM Journal on Applied Mathematics*, 42(6):1231–1251.

[40] Campbell, M. and Greated, C. A. (2001). *The musician's guide to acoustics*. Oxford Univ. Press, Oxford.

[41] Carrier, G. F. (1945). On the non-linear vibration problem of the elastic string. *Quarterly of Applied Mathematics*, 3:157–165.

[42] Chabassier, J. (2012). *Modélisation et simulation numérique d'un piano par modèles physiques*. PhD thesis, Ecole Polytechnique.

[43] Chabassier, J., Chaigne, A., and Joly, P. (2013). Modeling and simulation of a grand piano. *The Journal of the Acoustical Society of America*, 134(1):648–665.

[44] Chabassier, J. and Imperiale, S. (2013a). Introduction and study of fourth order theta schemes for linear wave equations. *Journal of Computational and Applied Mathematics*, 245:194–212.

[45] Chabassier, J. and Imperiale, S. (2013b). Stability and dispersion analysis of improved time discretization for simply supported prestressed Timoshenko systems. application to the stiff piano string. *Wave Motion*, 50(3):456–480.

[46] Chabassier, J. and Joly, P. (2010). Energy preserving schemes for nonlinear hamiltonian systems of wave equations: Application to the vibrating piano string. *Computer Methods in Applied Mechanics and Engineering*, 199(45):2779–2795.

[47] Chaigne, A. (1992). On the use of finite differences for musical synthesis. application to plucked stringed instruments. *Journal d'Acoustique*, 2(5):181–211.

[48] Chaigne, A. and Askenfelt, A. (1994a). Numerical simulations of piano strings. I. A physical model for a struck string using finite difference methods. *The Journal of the Acoustical Society of America*, 95(2):1112–1118.

[49] Chaigne, A. and Askenfelt, A. (1994b). Numerical simulations of piano strings. II. Comparisons with measurements and systematic exploration of some hammer-string parameters. *The Journal of the Acoustical Society of America*, 95(3):1631–1640.

[50] Chaigne, A. and Kergomard, J. (2016). *Acoustics of musical instruments*. Modern Acoustics and Signal Processing. Springer New York, New York, NY.

[51] Chatziioannou, V., Schmutzhard, S., and Bilbao, S. (2017). On iterative solutions for numerical collision models. In *Proceedings of the International Conference on Digital Audio Effects (DAFx)*, pages 72–79, Edinburgh, UK.

[52] Chatziioannou, V. and Van Walstijn, M. (2013). An energy conserving finite difference scheme for simulation of collisions. In *Proceedings of the Stockholm Musical Acoustics Conference/Sound and Music Computing Conference (SMAC/SMC)*, pages 584–591, Stockholm, Sweden.

[53] Chatziioannou, V. and Van Walstijn, M. (2015). Energy conserving schemes for the simulation of musical instrument contact dynamics. *Journal of Sound and Vibration*, 339:262–279.

[54] Chatziioannou, V. and Van Walstijn, M. (2017). On the contact duration accuracy of discrete-time collision models. In *Proceedings of the International Symposium on Musical Acoustics (ISMA)*, pages 95–98, Montreal, Canada.

[55] Cheng, Y., Wu, Y., and Guo, B.-Z. (2021). Absolute boundary stabilization for an axially moving Kirchhoff beam. *Automatica*, 129:109667.

[56] Cieśliński, J. L. and Ratkiewicz, B. (2006). On simulations of the classical harmonic oscillator equation by difference equations. *Advances in Difference Equations*, 2006:1–17.

[57] Cieśliński, J. L. (2011). On the exact discretization of the classical harmonic oscillator equation. *Journal of Difference Equations and Applications*, 17(11):1673–1694.

[58] Conklin, H. A. (1999). Generation of partials due to nonlinear mixing in a stringed instrument. *The Journal of the Acoustical Society of America*, 105(1):536–545.

[59] Cottrell, S. (2023). *Shaping Sound and Society: The Cultural Study of Musical Instruments*. Routledge, London, UK.

[60] Cuesta, C. and Valette, C. (1988). Evolution temporelle de la vibration des cordes de clavecin. *Acta Acustica united with Acustica*, 66(1):37–45.

[61] Dalmont, J.-P. and Maugeais, S. (2019). Piano strings with reduced inharmonicity. *Acta Acustica united with Acustica*, 105(4):714–717.

[62] Davis, R., Henshell, R., and Warburton, G. (1972). A Timoshenko beam element. *Journal of Sound and Vibration*, 22(4):475–487.

[63] Debut, V. and Antunes, J. (2020). Physical synthesis of six-string guitar plucks using the Udwadia-Kalaba modal formulation. *The Journal of the Acoustical Society of America*, 148(2):575–587.

[64] Debut, V., Antunes, J., Marques, M., and Carvalho, M. (2016). Physics-based modeling techniques of a twelve-string portuguese guitar: A non-linear time-domain computational approach for the multiple-strings/bridge/soundboard coupled dynamics. *Applied Acoustics*, 108:3–18.

[65] Dekoninck, B. and Nicaise, S. (2000). The eigenvalue problem for networks of beams. *Linear Algebra and its Applications*, 314(1):165–189.

[66] Derveaux, G., Chaigne, A., Joly, P., and Becache, E. (2004). Time-domain simulation of a guitar: Model and method. *The Journal of the Acoustical Society of America*, 114:3368–83.

[67] Desvages, C. (2018). *Physical modelling of the bowed string and applications to sound synthesis*. PhD thesis, The University of Edinburgh.

[68] Desvages, C. and Bilbao, S. (2016). Two-polarisation physical model of bowed strings with nonlinear contact and friction forces, and application to gesture-based sound synthesis. *Applied Sciences*, 6(5):135.

[69] Dickey, R. W. (1969). Infinite systems of nonlinear oscillation equations related to the string. *Proceedings of the American Mathematical Society*, 23(3):459–468.

[70] Dickey, R. W. (1980). Stability of periodic solutions of the nonlinear string. *Quarterly of Applied Mathematics*, 38(2):253–259.

[71] Ducceschi, M. and Bilbao, S. (2016). Linear stiff string vibrations in musical acoustics: Assessment and comparison of models. *The Journal of the Acoustical Society of America*, 140(4):2445–2454.

[72] Ducceschi, M. and Bilbao, S. (2019a). Conservative finite difference time domain schemes for the prestressed Timoshenko, shear and Euler–Bernoulli beam equations. *Wave Motion*, 89:142–165.

[73] Ducceschi, M. and Bilbao, S. (2019b). Non-iterative, conservative schemes for geometrically exact nonlinear string vibration. In *Proceedings of the International Congress on Acoustics (ICA)*, pages 5542–5549, Aachen, Germany.

[74] Ducceschi, M. and Bilbao, S. (2019c). Non-iterative solvers for nonlinear problems: The case of collisions. In *Proceedings of the Internatinal Conference on Digital Audio Effects (DAFx)*, pages 17–24, Birmingham, UK.

[75] Ducceschi, M. and Bilbao, S. (2019d). A physical model of the prepared piano. In *Proceedings of the International Congress on Sound and Vibration*, pages 5001–5009, Montreal, Canada.

[76] Ducceschi, M. and Bilbao, S. (2022a). Non-iterative simulation methods for virtual analog modelling. *IEEE/ACM Transactions on Audio, Speech, and Language Processing*, 30:3189–3198.

[77] Ducceschi, M. and Bilbao, S. (2022b). Real-time simulation of the struck piano string with geometrically exact nonlinearity via novel quadratic hamiltonian method. In *Proceedings of the 2020 European Nonlinear Dynamics Conference*, Lyon, France.

[78] Ducceschi, M. and Bilbao, S. (2022c). Simulation of the geometrically exact nonlinear string via energy quadratisation. *Journal of Sound and Vibration*, 534:117021.

[79] Ducceschi, M., Bilbao, S., and Desvages, C. (2016). Modelling collisions of nonlinear strings against rigid barriers: Conservative finite difference schemes with application to sound synthesis. In *Proceedings of the International Congress on Acoustics*, Buenos Aires, Argentina.

[80] Ducceschi, M., Bilbao, S., and Webb, C. J. (2021a). Non-iterative schemes for the simulation of nonlinear audio circuits. In *Proceedings of the International Conference on Digital Audio Effects (DAFx)*, pages 25–32, Vienna, Austria.

[81] Ducceschi, M., Bilbao, S., Willemsen, S., and Serafin, S. (2021b). Linearly-implicit schemes for collisions in musical acoustics based on energy quadratisation. *The Journal of the Acoustical Society of America*, 149(5):3502–3516.

[82] Ducceschi, M., Mousseau, A., Bilbao, S., and Russo, R. (2024). Fast simulation of the Kirchhoff-Carrier string with an energy-storing boundary condition using a scalar auxiliary variable approach. In *Proceedings of the IFAC Workshop on Lagrangian and Hamiltonian Methods for Non Linear Control (LHMNC), Besançon, France*, pages 220–225.

[83] Ducceschi, M. and Touzé, C. (2015). Modal approach for nonlinear vibrations of damped impacted plates: Application to sound synthesis of gongs and cymbals. *Journal of Sound and Vibration*, 334:313–331.

[84] Duindam, V., Macchelli, A., Stramigioli, S., and Bruyninckx, H. (2009). *Modeling and control of complex physical systems*. Springer Berlin Heidelberg, Berlin, Heidelberg.

[85] Dupont, P., Hayward, V., Armstrong, B., and Altpeter, F. (2002). Single state elasto-plastic friction models. *IEEE Transactions on Automatic Control*, 47(5):787–792.

[86] Duyne, S. A. V. and Smith, J. O. (1994). A simplified approach to modeling dispersion caused by stiffness in strings and plates. In *Proceedings of the International Computer Music Conference*, pages 407–410, Aarhus, Denmark.

[87] Eckel, G., Iovino, F., and Caussè, R. (1995). Sound synthesis by physical modelling with Modalys. *Proceedings of the International Symposium on Musical Acoustics*, pages 478–482.

[88] Erkut, C. (2002). *Aspects in analysis and model-based sound synthesis of plucked string instruments*. PhD thesis, Department of Electrical and Communications Engineering, Helsinki University of Technology.

[89] Erkut, C., Karjalainen, M., Huang, P., and Välimäki, V. (2002). Acoustical analysis and model-based sound synthesis of the kantele. *The Journal of the Acoustical Society of America*, 112(4):1681–1691.

[90] Evangelista, G. (2011). Physical model of the string-fret interaction. In *Proceedings of the International Conference on Digital Audio Effects (DAFx)*, pages 345–351, Paris, France.

[91] Evangelista, G. and Eckerholm, F. (2010). Player–instrument interaction models for digital waveguide synthesis of guitar: Touch and collisions. *IEEE transactions on audio, speech, and language processing*, 18(4):822–832.

[92] Fabre, F., Le Carrou, J.-L., and Chomette, B. (2023). Physical modelling of a harp from Central Africa. *The Journal of the Acoustical Society of America*, 154(4):2337–2348.

[93] Falaize, A. and Hélie, T. (2016). Passive guaranteed simulation of analog audio circuits: A port-hamiltonian approach. *Applied Sciences*, 6(10):273.

[94] Fletcher, N. H. and Rossing, T. D. (1998). *The physics of musical instruments*. Springer New York, New York, NY.

[95] Fontana, F. and Bozzo, E. (2019). Newton–Raphson solution of nonlinear delay-free loop filter networks. *IEEE/ACM Transactions on Audio, Speech, and Language Processing*, 27(10):1590–1600.

[96] Franklin, J. (2000). *Matrix theory*. Dover Publications, Mineola, NY, USA.

[97] Friedlander, F. (1953). On the oscillations of a bowed string. *Mathematical Proceedings of the Cambridge Philosophical Society*, 49(3):516–530.

[98] Galluzzo, P., Woodhouse, J., and Mansour, H. (2017). Assessing friction laws for simulating bowed-string motion. *Acta Acustica united with Acustica*, 103(6):1080–1099.

[99] Garber, E. and Garber, E. (1999). Vibrating strings and eighteenth-century mechanics. *The Language of Physics: The Calculus and the Development of Theoretical Physics in Europe, 1750–1914*, pages 31–62.

[100] Ghosh, R. (1948). Elastic impact of pianoforte hammer. *The Journal of the Acoustical Society of America*, 20(3):324–328.

[101] Giordano, N. (2015). Explaining the Railsback stretch in terms of the inharmonicity of piano tones and sensory dissonance. *The Journal of the Acoustical Society of America*, 138(4):2359–2366.

[102] Giordano, N. and Jiang, M. (2004). Physical modeling of the piano. *EURASIP Journal on Advances in Signal Processing*, 2004(1):981942.

[103] Gough, C. (1984). The nonlinear free vibration of a damped elastic string. *The Journal of the Acoustical Society of America*, 75(6):1770–1776.

[104] Graff, K. F. (1991). *Wave motion in elastic solids*. Dover publications, New York, USA.

[105] Guettler, K. (1994). Wave analysis of a string bowed to anomalous low frequencies. *Catgut Acoustical Society Journal*, 2(6):8–14.

[106] Guo, B.-Z. and Guo, W. (2007). Adaptive stabilization for a Kirchhoff-type nonlinear beam under boundary output feedback control. *Nonlinear Analysis: Theory, Methods & Applications*, 66(2):427–441.

[107] Gustafsson, B., Kreiss, H., Oliger, J., and Kreiss, H.-O. (2013). *Time dependent problems and difference methods*. Wiley, Hoboken, N.J, 2nd edition.

[108] Gwynne A. Evans, Jonathan M. Blackledge, P. D. Y. (1999). *Numerical methods for partial differential equations*. Springer, London, UK.

[109] Han, S. M., Benaroya, H., and Wei, T. (1999). Dynamics of transversely vibrating beams using four engineering theories. *Journal of Sound and Vibration*, 225(5):935–988.

[110] Hertz, H. (1882). Ueber die berührung fester elastischer körper. *Journal für die reine und angewandte Mathematik*, 92:156–171.

[111] Hiller, L. and Ruiz, P. (1971a). synthesizing musical sounds by solving the wave equation for vibrating objects: Part 1. *Journal of the Audio Engineering Society*, 19:462–470.

[112] Hiller, L. and Ruiz, P. (1971b). Synthesizing musical sounds by solving the wave equation for vibrating objects: Part 2. *Journal of the Audio Engineering Society*, 19:542–551.

[113] Horvay, G. and Veluswami, M. (1980). Hertzian impact of two elastic spheres in the presence of surface damping. *Acta Mechanica*, 35:285–290.

[114] Hsueh, W.-J. (1999). Free and forced vibrations of stepped rods and coupled systems. *Journal of Sound and Vibration*, 226(5):891–904.

[115] Hunt, K. H. and Crossley, E. (1975). Coefficient of restitution interpreted as damping in vibroimpact. *Journal of Applied Mechanics*, 42:440–445.

[116] Hélie, T. and Roze, D. (2008). Sound synthesis of a nonlinear string using Volterra series. *Journal of Sound and Vibration*, 314(1-2):275–306.

[117] Issanchou, C., Acary, V., Pérignon, F., Touzé, C., and Le Carrou, J.-L. (2018a). Nonsmooth contact dynamics for the numerical simulation of collisions in musical string instruments. *The Journal of the Acoustical Society of America*, 143(5):3195–3205.

[118] Issanchou, C., Le Carrou, J.-L., Touzé, C., Fabre, B., and Doaré, O. (2018b). String/frets contacts in the electric bass sound: Simulations and experiments. *Applied Acoustics*, 129:217–228.

[119] Jelenić, G. and Crisfield, M. (1999). Geometrically exact 3d beam theory: implementation of a strain-invariant finite element for statics and dynamics. *Computer Methods in Applied Mechanics and Engineering*, 171(1):141–171.

[120] Jiang, M., Zhang, Z., and Zhao, J. (2022). Improving the accuracy and consistency of the scalar auxiliary variable (SAV) method with relaxation. *Journal of Computational Physics*, 456:110954.

[121] Jiolat, J.-T., d'Alessandro, C., Le Carrou, J.-L., and Antunes, J. (2021). Toward a physical model of the clavichord. *The Journal of the Acoustical Society of America*, 150(4):2350–2363.

[122] Johnson, J. and Bajaj, A. (1989). Amplitude modulated and chaotic dynamics in resonant motion of strings. *Journal of Sound and Vibration*, 128(1):87–107.

[123] Júnior, D. S. A. (2014). Conservative semidiscrete difference schemes for Timoshenko systems. *Journal of Applied Mathematics*, 2014(1):686421.

[124] Karplus, K. and Strong, A. (1983). Digital synthesis of plucked-string and drum timbres. *Computer Music Journal*, 7(2):43.

[125] Kartofelev, D., Stulov, A., Lehtonen, H.-M., and Välimäki, V. (2013). Modeling a vibrating string terminated against a bridge with arbitrary geometry. In *Proceedings of the Stockholm Music Acoustics Conference*, pages 626–632.

[126] Kerschen, G., Peeters, M., Golinval, J., and Vakakis, A. (2009). Nonlinear normal modes, part I: A useful framework for the structural dynamicist. *Mechanical Systems and Signal Processing*, 23(1):170–194.

[127] Kirchhoff, G. (1883). *Vorlesungen über mechanic*. B.G. Teubner, Leipzig, Germany.

[128] Krishnaswamy, A. and Smith, J. O. (2003). Methods for simulating string collisions with rigid spatial obstacles. In *2003 IEEE Workshop on Applications of Signal Processing to Audio and Acoustics (IEEE Cat. No. 03TH8684)*, pages 233–236.

[129] Kurmyshev, E. (2003). Transverse and longitudinal mode coupling in a free vibrating soft string. *Physics Letters A*, 310(2-3):148–160.

[130] Lang, S. (1987). *Linear algebra*. Springer New York, New York, USA, third edition.

[131] Laurson, M., Erkut, C., Välimäki, V., and Kuuskankare, M. (2001). Methods for modeling realistic playing in acoustic guitar synthesis. *Computer Music Journal*, 25(3):38–49.

[132] le Li, F. and zhong Sun, Z. (2007). A finite difference scheme for solving the Timoshenko beam equations with boundary feedback. *Journal of Computational and Applied Mathematics*, 200(2):606–627.

[133] le Rond D'Alembert, J. (1747). Récherches sur la courbe que forme une corde tenduë mise en vibration. *Memoires de l'Academie royale des sciences et belles lettres. Classe de mathematique*, 3:214–219.

[134] Leamy, M. J. and Gottlieb, O. (2000). Internal resonances in whirling strings involving longitudinal dynamics and material non-linearities. *Journal of Sound and Vibration*, 236(4):683–703.

[135] Lee, J. W., Jun Choi, M., and Lee, K. (2024). String sound synthesizer on gpu-accelerated finite difference scheme. In *IEEE International Conference on Acoustics, Speech and Signal Processing (ICASSP)*, pages 1491–1495, Seoul, Korea.

[136] Legge, K. A. and Fletcher, N. H. (1984). Nonlinear generation of missing modes on a vibrating string. *The Journal of the Acoustical Society of America*, 76(1):5–12.

[137] LeVeque, R. (2007). *Finite difference methods for ordinary and partial differential equations. Steady state and time dependent problems*. SIAM, Philadelphia, USA.

[138] Lewy, H., Friedrichs, K., and Courant, R. (1928). Über die partiellen differenzengleichungen der mathematischen physik. *Mathematische Annalen*, 100:32–74.

[139] Li, Y. X. and Sun, L. Z. (2016). Transverse vibration of an undamped elastically connected double-beam system with arbitrary boundary conditions. *Journal of Engineering Mechanics*, 142(2):04015070.

[140] Lopes, N., Hélie, T., and Falaize, A. (2015). Explicit second-order accurate method for the passive guaranteed simulation of port-hamiltonian systems. In *Proceedings of the IFAC Workshop on Lagrangian and Hamiltonian Methods for Nonlinear Control (IFAC)*, pages 223–228, Lyon, France.

[141] Maestre, E., Spa, C., and Smith, J. O. (2014). A bowed string physical model including finite-width thermal friction and hair dynamics. In *Proceedings of the International Computer Music Conference/Sound and Music Computing Conference (ICMC/SMC)*, pages 1305–1311, Athens, Greece.

[142] Mandal, A. and Wahi, P. (2015). Natural frequencies, modeshapes and modal interactions for strings vibrating against an obstacle: Relevance to sitar and veena. *Journal of Sound and Vibration*, 338:42–59.

[143] Marazzato, F., Ern, A., Mariotti, C., and Monasse, L. (2019). An explicit pseudo-energy conserving time-integration scheme for hamiltonian dynamics. *Computer Methods in Applied Mechanics and Engineering*, 347:906–927.

[144] Marques, M., Antunes, J., and Debut, V. (2013). Guitar strings loaded with localized masses. In *Proceedings of the International Conference on Vibration Problems*, Lisbon, Portugal.

[145] Marques, M., Inàcio, O., Debut, V., and Antunes, J. (2012). On the dynamical behaviour of worn guitar strings. In *Proccedings of the International Congress of Sound and Vibration*, Vilnus, Lithuania.

[146] McIntyre, M. and Woodhouse, J. (1979). On the fundamentals of bowed string dynamics. *Acta Acust. united Acust.*, 43:93–108.

[147] McIntyre, M. E., Schumacher, R. T., and Woodhouse, J. (1983). On the oscillations of musical instruments. *The Journal of the Acoustical Society of America*, 74(5):1325–1345.

[148] Meirovitch, L. and Parker, R. (2001). *Fundamentals of vibrations*. McGraw-Hill, New York, USA.

[149] Michon, R., Martin, S. R., and Smith, J. O. (2017). MESH2FAUST: A modal physical model generator for the Faust programming language-Application to bell modeling. In *Proceedings of the 2017 International Computer Music Conference, ICMC.*, Shanghai, China.

[150] Miles, J. W. (1965). Stability of forced oscillations of a vibrating string. *The Journal of the Acoustical Society of America*, 38(5):855–861.

[151] Morrison, J. D. and Adrien, J.-M. (1993). Mosaic: A framework for modal synthesis. *Computer Music Journal*, 17(1):45–56.

[152] Morse, P. and Ingard, U. (1968). *Theoretical acoustics*. Princeton University Press, Princeton, NJ, USA.

[153] Murthy, G. S. S. and Ramakrishna, B. S. (1965). Nonlinear character of resonance in stretched strings. *The Journal of the Acoustical Society of America*, 38(3):461–471.

[154] Narasimha, R. (1968). Non-linear vibration of an elastic string. *Journal of Sound and Vibration*, 8(1).

[155] Oplinger, D. W. (1960). Frequency response of a nonlinear stretched string. *The Journal of the Acoustical Society of America*, 32(12):1529–1538.

[156] O'Reilly, O. and Holmes, P. (1992). Non-linear, non-planar and non-periodic vibrations of a string. *Journal of Sound and Vibration*, 153(3):413–435.

[157] Orr, S. and Van Walstijn, M. (2009). Modal representation of the resonant body within a finite difference framework for simulation of string instruments. pages 213–220. Proceedings of the International Conference on Digital Audio Effects (DAFx).

[158] Paiva, G. O., Ablitzer, F., Gautier, F., and dos Santos, J. M. C. (2019). Collisions in double string plucked instruments: Physical modelling and sound synthesis of the viola caipira. *Journal of Sound and Vibration*, 443:178–197.

[159] Pakarinen, J., Karjalainen, M., and Välimäki, V. (2003). Modeling and real-time synthesis of the kantele using distributed tension modulation. In *Proceedings of the Stockholm Music Acoustics Conference (SMAC)*, pages 409–412, Stockholm, Sweden.

[160] Pakarinen, J., Välimäki, V., and Karjalainen, M. (2005). Physics-based methods for modeling nonlinear vibrating strings. *Acta Acustica*, 91(2):312–325.

[161] Papetti, S., Avanzini, F., and Rocchesso, D. (2011). Numerical methods for a nonlinear impact model: A comparative study with closed-form corrections. *IEEE Transactions on Audio, Speech, and Language Processing*, 19(7):2146–2158.

[162] Pierce, J. R. and Van Duyne, S. A. (1997). A passive nonlinear digital filter design which facilitates physics-based sound synthesis of highly nonlinear musical instruments. *The Journal of the Acoustical Society of America*, 101(2):1120–1126.

[163] Pitteroff, R. and Woodhouse, J. (1998a). Mechanics of the contact area between a violin bow and a string. part II: Simulating the bowed string. *Acta Acustica united with Acustica*, 84(4):744–757.

[164] Pitteroff, R. and Woodhouse, J. (1998b). Mechanics of the contact area between a violin bow and a string. part III: Parameter dependence. *Acta Acustica united with Acustica*, 84(5):929–946.

[165] Raman, C. V. (1918). On the mechanical theory of the vibrations of bowed strings and of musical instruments of the violin family, with experimental verification of the results. *Indian Association for the Cultivation of Science Bulletin*, 15:243–276.

[166] Raman, C. V. (1921). On some indian stringed instruments. *Proceedings of the Indian Association for the Cultivation of Science*, 7:468–472.

[167] Raman, C. V. and Banerji, B. (1920). On Kaufmann's theory of the impact of the pianoforte hammer. *Proceedings of the Royal Society of London. Series A, Containing Papers of a Mathematical and Physical Character*, 97(682):99–110.

[168] Rank, E. and Kubin, G. (1997). A waveguide model for slapbass synthesis. In *1997 IEEE International Conference on Acoustics, Speech, and Signal Processing*, volume 1, pages 443–446.

[169] Renton, J. (2001). A check on the accuracy of Timoshenko's beam theory. *Journal of Sound and Vibration*, 245(3):559–561.

[170] Richtmyer, R. D. and Morton, K. W. (1968). *Difference methods for initial-value problems*. John Wiley & Sons, Ltd, Chichester, UK.

[171] Roads, C. (2023). *The computer music tutorial*. The MIT Press, Cambridge, Massachusetts London, second edition edition.

[172] Rokni, E., Neldner, L. M., Adkison, C., and Moore, T. R. (2017). The production of phantom partials due to nonlinearities in the structural components of the piano. *The Journal of the Acoustical Society of America*, 142(4):EL344–EL349.

[173] Rossing, T. D. (2010). *The science of string instruments*. Springer New York, New York, NY.

[174] Rowland, D. R. (2011). The potential energy density in transverse string waves depends critically on longitudinal motion. *European Journal of Physics*, 32(6):1475.

[175] Roze, D. (2022). Interactions between nonlinear resonators represented in Volterra series. *Journal of Sound and Vibration*, 520:116590.

[176] Roze, D. and Hélie, T. (2014). Introducing a Green–Volterra series formalism to solve weakly nonlinear boundary problems: Application to Kirchhoff's string. *Journal of Sound and Vibration*, 333(7):2073–2086.

[177] Roze, D., Raibaud, M., and Geoffroy, T. (2024). Passive-guaranteed modeling and simulation of a finite element nonlinear string model. In *Proceedings of the IFAC Workshop on Lagrangian and Hamiltonian Methods for Non Linear Control (LHMNC)*, pages 226–231, Besançon, France.

[178] Rubin, M. and Gottlieb, O. (1996). Numerical solutions of forced vibration and whirling of a non-linear string using the theory of a cosserat point. *Journal of Sound and Vibration*, 197(1):85–101.

[179] Ruiz, P. (1969). *A technique for simulating the vibration of strings with a digital computer*. PhD thesis, University of Illinois Urbana-Champaign.

[180] Russo, R., Ducceschi, M., and Bilbao, S. (2022). Efficient simulation of the bowed string in modal form. In *Proceedings of the International Conference on Digital Audio Effects (DAFx)*, pages 122–129, Vienna, Austria.

[181] Russo, R., Ducceschi, M., and Bilbao, S. (2023). Efficient simulation of the yaybahar using a modal approach. In *Proceedings of the 26th International Conference on Digital Audio Effects (DAFx)*, pages 69–76, Copenhagen, Denmark.

[182] Russo, R., Serafin, S., Michon, R., Orlarey, Y., and Letz, S. (2021). Introducing finite difference schemes synthesis in FAUST: A cellular automata approach. In *Proceedings of the 18th Sound and Music Computing Conference (SMC), Online*, pages 11–18.

[183] Sarigül (Aydin), A. and Aksu, G. (1986). A finite difference method for the free vibration analysis of stepped Timoshenko beams and shafts. *Mechanism and Machine Theory*, 21(1):1–12.

[184] Schelleng, J. C. (1974). The physics of the bowed string. *Scientific American*, 230(1):87–95.

[185] Schlecht, S., Parker, J., Schäfer, M., and Rabenstein, R. (2022). Physical modeling using recurrent neural networks with fast convolutional layers. In *Proceedings of the International Conference on Digital Audio Effects (DAFx)*, pages 138–145, Vienna, Austria.

[186] Serafin, S. (2004). *The sound of friction: Real-time models, playability and musical applications*. PhD thesis, Stanford University.

[187] Serafin, S., Avanzini, F., Rocchesso, D., et al. (2003). Bowed string simulation using an elasto-plastic friction model. In *Proceedings of the Stockholm Music Acoustics Conference (SMAC)*, pages 95–98, Stockholm, Sweden.

[188] Shen, J., Xu, J., and Yang, J. (2018). The scalar auxiliary variable (SAV) approach for gradient flows. *Journal of Computational Physics*, 353:407–416.

[189] Sherman, J. and Morrison, W. J. (1950). Adjustment of an inverse matrix corresponding to a change in one element of a given matrix. *Ann. Math. Stat.*, 21:124–127.

[190] Singh, H. and Wahi, P. (2017). Non-planar vibrations of a string in the presence of a boundary obstacle. *Journal of Sound and Vibration*, 389:326–349.

[191] Smith, J. (1991). Viewpoints on the history of digital synthesis. In *Proceedings of the International Computer Music Conference*, pages 1–10, Montreal, Canada.

[192] Smith, J. and Woodhouse, J. (2000). The tribology of rosin. *J. Mech. Phys. Solids*, 48:1633–1681.

[193] Smith, J. O. (1985). A new approach to digital reverberation using closed waveguide networks. In *International Computer Music Conference*, pages 47–53.

[194] Smith, J. O. (1992). Physical modeling using digital waveguides. *Computer Music Journal*, 16(4):74–91.

[195] Smith, J. O. (2010). *Physical audio signal processing*. Stanford, California. http://ccrma.stanford.edu/ jos/pasp/. Online book, accessed: October 2024.

[196] Soares, F., Antunes, J., and Debut, V. (2021). Multi-modal tuning of vibrating bars with simplified undercuts using an evolutionary optimization algorithm. *Applied Acoustics*, 173:107704.

[197] Stephen, N. G. (2002). On "a check on the accuracy of Timoshenko's beam theory". *Journal of Sound and Vibration*, 257(4):809–812.

[198] Strikwerda, J. C. (2004). *Finite difference schemes and partial differential equations*. Society for Industrial and Applied Mathematics, Philadelphia, 2nd edition.

[199] Südholt, D., Russo, R., and Serafin, S. (2021). A faust implementation of coupled finite difference schemes. In *Proceedings of the 2nd Nordic Sound and Music Conference, Copenhagen, Denmark*, pages 17–22.

[200] Ta-Tsien, L. (1994). *Global classical solutions for quasilinear hyperbolic systems*. Wiley, Michigan, USA.

[201] Thomée, V. (2001). From finite differences to finite elements: A short history of numerical analysis of partial differential equations. *Journal of Computational and Applied Mathematics*, 128(1):1–54.

[202] Thwaites, S. and Fletcher, N. H. (1981). Some notes on the clavichord. *The Journal of the Acoustical Society of America*, 69(5):1476–1483.

[203] Tolonen, T., Valimaki, V., and Karjalainen, M. (2000). Modeling of tension modulation nonlinearity in plucked strings. *IEEE Transactions on Speech and Audio Processing*, 8(3):300–310.

[204] Trautmann, L. and Rabenstein, R. (2000). Sound synthesis with tension modulated nonlinearities based on functional transformations. *Acoustics and Music: Theory and Applications (AMTA), NE Mastorakis (Ed.)*, pages 444–449.

[205] Trautmann, L. and Rabenstein, R. (2003). *Digital sound synthesis by physical modeling using the functional transformation method* . Kluwer Academic / Plenum Publishers, New York, USA.

[206] Valette, C. and Cuesta, C. (1993). *Mécanique de la corde vibrante*. Hermès, Paris.

[207] Valette, C., Cuesta, C., Castellengo, M., and Besnainou, C. (1991). The tampura bridge as a precursive wave generator. *Acta Acustica united with Acustica*, 74(3):201–208.

[208] Valimaki, V., Tolonen, T., and Karjalainen, M. (1999). Plucked-string synthesis algorithms with tension modulation nonlinearity. In *1999 IEEE International Conference on Acoustics, Speech, and Signal Processing. Proceedings. ICASSP99 (Cat. No.99CH36258)*, volume 2, pages 977–980 vol.2.

[209] van den Doel, K. and Pai, D. K. (2003). *Modal synthesis for vibrating objects*, pages 99–120. K. Greenebaum and R. Barzel (Eds.), Natick, Massachusetts.

[210] van der Schaft, A. and Jeltsema, D. (2014). Port-hamiltonian systems theory: An introductory overview. *Foundations and Trends® in Systems and Control*, 1(2-3):173–378.

[211] Van Walstijn, M. and Bridges, J. (2016). Simulation of distributed contact in string instruments: a modal expansion approach. In *2016 24th European signal processing conference (EUSIPCO)*, pages 1023–1027.

[212] Van Walstijn, M., Bridges, J., and Mehes, S. (2016). A real-time synthesis oriented tanpura model. In *Proceedings of the International Conference on Digital Audio Effects (DAFx)*, pages 175–182, Brno, Czech Republic.

[213] Van Walstijn, M. and Chatziioannou, V. (2014). Numerical simulation of tanpura string vibrations. In *Proceedings of the International Symposium on Musical Acoustics (ISMA)*, pages 609–614, Le Mans, France.

[214] Van Walstijn, M., Chatziioannou, V., and Athanasopoulos, N. (2024a). An explicit scheme for energy-stable simulation of mass-barrier collisions with contact damping and dry friction. In *Proceedings of the IFAC Workshop on Lagrangian and Hamiltonian Methods for Nonlinear Control (LHMNC)*, pages 214–219, Besançon, France.

[215] Van Walstijn, M., Chatziioannou, V., and Bhanuprakash, A. (2023). Tunable collisions: Hammer-string simulation with time-variant parameters. In *Proceedings of the International Conference of Digital Audio Effects (DAFx)*, pages 61–68, Copenhagen, Denmark.

[216] Van Walstijn, M., Chatziioannou, V., and Bhanuprakash, A. (2024b). Implicit and explicit schemes for energy-stable simulation of string vibrations with collisions: refinement, analysis, and comparison. *Journal of Sound and Vibration*, 569:117968.

[217] Vijayan, K. and Woodhouse, J. (2013). Shock transmission in a coupled beam system. *Journal of Sound and Vibration*, 332(16):3681–3695.

[218] von Helmholtz, H. L. (1862). *Die lehre von den tonempfindungen: als physiologische grundlage für die theorie der musik*. Vieweg, Braunschweig.

[219] Vyasarayani, C. P., Birkett, S., and McPhee, J. (2009). Modeling the dynamics of a vibrating string with a finite distributed unilateral constraint: Application to the sitar. *The Journal of the Acoustical Society of America*, 125(6):3673–3682.

[220] Välimäki, V., Pakarinen, J., Erkut, C., and Karjalainen, M. (2005). Discrete-time modelling of musical instruments. *Reports on Progress in Physics*, 69(1):1.

[221] Välimäki, V., Penttinen, H., Knif, J., Laurson, M., and Erkut, C. (2004). Sound synthesis of the harpsichord using a computationally efficient physical model. *EURASIP Journal on Advances in Signal Processing*, 2004(7):860718.

[222] Wheeler, G. F. and Crummett, W. P. (1987). The vibrating string controversy. *American Journal of Physics*, 55(1):33–37.

[223] Willemsen, S. (2021). *The emulated ensemble: Real-time simulation of musical instruments using finite-difference time-domain methods*. PhD thesis, Aalborg University.

[224] Willemsen, S., Andersson, N., Serafin, S., and Bilbao, S. (2019a). Real-time control of large-scale modular physical models using the Sensel Morph. In *Proceedings of the Sound and Music Computing Conference (SMC)*, pages 151–158.

[225] Willemsen, S., Bilbao, S., and Serafin, S. (2019b). Real-time implementation of an elasto-plastic friction model applied to stiff strings using finite difference schemes. In *Proceedings of the International Conference on Digital Audio Fffects (DAFx)*, pages 40–46.

[226] Woinowsky-Krieger, S. (1950). The effect of an axial force on the vibration of hinged bars. *Journal of Applied Mechanics*, 17(1):35–36.

[227] Woodhouse, J. (2003). Bowed string simulation using a thermal friction model. *Acta Acustica united with Acustica*, 89(2):355–368.

[228] Wriggers, P. (2006). *Computational contact mechanics: with 12 tables*. Springer, Berlin Heidelberg, 2nd edition.

[229] Yang, X. (2016). Linear, first and second-order, unconditionally energy stable numerical schemes for the phase field model of homopolymer blends. *Journal of Computational Physics*, 327:294–316.

[230] Yang, X. and Ju, L. (2017). Linear and unconditionally energy stable schemes for the binary fluid–surfactant phase field model. *Computer Methods in Applied Mechanics and Engineering*, 318:1005–1029.

[231] Zama, F., Ducceschi, M., and Bilbao, S. (2024). Role of shift constant in energy shifted SAV for hamiltonian systems. *Journal of Physics: Conference Series*, 2701(1):012089.

[232] Zhang, Q., Ye, L., and Pan, Z. (2005). Physically-based sound synthesis on gpus. In *Proceedings of the International Conference on Entertainment Computing (ICEC)*, pages 328–333, Sanda, Japan.

[233] Zhao, J., Wang, Q., and Yang, X. (2017). Numerical approximations for a phase field dendritic crystal growth model based on the invariant energy quadratization approach. *International Journal for Numerical Methods in Engineering*, 110(3):279–300.